

# **Defects and Interfaces: Their Role during Phase Transformations in Aluminium-Silver Alloys**



**Zezhong Zhang**

Department of Materials Science and Engineering  
Monash University

This thesis is submitted for the degree of  
*Doctor of Philosophy*

June 2018



## **Copyright Notices**

### **Notice 1**

©Zezhong Zhang (2018)

Under the Copyright Act 1968, this thesis must be used only under the normal conditions of scholarly fair dealing. In particular, no results or conclusions should be extracted from it, nor should it be copied or closely paraphrased in whole or in part without the written consent of the author. Properly written acknowledgement should be made for any assistance obtained from this thesis.

### **Notice 2**

©Zezhong Zhang (2018)

I certify that I have made all reasonable efforts to secure copyright permissions for third-party content included in this thesis and have not knowingly added copyright content to my work without the owner's permission.



To my loving parents.



## **Declaration**

I hereby declare that except where specific reference is made to the work of others, the contents of this thesis are original and have not been submitted in whole or in part for consideration for any other degree or qualification in this, or any other university. In particular, I independently performed the alloy processing, electron microscopy, simulations, calculations and analysis presented in this thesis. This thesis is my own work and contains nothing which is the outcome of work done in collaboration with others, except as specified in the text and Acknowledgements.

---

Zezhong Zhang  
June 2018



## Acknowledgements

I wish to express my sincere thanks to Laure Bourgeois and Nikhil V. Medhekar for their unconditional support and guidance throughout my PhD. I always feel fortunate with such good supervisors and project that I can see the beauty of science.

My gratitude also extends to Matthew Weyland for his training on electron tomography and aberration-corrected instrument, Scott Findlay for his help on image simulations, Tim Williams, Russell King, Renji Pan and Yu Chen for their training and assistance. I want to thank Tianyu Liu for a Gatan Digital Micrograph script, Changlin Zhen for his suggestions on quantitative STEM, Peter Miller for X-ray absorption analysis, Jonathan Peter for discussing geometric phase analysis, Yueming Guo for discussing electron diffraction theory, Yuefeng Yin and Runhong Huang for helps on supercomputation, Yong Zhang for his support and day-to-day discussions, Julian M. Rosalie and Xiang Gao for alloy casting, Jian-Feng Nie and Ian Polmear for metallurgy discussions and advice, Philip N.H. Nakashima and Nick Birbilis for encouragement, Jane Moodie, Espen Bojesen, Yiqiang Chen and Xuan Chen for reading manuscripts.

I am thankful to Monash University for a Monash Graduate Scholarship, a Monash International Postgraduate Research Scholarship and a Monash Centre for Electron Microscopy Postgraduate Scholarship.

I acknowledge the funding from the Australian Research Council (LE0454166, LE110100223), the Victorian State Government and Monash University for instrumentation, and use of the facilities within the Monash Centre for Electron Microscopy. Grateful acknowledgement also goes to the computational support from Monash Sun Grid cluster, the National Computing Infrastructure and Pawsey Supercomputing Centre.

I place my sense of gratitude to one and all, who directly or indirectly, have their assistance in this adventure.



## Abstract

Physical metallurgy concerns the fundamentals and applications of phase transformations – the process by which atoms arrange themselves from one structure to another in metallic systems. Al-Ag alloys have served as a textbook system for understanding solid-state phase transformations. Apart from being a model system, Ag is an important micro-alloying element in various high-strength aluminium alloys. Using scanning transmission electron microscopy (STEM) and atomistic calculations, we revisited the phase transformations associated with solid-state precipitation in the Al-Ag system. This thesis aims to understand the role of defects and interfaces during phase transformations and suggest how these can be used to tailor precipitation behaviour.

Using conventional heat treatments, the face-centred cubic (FCC) GP zone  $\epsilon$  phase and the hexagonal close-packed (HCP)  $\gamma'$  phase were studied in details. GP zone  $\epsilon$  displays an inhomogeneous modulated Ag distribution, in contrast to the “core-shell” model proposed many years ago. Meanwhile,  $\gamma'$  phase nucleates heterogeneously on the quenched-in defects as previously reported. We studied the atomic mechanisms of  $\gamma'$  nucleation on frank dislocation loops via electron tomography and atomistic simulations. Interestingly, those precipitate assemblies did not coarsen with increasing ageing time until being replaced by individual  $\gamma'$  precipitates. Quenched-in voids were found to be embedded within GP zones  $\epsilon$ , the collapse of which led to the rare appearance of a new ordered phase. Realising the importance of defects during phase transformations, we explored ways to manipulate them. By adjusting the quenching media, we reduced the quenched-in defects and hence suppressed  $\gamma'$  nucleation. Building upon conventional heat treatments, we developed a new processing strategy to manipulate phase transformation pathways through the interaction between defects and pre-existing phases. Defects were introduced to pre-aged alloys and secondary ageing was performed. Using this strategy for both nanoscale and bulk samples, we discovered a new precipitate phase  $\zeta$  in the Al-Ag system. This study casts light on microstructure design via the phase transformations induced by lattice defects. Moreover, the associated mechanism is potentially relevant to the alloy stabilities against environmental degradation.

The newly discovered  $\zeta$  phase has a characteristic bi-layered structure enriched in Al and Ag on alternating the close-packed planes. A wide range of advanced microscopy techniques was used, which showed that the  $\zeta$  phase has a space group of  $R\bar{3}m$ , a composition close to AgAl and alternating inter-planar spacing echoing the bi-layered chemistry. In addition, in-situ STEM experiments revealed the  $\zeta$  phase is an intermediate phase between the FCC  $\epsilon$  GP zone and the HCP  $\gamma'$  phase. High-resolution time-resolved STEM also manifested the role of defects during phase transformations. According to our first-principles calculations, the structure of the  $\zeta$  phase can be understood in terms of Ag's preferred clustering configurations in Al. The intrinsic properties of Ag clustering are strongly related to the Ag segregation at precipitate interfaces in various aluminium alloys, including some of the highest strength alloys currently in service.

The FCC/HCP interface of  $\gamma'/\gamma$  ( $\text{Ag}_2\text{Al}$ ) precipitate is another classic topic investigated in this thesis. It is well accepted that the growth of  $\gamma'$  precipitate involves the movement of Shockley partial dislocations ( $\vec{b} = 1/6\langle 112 \rangle$ ) at the interfaces. The coherent interface ( $\{0001\}_{\gamma'} \parallel \{111\}_{\text{Al}}$ ) was shown to have strong Ag segregation at the early stages of  $\gamma'$  precipitation. Our first-principles calculations explained the Ag segregation with interfacial energy reduction for a thin  $\gamma'$  precipitate. Two types of semicoherent interfaces ( $\{1\bar{1}00\}_{\gamma'} \parallel \{112\}_{\text{Al}}$ ) were identified, both of which are reconstructed by nano-facets parallel to low-index planes ( $\{10\bar{1}1\}_{\gamma'} \parallel \{111\}_{\text{Al}}$  and  $\{10\bar{1}1\}_{\gamma'} \parallel \{002\}_{\text{Al}}$ ) and involve distinct Ag depletions periodically spaced along the interfaces. The observed interfacial reconstruction was explained with DFT-deduced interfacial energies. The experimentally-informed 3D models of the semi-coherent interfaces were built by locating the atomic positions on HAADF-STEM images and applying periodicities in the viewing direction. Burgers vector analysis was performed for those 3D models and Shockley partial dislocations ( $\vec{b} = 1/6\langle 112 \rangle$ ) were revealed at the Type-I interface as expected. However, our atomistic simulations suggested that the three Shockley partial dislocations can react into a  $90^\circ$  Shockley partial dislocation, a Lomer-Cottrell dislocation ( $\vec{b} = 1/6\langle 110 \rangle$ ) and a Hirth dislocation ( $\vec{b} = 1/3\langle 001 \rangle$ ), which may be present at the Type-II interface. Sessile dislocations were found at the precipitate-precipitate junctions. Depending on the contacting angle, two Shockley partial dislocations react to form a Lomer-Cottrell dislocation ( $\vec{b} = 1/6\langle 110 \rangle$ ) or a Hirth dislocation ( $\vec{b} = 1/3\langle 001 \rangle$ ). Interestingly, each type of dislocation is associated with a unique chemical distribution at the dislocation core. Our bulk and in-situ heat treatments demonstrated different growth behaviours of  $\gamma'$  precipitate phase with different interfacial structures. This study points a direction of controlling precipitation through the nature of interfacial dislocations.

# Table of contents

<b>List of figures</b>	<b>xvii</b>
<b>List of tables</b>	<b>xxxix</b>
<b>1 Introduction</b>	<b>1</b>
1.1 A Brief History of Precipitation Hardening . . . . .	1
1.2 Open Questions about Precipitation . . . . .	2
1.3 Why Al-Ag Alloys? . . . . .	4
1.4 Aims of this Research . . . . .	5
1.5 Overview of the Thesis . . . . .	6
<b>2 Literature Review</b>	<b>7</b>
2.1 Precipitation in Aluminium Alloys . . . . .	8
2.1.1 The Dynamic Nature of Precipitation . . . . .	8
2.1.2 Precipitation Control via the Engineering of Interfacial Structure . .	11
2.1.3 Precipitation Control via Introduced Defects . . . . .	17
2.2 The Al-Ag Alloy System . . . . .	22
2.2.1 The Binary Al-Ag System . . . . .	22
2.2.1.1 FCC Phases: GP zones $\epsilon$ and $\eta$ . . . . .	25
2.2.1.2 HCP Phases: $\gamma'/\gamma$ . . . . .	26
2.2.1.3 Predicted Phases and Phase Diagrams . . . . .	41
2.2.2 Multi-element Aluminium Alloys with Ag Additions . . . . .	41
2.3 Characterisation and Modelling Strategies . . . . .	52
2.4 Summary and Research Scope . . . . .	55
<b>3 Research Methods</b>	<b>57</b>
3.1 Alloy Fabrication, Treatments and Processing . . . . .	58
3.2 Transmission Electron Microscopy . . . . .	59
3.2.1 Microscopes and Imaging Conditions . . . . .	61

3.2.2	Aberration Correction for Scanning Transmission Electron Microscopy	62
3.2.3	<i>In situ</i> Scanning Transmission Electron Microscopy . . . . .	65
3.2.4	Electron Tomography . . . . .	65
3.2.5	Energy Dispersive X-ray Spectroscopy . . . . .	68
3.2.6	Image and Diffraction Pattern Simulations . . . . .	71
3.2.7	Quantitative Scanning Transmission Electron Microscopy . . . . .	74
3.2.8	Atomic Positions Refinement and Experimentally-informed Model Building . . . . .	76
3.2.9	Geometric Phase Analysis . . . . .	77
3.3	Atomistic Calculations . . . . .	78
3.3.1	Density Functional Theory . . . . .	79
3.3.2	Embedded Atom Method . . . . .	86
3.3.3	Local Structure Identification . . . . .	87
3.3.4	Dislocation Identification . . . . .	88
<b>4</b>	<b>Modifying Phase Transformation Pathways through the Interaction Between Defects and Pre-existing Phases</b>	<b>91</b>
4.1	Introduction . . . . .	91
4.2	The Microstructure of Conventional Heat Treatments . . . . .	92
4.2.1	Overview . . . . .	92
4.2.2	Nucleation and Growth of $\gamma'$ Precipitate Phase . . . . .	94
4.2.3	Nucleation and Growth of GP Zones $\epsilon$ . . . . .	97
4.3	Defects-induced Phase Transformations on Pre-existing Phases . . . . .	105
4.3.1	Nanoscale Processing: <i>In-situ</i> Annealing . . . . .	105
4.3.2	Bulk Processing: Deformation and Secondary Ageing . . . . .	107
4.4	Discussion . . . . .	110
4.5	Conclusions . . . . .	113
<b>5</b>	<b>Atomic Structure and Phase Transformations of The Bi-layered Precipitate <math>\zeta</math> Phase</b>	<b>115</b>
5.1	Introduction . . . . .	115
5.2	Atomic Structure: HAADF-STEM Imaging, Simulation and Analysis . . . . .	116
5.3	Transformation Pathways: <i>In-situ</i> Scanning Transmission Electron Microscopy	127
5.4	Thermodynamics: First-principles Calculations, Strain Energy and Entropy	131
5.5	Discussion . . . . .	135
5.6	Conclusion . . . . .	137

---

<b>6</b>	<b>Interfacial Structures of the HCP Precipitate <math>\gamma'/\gamma</math> Phases</b>	<b>139</b>
6.1	Introduction . . . . .	139
6.2	The Coherent Precipitate-Matrix Interface . . . . .	140
6.3	The Semicoherent Precipitate-Matrix Interface . . . . .	145
6.4	Precipitate-Precipitate Junctions . . . . .	155
6.5	Discussion . . . . .	161
6.6	Conclusion . . . . .	166
<b>7</b>	<b>Conclusions and Future Work</b>	<b>167</b>
7.1	Modifying Phase Transformation Pathways through the Interaction Between Defects and Pre-existing Phases . . . . .	168
7.2	Atomic Structure and Phase Transformations of The Bi-layered Precipitate $\zeta$ Phase . . . . .	169
7.3	Interfacial Structures of the HCP Precipitate $\gamma'/\gamma$ Phases . . . . .	170
7.4	Future Work . . . . .	171
	<b>References</b>	<b>173</b>
	<b>Appendix A Thermodynamics and Kinetics of Interfaces during Precipitation</b>	<b>189</b>
A.1	Interfaces in General . . . . .	189
A.2	Nucleation . . . . .	190
A.3	Growth . . . . .	196
A.4	Coarsening . . . . .	199
	<b>Appendix B Publication List</b>	<b>201</b>



# List of figures

1.1	(a) The Wright engine cast by an Al-8 wt.% Cu alloy. Courtesy: The Library of Congress, USA. (b) First flight of the Wright Flyer I, December 17, 1903, Orville piloting, Wilbur running at wingtip. Courtesy: J. T. Daniels. . . . .	2
1.2	(a) External liquid fuel tank for launching the space shuttle. (b) Self-portrait of Curiosity (a car-sized rover) at the foothill of Mount Sharp, Mars. (c) Orion spacecraft orbiting around the earth, aiming to facilitate human exploration of asteroids and of Mars. Courtesy: NASA. . . . .	4
2.1	(a) Al-rich side of the Al-Cu binary phase diagram, (b-e) Structure and morphology of GP zone, $\theta''$ , $\theta'$ and $\theta$ respectively, where $\circ$ represents Al and $\cdot$ represents Cu. Reprinted from Ref. [15], p. 293 with permission from Taylor & Francis. . . . .	8
2.2	Hardness <i>versus</i> time for Al-Cu alloys with various compositions at (a) 130°C and (b) 190°C. Reprinted from Ref. [7]. Courtesy: J. M. Silcock, T. Heal and H. K. Hardy. . . . .	9
2.3	Schematic diagram showing the topological arrangement of precipitates and the strengthening contribution. (a) circular plates on $\{100\}_{Al}$ planes and (b) its projection in a $\{111\}_{Al}$ plane as the slip plane; (c) circular plates on $\{111\}_{Al}$ planes; (d) $\langle 100 \rangle_{Al}$ rods. (e) Variation in the ratio of critical resolved shear stress $\Delta\tau$ (plate, rod)/ $\Delta\tau$ (sphere) with aspect ratio for Orowan strengthening attributable to $\{111\}_{Al}$ and $\{100\}_{Al}$ precipitate plates and $\langle 100 \rangle_{Al}$ precipitate rods. The volume fraction of precipitates is 0.05. Reprinted from Ref. [4], p. 64 and Ref. [9], p.2058 with permission from Elsevier. . . . .	10
2.4	HAADF-STEM images showing (a) segregation of Cu atoms in the coherent interface of $\theta'$ precipitates in the combination of crystal models and STEM simulations (viewing $\langle 100 \rangle_{Al}$ ); (b,c) complex semicoherent interface of $\theta'$ ((viewing $\langle 100 \rangle_{Al}$ ) and $\langle 110 \rangle_{Al}$ ) respectively). Reprinted from Ref. [11, 12] with permission from Elsevier and American Physical Society. . . . .	11

2.5	First-principles calculated nearest-neighbour solute–vacancy binding energies as a function of the solute impurity volume. The impurity volume is calculated from the change in volume upon adding a single solute impurity to pure Al. Note the correlation between solute–vacancy binding and size of the impurity atoms, with larger solutes having a larger binding energy with vacancies. The correlation is particularly clear if one excludes the 3d transition metals, Sc–Zn, connected by dashed lines. Reprinted from Ref. [24] with permission from Elsevier. . . . .	13
2.6	(a) Age hardening response of Al-4Cu and Al-4Cu-0.05Sn(wt.%) alloys at 130° and 190°C. Taken from Ref. [25] with courtesy: H. K. Hardy. TEM images showing the distribution of $\theta'$ precipitate in peak-aged samples of (b) Al-4Cu, and (c) Al-4Cu-0.05Sn (wt.%) alloys. Reprinted from Ref. [9], p. 2027 with permission from Elsevier. . . . .	13
2.7	An early-stage $\theta'$ precipitate with 4 unit cells thick found in an Al-Cu-Au alloy aged at 160 °C for 3 h: (a) atomic-resolution ADF imaging, and the background-subtracted X-ray maps (b) Cu- $K_\alpha$ and (c) the Au- $L_\alpha$ for the white dashed region in (a). (d) Vickers hardness curve of the binary Al-1.7Cu and ternary Al-1.7Cu-0.02Au (at.%) alloys aged at 160 °C. Reprinted from Ref. [31] with permission from Elsevier. . . . .	14
2.8	HAADF-STEM images of (a) the S phase, reprinted from Ref. [34] with permission from Elsevier, and (b) the $\Omega$ phase, reprinted from Ref. [20] with permission from Elsevier. (c) Age hardening response of Al–2.5Cu–1.5 Mg and Al–2.5Cu–1.5Mg–0.5Ag (wt%) alloys, reprinted from Ref. [19] with permission from Nature. (d) Atom probe tomography showing segregation of Mg and Ag atoms at the $\Omega$ -Al interface. Mg and Ag atoms are represented by green and yellow colour respectively, reprinted from Ref. [35] with permission from Elsevier. . . . .	15
2.9	Schematic diagrams showing (a and c) heat treatment schemes for age hardening, and (b) part of a binary phase diagram for precipitation hardenable alloys. Adapted from Ref. [9], p.2010 with permission from Elsevier. . . . .	18
2.10	(a) Thin plates of the $T_1$ phase ( $\text{Al}_2\text{CuLi}$ ) in an Al–Li–Cu–Zr alloy overaged (500 h) at 170°C. Courtesy: Gregson, P. J. (b) Atomic-resolution high-angle annular dark-field scanning transmission electron microscopy images and simulated images and the structural model of $T_1$ . From Ref. [45], reprinted by permission from American Physical Society. . . . .	20

- 
- 2.11 Schematic illustration of the atomic layer stackings for (a) face-centred cubic (FCC) structure and (b) hexagonal close-packed (HCP) structure. Redrawn from Ref. [48], p.1086. . . . . 22
- 2.12 The equilibrium Ag-Al phase diagram. From Ref. [52], reprinted by permission from Springer. . . . . 24
- 2.13 The partial phase diagram in the Al-enriched side showing the asymmetric miscibility gap of GP zones. Adapted from Ref. [52] with permission from Springer. . . . . 24
- 2.14 The coherent spinodal and the nucleation energy barrier  $\Delta G^*=25kT$  curve in FCC Al-Ag, based upon (a) the calculated GP zone solvus and (b) the experimental GP zone solvus. From Ref.[57], reprinted by permission from Elsevier. . . . . 26
- 2.15 GP zones are readily sheared by moving dislocations in ECAP processed Al-Ag alloys. (a) Reconstructed 3D volume; (b) enlarged view from the boxed region in (a). (c) High-resolution TEM image obtained from a similar region showing ellipsoidal GP zones within the shear band, clearly indicated by the black dotted lines. From Ref.[50], reprinted by permission from Elsevier. 27
- 2.16 Quantification of HAADF STEM images. (a) Experimental HAADF STEM image of nanometre-sized Ag clusters embedded in an Al matrix in  $[10\bar{1}]$  zone-axis orientation, together with the corresponding electron diffraction pattern. (b) Simulated image of the boxed region by Gaussian peak fitting. (c) The number of Ag atoms per column. (d) The computed 3D reconstruction. From Ref.[51], reprinted by permission from Nature. . . . . 27
- 2.17 Crystal structures of phases in Al-Ag alloys. (a) Structure of solid solution matrix (FCC), (b) structure of transition phase  $\gamma'$  (HCP), and (c) structure of equilibrium precipitate phase,  $\gamma$  (HCP). From Ref.[67] Used with permission of The Minerals, Metals & Materials Society. . . . . 28
- 2.18 Proposed atomic structures of  $\gamma$  phase ( $Ag_2Al$ ): (a) Neumann's model [68] and (b) Howe's model [69]. . . . . 28
- 2.19 Two  $\langle 110 \rangle_{Al} // \langle 11\bar{2}0 \rangle_{\gamma'}$  CBED patterns obtained from  $\gamma'$  precipitates. The 000L, L=odd, precipitate reflections in (a) display strong uniform intensities, indicating that they are allowed, while the same reflections in (b) contain G-M lines, indicating that they are kinematically forbidden. Reprinted from Ref.[69] with permission from Taylor & Francis. . . . . 29

- 2.20 HAADF-STEM images and simulations for (a) ordered and (b) disordered  $\gamma'$  precipitates. The recorded image (labelled “Exp”) is compared with simulations for foil thicknesses of 14–70 nm. The red outline indicates a single HCP unit cell. From Ref.[70], reprinted by permission from Elsevier. 30
- 2.21 Convergent beam electron diffraction patterns of a  $\gamma'$  precipitate. (a) A HAADF-STEM image of the region of interest. (b) The CBED pattern for the matrix adjacent to the precipitate. (c) A CBED pattern from the  $\gamma'$  precipitate. The main diffraction discs are assigned in (d). Filled and open circles indicate matrix and precipitate reflections, respectively. Note the absence of diffraction intensity in the  $\pm 0001$  positions (labelled “x” in (d)). From Ref.[70], reprinted by permission from Elsevier. . . . . 31
- 2.22 (a) TEM image of an HCP  $\gamma'$  precipitate viewed edge-on along  $\langle 110 \rangle_{Al}$ . From Ref. [75], reprinted by permission from Elsevier. (b) SEM image of an  $Ag_2Al$  precipitate in a deeply etched Al matrix after ageing at 410°C for 430 h, elucidating its characteristic hexagonal shape. From Ref. [76], reprinted by permission from Elsevier. . . . . 32
- 2.23 Schematic illustration of the shape-change accompanying the nucleation of an HCP phase in an FCC matrix. (a) Atomic model showing three Burgers vectors of  $1/6\langle 112 \rangle$  on the close-packed planes to transform FCC (ABCABC stacking) to HCP (ABAB stacking) viewed in a  $\langle 111 \rangle$  direction. (b) I: shown as a series of stacking disks on  $\{111\}$  habit planes, each representing a single close-packed layer; II: the precipitate is sheared in one direction, resulting in a considerable shape change of  $\sim 0.35$ , and consequently high shear strain energy; III: the precipitate are sheared through three Shockley partial dislocations and achieves self-accommodation. Reprinted from Ref. [15, 77] with permission from Taylor & Francis and J. M. Rosalie. . . . . 33

- 2.24  $\gamma'$  precipitation on helical dislocations. (a) TEM image showing the microstructure of an Al-16 wt.% Ag (equivalently Al-4.5 at.% Ag) sample aged at 160°C for 1 day after water quenching from 520°C. From Ref. [54], reprinted by permission from Elsevier. (b and c) Schematic diagrams describing the nucleation and growth of  $\gamma'$  on a helical dislocation. The helical dislocation has Burgers vector  $\vec{b}=1/2\langle 110 \rangle$  and helical axis of  $\langle 110 \rangle_{\text{Al}}$ . The loop dissociates into two Shockley partial dislocations with a narrow stacking fault separating them. The absorption of silver on the stacking fault leads to the formation of  $\gamma'$ . The length of the  $\gamma'$  precipitate,  $l$ , however, is limited by the diameter of the helix. From Ref. [78], p. 11 with permission from J. M. Rosalie. . . . . 34
- 2.25 (a) Hexagonal Frank dislocation loop viewed along a  $\langle 111 \rangle_{\text{Al}}$  direction. (b) The dissociation of a Frank dislocation loop into Shockley partial dislocations and Lomer–Cottrell dislocations, viewed along a  $\langle 110 \rangle_{\text{Al}}$  direction. Taken from Ref. [78], p. 10. (c) The  $\gamma'$  precipitate assemblies at the early stage of ageing (0.5 h at 200°C for an Al-1.7 at.%Ag alloy), where the arrows indicate the peripheral precipitate with diffuse contrast in addition to the central precipitate. From Ref. [78], p. 49. (d) The  $\gamma'$  assemblies after ageing at 200°C for 8 h for an Al-1.7 at.%Ag alloy, where peripheral precipitates (labelled P) are comparable with the centre precipitate (labelled C). Tilting experiments showed that the apparent overlap of precipitates at points A and B was an effect of projection. From Ref. [81], p. 49, 51, 138 reprinted with permission from J. M. Rosalie. . . . . 35
- 2.26 The lengthening of a  $\gamma'$  embedded within a TEM foil through the ledge mechanism while *in situ* annealed at 350°C. The electron beam direction was parallel to  $\langle 111 \rangle_{\text{Al}}$ . Reprinted from Ref. [49] with permission from Elsevier. 37
- 2.27 (a) TEM image showing a series of single-atom ledges migrating on the coherent interfaces of a  $\gamma'$  precipitate. (b) Atomically smooth solid-solid interface with atoms represented by cubes, illustrating the terrace-ledge-kink mechanism growth. Reprinted from Ref. [69] with permission from Taylor & Francis. . . . . 37
- 2.28 HAADF-STEM images and simulations of Ag segregation to the coherent interface of a 3 unit cell  $\gamma'$  precipitate. Reprinted from Ref. [70] with permission from Elsevier. . . . . 39

- 2.29 High-resolution TEM image showing the saw-tooth semicoherent interface, as indicated by lines and arrows. Reprinted from Ref. [84], p.234 with permission from J. M. Howe. HAADF-STEM image showing periodic Ag depletion at the saw-tooth interface, as indicated by asterisks. Reprinted from Ref. [70] with permission from Elsevier. . . . . 40
- 2.30 First-principles calculated composition-temperature phase diagram for (a) the FCC-based structure, reprinted from Ref. [58] with permission from Elsevier; and (b) the HCP-based structure in the Ag-Al system, reprinted from Ref. [74] with permission from American Physical Society. . . . . 41
- 2.31 Predicted AgAl phases with (a) FCC-based structure [88] and (b) HCP-based structure [74]. Black solid lines indicate the unit cells of the predicted AgAl phases with the prescribed chemical stacking, while grey dashed lines indicate the cubic or trigonal/hexagonal unit cell of the original FCC and HCP structures. Solid and dashed circles indicate atoms at different heights along the viewing directions. . . . . 42
- 2.32 HAADF-STEM showing the cross-section of an Ag-containing  $\beta'$  precipitate in an Al-Mg-Si-Ag alloy. The white box delimits an area shown enlarged in (b), where the anti-phase boundary and periodicity of Ag occupancies are indicated. Reprinted from Ref. [92] with permission from Taylor & Francis. 43
- 2.33 (a) HAADF-STEM image showing the cross-section of a Q phase precipitate in an Al-Mg-Si-Cu alloy. Reprinted from Ref. [93] with permission from Elsevier. (b) Original and (c) Fourier-filtered HAADF-STEM images showing the cross-section of a C phase precipitate in an Al-Mg-Si-Cu alloy. Image courtesy: M. Fiawoo. Atomic-resolution (d) ADF and (e) EDS images of a Q phase, using non-rigid registration and symmetry average techniques to correct non-linear distortion. Reprinted from Ref. [94] with permission from Elsevier. . . . . 44
- 2.34 (a) and (b) HAADF-STEM images of the cross-section of a  $Q'$  phase precipitate in an Al-Mg-Si-Cu-Ag alloy, taken respectively before and during the STEM-EELS acquisition. (c) and (d) EELS elemental maps of Cu and Ag. The locations of Cu atomic columns are indicated by yellow circles while areas rich in Ag are indicated by blue circles as marked in (b). Reprinted from Ref. [95] with permission from Elsevier. . . . . 45

- 2.35 (a) and (b) HAADF-STEM images of the cross-section of a *C* precipitate phase in an Al-Mg-Si-Cu-Ag alloy, taken respectively before and during the STEM-EELS acquisition. (c) and (d) EELS elemental maps of Cu and Ag in areas marked in (a). The location of Cu atomic columns and areas rich in Ag are marked in (b). Cu columns in a *C* phase are connected by lines. Reprinted from Ref. [95] with permission from Elsevier. . . . . 46
- 2.36 TEM images of the vicinity of grain boundaries in the (a) Al-Zn-Mg ternary and (b) Al-Zn-Mg-Ag alloys aged at 160°C for 1 hr. Reprinted from Ref. [97] with permission from Elsevier. . . . . 46
- 2.37 HAADF-STEM showing precipitate assembly formed on the dislocations loops on  $\{110\}_{\text{Al}}$  planes. (a) Low-magnification image showing two  $\theta'$  precipitates formed at the end of the assemblies with zig-zag  $\gamma'$  precipitates in between. (b) High-magnification showing bi-layer Ag segregation to  $\theta'$  precipitate interfaces. Reprinted from Ref. [85] with permission from Elsevier. 47
- 2.38 Segregation of a single layer of Ag atoms at the  $\Omega$ /matrix interface. Atoms of Ag, Mg, Cu, and Al are coloured in white, green, red/yellow/orange, and blue, respectively, in the schematic diagram. Adapted from Ref. [13] with permission from Elsevier. . . . . 49
- 2.39 (a) HAADF-STEM images showing the cross-section of the Z phase along  $\langle 100 \rangle_{\text{Al}}$  in a base Al-Mg-Cu alloys. (b) HAADF-STEM images showing icosahedral quasi-crystalline of Z phase along  $\langle 112 \rangle_{\text{Al}}$  in an Ag-added alloy. Reprinted from Ref. [101] with permission from Elsevier. . . . . 50
- 2.40 (a) HAADF-STEM images showing Ag segregation to the  $T_1$  phase along  $\langle 112 \rangle_{\text{Al}}$  in an Al-Cu-Li-Mg-Ag alloy. Reprinted from Ref. [46] with permission from Elsevier. (b) Atom probe map showing segregation of silver atoms in the  $T_1$ /matrix interface in alloy AA2198 (Al-Cu-Li-Mg-Ag-Zr), where green and black dots represent magnesium and silver atoms respectively. Reprinted from Ref. [108] with permission from Elsevier. . . . . 51
- 3.1 (a) Selection of heat treatment temperatures in reference to the Al-Ag phase diagram, adapted from Ref. [52] with permission from Springer. (b) Schematic diagram illustrating the conventional processing (involves solutionising, quenching and ageing) and the new scheme (deform the pre-aged alloys and perform secondary ageing). . . . . 58

- 3.2 (a) Schematic diagram illustrating the semi-convergence angle of an electron probe and collection semi-angles for the bright field (BF) and high-angle annular dark-field (HAADF) in scanning transmission electron microscopy (STEM). (b) A diffraction pattern demonstrates the angular coverage of BF (40 mrad) and HAADF (55-200 mrad) detectors used in the Titan<sup>3</sup> FEGTEM. 61
- 3.3 (a) Ray diagram illustrating spherical aberration, which causes deviation from the perfect wavefront. As a result, the rays will not come back to a single point in the Gaussian image plane, instead, they form a disk. The smallest disk along the optical axis is formed at the plane of least confusion. Reprinted from Ref. [16], p. 103 with permission from Springer. (b) The contributions from the diffraction limit, source size and lens spherical aberration to the probe size as a function of the convergence semi-angle, reprinted from Ref. [16], p. 84 with permission from Springer. (c) Ronchigrams and probes with spherical aberrations of 1  $\mu\text{m}$  and 1 mm (with 0.7  $\text{\AA}$  source radius and no other aberrations), simulated by the Dr. Probe light software [123] with kind license from J. Barthel. . . . . 63
- 3.4 (a-b) Zemlin tableau for measurement of aberration coefficients. It consists of an initial STEM image and deconvoluted under- and over-focused probe shapes obtained at different incident directions with a given tilt angle. (c) Phase plate calculated from aberration measurements and condenser aperture (CA) applied. In this particular case, B2 aberration limits the  $\pi/4$  phase shift at 20 mrad, A4 aberration limits the  $12\pi$  phase shift at 57 mrad, and the condenser aperture with a convergence semi-angle of 15 mrad is applied. (d) HAADF-STEM of gold nano-particles captured after aberration correction and (e) its fast Fourier transform (FFT) showing the frequencies up to 0.83  $\text{\AA}^{-1}$ , or equivalently 1.2  $\text{\AA}$  resolution in real space, were obtained. . . . . 64
- 3.5 (a) The Radon transformation defines the projection of an object D in Cartesian space (x,y) through the line integral L (in all possible angles). (b-c) Demonstration of Radon transformation, for an object over a full range of tilt  $\theta \pm 180^\circ$ . The circled point in the Cartesian space becomes a sinusoidal line in Radon space, as indicated by dashed lines. The amplitude of the line in  $l$  is a function of its distance from the centre of the volume. Reprinted from Ref. [113], p.345 with permission from Springer. . . . . 66

- 3.6 (a) Illustration of the two-stage tomography process with (left) acquisition of an ensemble of images (projections) about a single tilt axis and (right) the back-projection of these images into 3D object space. (b) Representation in Fourier space of the ensemble of projections, indicating the undersampling of high-spatial-frequency information and the missing wedge of information brought about by a restricted tilt range.  $\theta$  is the tilt increment between successive images and  $\alpha$  is the maximum tilt angle. Reprinted from Ref. [125] with permission from Nature. . . . . 67
- 3.7 Compositional analysis for an embedded, spherical precipitate by energy-dispersive X-ray spectroscopy (EDXS). (a) HAADF-STEM image showing the measurements of a precipitate. The diameter of a precipitate,  $d$ , in the electron transmission direction was estimated by its averaged size on the HAADF-STEM image. The electron beam was parallel to  $\langle 110 \rangle_{\text{Al}}$ . (b) The thickness,  $t$ , in the vicinity of a precipitate was determined by comparing an on-zone position-averaged convergent beam electron diffraction (PACBED) pattern of its surrounding matrix with simulations (Titan, 300 KeV). (c) A position-averaged spectrum was taken at the centre of the precipitate and the composition was quantified by the software supplied with TEM, using the Cliff-Lorimer ratio method. The sample was tilted away from its zone axis to the optimal angle for EDXS detector and avoiding strong dynamical diffraction conditions (the electron channelling would be problematic otherwise). We ignored the thin oxide film on the sample surface. (d) A schematic diagram illustrating the parameters needed for determining the composition as written in the Eq. 3.7. . . . . 69
- 3.8 Calculated X-ray transmission spectrum for Al with different thicknesses [131], showing the absorption of Ag characteristic peak  $L_{\alpha}=3$  KeV is negligible in a thin Al foil ( $\sim 2\%$  for 100 nm or  $\sim 5\%$  for 200 nm). . . . . 70
- 3.9 (a) Schematic diagram demonstrating the projection of atomic potentials within each finite slice. (b) Schematic diagram demonstrating the propagation of electron wave from one slice to the next. The wavefront at the depth  $Z$  is scattered by the projected atomic potentials and emits a spherically outgoing wave, which contributes to the wave front of the next slice. Reprinted from Ref. [136], p, 138 with permission from Springer. . . . . 72
- 3.10 Mapping of the HAADF detector response with the efficiency normalised against the averaged intensity of the active area. . . . . 75

- 3.11 The workflow of density functional theory calculations. At first, a trial density  $n(\vec{r})$  is proposed with the input atomic structures, which is used to construct the effective potential  $V_{eff}(\vec{r})$ . The Kohn-Sham equation is solved with the effective potential, which yields the wave function  $\psi_i(\vec{r})$  and the corresponding energy  $E_{tot}[n(\vec{r})]$ . As long as the electron density  $n'(\vec{r})$  calculated from the wave function does not converge with the input  $\rho(\vec{r})$ , the procedure is continued with the mixed electron density as the new input and loop again. When the two electron densities are self-consistent, the calculation is finished with the output quantities. . . . . 81
- 3.12 Cohesive energy as a function of energy cut-off and k-point sampling for (a) Al, (b) Ag and (c) Ag<sub>2</sub>Al, where green shaded regions indicate a good convergence ( $\ll 1\text{meV/atom}$ ) with the selected energy cut-off (500 eV) and k-points ( $\sim 2000/\text{atom}$ ). . . . . 84
- 3.13 Illustrating the common neighbour analysis index for the FCC structure. Each FCC atom has 12 nearest neighbours (coloured in green) and every neighbour has 4 bonds (coloured in red) to other neighbours of the central atom. Those 4 bonded neighbour-neighbour atoms have 2 bonds connecting between them (coloured in light blue), and the maximum length of those two bonds is 1. Reprinted from Ref. [183], p.327 with permission from Springer. 87
- 3.14 Burgers circuit method to identify a dislocation and its associated Burgers vector. A closed circuit around a dislocation in (a) is mapped to the perfect crystal in (b). The closure failure defines the Burgers vector. Reprinted from Ref. [183] p.331 with permission from Springer. . . . . 88
- 3.15 Illustration of dislocation extraction algorithm. (a) Delaunay tessellation of a dislocated crystal with the core atoms coloured in black, as identified by common neighbour analysis. (b) Delaunay tessellation is highlighted by coloured arrows indicating the corresponding perfect lattice vectors. The grey region indicates the defected crystal which cannot map to the perfect reference lattice in (c). (d) Sweeping of the Burgers circuit in a step-wise manner – triangle by triangle on the interface mesh – resolves the continuous dislocation line. Reprinted from Ref. [183] p.333,334 with permission from Springer. . . . . 90

- 4.1 HAADF-STEM images of the typical microstructure for Al-1.68 at.% Ag aged 2 h at 200°C after water quenching. (a) Low magnification image of  $\gamma'$  precipitate assemblies and GP zones; (b) high magnification image showing a  $\gamma'$  precipitate with the enlarged inset illustrating the characteristic stacking fault associated with a HCP precipitate (AB... stacking) embedded within the FCC matrix (ABC... stacking); (c) high magnification images showing the  $\epsilon$  GP zones with the enlarged inset show the Ag depletion area inside a GP zone. (d) High magnification image of small Ag clusters formed in the as-water-quenched state. The electron beam is parallel to  $\langle 110 \rangle_{\text{Al}}$ . . . . . 93
- 4.2 Simulations of dislocation reaction for Frank dislocation loops ( $\vec{b} = 1/3\langle 111 \rangle$ ) in an Al-Ag alloy. (a) Formation of stacking fault quasi-bi-tetrahedron from a hexagonal vacancy disk. (b) Formation of stacking fault tetrahedron from a trigonal vacancy disk. The local crystal structure was recognised by common neighbour analysis [145]. Atoms at FCC sites were deleted for visualising the defect structure, while atoms at HCP sites were coloured in red, and atoms with the coordinate number other than 12 were coloured in white. The Frank partial dislocations were coloured in blue, the Shockley partial dislocations were coloured in green and Lomer-Cottrell dislocations were coloured in purple, as computed by the dislocation extraction algorithm [144]. . . . . 94
- 4.3 The topology of the  $\gamma'$  precipitate assemblies. (a) Electron tomography of the microstructure in an Al-1.68 at.% Ag aged 2 h at 200°C after water quenching. The precipitate assemblies in the centre of the reconstructed volume are highlighted by rendering the isosurface, showing a truncated bi-tetrahedron assembly labelled as BT, and a tetrahedron assembly labelled as T in the image. The geometry of a truncated bi-tetrahedron is illustrated with two truncated tetrahedron (one facing up, one facing down) with 60° rotation. (b-c) Comparing the precipitate assemblies between the early stage microstructure (aged at 200°C for 30 min) and the simulations viewed along a  $\langle 110 \rangle_{\text{Al}}$  zone axis. The green arrows indicate the precipitate plates tilting  $\pm 60^\circ$  from the viewing direction. . . . . 96
- 4.4 Evolution of the microstructure while ageing at 200°C as a function of time: (a) 30 min, (b) 2 hr, (c) 4 hr, (d) 24 hr. The  $\gamma'$  precipitate assemblies and GP zones are replaced by large individual  $\gamma'$  plate. Electron beam along a  $\langle 110 \rangle_{\text{Al}}$  zone axis. . . . . 98

- 4.5 Low and high magnification HAADF-STEM images showing the  $\gamma'$  precipitate assemblies after ageing at 200°C for (a-b) 30 min and (c-d) 24 hr. The Ag depletions precipitate-precipitate junctions are highlighted with purple asterisks. The inset images show the thicknesses of the  $\gamma'$  precipitates are the same with 1 stacking fault for both ageing conditions. The electron beam is parallel to  $\langle 110 \rangle_{\text{Al}}$ . . . . . 99
- 4.6 The as-quenched Ag clusters obtained by quenching the alloy in different media: (a) water; (b) oil and (c) air. The electron beam is parallel to  $\langle 110 \rangle_{\text{Al}}$ . 100
- 4.7 Low magnification HAADF-STEM images showing the microstructure for Al-1.68 at.% Ag aged 2 h at 200°C after quenched in (a) water, (b) oil and (c) air from the solid solution temperature at 525°C. The differences in the microstructures between those conditions are caused by the quenched-in vacancies and defects that provide heterogeneous nucleation sites for  $\gamma'$  precipitates. The electron beam is parallel to  $\langle 110 \rangle_{\text{Al}}$ . . . . . 100
- 4.8 Atomic resolution HAADF-STEM of the core-shell structure of a void embedded with a GP zone  $\epsilon$ , viewed along (a)  $\langle 110 \rangle_{\text{Al}}$  and (b)  $\langle 100 \rangle_{\text{Al}}$  directions. The truncated octahedron geometries in those directions are shown as insert images at the corner. (c-f) Electron tomography of a void and surrounding GP zones  $\epsilon$  with orthogonal slices at the centre. The sample was water-quenched and aged at 200°C for 2 h. . . . . 101
- 4.9 HAADF-STEM image of the rare occurrence of a  $\gamma'$  assembly nucleated inside a GP zone with Ag depletion. The single stacking fault associated with the  $\gamma'$  phase is shown in the enlarged orange-framed insert image. The formation of  $\gamma'$  introduces partial ordering on the coherent interface of  $\gamma'$  plate, as indicated by yellow arrows. There is a fully ordered structure  $\zeta$  at the tail of the  $\gamma'$  assembly, as shown in the enlarged white-framed image. The electron beam is parallel to  $\langle 110 \rangle_{\text{Al}}$ . Image courtesy: Laure Bourgeois. 102
- 4.10 HAADF-STEM images of GP zones aged at 200°C after quenching in oil for various ageing times: (a) as-oil-quenched (b) 1 h; (c) 2 h; (d) 24 h; (e) 7 days. The ordering of Ag solute becomes increasingly defined on the  $\{111\}_{\text{Al}}$  planes while the width of the Ag depletion remains about two to four  $\{111\}_{\text{Al}}$  layers. The electron beam is parallel to  $\langle 110 \rangle_{\text{Al}}$ . . . . . 103

- 4.11 HAADF-STEM images of the microstructure before and after *in situ* annealing at 200°C for 3 min. The original sample is oil quenched and aged at 200°C for 7 days. (a) Before *in situ* annealing, where the enlarged image shows the GP zone before transformation; (b) after *in situ* annealing, where the enlarged image shows the GP zone shown in (a) now containing  $\gamma'$  precipitates; (c) after *in situ* annealing in a different area from (a), where the enlarged images show several examples of the transformed GP zones with a layered structure, while other transformed GP zones are indicated with grey frames. The electron beam is parallel to  $\langle 110 \rangle_{\text{Al}}$ . . . . . 104
- 4.12 HAADF-STEM images showing the shrinkage of small GP zones during *in situ* annealing at 200°C. The embedded void collapsed within a GP zone  $\epsilon$  that resulted in the nucleation of a small  $\gamma'$  precipitate assembly. The original sample was water quenched and aged at 200°C for 2 h. The electron beam is parallel to  $\langle 110 \rangle_{\text{Al}}$ . . . . . 105
- 4.13 HAADF-STEM images showing the  $\zeta$  phase and  $\gamma'$  phase were found in a sample *in situ* annealed at 200°C for 3 min without beam irradiation during *in situ* annealing. The original sample was oil quenched and aged at 200°C for 7 days. The electron beam is parallel to  $\langle 110 \rangle_{\text{Al}}$ . . . . . 106
- 4.14 Vacancy flux from the surface as a function of temperature and distance for a thin aluminium foil. . . . . 106
- 4.15 BF- and HAADF-STEM images showing the microstructures during different stages of the bulk processing scheme. (a-b) The microstructure before and after deformation, with dislocation line visible in the BF image. (c-e) The microstructure as a function of secondary ageing time at 200°C. The original sample is water quenched, aged at 200°C for 7 days. The electron beam is parallel to  $\langle 110 \rangle_{\text{Al}}$ . . . . . 107
- 4.16 HAADF-STEM image showing the ordered structure  $\zeta$  was also found with the bulk treatment. The sample is water quenched, aged at 200°C for 7 days, deformed by 7% and aged at 200°C for 10 min. The electron beam is parallel to  $\langle 110 \rangle_{\text{Al}}$ . . . . . 108

- 4.17 BF-STEM images showing the gliding of dislocations and formation of  $\gamma'$  precipitate plates during *in situ* annealing at 150°C. (a-b) The gliding of a dislocation within 20 s, with the position of the dislocation indicated by yellow arrows. (c-d) Formation of  $\gamma'$  precipitate plates within GP zone  $\varepsilon$  on a dislocation line as indicated by red arrows. The original sample was water-quenched, aged at 200°C for 7 days and deformed by 7% by cold rolling. The electron beam is parallel to  $\langle 110 \rangle_{\text{Al}}$ . . . . . 109
- 4.18 HAADF-STEM images showing the shearing of GP zones by large deformation and nucleation of  $\gamma'$  precipitate plates in the matrix. The original sample was oil-quenched, aged at 200°C for 24 hr and deformed by 70%, secondary aged at 200°C for 10 min. The electron beam is parallel to  $\langle 110 \rangle_{\text{Al}}$ . . . . . 110
- 5.1 HAADF-STEM images of the bi-layered phase formed on  $\{111\}_{\text{Al}}$  planes and viewed along  $\langle 110 \rangle_{\text{Al}}$ , where the green framed region shows in which the bi-layered phase has an ABCABC stacking as the white framed region of FCC aluminium matrix, while the orange framed region shows the characteristic stacking fault of  $\gamma'$ . . . . . 117
- 5.2 HAADF-STEM images of the bi-layered phase formed on  $\{111\}_{\text{Al}}$  planes and viewed along  $\langle 112 \rangle_{\text{Al}}$ , where the white framed region shows the uniformly enriched Ag layers while the red framed region shows non-uniformly enriched Ag layers as indicated by a yellow arrow. Image courtesy: Laure Bourgeois. . . . . 118
- 5.3  $\gamma'$  plates formed inside a GP zone introducing ordering at their coherent interfaces as indicated by yellow arrows . . . . . 119
- 5.4 (a) HAADF-STEM images of a bi-layered phase viewed along the  $\langle 110 \rangle_{\text{Al}}$  zone axis, showing domains formed by two variants of  $\{111\}_{\text{Al}}$  bi-layers. (b-i) HAADF-STEM tilt series of the same bi-layered precipitate phase for a tilt range from -73° to 64°. The tilt angles are as labelled in each image. (j) Electron tomography reconstruction, where the blue-framed precipitate is  $\zeta$  phase while other precipitates are GP zones  $\varepsilon$ . (k) An enlarged view of the  $\zeta$  phase along the  $\langle 110 \rangle_{\text{Al}}$  zone axis. . . . . 120

- 5.5 Atomic-resolution HAADF-STEM images obtained from experiments and simulations for a  $\zeta$  precipitate: (a) raw image section of embedded  $\zeta$  precipitate; (b) simulated image of bi-layered AgAl [thickness: 30 nm] with the atomic structure overlaid [grey: Ag, blue: Al]; (c) raw image section of the matrix near the embedded  $\zeta$  shown in (a); simulated image of Al [thickness: 30 nm] with the atomic structure overlaid. (e) The intensity profile of the experimental and simulated images in  $\zeta$  compared to that of the Al matrix. The orientation of the intensity profile is aligned with images (a) and (c). The electron beam is parallel to  $\langle 110 \rangle_{\text{Al}}$ . . . . . 122
- 5.6 Lattice displacements mapping of a  $\zeta$  precipitate in aluminium. Original (a) BF-STEM and (b) HAADF-STEM images for geometric phase analysis (GPA). The GPA results were compared with simulations based on the DFT-optimised structure of the bi-layered AgAl model (in the white box) in the following directions (c) normal, (d) parallel and (e) sheared with respect to the  $\zeta$  basal planes. . . . . 124
- 5.7 Nonlinear drift correction for geometric phase analysis, in comparison to simulations of bulk AgAl structure. HAADF images (with enlarged inserts), Fourier transform amplitudes and strain field measurements for (a) vertical scan direction, (b) horizontal scan direction, (c) drift-corrected images. (d) Simulations ( $\mu$ STEM and elastic lattice strain calculations) of bulk AgAl structure respectively. The arrows in (a) and (b) indicate the fast scanning directions for each case. The electron beam is parallel to  $\langle 110 \rangle_{\text{Al}}$ . There is noticeable noise in the direction normal to the fast scanning direction as shown in the GPA results, which corresponds to the strikes in Fourier transformations. The kinematic diffraction pattern was calculated by CrystalMaker SingleCrystal software, based on bulk AgAl structure after optimisation by DFT calculations. Red circles highlight the reflections of AgAl that are overlapped with Al (the reflections are indexed). . . . . 125
- 5.8 Contour plots of deformed charge density  $\Delta\rho$  on  $\{110\}$  plane section for (a) Al, (b) Ag and (c) proposed AgAl model. Contours are at  $0.01e^{-\text{\AA}^{-3}}$  interval, with the first dark line showing  $\Delta\rho = 0e^{-\text{\AA}^{-3}}$ . . . . . 126

- 5.9 Time-resolved HAADF-STEM images showing the  $\varepsilon$ - $\zeta$ - $\gamma'$  transformation while *in situ* annealed at 150°C. The original sample was oil quenched and aged at 200°C for 7 days. The recording was started 560 s after *in situ* annealing began, giving time to correct drift and reorientation of the crystal due to heating. We should note that the distortions in the images and movie were due to the thermal drift during acquisition. The electron beam is parallel to  $\langle 110 \rangle_{\text{Al}}$ . . . . . 127
- 5.10 Time-resolved BF- and HAADF-STEM images showing the nucleation of  $\gamma'$  assemblies on defects inside of a GP zone  $\varepsilon$ . The nucleation of a stacking fault is indicated by yellow arrows in BF-STEM images. . . . . 128
- 5.11 HAADF-STEM images showing the evolution of  $\zeta$  into  $\gamma'$  during *in situ* annealing at 200°C for times as labelled. The original sample was oil quenched and aged at 200°C for 24 h. The electron beam is parallel to  $\langle 110 \rangle_{\text{Al}}$ . 129
- 5.12 HAADF-STEM images of the  $\zeta$ - $\gamma'$  transformation under electron irradiation at room temperature. The electron beam is parallel to  $\langle 110 \rangle_{\text{Al}}$ . The change of stacking is indicated by orange arrows, while the depletion of Ag is indicated by blue arrows. . . . . 130
- 5.13 DFT calculations illustrating the preference of  $\{111\}_{\text{Al}}$  planes for Ag aggregation in aluminium. (a) The energetics of two Ag  $\{111\}_{\text{Al}}$  planes separated by a varying number “n” of Al planes. For instance, “2” means there are two Al atomic layers between two Ag layers as shown in the schematic diagram. (b) Energetics of different periodic arrays with a composition of AgAl. For instance, “1-1” means the modulation of one Ag layer and one Al layer as shown in the schematic diagram. . . . . 132
- 5.14 Energetics of Ag clustering from the solid solution to the equilibrium  $\gamma$  phase. Different configurations of Ag on  $\{111\}_{\text{Al}}$  planes are shown in blue while configurations of Ag clustering on other crystallographic planes are shown in red. The phases in the transformation sequence are highlighted with a bold unbroken line with their corresponding names and atomic structures, while other configurations calculated are shown as dashed lines. . . . . 133

- 6.1 HAADF-STEM images of  $\gamma'$  coherent precipitate-matrix interface viewed in a  $\langle 110 \rangle_{\text{Al}}$  direction. (a-b) Low magnification and high magnification images of the alloy aged at 200°C for 30 min, where blue arrows indicate the Ag segregation as reported in [70] while red arrows indicate the Ag segregation found in this study. (c-d) Low magnification and high magnification images of the alloy aged at 200°C for 7 days, where the interfacial Ag segregation was not clear. Intensities across the precipitates are plotted for both high magnification images. . . . . 141
- 6.2 HAADF-STEM images of the  $\gamma'$  coherent precipitate-matrix interface viewed in a  $\langle 112 \rangle_{\text{Al}}$  direction. The alloy aged at 200°C for (a) 30 min, (b) 8 hr and (d) 24 hr, where the blue arrows indicate the Ag segregation as reported by previous authors in [70], while the red arrows indicate the Ag segregation identified in this study. . . . . 142
- 6.3 Simulated HAADF-STEM images of an embedded  $\gamma'$  precipitate. (a) Precipitate with and (b) without interfacial Ag segregation, as viewed in a  $\langle 110 \rangle_{\text{Al}}$  direction. (c) Plots of intensities across the precipitates with and without interfacial Ag segregation shown in (a-b). (d-f) Two variants of the Neumann's model and the randomly mixed model for a precipitate with interfacial Ag segregation, when viewed in a  $\langle 112 \rangle_{\text{Al}}$  direction. . . . . 143
- 6.4 Energetics of Ag segregation at the coherent interface of  $\gamma'$  precipitate as calculated by DFT. (a) Energy reduction associated with interfacial Ag segregation as a function of precipitate thickness, compared to the energy state of Ag in solid solution. The energy of an Ag mono-layer on  $\{111\}_{\text{Al}}$  planes (-0.15 eV/Ag atom) is displayed as a dashed line for comparison. (b) The interfacial energies of models with and without interfacial Ag segregation as a function of precipitate thickness. . . . . 144
- 6.5 (a-b) Two types of semicoherent interfaces of the  $\gamma'$  precipitate plate. The blue lines indicate steps parallel to  $\{111\}_{\text{Al}}$  planes and the red lines indicate steps parallel to  $\{002\}_{\text{Al}}$  planes. The white asterisks are near to the 1-column Ag depletion at the ridges of the interface, while the purple asterisks are near to the 3-column Ag depletion. The insets show the enlarged sections of the Ag depletion features at the two types of interfaces. (c) Schematic diagram illustrating the reconstruction of the  $\{1\bar{1}00\}_{\gamma'} \parallel \{112\}_{\text{Al}}$  orientation relationship by a four-layer step parallel to  $\{111\}_{\text{Al}}$  planes and a two-layer step parallel to  $\{002\}_{\text{Al}}$  planes. The electron beam is parallel to a  $\langle 110 \rangle_{\text{Al}}$  direction. . . . . 146

- 6.6 HAADF-STEM images of semicoherent interfaces at two sides of a  $\gamma'$  precipitate. (a) Low magnification image where the arrow indicates a two-layer-thick ledge. (b-c) High magnification images of semicoherent interfaces at both sides, where a red line indicate the same close-packed layer that runs through the precipitate. The electron beam is parallel to a  $\langle 110 \rangle_{\text{Al}}$  direction. 147
- 6.7 Atomic models of (a)  $\{1\bar{1}00\}_{\gamma'} \parallel \{112\}_{\text{Al}}$ , (b)  $\{10\bar{1}1\}_{\gamma'} \parallel \{111\}_{\text{Al}}$  and (c)  $\{10\bar{1}1\}_{\gamma'} \parallel \{002\}_{\text{Al}}$  interfaces, viewed in a  $\langle 110 \rangle_{\text{Al}}$  direction. Each supercell contains an equal number of atomic layers  $n$  for both FCC Al and HCP  $\text{Ag}_2\text{Al}$  phases. The crystallographic directions are indicated by the projected unit cell of FCC and HCP phases. (d) Atomic model of  $\{1\bar{1}00\}_{\gamma'} \parallel \{112\}_{\text{Al}}$  interface reconstructed by nano-steps parallel to  $\{10\bar{1}1\}_{\gamma'} \parallel \{111\}_{\text{Al}}$  and  $\{10\bar{1}1\}_{\gamma'} \parallel \{002\}_{\text{Al}}$  planes. (e) Variation of formation energy per plane  $\Delta E^f/n$  vs.  $1/n$  for deducing the interfacial energies. . . . . 149
- 6.8 Resolving dislocation structures at the FCC/HCP semicoherent interface. (a) Original HAADF-STEM image of a  $\gamma'$  semicoherent interface (Image Courtesy: Laure Bourgeois, taken from Ref. [70]). (b) Refined atomic column positions by parameter estimation theory as indicated by green and red plus signs. (c) The composition used in the 3D model. (d) Dislocation structure in the 3D model as identified by dislocation extraction algorithm. Three pairs of Shockley partial dislocations are periodically located at the FCC/HCP interface, where red atoms are HCP, green atoms are FCC and white atoms are those at the dislocation cores. . . . . 150

- 6.9 Proposed dislocation reaction at the FCC/HCP semicoherent interface. (a) Input structure viewed near a  $\langle 111 \rangle_{\text{Al}}$  direction, where Shockley partial dislocations are periodically spaced along the interfaces. (b) EAM optimised structure viewed near a  $\langle 111 \rangle_{\text{Al}}$  direction, where a  $90^\circ$  Shockley partial, a Lomer-Cottrell and a Hirth dislocation are periodically spaced along the interface. (c) Detailed dislocation reaction process during EAM optimisation, viewed in a  $\langle 110 \rangle_{\text{Al}}$  direction, where only the Burgers vectors are shown. Step 1 shows the initial structure with three pairs of Shockley partial dislocations. Step 2 shows the climbing of two  $30^\circ$  Shockley partial dislocations. Step 3 shows the combining of two  $30^\circ$  Shockley partial dislocations into a  $90^\circ$  anti-Shockley partial dislocation. Step 4 shows the decomposition of the  $90^\circ$  anti-Shockley partial dislocation into a Lomer-Cottrell dislocation and a Hirth dislocation. Step 5 shows the separation of the Lomer-Cottrell dislocations and the Hirth dislocations to the original positions of the two  $30^\circ$  Shockley partial dislocations. . . . . 152
- 6.10 Demonstration of the change of stacking for an atom at the FCC/HCP interface viewed in a  $\langle 111 \rangle_{\text{Al}}$  direction. The Burgers vectors of the three Shockley partial dislocations are coloured in green while the Burgers vector of the anti-Shockley partial dislocation is coloured in orange. The accommodation sites of the close-packed layers are labelled as AB/ABC for HCP/FCC respectively. 153
- 6.11 The spatial relationship between Burgers vectors of different dislocations at the FCC/HCP interface. (a) The Shockley partial dislocations (green) before reaction and the metastable anti-Shockley partial dislocation (orange). These vectors are co-planar on  $\{111\}_{\text{Al}} \parallel \{0001\}_{\gamma}$  planes. (b) The remaining  $90^\circ$  Shockley partial dislocation (green), Lomer-Cottrell dislocation (purple) and Hirth dislocation (yellow) after the reaction. Those vectors are co-planar on  $\{110\}_{\text{Al}} \parallel \{1\bar{2}10\}_{\gamma}$  planes. (c) Perspective view of all Burgers vectors involved in the interfacial dislocation reaction. The lengths of the Burgers vectors are computed from the modulus of vectors ( $|\vec{b}|$ ) times the lattice parameter of aluminium, units in Å. . . . . 154

- 6.12 The atomic structure and chemistry of Lomer-Cottrell dislocations at the precipitate-precipitate junctions of  $\gamma'$  phase viewed in a  $\langle 110 \rangle_{\text{Al}}$  direction. (a-b) HAADF-STEM images showing precipitates are on the close-packed planes tilted  $70.5^\circ$  relative to each other. The junctions have three-column Ag depletion at the dislocation cores. The sample was water quenched and aged at  $200^\circ\text{C}$  for 30 min. (c) Dislocation extraction analysis based on the experimentally informed 3D model with the colour representation of the local crystal structures and dislocations as labelled. (d) Simulated HAADF-STEM image with Burgers vector analysis. Stacking faults are indicated by dashed lines. The position of the Lomer-Cottrell dislocation as an edge dislocation is indicated with a “ $\perp$ ” symbol. The crystallographic directions are indicated by an Al unit cell in a  $\langle 110 \rangle_{\text{Al}}$  direction. . . . . 156
- 6.13 The atomic structure and chemistry of Hirth dislocations at the precipitate-precipitate junctions of  $\gamma'$  precipitates viewed in a  $\langle 110 \rangle_{\text{Al}}$  direction. (a-b) HAADF-STEM images showing precipitates are on the close-packed planes tilted  $109.5^\circ$  relative to each other. The junctions have a pair of two-column Ag depletion at the dislocation cores. The sample is an Al-0.85at.%Ag-0.85at.%Cu alloy water quenched and aged at  $200^\circ\text{C}$  for 4 hr. Alloy courtesy: Julian M. Rosalie (fabrication details are recorded in Ref. [78]). (c) Dislocation extraction analysis based on the experimentally informed 3D model with the colour representation of the local crystal structures and dislocations as labelled. (d) Simulated HAADF-STEM image with Burgers vector analysis. Stacking faults are indicated by dashed lines. The position of the Hirth dislocation as an edge dislocation is indicated with a “ $\perp$ ” symbol. The crystallographic directions are indicated by an Al unit cell in a  $\langle 110 \rangle_{\text{Al}}$  direction. . . . . 157
- 6.14 Intersections of individual  $\gamma'$  precipitate plates in over-aged samples. (a-b) Twinning at the centre of the precipitate-precipitate junction. The twin boundaries are indicated by blue lines while the basal planes of the HCP  $\gamma'$  phase are indicated by red lines. The sample was aged at  $200^\circ\text{C}$  for 7 days and *in situ* annealed at  $200^\circ\text{C}$  for 3 min. (c-d) Penetration of one precipitate through another at the precipitate-precipitate junction. The sample was aged at  $200^\circ\text{C}$  for 7 days. . . . . 159

- 6.15 Periodic segregation of Al in  $\{10\bar{1}1\}$   $\gamma$  twin boundary. (a) An enlarged view of HAADF-STEM image in Fig. 6.14(b). (b) Atomic model of the  $\{10\bar{1}1\}$  twin structure. (c) Schematic illustration and (d)  $[1\bar{2}10]$ -perspective view of HCP  $\gamma$  structure. . . . . 160
- 6.16 *In situ* STEM showing the growth behaviours of  $\gamma'$  assemblies and individual  $\gamma'$  plates while annealing at 200°C. The original sample was water-quenched, aged at 200°C for 2 hr. . . . . 161
- A.1 The free energy change associated with homogeneous nucleation. The nucleation energy barrier emerges as the competition between the interfacial energy term and volumetric energy term. Adapted from Ref. [15], p. 264 with permission from Taylor & Francis. . . . . 191
- A.2 (a) A possible  $[110]$  section through the  $\gamma$ -plot of an FCC crystal. The length OA represents the free energy of a surface plane whose normal lies in the direction OA. Thus  $OB=\gamma_{(001)}$ ,  $OC=\gamma_{(111)}$  etc. Wulff planes are those such as that which lies normal to the vector OA. In this case, the Wulff planes at the cusps (B, C, etc.) give the inner envelope of all Wulff planes and thus the equilibrium shape. (b) The equilibrium shape in three dimensions showing  $\{100\}$  (square faces) and  $\{111\}$  (hexagonal faces). Reprinted from Ref. [15], p. 121 with permission from Taylor & Francis. . . . . 192
- A.3 A section through a  $\gamma$ -plot for a precipitate showing one coherent or semi-coherent interface, together with the equilibrium shape (a disc). The Wulff theorem would then predict the equilibrium shape to be a disc with a thickness/diameter ratio of  $\gamma_b/\gamma_e$  where  $\gamma_b$  and  $\gamma_e$  are the specific interfacial energies of the board and edge interfaces respectively. Reprinted from Ref. [15], p. 154 with permission from Taylor & Francis. . . . . 192
- A.4 Schematic diagrams illustrating diffusional precipitate growth. (a) The lengthening and thickening directions of a precipitate plate. The edge curvature has a radius of  $r$ . The dashed line circles the solute depletion field around the precipitate. (b) Plot of the solute composition against the distance away from the precipitate-matrix interface, with the orange line represents the lengthening direction and the blue line represents the thickening direction, respectively. (c) Gibbs free energy against composition for the broad and edges interfaces, illustrating the Gibbs-Thompson effects, reprinted from Ref. [15], p.44 with permission from Taylor & Francis. . . . . 195

- 
- A.5 Typical plots of thickness (or half-thickness) vs. time for precipitate plates in (a) Fe-0.22% C [219], reprinted with permission from Springer and (b) Al-15% Ag [49] (in weight percent), reprinted with permission from Elsevier. 197
- A.6 Schematic illustration of migration of an interphase boundary by lateral motion of ledges. Adapted from Ref. [15], p. 283 with permission from Taylor & Francis. . . . . 197

# List of tables

3.1	Microscopes and their imaging conditions used in the present study. . . . .	61
3.2	Lattice parameters and energetics of different phases in the Al-Ag alloy system.	85
5.1	Atomic coordinates of the precipitate $\zeta$ phase. The listed coordinates are fractional in respect to the simplest trigonal cell with a space group of $P3$ . It is equivalent to a trigonal cell with a space group of $R\bar{3}m$ (hexagonal axis) and Wyckoff positions of Ag at (0 0 0.878) and Al at (0 0 0.375). The experimental parameters are $a_{\text{exp}}=2.88 \pm 0.05 \text{ \AA}$ and $c_{\text{exp}}=27.35 \pm 0.05 \text{ \AA}$ . The DFT-optimised parameters are $a_{\text{DFT}}=2.97 \text{ \AA}$ and $c_{\text{DFT}}=26.88 \text{ \AA}$ for the bulk $\zeta$ phase and $a_{\text{DFT}}^{\text{emb}}=2.92 \text{ \AA}$ and $c_{\text{DFT}}^{\text{emb}}=27.26 \text{ \AA}$ for the embedded $\zeta$ precipitate phase. The uncertainty in the experimentally determined z coordinates is 0.005. . . . .	123
5.2	DFT calculations for the preference of Ag clustering in Al matrix. $E_{\text{F}}^{\text{Ag}}$ is the formation energy per Ag atom. The 1 <sup>st</sup> nearest neighbour stands for two Ag atoms in the nearest neighbour configuration in a $\langle 110 \rangle_{\text{Al}}$ direction in FCC Al lattice. Similarly, the 2 <sup>nd</sup> nearest neighbour is two Ag atoms next to each other in a $\langle 001 \rangle_{\text{Al}}$ direction. . . . .	132



# Chapter 1

## Introduction

### 1.1 A Brief History of Precipitation Hardening

The history of metallurgy is a history of civilisation. Our footprint on the sky, from airliners that link the world on a daily basis to the spacecraft aiming at Mars, is dependent on light alloys with their mechanical properties largely provided by precipitation hardening. Aluminium has pinned its special position in the aerospace history from its very inception: an Al-8 wt.% Cu alloy was used in the engine that enabled the Wright Brothers' first powered flight in 1903 [1]. Previously, their planes were gliding the sky like a bird without flapping its wings. In order to obtain a lightweight engine, the Wright Brothers reached out to several engine manufacturers, but none met their needs [2]. They turned to their shop mechanic, Charlie Taylor, who built an engine in just six weeks in close consultation with the brothers [2]. To keep the weight low enough, Taylor performed a rare practice for the time – casting the engine block from aluminium, Fig. 1.1(a). In fact, until the mid-1880s, aluminium was more valuable than gold and was only used for special occasions <sup>1</sup>. Only since 1886 with the invention of the alternator system for industrial electricity generation, has the massive production of aluminium become possible through the electrolysis method of aluminium salt reduction. The aluminium engine worked well: "The power is ample" as Wilbur Wright recalled the moment when he was running at wingtip to balance the plane while Orville Wright was piloting, Fig. 1.1(b) [2].

The application of precipitation hardening was ahead of its discovery. In 1906, Alfred Wilm was working on strengthening aluminium alloy to replace brass in the cartridge of guns.

---

<sup>1</sup>For example, an aluminium bar was presented as a highlight of the Exposition Universelle of 1855; aluminium utensils were reserved for the most honoured guests to Napoleon III of France while less favoured guests were treated with gold; 2.8 kg aluminium was placed as the capstone of Washington Monument in 1884 [3].

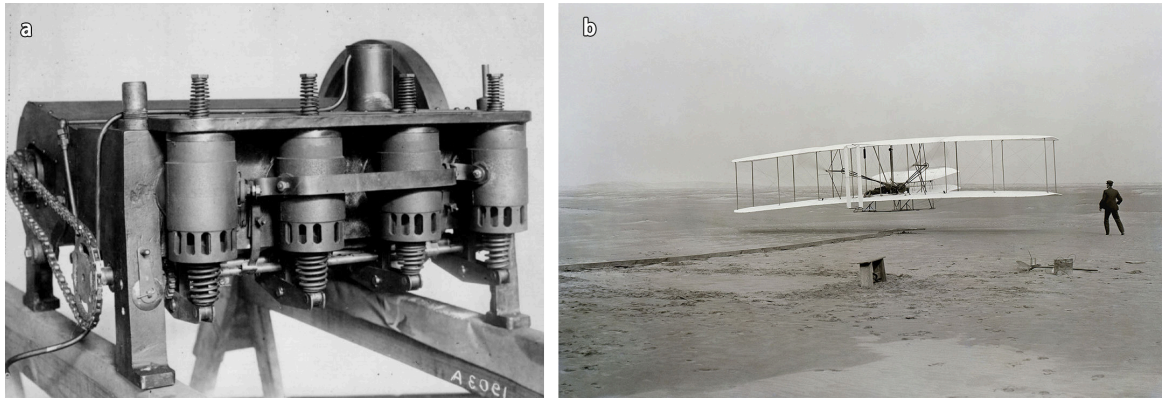


Fig. 1.1 (a) The Wright engine cast by an Al-8 wt.% Cu alloy. Courtesy: The Library of Congress, USA. (b) First flight of the Wright Flyer I, December 17, 1903, Orville piloting, Wilbur running at wingtip. Courtesy: J. T. Daniels.

His initial plan is to reproduce the water-quenched hardening of steels in aluminium [4]. To his frustration, the practice softened aluminium alloys instead of hardening them. Getting disappointed with the results, some of the hardness measurements were left to the following week [4]. To his astonishment, the hardness had increased considerably. Despite Wilm's initial confusion, his discovery quickly led to the first commercial precipitation-hardened alloys (Al-Cu-Mg-Mn) called "duralumin"<sup>2</sup> [1, 3]. After Wilm optimised the heat treatment, duralumin found its immediate application in the construction of the airship "Zeppelin" [1] and later the aircraft "Junkers" in Germany [3]. In 1938, with X-ray diffraction as the most advanced characterisation tool, Guinier [5] and Preston [6] independently reported the existence of nanometre-sized coherent plate precipitates in a naturally aged Al-4 wt.% Cu alloy; these have since been known as Guinier-Preston or GP zones. A modern examination of the Wright Brothers' crankcase using transmission electron microscopy (TEM) confirmed that nanometre-sized GP zones were indeed in place, which empowered their first flight in a state-of-the-art engine [1].

## 1.2 Open Questions about Precipitation

A central topic in metallurgy is understanding the relationships between composition, processing, microstructure and performance. For a given composition, the thermodynamics of the equilibrium phases are well-established. However, precipitation is a dynamic process with complicated phase transformation pathways before equilibrium is reached [7]. Often, the phases that nucleate first are metastable and their distribution can be heterogeneous and

<sup>2</sup>In French, "dur" means hard and strong.

influenced by the presence of defects [8]. Thus, the same alloy processed by different treatments can display various microstructures and hence properties. In addition, the orientation relationship between the precipitate phase and the matrix is often critical in determining the mechanical properties [9]. However, the method to manipulate such orientation relationship is unclear. Despite an enormous number of studies, the complicated nature of precipitation is not fully resolved.

An essential part of this long-standing problem is revealing the role of interfaces and defects during precipitation. An interface is the critical boundary that distinguishes two structurally and/or compositionally different phases. Once a secondary phase forms within the matrix, the precipitate-matrix interfaces are generated and accompany the phase transformations. In the classical theory of precipitation, interfacial energy determines the nucleation energy barrier and growth kinetics [10]. However, the atomic structures of the interfaces have rarely been characterised at the atomic scale until recently [11–13]. Furthermore, the associated atomic mechanisms that underpin phase transformations remain poorly understood. This lack of understanding prevents the prediction of precipitation from first principles even for the simplest cases [14].

Manipulating the interfacial structures requires another degree of understanding, particularly, how do interfaces change with different alloying elements? Micro-additions of certain elements can dramatically improve the ageing response [4]. Those microalloying additions are often found to segregate at the precipitate-matrix interfaces and facilitate precipitation. Understanding how those elements segregate and modify the interfaces has both scientific and practical significance. A critical step towards such understanding is determining the solute clustering behaviour in aluminium and the interactions between solute and precipitate phases.

In practice, precipitation is often manipulated through processing. Precipitate phases are often found to heterogeneously nucleate on dislocations, which accommodates the strain of the structural transformation from one crystal structure to another [8]. Thus, defects are generated intentionally with specific thermal and mechanical treatments prior to ageing, which takes the system away from equilibrium and triggers precipitation. Different kind of defects exist, but their explicit roles in precipitation are not clear. For instance, will dislocations with different Burgers vectors yield different precipitation behaviours? Is it possible to tailor the microstructure by taking the advantage of various types of defects? In additions, defects are not just introduced to alloy before ageing, but also after ageing. For example, thermal and mechanical loading could generate dislocations in alloy components during their servicing. The accumulated dislocations in this post-ageing condition are critical

for evaluating the stability of alloys [4]. However, the effects of those defects on the alloy microstructure are largely unknown.

### 1.3 Why Al-Ag Alloys?

To answer these fundamental questions concerning precipitation, it is necessary to choose a simple alloy system. We chose Al-Ag alloys as a textbook alloy system for several reasons. First, one of the precipitations involves a classic transformation from face-centred cubic (FCC) to hexagonal close-packed (HCP) that is well-established [10, 15]. Second, Al and Ag have almost the same atomic size that yields a minimum strain to affect the solute clustering and phase transformations. Third, their microstructures involve precipitate plates on close-packed planes that are common to many high-strength aluminium alloys. In addition, Al and Ag have very different atomic numbers that are particularly favourable for TEM imaging [16].

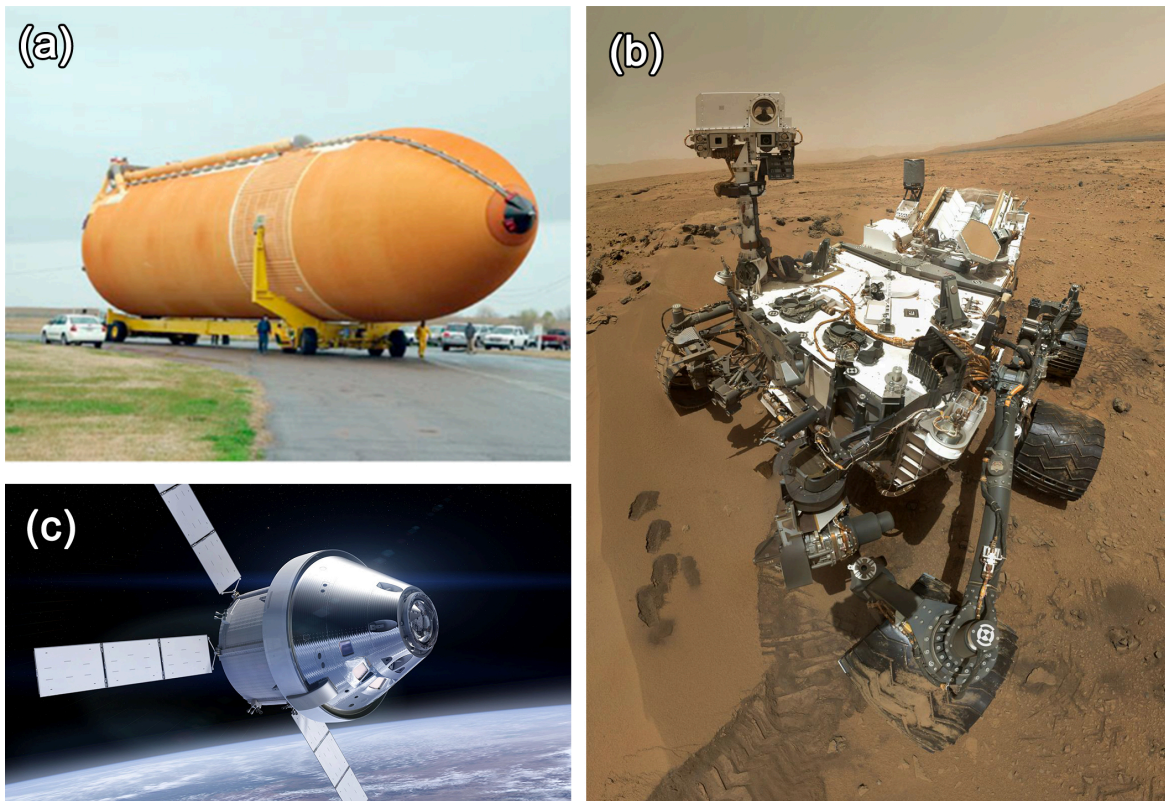


Fig. 1.2 (a) External liquid fuel tank for launching the space shuttle. (b) Self-portrait of Curiosity (a car-sized rover) at the foothill of Mount Sharp, Mars. (c) Orion spacecraft orbiting around the earth, aiming to facilitate human exploration of asteroids and of Mars. Courtesy: NASA.

Beside the scientific significance of Al-Ag system, Ag is also an important microalloying addition in high-strength aluminium alloys. A well-known example is the construction of the disposable external fuel tank of the space shuttle (1981-2011). As shown in Fig. 1.2, the tank was 47 m in length and 8.5 m in diameter, originally weighted up to 34 tons. The use of an Ag-microalloyed aluminium alloy reduced the weight of the space shuttle by 2.8 tons. This metallurgical innovation saved a significant cost during the construction of the International Space Station [17]. Ag-microalloyed aluminium alloys are still used in the current generation of spacecraft, e.g. Curiosity (2012) and Orion (2014), see Fig. 1.2(b-c). These applications originated from the finding that a minor addition of Ag can stimulate a major response in age hardening with improved microstructure stabilities against environmental degradation [18, 19]. The presence of Ag promotes precipitation of a wide range of precipitate phases or even changes the type of phase that forms. Recent studies have shown that in this role, Ag segregates at the precipitate-matrix interfaces [13, 20]. However, the atomic mechanisms of Ag microalloying effects are not fully understood. In particular, how does interfacial Ag segregation manipulate phase transformations? Such understanding is critical for the alloy design of the next generation of spacecraft.

## 1.4 Aims of this Research

This project aims to investigate the role of interfaces and defects during precipitation in aluminium alloys and more specifically, the textbook Al-Ag alloy system. Scanning transmission electron microscopy and atomistic calculations are combined to observe the atomic structures of different phases and determine the underlying mechanisms. Insights of phase transformations gained in this research will hopefully lead to a new strategy of tailoring precipitation behaviour. To achieve the aim, this project has following objectives:

(a) Characterising the atomic structures of different phases with high resolution scanning transmission electron microscopy. Special attention should be cast to the precipitate interfaces, focusing on their atomic structures and chemistries. The observed interfaces should be analysed in context with precipitate nucleation and growth behaviours.

(b) Simulating the microstructure evolution and understanding the underlying thermodynamics and atomic mechanisms of the associated phase transformations. The atomic structures characterised by electron microscopy should be implemented in the structure models for atomistic calculations.

(c) Manipulating precipitation with defects to understand their role during phase transformations. The explicit type of defects need to be identified unambiguously in both electron

microscopy and atomistic simulations. This requires us to formulate advanced structure analysis strategies and develop a deep understanding of defects during precipitation.

## 1.5 Overview of the Thesis

This thesis starts with a literature review in Chapter 2, covering the current knowledge of interfaces and defects during precipitation, the expected phases in the Al-Ag system and the microalloying effects of Ag in various aluminium alloys. The thermodynamics and kinetics of precipitation are reviewed independently in Appendix A. Chapter 2 also briefly evaluates the characterisation and modelling methods suitable for this study. The knowledge gap specified in this review defines the research scope for the following three results chapters.

Chapter 3 is a comprehensive presentation of the techniques used in this study in terms of alloy processing, electron microscopy and atomistic calculations. Alloy processing includes the alloy fabrication, heat treatments and sample preparation. In particular, our new processing strategy is specified to manipulate defects and phase transformations. Various electron microscopy techniques were detailed in this chapter, ranging from the aberration correction of electron optics to the mapping of atomic positions. Atomistic calculations include the density functional theory, embedded atom method and methods for structure classification and dislocation analysis.

Chapter 4 examines the microstructures obtained via conventional heat treatments. The importance of lattice defects was identified via both experiments and simulations. By controlling defects, new processing schemes enabled the manipulation of phase transformation pathways and resulted in new microstructures. A highlight of this chapter is the discovery of a new ordered precipitate phase  $\zeta$  in the Al-Ag system.

Chapter 5 characterises the atomic structure of the  $\zeta$  phase in details. The dynamics of its associated phase transformations are revealed with high temporal and spacial resolution. In addition, first-principles calculations elucidate the preference of Ag clustering in aluminium.

Chapter 6 is dedicated to the study of the structures and chemistries of the FCC/HCP interfaces of  $\gamma'/\gamma$  phases. We systematically studied the coherent, semicoherent precipitate-matrix interfaces and precipitate-precipitate junctions. Several new interfacial structures were discovered and explained from energetics perspective. In addition, we proposed an interfacial dislocation reaction model that explains the existence of two types of semicoherent interfaces. We demonstrated the coupling between interfacial dislocations with unique local chemical environments, which is critical in determining the precipitate growth behaviours.

Chapter 7 summarises the main findings of this work and suggests directions for future work.

# Chapter 2

## Literature Review

Physical metallurgy concerns the fundamentals and applications of phase transformations: the process in which atoms arrange themselves from one structure to another. While pure metals are genuinely soft, metal alloys can be greatly strengthened by precipitation, the formation of intermetallic phases, thus enabling the use of alloys in various engineering applications. The significantly improved strength comes from the fine microstructure, usually dealing with nanometre-sized, 2D or 1D-shaped precipitates in aluminium alloys. The underlying atomic mechanisms of precipitation are complicated and remain largely unknown. Hence, the methods to manipulate precipitation are highly empirical. This chapter reviews the precipitation studies that attempted to answer the question of how precipitation can be controlled. We will start with some general concepts of precipitation control through the role of interfaces and defects during phase transformations. Then, the review focuses on the Al-Ag system, which is the subject of this thesis.

The physical metallurgy part in Section. 2.1 outlines the background information about age hardening and ways of controlling the process. Section 2.1.1 explains the dynamic nature of precipitation, suggesting two approaches to tailor precipitation behaviours. Section 2.1.2 demonstrates the complexity of precipitate interfaces and engineering the interfacial structures with microalloying elements. Section 2.1.3 illustrates precipitation control with defects, which are introduced during processing and servicing.

The Al-Ag part in Section. 2.2 surveys the current knowledge of alloying silver in aluminium. Section 2.2.1 reviews the studies of Al-Ag binary alloys, including the atomic structures of GP zones,  $\gamma/\gamma'$  precipitates and their transformations pathways. Section 2.2.2 examines the microalloying effects of Ag in various aluminium alloys.

The strategy part in Section. 2.3 reviews the characterisation and modelling methods relevant to precipitation studies. Transmission electron microscopy and density functional theory

are two important methods to resolve the atomic structures and appreciate the underlying electronic structures.

## 2.1 Precipitation in Aluminium Alloys

### 2.1.1 The Dynamic Nature of Precipitation

The strength of a metal is measured by its resistance against deformation. The macroscopic plastic deformation is achieved by the generation and movement of crystal defects, like dislocations and twins. At the microscopical level, precipitation hardening is all about hindering the dislocation motion using precipitates. Dislocations choose the mode in which takes the least resistance, which depends on the characteristics of the precipitates [21]. For soft precipitates (like GP zones), dislocations cut through particles directly, which leads to sheared precipitates. For hard precipitates, dislocations prefer bypassing the particles and leaving dislocation loops around them. The contribution of precipitation hardening can be calculated by the Orowan equation, which correlates the microstructure with the improved shear strength [9].

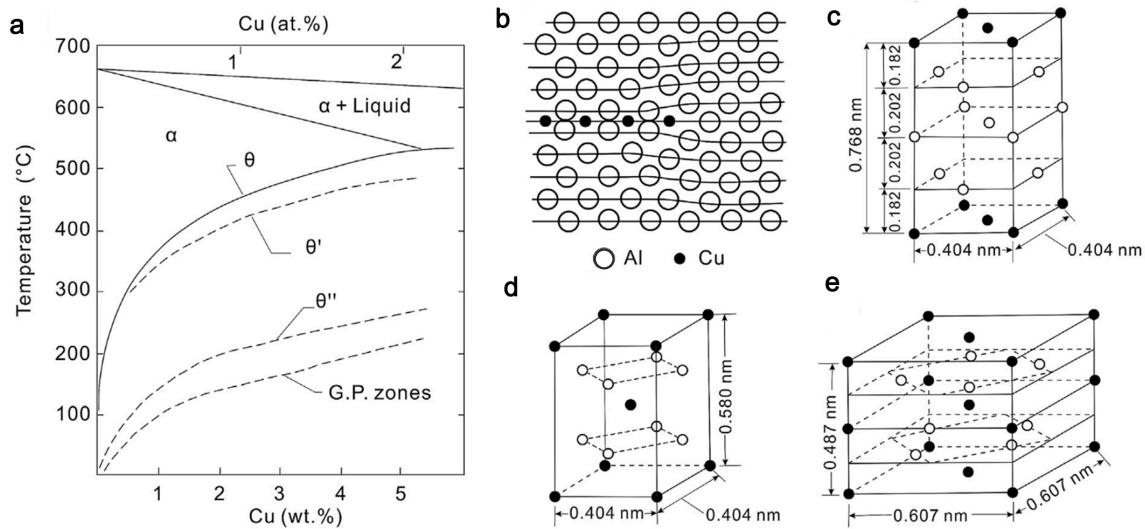


Fig. 2.1 (a) Al-rich side of the Al-Cu binary phase diagram, (b-e) Structure and morphology of GP zone,  $\theta''$ ,  $\theta'$  and  $\theta$  respectively, where  $\circ$  represents Al and  $\cdot$  represents Cu. Reprinted from Ref. [15], p. 293 with permission from Taylor & Francis.

However, microstructure evolves during ageing: not only do the density and distribution of precipitates change with time and temperature but also the type of precipitate phase in

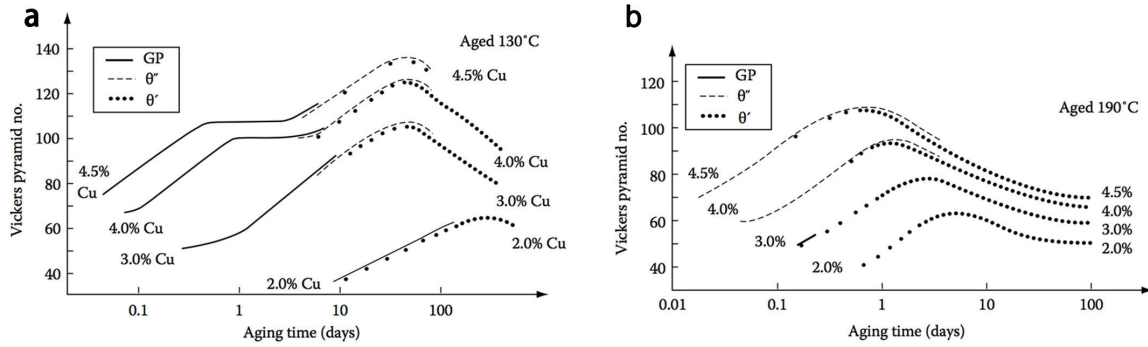


Fig. 2.2 Hardness *versus* time for Al-Cu alloys with various compositions at (a) 130°C and (b) 190°C. Reprinted from Ref. [7]. Courtesy: J. M. Silcock, T. Heal and H. K. Hardy.

presence varies. For example, the transformation sequence of the Al-Cu system is known as [15]:

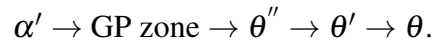


Fig. 2.1 shows the atomic structures of these phases and the metastable phase diagram. The sequential precipitation is a common phenomenon in metallurgy, with energetics and kinetics reasons. Though an equilibrium phase has a larger energy driving force to form, a higher energy barrier prevents its direct precipitation, usually due to the bad matching with the matrix [15]. The evolving microstructure results in the changing hardness of the alloy. For instance, the formation of coherent GP zones corresponds to the rapid increase in hardness at the early stage, Fig. 2.2. A plateau emerges due to the dynamic balance among the GP zones nucleation, growth and coarsening, before a second rise due to the formation of coherent  $\theta''$  [7]. The peak ageing is achieved with the semicoherent precipitate phase  $\theta'$ . After that, the hardness decrease with the ageing time due to the microstructure coarsening with the formation of incoherent equilibrium phase  $\theta$ . Note that a lower ageing temperature (130°C vs 190°C) gives a higher peak hardness but with a longer ageing time, due to a larger driving force but a slower kinetics [7]. The kinetic nature of precipitation makes precipitation hardening the art of controlling the dynamics.

It is agreed that the desired microstructure should consist of a small volume fraction of fine, dense and hard particles. In high strength aluminium alloys, a common feature is the presence of shear-resistant, plate-shape precipitates with large aspect ratios on  $\{111\}_{\text{Al}}$  or  $\{100\}_{\text{Al}}$  planes, sometimes also with the presence of rods in  $\langle 100 \rangle_{\text{Al}}$  [4]. The Orowan equation gives an insight into the phenomenon by relating the critical resolved stress to the precipitate characteristics. Given the same volume fraction of precipitates, the hardening effect is highly orientation dependent [9], Fig. 2.3(e). Specifically, the strength gained

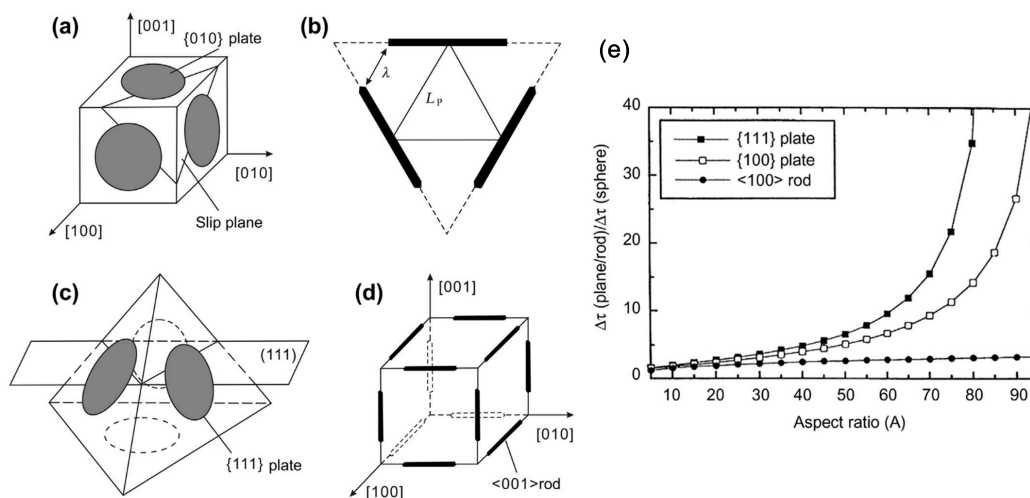


Fig. 2.3 Schematic diagram showing the topological arrangement of precipitates and the strengthening contribution. (a) circular plates on  $\{100\}_{Al}$  planes and (b) its projection in a  $\{111\}_{Al}$  plane as the slip plane; (c) circular plates on  $\{111\}_{Al}$  planes; (d)  $\langle 100 \rangle_{Al}$  rods. (e) Variation in the ratio of critical resolved shear stress  $\Delta\tau$  (plate, rod)/ $\Delta\tau$  (sphere) with aspect ratio for Orowan strengthening attributable to  $\{111\}_{Al}$  and  $\{100\}_{Al}$  precipitate plates and  $\langle 100 \rangle_{Al}$  precipitate rods. The volume fraction of precipitates is 0.05. Reprinted from Ref. [4], p. 64 and Ref. [9], p.2058 with permission from Elsevier.

from precipitates on  $\{111\}_{Al}$  planes is much larger than the others, particularly at large aspect ratios. The effect can be even more significant when precipitates are deformed above their threshold. Upon the shearing of a precipitate, the interfacial energy contributes to the strengthening with the increased interfacial areas. Assumed the interfacial energy is isotropic, the difference can be more than a 1000 times when comparing the  $\{111\}_{Al}$  plates with spheres [9]. A physical reasoning why the  $\{111\}_{Al}$  plates are so effective is their small inter-particle distance: they are on the slip planes for FCC crystals, ready to block dislocation motions; while precipitates on other crystallography planes have to project their existence on to the slip planes. This points out an alternative strategy to strengthen the alloy by manipulating the orientation relationship between the precipitates phase and the matrix. It sounds improbable because a precipitate phase has its preferred crystal structure and orientation relationship determined by nature. However, in theory, it is possible to control precipitation behaviours by adjusting the interfacial structures. Section. 2.1.2 shows the importance and complexity of interfacial structures. In practice, engineering new interfacial structures have been already achieved with microalloying additions. But there is hope for fundamental understandings and further improvements.

### 2.1.2 Precipitation Control via the Engineering of Interfacial Structure

An interface is the boundary that distinguishes two compositionally or structurally different phases. Therefore, as soon as a precipitate nucleates from the matrix, precipitate-matrix interfaces are created. The analysis in Appendix A will rationalise the critical role of interfaces from the theoretical perspective. In short, the interfacial energy controls the orientation relationship and the precipitation kinetics, including the nucleation, growth and coarsening of a precipitate phase. However, the interfacial energy is difficult to evaluate both experimentally and computationally. Thus, our knowledge on this subject is highly empirical, even for the simplest cases.

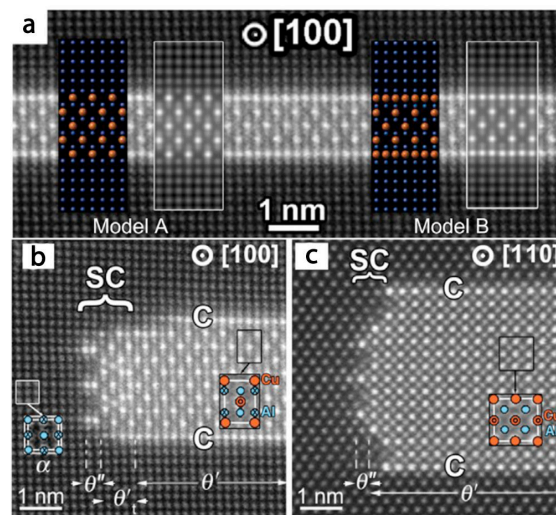


Fig. 2.4 HAADF-STEM images showing (a) segregation of Cu atoms in the coherent interface of  $\theta'$  precipitates in the combination of crystal models and STEM simulations (viewing  $\langle 100 \rangle_{Al}$ ); (b,c) complex semicoherent interface of  $\theta'$  ((viewing  $\langle 100 \rangle_{Al}$ ) and  $\langle 110 \rangle_{Al}$ ) respectively). Reprinted from Ref. [11, 12] with permission from Elsevier and American Physical Society.

Moreover, when using analytical equations to understand the precipitation behaviours, the interface is often assumed to be sharp (a brutal combination of precipitate phase and the matrix) or diffuse (a gradual change from the precipitate phase to the matrix). However, the reality is sometimes more complicated than expected. The  $\theta'$  precipitate in the binary Al-Cu alloys was examined using atomic-resolution Z-contrast scanning transmission electron microscopy [11, 12]. Extra Cu atoms are clearly present at the interstitial sites of  $\theta'$  phase on the coherent precipitate interface, which makes the interface rather similar to a GP zone [11]. Such interfacial single layer of Cu is apparent for thin  $\theta'$  precipitates at the early stage of

ageing but becomes less obvious at later stages, which suggests that the interfacial Cu atoms play an important role during the precipitate nucleation and thickening. The semicoherent interface is even more complicated: it consists of the structure of  $\theta''$  and another well-defined intermediate structure denoted as  $\theta'_i$  in Fig. 2.4(b-c) [12]. Such interfacial structures were not considered in previous attempts to estimate the interfacial energies of the  $\theta'$  phase. They may serve as a key factor to resolve the disagreement between experiments and simulations on the growth kinetics. For instance, the predicted aspect ratio was about  $\sim 4$ -5 times smaller and the predicted growth rate was more than 10 times slower than the experimental results [22, 23]. The apparent departure prevents a prediction from first-principles – a reason why empirical parameters are used even for a textbook precipitate like  $\theta'$  phase. It becomes a question whether such interfacial structures exist commonly in aluminium alloys. In addition, what are their roles during phase transformations, in terms of both the interfacial energies (phenomenological understanding) and atomistic transformation mechanisms (microscopic understanding)? A detailed answer to this fundamental question has direct implications in manipulating precipitates with tailored interfacial structures. One fruitful way has been microalloying additions, such as Ag, which we will describe in detail.

Normally, one expects a linear relationship between the degree of precipitation hardening and the amount of alloying. However, certain elements tell a different story: minor amounts ( $< 1$  at.%) or even traces ( $< 0.1$  at.%) can stimulate a dramatic ageing response. Such effect is not commensurate with their quantities, suggesting the operating mechanisms are different from the major ( $> 1$  at.%) alloying elements. Despite various mechanisms, the principle of microalloying is straightforward: increasing the driving force (enthalpy difference) and decreasing the barrier (interfacial energy and strain energy) for precipitation as discussed in Appendix A. Several possible mechanisms have been proposed as follows; a practical case may involve their combination [4].

1. Interaction of microalloying solute with vacancies that changes the heterogeneous nucleation sites biased on defects.
2. Solute segregation at the interfaces with the concomitant reduction in interfacial energy between the precipitate phase and the matrix.
3. Accommodation of volumetric and/or shear strain associated with precipitation.
4. Reduction in the enthalpy of the precipitate phase.

Microalloying additions have engineering significance, mainly in improving mechanical properties through shortened ageing time at a limited cost (due to their minor amounts). A classic example is the minor additions of tin to the binary Al-Cu alloys, where the natural

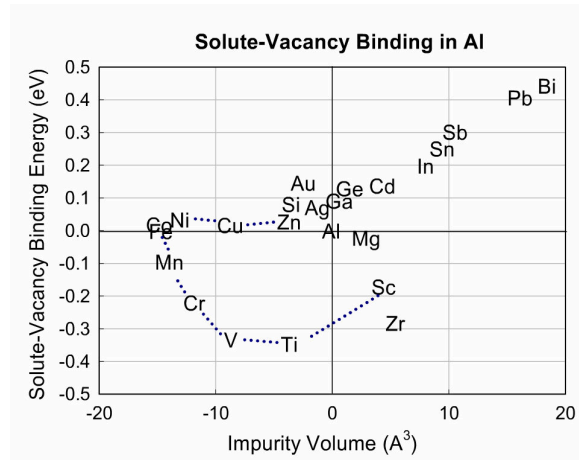


Fig. 2.5 First-principles calculated nearest-neighbour solute–vacancy binding energies as a function of the solute impurity volume. The impurity volume is calculated from the change in volume upon adding a single solute impurity to pure Al. Note the correlation between solute–vacancy binding and size of the impurity atoms, with larger solutes having a larger binding energy with vacancies. The correlation is particularly clear if one excludes the 3d transition metals, Sc–Zn, connected by dashed lines. Reprinted from Ref. [24] with permission from Elsevier.

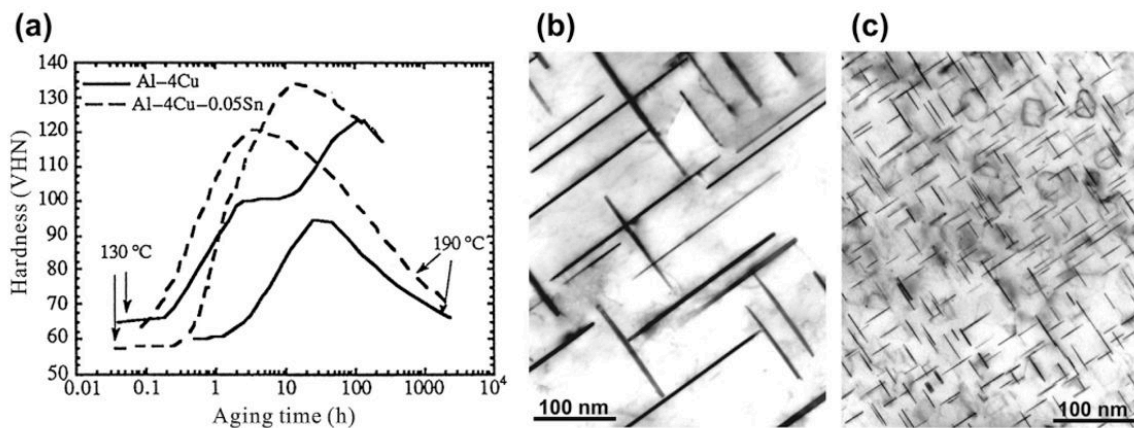


Fig. 2.6 (a) Age hardening response of Al-4Cu and Al-4Cu-0.05Sn(wt.%) alloys at 130° and 190°C. Taken from Ref. [25] with courtesy: H. K. Hardy. TEM images showing the distribution of  $\theta'$  precipitate in peak-aged samples of (b) Al-4Cu, and (c) Al-4Cu-0.05Sn (wt.%) alloys. Reprinted from Ref. [9], p. 2027 with permission from Elsevier.

ageing is suppressed but the artificial ageing is greatly promoted, Fig. 2.6 [9]. The stimulated ageing response is from the refined microstructure with direct  $\theta'$  precipitation on Sn particles, which bypasses GP zone and  $\theta''$  phase. TEM studies demonstrated that Sn-added Al-Cu alloys have a much finer and more uniform dispersion of  $\theta'$  precipitates, with Sn particles or even single Sn atoms segregating at their semicoherent interfaces (mechanism 2) [26–28]. The  $\theta'$  precipitate phase has a large invariant plane strain in its plate length direction ( $([100]_{\theta'})$ ) and does not match the matrix perfectly in its plate thickness direction ( $([001]_{\theta'})$ ). Thus, Sn with a different atomic size was also suspected to accommodate the strain associated with precipitation (mechanism 3) [28]. As Sn has almost no solubility but a high diffusivity in Al, the thermal instability of Sn in solid solution leads to a quick precipitation of Sn particles with only a few nanometres in size. In addition, Sn has a positive binding energy with vacancies due to its larger atomic size compared to Al atoms (confirmed by first-principles calculations [24], see Fig. 2.5). Thus, quenched-in vacancies are trapped by those nano-sized Sn particles (mechanism 1), giving less chance for diffusional events in the matrix (e.g. suppressing GP zone formation during natural ageing). In, Sb and Cd have a similar microalloying effect as that of Sn [29]. A recent study showed that the InSb particles can segregate at the coherent or the semicoherent interfaces of the  $\theta'$  phase by adjusting the quenched-in vacancies [30].

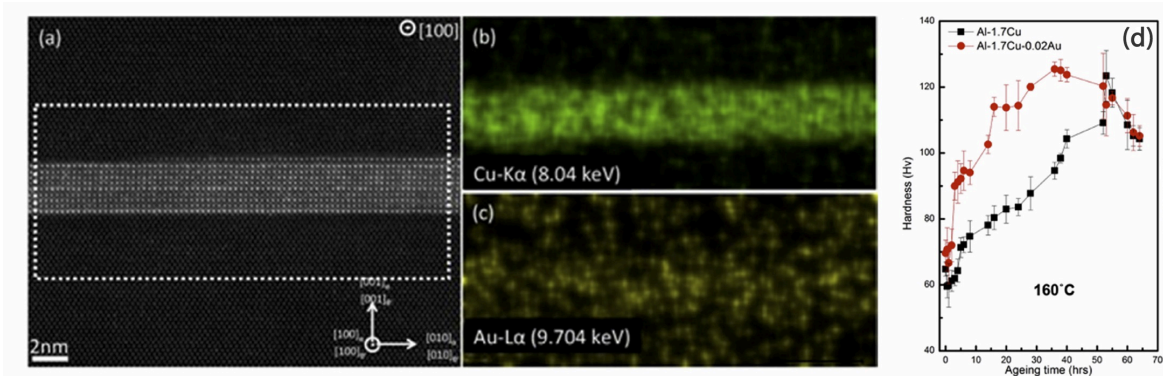


Fig. 2.7 An early-stage  $\theta'$  precipitate with 4 unit cells thick found in an Al-Cu-Au alloy aged at 160 °C for 3 h: (a) atomic-resolution ADF imaging, and the background-subtracted X-ray maps (b) Cu- $K_{\alpha}$  and (c) the Au- $L_{\alpha}$  for the white dashed region in (a). (d) Vickers hardness curve of the binary Al-1.7Cu and ternary Al-1.7Cu-0.02Au (at.%) alloys aged at 160 °C. Reprinted from Ref. [31] with permission from Elsevier.

Microalloying elements are often seen to segregate at the precipitate-matrix interface, but sometimes they can dissolve inside precipitate phases, such as the addition of Au in the Al-Cu alloys. As shown in Fig. 2.7(d), minor additions of Au promote the ageing response of an Al-Cu-Au alloy dramatically at the early stage of ageing [31]. Scanning transmission

electron microscopy and energy-dispersive X-ray spectroscopy, Fig. 2.7(a-c), confirmed that Au atoms dissolve inside of  $\theta'$  phase. It was suggested that Au lowers the formation energy of  $\theta'$  phase and thus increases the driving force for nucleation [31]. Using alloying elements to adjust the enthalpy of a particular phase is not a new strategy. For instance, it is a common practice to add Mn or Ni to stabilise the high-temperature phase austenite to room temperature [32]. But austenitic steels need a significant amount of alloying (more than 8% of Ni or 18% of Mn). The example of Au in Al-Cu alloys shows the enthalpy change can be adapted with minor additions to overcome the critical stage of precipitate nucleation. It originates from the fact that the  $\eta$  ( $\text{Al}_2\text{Au}$ ) phase in the Al-Au system shares almost the same crystal structure as the  $\theta'$  ( $\text{Al}_2\text{Cu}$ ) phase in the Al-Cu system [33]. But the formation energies of Au in both the solid solution and the precipitate phase are much lower, compared to that of Cu. Thus, Au and Cu atoms cooperate during the nucleation of Au-containing  $\theta'$  phase.

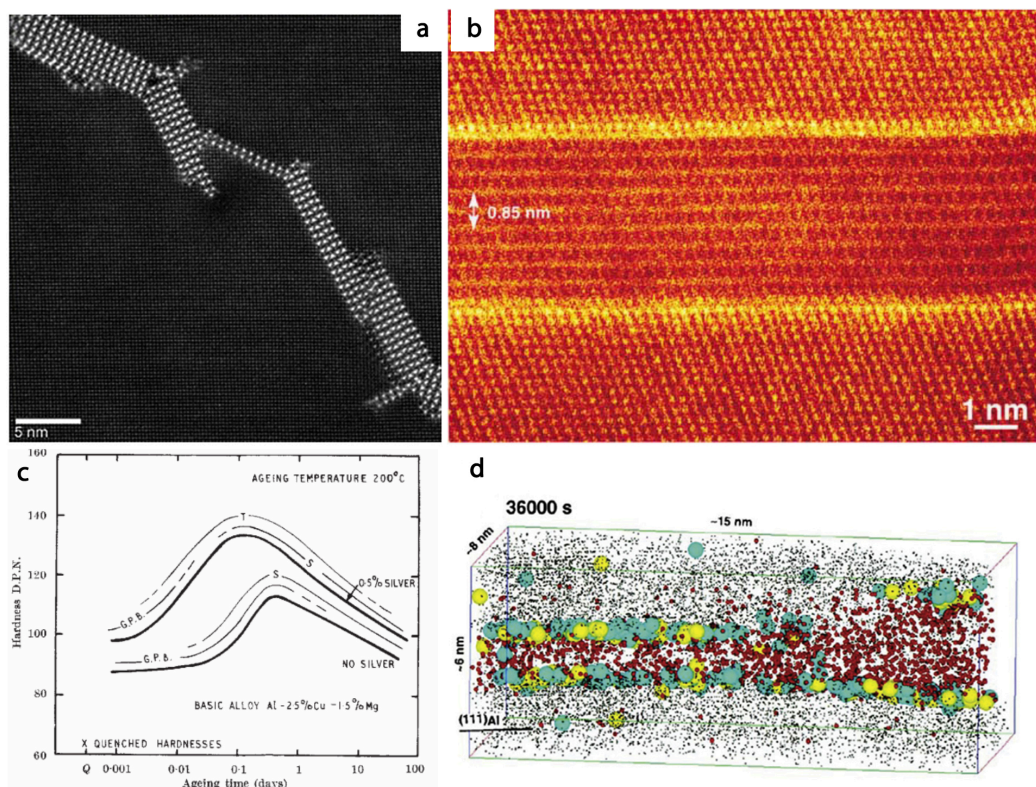


Fig. 2.8 HAADF-STEM images of (a) the S phase, reprinted from Ref. [34] with permission from Elsevier, and (b) the  $\Omega$  phase, reprinted from Ref. [20] with permission from Elsevier. (c) Age hardening response of Al-2.5Cu-1.5 Mg and Al-2.5Cu-1.5Mg-0.5Ag (wt%) alloys, reprinted from Ref. [19] with permission from Nature. (d) Atom probe tomography showing segregation of Mg and Ag atoms at the  $\Omega$ -Al interface. Mg and Ag atoms are represented by green and yellow colour respectively, reprinted from Ref. [35] with permission from Elsevier.

Different from other microalloying elements working in specific systems, the microalloying effects of Ag appear in almost all heat-treatable aluminium alloys. A comprehensive review will be given in Section. 2.2.2. In particular, Ag microalloying additions have a unique phenomenon compared to other elements: the ageing response is not only improved by promoting existing phases but also sometimes by initiating new phases. A well-known case is the addition of Ag in Al-Cu-Mg alloys, which suppresses the  $S'$  and S phases (laths on  $\{210\}_{\text{Al}}$  planes in  $\langle 100 \rangle_{\text{Al}}$  directions, see Fig. 2.8(a)) and promotes the  $\Omega$  phase (plates on  $\{111\}_{\text{Al}}$  planes, see Fig. 2.8(b)). Precipitation hardening (see Fig. 2.8(c)) benefits from the change of precipitate habit plane from  $\{210\}_{\text{Al}}$  to  $\{111\}_{\text{Al}}$  with large aspect ratios, as illustrated in Section. 2.1.1. It brings other advantages including excellent thermal stability, resistance to fatigue and stress corrosion cracking [36]. A pertinent question is how does Ag control the type of precipitate that forms? Atom probe studies [35, 37] and scanning transmission electron microscopy studies [13, 20] have shown that Ag segregates at the coherent Al- $\Omega$  interfaces, see Fig. 2.8 (b and d). This segregation is already present at the early stage of precipitation, which can be as short as 15 s of ageing [35]. The clustering of Ag on  $\{111\}_{\text{Al}}$  planes was suspected to lower the interfacial energy for  $\Omega$  nucleation (mechanism 2) [13, 35]. But what drives Ag to aggregate in the first place remains unknown. Furthermore, how such solute aggregation leads to a different type of precipitate phase is still under debate.

The current knowledge on interfacial structures and microalloying elements relies heavily on experimental observations. The “test and learn” strategy has been applied to explore the elemental effects and their possible combinations. But the lack of fundamental understanding prevents a rational design of precipitation. Such understanding is not limited to scientific interests but also relevant to some practical questions: i.e. how effective a certain microalloying element would display under different processing conditions. For instance, Sn particles nucleate predominantly on dislocations in pre-strained Al-Cu-Sn samples, which destroys its refinement effect [29]. In contrast, dislocations do not interrupt the microalloying phenomenon of Ag. In fact, many Ag-microalloyed aluminium alloys are pre-strained to reach their best mechanical properties during ageing. In a sense, lattice defects can be considered as another element that can be tailored by processing, or even after processing, during the product servicing life. The topic is beyond microalloying itself: one has to consider the intimate interplay between precipitation and lattice defects from a much broader perspective, as discussed in the next section.

### 2.1.3 Precipitation Control via Introduced Defects

Lattice defects are defined as imperfections in an otherwise perfect crystal. These defects often have profound effects on all sorts of materials properties and each defect behaves differently. One of the simplest and most common defects is the vacancy: missing of an atom at one of the lattice sites. Microscopically, a vacancy imposes an elastic strain field in which the surrounding atoms are relaxed from their original position. In addition, the surrounding electronic structure is distorted in accordance with the lattice distortion. For instance, first-principles calculations showed that the charge accumulation is anisotropic between the nearest neighbouring atoms of a mono-vacancy in Al [38]. The redistribution of electronic structure and the strain field require extra energy for the vacancy formation. Statistically, the existence of vacancy contributes entropy (degree of disorder) to the thermodynamics of the system. Configurational entropy increases with vacancies because of the increasing number of distinguishable configurations that atoms can adopt. Vibrational entropy increases as well: since a vacancy releases the bonding constraints of its surrounding atoms, more microstates are added during their thermal vibrations. The balance between increased entropy and increased vacancy formation energy leads to the equilibrium vacancy concentration at evaluated temperature, described by the Arrhenius equation as:

$$C_v = e^{\frac{-\Delta S_v}{k}} e^{\frac{-\Delta H_v}{kT}}, \quad (2.1)$$

where the vacancy concentration  $C_v$  varies exponentially with temperature  $T$ .  $k$  is Boltzmann constant,  $\Delta S_v$  is the vacancy vibrational entropy and  $\Delta H_v$  is the vacancy formation energy. Typically, the vibrational entropy contribution  $\exp(\frac{-\Delta S_v}{k})$  ranges between 2 and 10 for different crystals [39].

On the role of defects during precipitation, one has to realise that diffusional phase transformations are rare events, in terms of both solute diffusion and the compositional/structural transformations. For solute diffusion, the atomic action is the successful jumping of solute atoms from one lattice site to another. In most metals, atoms vibrate at a frequency  $\approx 10^{13}/s$ . But few atoms can overcome the nearest neighbour distance to jump to one of their neighbourhood sites. For substitutional diffusion of a solute, the barrier is associated with the migration energy of solute and the availability of a vacancy at the nearest neighbour sites [10]. The diffusivity  $D_s$  is also described by the Arrhenius equation with a pre-factor  $D_0$  as:

$$D_s = D_0 e^{\frac{-Q}{kT}}, \quad (2.2)$$

where the diffusion activation energy barrier  $Q$  is the sum of the migration energy barrier  $\Delta H_m$  and is the vacancy formation energy  $\Delta H_v$ .  $D_0$  is determined by the vibrational frequency  $\mu$ , nearest neighbour distance  $\alpha$ , coordination number  $z$ , vibrational entropy associated with migration  $\Delta S_m$  and vacancy formation  $\Delta S_v$ , as:

$$D_0 = \frac{1}{6} \alpha^2 z \mu e^{\frac{\Delta S_m + \Delta S_v}{k}}. \quad (2.3)$$

If more vacancies are retained in an alloy than of equilibrium, the diffusion process can be greatly accelerated. Dislocations have a similar diffusion accelerating effect but via a different approach: they act as a pipeline with a lowered migration energy for the solute to diffuse [15].

In terms of compositional/structural transformations, defects usually attract solute to segregate and reduce the strain to transformations. For instance, solute segregation mitigates the energy associated with lattice distortion. As a consequence, the solute-enriched environment and the pre-existing strain at the defects significantly reduce the nucleation barrier for heterogeneous precipitation. For example, the nucleation of  $\theta'$  phase in Al-Cu alloys often takes place on dislocations [8]. Despite  $\theta'$  precipitates having excellent coherency on their broad interface, the invariant plane strain requires a large shear component of  $\sim 33\%$  [8]. As a consequence, a single unit cell of  $\theta'$  is rarely observed. Experimentally,  $\theta'$  precipitates invariably nucleate on dislocation shear loops ( $\vec{b} = a/2\langle 100 \rangle_{\text{Al}}$ ), which form by dissociation of the climbing perfect dislocations ( $\vec{b} = a/2\langle 110 \rangle_{\text{Al}}$ ). Thus, dislocations are effective heterogeneous nucleation sites.

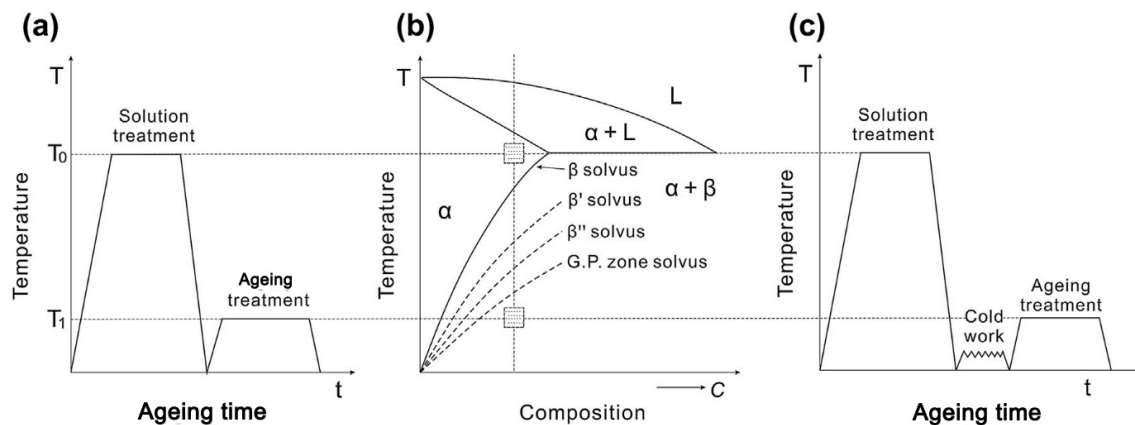


Fig. 2.9 Schematic diagrams showing (a and c) heat treatment schemes for age hardening, and (b) part of a binary phase diagram for precipitation hardenable alloys. Adapted from Ref. [9], p.2010 with permission from Elsevier.

To promote precipitation, defects are added deliberately through thermomechanical treatments. A general heat treatment scheme for a precipitate hardening alloy includes the following procedures, see Fig. 2.9:

1. Solid solution treatment at  $T_0$  in the single-phase region to dissolve coarse second-phase particles.
2. Rapid quenching to obtain a supersaturation of solid solution of alloying elements and quenched-in vacancies.
3. Ageing at a given temperature  $T_1$ . It may involve cold working before ageing to introduce dislocations and thus facilitate fine dispersion of precipitates.

Quenching from the solute solution treatment allows supersaturation of solutes, which promotes precipitation: the driving force  $\Delta G_v$  is proportional to the solute supersaturation  $\Delta C = C_0 - C_e$ , where  $C_0$  is the alloy composition and  $C_e$  is the equilibrium concentration [9]. Moreover, one should not forget that vacancy concentration rises exponentially with temperature. For instance, aluminium alloys have an equilibrium vacancy concentration of  $\sim 10^{-4}$  at a solid solution temperature above  $500^\circ\text{C}$  but an equilibrium concentration of  $\sim 10^{-11}$  at the room temperature. The drastic cooling rate leaves little time for vacancies to escape to their sinks (e.g. grain boundaries). Thus, the vacancy concentration is retained at value orders of magnitude higher than the equilibrium. The quenched-in defects – either vacancies or various secondary defects arising from the condensation of vacancies – drive the kinetics of the system far away from equilibrium by accelerating diffusion and providing heterogeneous nucleation sites. In fact, Guinier's X-ray results [40] were criticised by Laves [41] as those required a diffusion coefficient much higher than the equilibrium value at room temperature. At that time, the role of vacancies was not understood. Among many arguments in the field, quenched-in vacancies were proposed to be responsible for rapid precipitation and this is the only theory survived [42]. The mechanism of "vacancy pump" [43] was then developed: solute atoms and vacancies are assumed to bind strongly and diffuse together towards solute-enriched zones. Upon reaching those zones, the solute atoms are attracted more strongly to the zones, thus they stay there, while vacancies depart and bind to new solute atoms again until they run out (i.e. being absorbed by vacancy sinks like grain boundaries and dislocations). The role of quenched-in defects can be appreciated with the occurrence of the precipitate-free zone near grain boundaries. The major part of a precipitate-free zone is depleted of defects, rather than solute, for precipitation [44].

Quenched-in defects sometimes are not enough – in terms of their total amount and the distribution. In addition, because each type has a different nature, the quenched-in defects

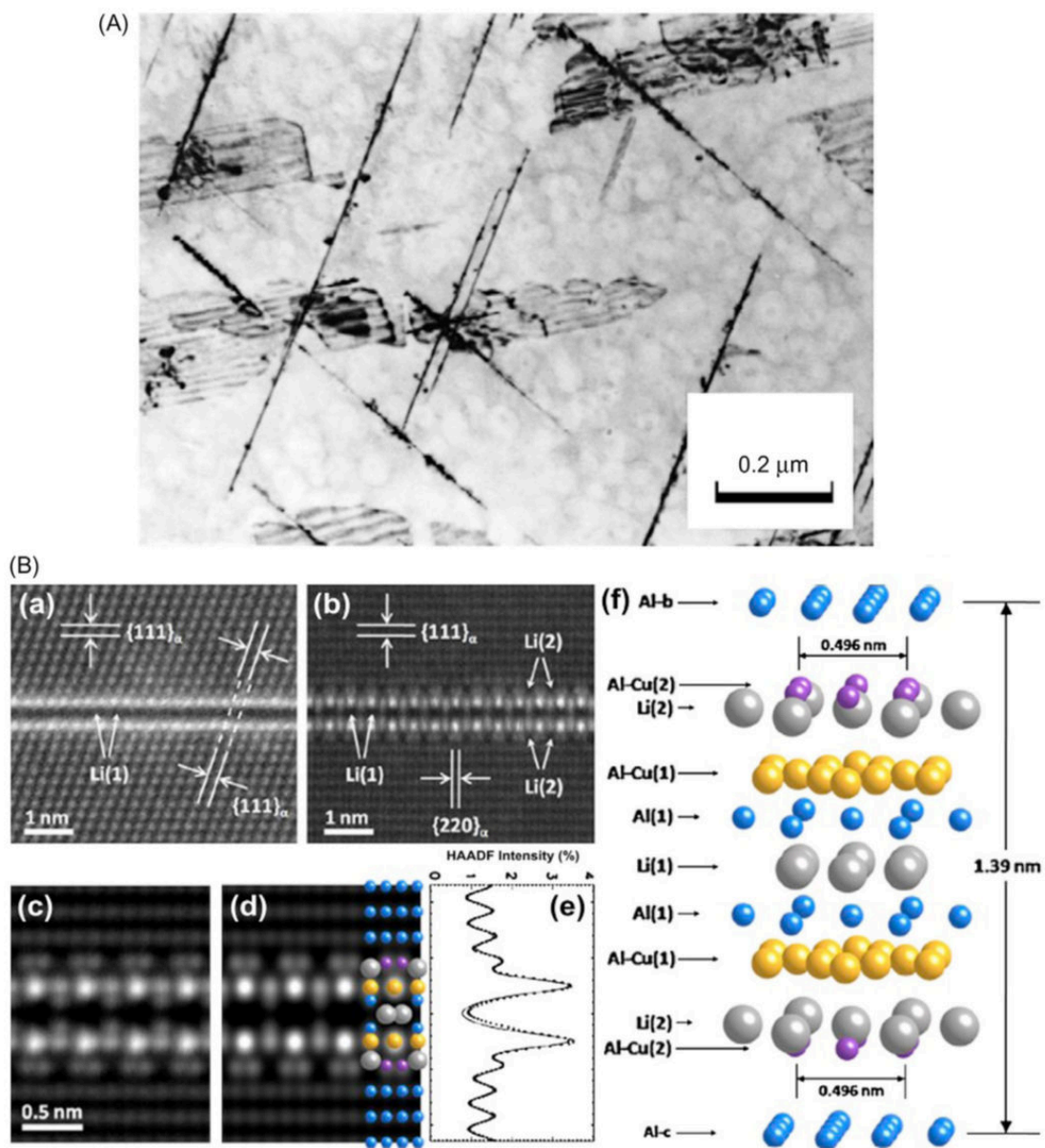


Fig. 2.10 (a) Thin plates of the  $T_1$  phase ( $\text{Al}_2\text{CuLi}$ ) in an Al–Li–Cu–Zr alloy overaged (500 h) at  $170^\circ\text{C}$ . Courtesy: Gregson, P. J. (b) Atomic-resolution high-angle annular dark-field scanning transmission electron microscopy images and simulated images and the structural model of  $T_1$ . From Ref. [45], reprinted by permission from American Physical Society.

may not be the most effective type in promoting precipitation. Dislocations have overall quite a different role from vacancies: they tend to accommodate the shear strain associated with the structural transformations. Dislocations can be introduced by cold working after quenching and prior to artificial ageing. This practice is commonly coded as the T8 in the aluminium temper scheme [17]. For example, the  $T_1$  precipitate phase in Al-Cu-Li alloys forms with difficulties, as its associated transformation shear strain is as large as  $\sim 35\%$  [9]. Because the  $T_1$  phase has a hexagonal lattice [45] and the aluminium matrix is face-centred cubic, the structural transformation requires Shockley partial dislocations ( $\vec{b} = a/6\langle 11\bar{2} \rangle_{\text{Al}}$ ), that usually dissociate from perfect dislocations ( $\vec{b} = a/2\langle 110 \rangle_{\text{Al}}$ ). Thus, similar to the  $\theta'$  phase in the Al-Cu system, the  $T_1$  phase nucleates predominantly on dislocations. To promote a uniform distribution, many Li-containing aluminium alloys are often processed under the T8 condition. Ag and Mg are microalloyed to these Al-Cu-Li alloys to promote fine-scale precipitation: they segregate at the coherent precipitate-matrix interface of  $T_1$  phase [46]. A celebrated example is the *Weldalite*<sup>TM</sup> alloy (Al-Cu-Li-Mg-Ag-Zr) from Lockheed Martin<sup>3</sup>, demonstrating yield strength over 700 MPa – one of the strongest aluminium alloys ever produced. On the basis of its strength-to-weight ratio, this alloy is equivalent to steels with a strength of more than 2 GPa [17]. Alloy 2219 is a modified version of the *Weldalite*<sup>TM</sup> alloy that was used for constructing the first version of the disposable external fuel tank of the space shuttle, see Fig. 1.2. The T8 treatment promotes the  $T_1$  precipitation and disperses the precipitates uniformly on  $\{111\}_{\text{Al}}$  planes, thus, significantly strengthens the alloy.

Defects can accumulate in alloys while they bear thermal and mechanical loadings as engineering structural components. For instance, aluminium aircraft wings bear cyclic loading during flight, which leads to crack initiation and propagation under a stress lower than the yield strength, known as fatigue. Alloys are also deformed slowly but permanently under the influence of mechanical stresses, known as creep, though the stress is below the yield strength. Fatigue and creep properties are critical in evaluating the reliability of alloys. Unfortunately, those properties are generally disappointing for heat-treatable aluminium alloys compared to magnesium alloys and steels [47]. There are several reasons, one of which is the metastable nature of microstructure [4]. The atomic mechanisms of microstructure evolution during alloy servicing are largely unknown.

In summary, it is clear that precipitate interfaces and defects are important in controlling precipitation behaviours. Some successful applications with microalloying additions have been reviewed, though the knowledge of how they promote precipitation is practically empirical. Ag microalloying in Al is particularly interesting, as it alters the type of precipitate phase into one with the desired orientation relationship. Introducing defects from processing

<sup>3</sup>Lockheed Martin is the key contractor for NASA and US defence.

is another approach to stimulate diffusional phase transformations. Since different precipitate phases require dislocations with different Burgers vectors for their formation, it is possible to tailor the precipitation behaviours with different defects. However, to our best knowledge, tailoring precipitation through the Burgers vectors of dislocations is rarely Reported. In addition, during the servicing of alloys as engineering structural components, the microstructure stability with accumulated defects are largely unknown. Resolving the atomic mechanisms of interfaces and defects is a long-standing scientific goal in the field of metallurgy. In order to improve one's understanding of the role of interfaces, microalloying elements and defects during precipitation, it is intuitive to study a simple alloy system first. The Al-Ag alloy system is one such simple model system that has been used in the development of precipitation theory. This classic system is chosen in the current study, not just because of its simplicity, but because of the significance of Ag microalloying in aluminium, as now reviewed.

## 2.2 The Al-Ag Alloy System

### 2.2.1 The Binary Al-Ag System

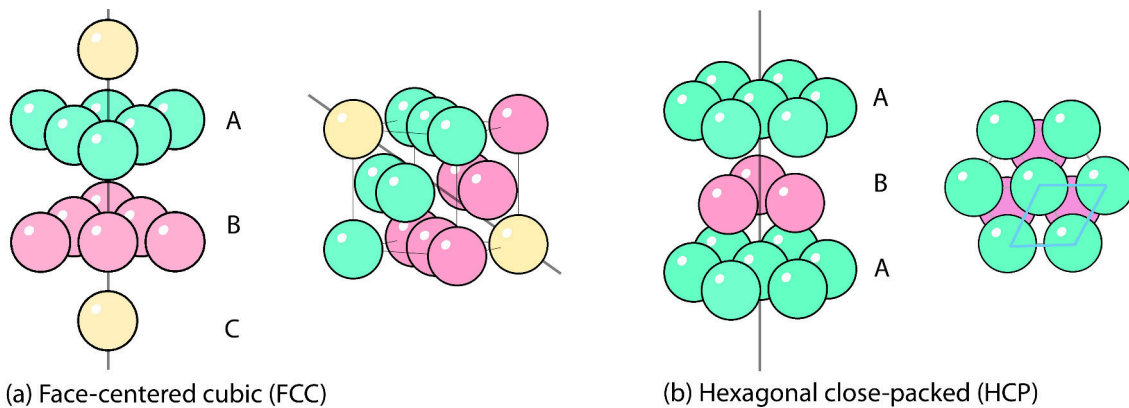


Fig. 2.11 Schematic illustration of the atomic layer stackings for (a) face-centred cubic (FCC) structure and (b) hexagonal close-packed (HCP) structure. Redrawn from Ref. [48], p.1086.

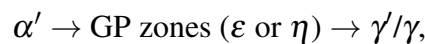
Al-Ag alloys have been studied extensively since the last centenary and now serve as a textbook alloy system [10, 15, 40]. As mentioned in Chapter 1, it is a model system to study solid-state phase transformations for several reasons. First, the associated FCC-HCP transformation is simple and well-established, Fig. 2.11. Second, the atomic size difference between Al and Ag is negligible ( $\sim 0.5\%$ ), which gives a minimal volumetric strain associated

with the solute clustering and phase transformations. Third, the alloy microstructure involves precipitate plates on  $\{111\}_{\text{Al}}$  planes, which is a common feature for many high strength aluminium alloys. In addition, the large difference between the atomic numbers of Al and Ag ( $Z_{\text{Al}} = 13$  and  $Z_{\text{Ag}} = 47$ ) is particularly favourable for imaging with the transmission electron microscope [16]. Thus, Al-Ag alloys are often chosen to demonstrate advanced electron microscopy techniques, such as *in situ* annealing to observe the precipitates growth in real time [49] and electron tomography to reconstruct embedded precipitates with a high spatial resolution [50, 51].

A glimpse of the equilibrium phases in the Al-Ag phase diagram is given in Fig. 2.12, where the phase boundaries were determined metallographically, electrochemically or via X-ray diffractions [52]. The equilibrium phases are listed as:

- the liquid, L;
- the Ag-rich terminal solid solution, with maximum solubility of 20.4 at% Al at about 450°C;
- the Al-rich terminal solid solution, with maximum solubility of 23.5 at% Ag at about 567°C;
- the HCP intermetallic phase  $\gamma$  ( $\text{Ag}_2\text{Al}$ );
- the high-temperature intermetallic body-centred cubic (BCC) phase  $\beta$  ( $\text{Ag}_3\text{Al}$ );
- the low-temperature intermetallic phase  $\mu$  ( $\text{Ag}_3\text{Al}$ ) with the complex cubic  $\beta$ -Mn structure.

Now focusing on the Al-rich side, the precipitation sequence is commonly recognised as [10]:



where  $\alpha'$  represents the supersaturated solid solution. GP zones are the early-stage solute-enriched coherent particles.  $\gamma'$  is a metastable HCP precipitate phase before the equilibrium  $\gamma$ .

In the following sections, each precipitate phase will be reviewed in detail, emphasising their atomic structures and phase transformations. We will also review the computational efforts to construct the phase diagram from first-principles and the prediction of a new AgAl phase.

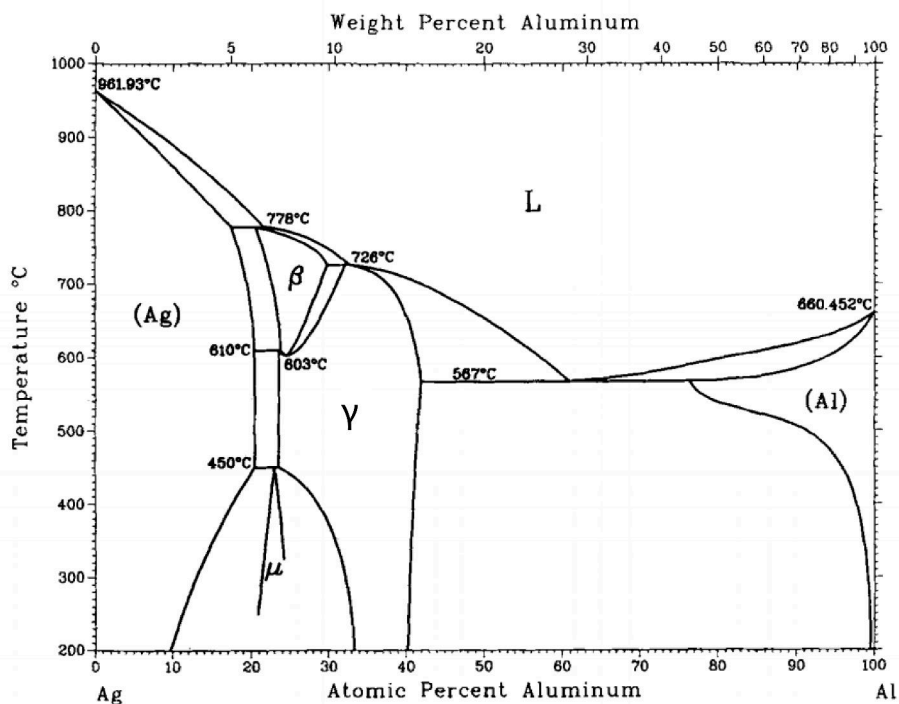


Fig. 2.12 The equilibrium Ag-Al phase diagram. From Ref. [52], reprinted by permission from Springer.

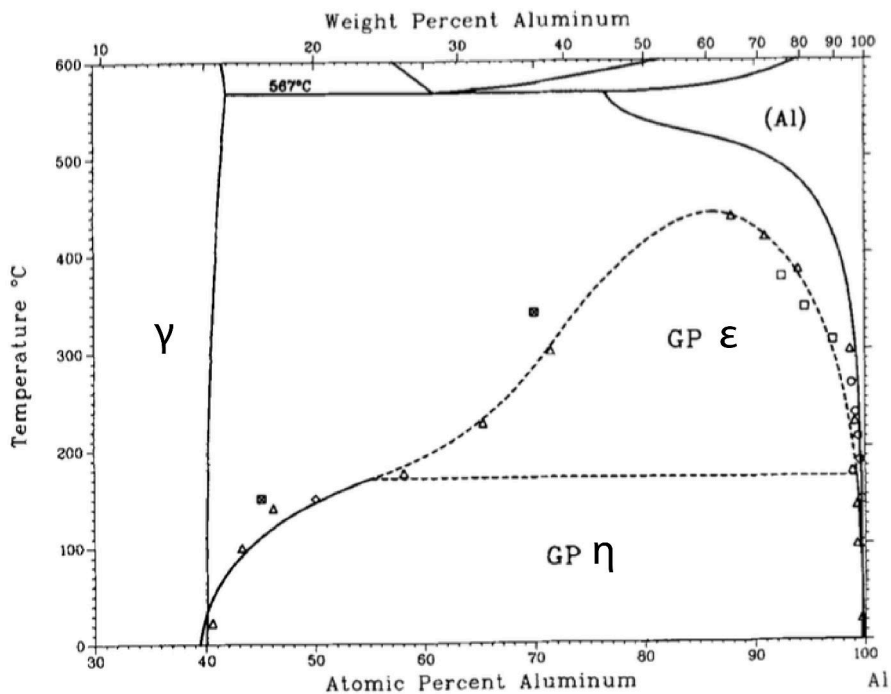


Fig. 2.13 The partial phase diagram in the Al-enriched side showing the asymmetric miscibility gap of GP zones. Adapted from Ref. [52] with permission from Springer.

### 2.2.1.1 FCC Phases: GP zones $\epsilon$ and $\eta$

Unlike most aluminium alloys, GP zones in the Al-Ag system form immediately after quenching [53] and demonstrate a remarkable thermal stability: a full dissolution requires a temperature up to 465°C [54]. Given an asymmetric miscibility gap, Fig. 2.13, two types of GP zones are proposed, with their compositions depending on ageing temperature:  $\epsilon$  forms at high temperature ( $> 170$  °C) with relatively low Ag concentration (below 44 at.%) while  $\eta$  forms at low temperature ( $< 170$  °C) with relatively high Ag concentration (44 at.%-60 at.%) [53, 55, 56]. Fig.2.14 shows the interpretation of the GP zones formation based on the classical theories of homogeneous nucleation and spinodal decomposition [57]. As the homogeneous nucleation curve ( $\Delta G^*=25kT$ ) is so close to the GP zones solvus line (due to small interfacial energy), there is little chance for spinodal decomposition to occur. It means that GP zones are nucleated homogeneously, unless rapid quenching techniques are used for a particular alloy composition ( $\sim 15$  at.% Ag). However, the calculated curve is significantly different from the experimental solvus, particularly at the temperature for the  $\epsilon$ - $\eta$  transition. For such a basic system, the partition of two types of GP zones cannot be understood from the classical thermodynamics. Asta and Hoyt investigated the thermodynamics with first-principles calculations [58]. The short-range order was found to contribute considerably to the stability of  $\epsilon$  phase, which is not included in the Bragg-Williams approximation (the regular solution model with a random chemical distribution). Applying the first-principles results to a Monte-Carlo simulation, the Ag concentration in a simulated GP zone  $\epsilon$  at 177°C indeed matched with that indicated by the GP zone solvus line [58]. The mystery of the asymmetric miscibility gap is still unsolved (not in this thesis as well). However, first-principles calculations have the potential to address the underlying mechanisms.

The morphology of GP zones is irregular at the early stage and gradually evolves into a sphere truncated by  $\{111\}_{Al}$  facets, as first reported by an X-ray study [59] and then confirmed by STEM [60] and atom probe [61] studies. GP zone  $\eta$  has a uniform composition while GP zone  $\epsilon$  is believed to have a core-shell structure and there has been much debate as to whether Ag enriches the core or the shell [62, 63]. We will address the structure and composition of GP zone  $\epsilon$  in a later result chapter. The high contrast and perfect coherency of GP zones are favoured for electron tomography studies. For example, Fig. 2.15 shows the 3D reconstruction of the microstructure after equal channel angular pressing (ECAP), where GP zones in the shear bands were deformed into an elliptical shape. Fig. 2.16 shows the first demonstration of crystalline particles reconstructed with atomic resolution using discrete tomography [51]. By imaging in two major zone-axes and quantifying the scattered intensity with simulations, the number of Ag atoms was refined in each atomic column. Note that these authors assumed that GP zone  $\eta$  consists of 100% Ag, which is wrong, but a reasonable

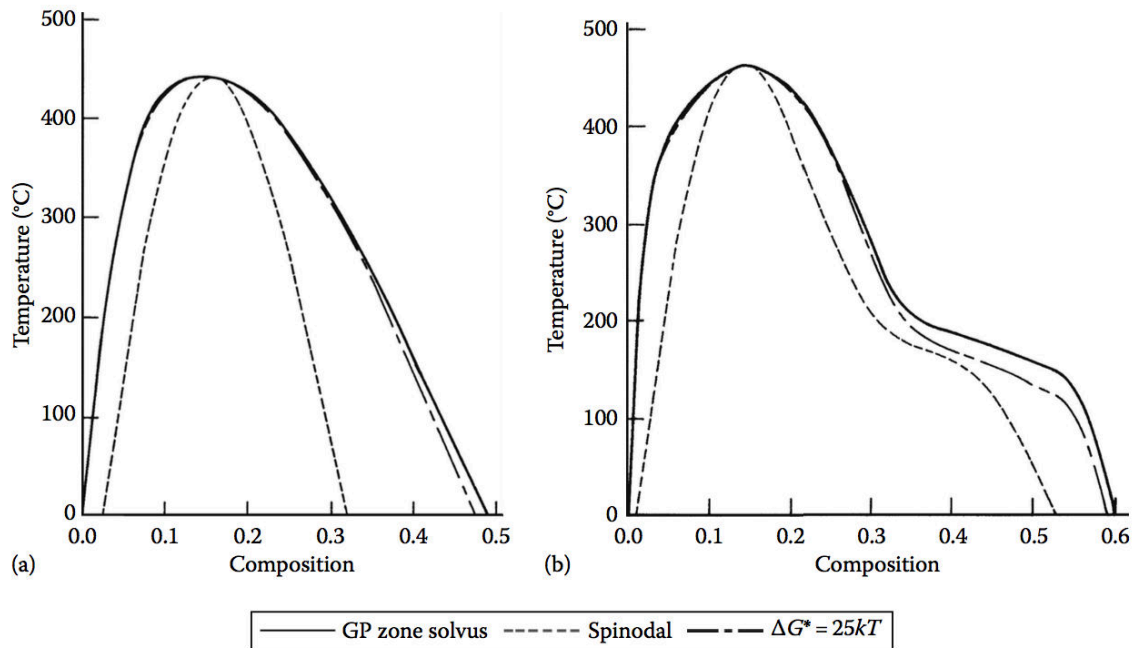


Fig. 2.14 The coherent spinodal and the nucleation energy barrier  $\Delta G^* = 25kT$  curve in FCC Al–Ag, based upon (a) the calculated GP zone solvus and (b) the experimental GP zone solvus. From Ref.[57], reprinted by permission from Elsevier.

starting point for a difficult problem. This study has promoted the on-going movement of atomic electron tomography [64–66], resolving a long-standing scientific problem: in 1959, Richard Feynman challenged the microscopy society to locate each individual atoms in substances.

### 2.2.1.2 HCP Phases: $\gamma'/\gamma$

The  $\gamma'$  phase is a metastable precipitate phase formed before the equilibrium  $\gamma$  phase. Both phases display the same composition ( $\text{Ag}_2\text{Al}$ ) and the same atomic structure but with slightly different lattice parameters as shown in Fig. 2.17. There is a dispute regarding the detailed structure of  $\gamma'/\gamma$ . Based on the X-ray diffraction of single crystals, Neumann proposed a model in which each basal plane has the same composition of  $\text{Ag}_2\text{Al}$  (HCP with space group  $P6_3/mmc$ ) [68]. In Neumann's model, the short-range order exists within the basal planes such that every Al atom is surrounded by 6 Ag atoms. On the other hand, Nicholson and Nutting noted the appearance of  $\pm 0001$  reflections during the thickening of  $\gamma'$  in a  $\langle 110 \rangle_{\text{Al}}$  selected area diffraction pattern, suggesting the long-range order in alternating basal planes with the composition of  $\text{Al}_2\text{Ag}$  and pure Ag (HCP with space group  $P6\bar{2}m$ ) [54]. Howe developed this model with detailed TEM studies using convergent beam electron diffraction

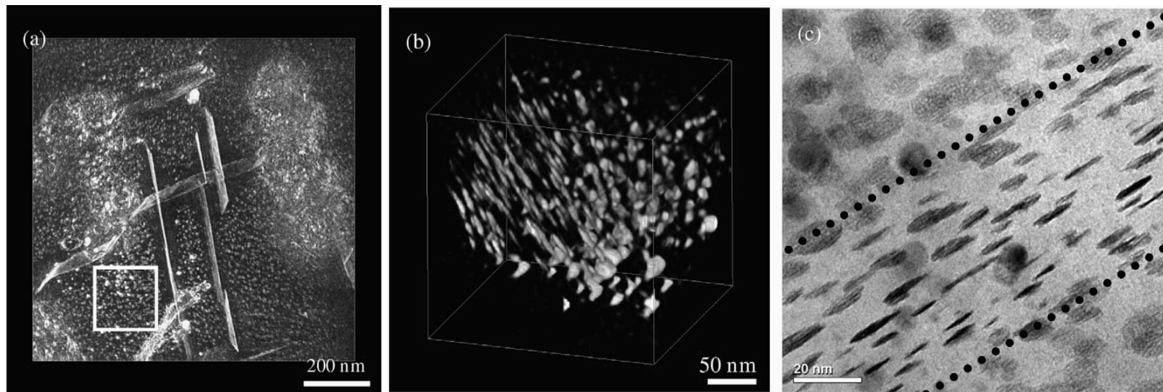


Fig. 2.15 GP zones are readily sheared by moving dislocations in ECAP processed Al–Ag alloys. (a) Reconstructed 3D volume; (b) enlarged view from the boxed region in (a). (c) High-resolution TEM image obtained from a similar region showing ellipsoidal GP zones within the shear band, clearly indicated by the black dotted lines. From Ref.[50], reprinted by permission from Elsevier.

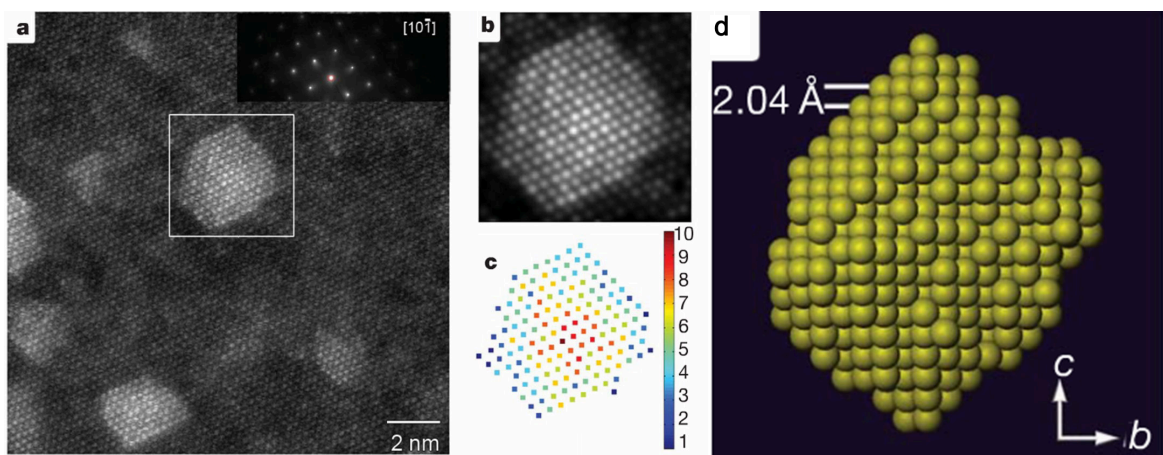


Fig. 2.16 Quantification of HAADF STEM images. (a) Experimental HAADF STEM image of nanometre-sized Ag clusters embedded in an Al matrix in  $[10\bar{1}]$  zone-axis orientation, together with the corresponding electron diffraction pattern. (b) Simulated image of the boxed region by Gaussian peak fitting. (c) The number of Ag atoms per column. (d) The computed 3D reconstruction. From Ref.[51], reprinted by permission from Nature.

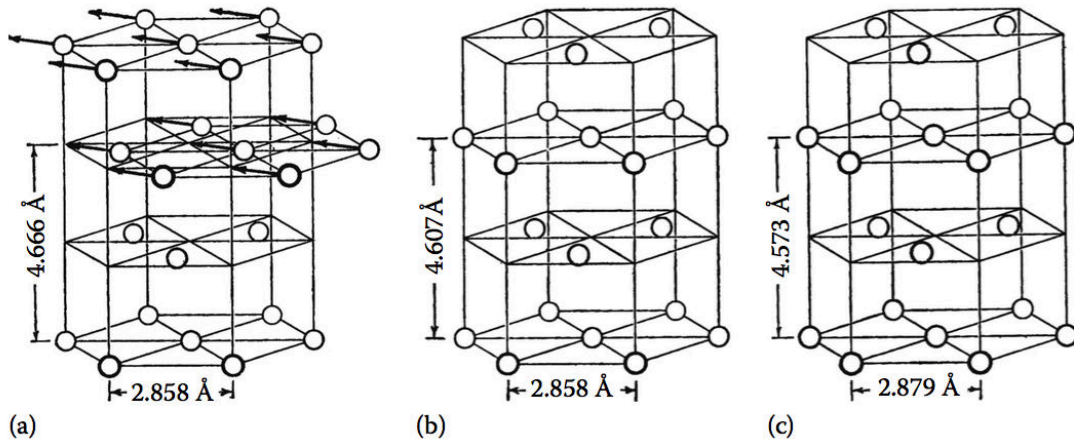


Fig. 2.17 Crystal structures of phases in Al–Ag alloys. (a) Structure of solid solution matrix (FCC), (b) structure of transition phase  $\gamma'$  (HCP), and (c) structure of equilibrium precipitate phase,  $\gamma$  (HCP). From Ref.[67] Used with permission of The Minerals, Metals & Materials Society.

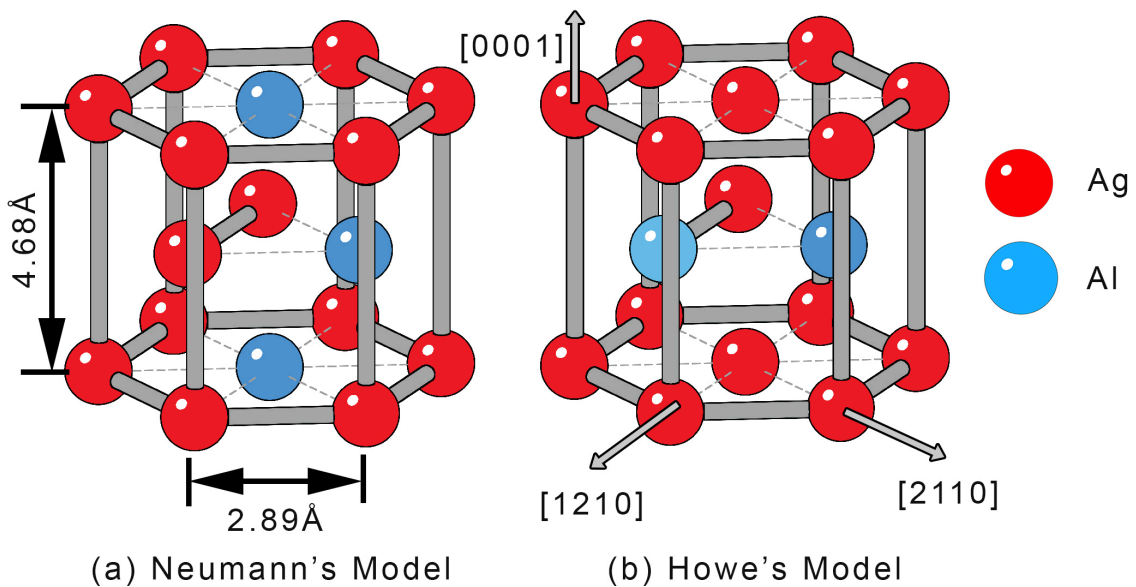


Fig. 2.18 Proposed atomic structures of  $\gamma$  phase ( $\text{Ag}_2\text{Al}$ ): (a) Neumann's model [68] and (b) Howe's model [69].

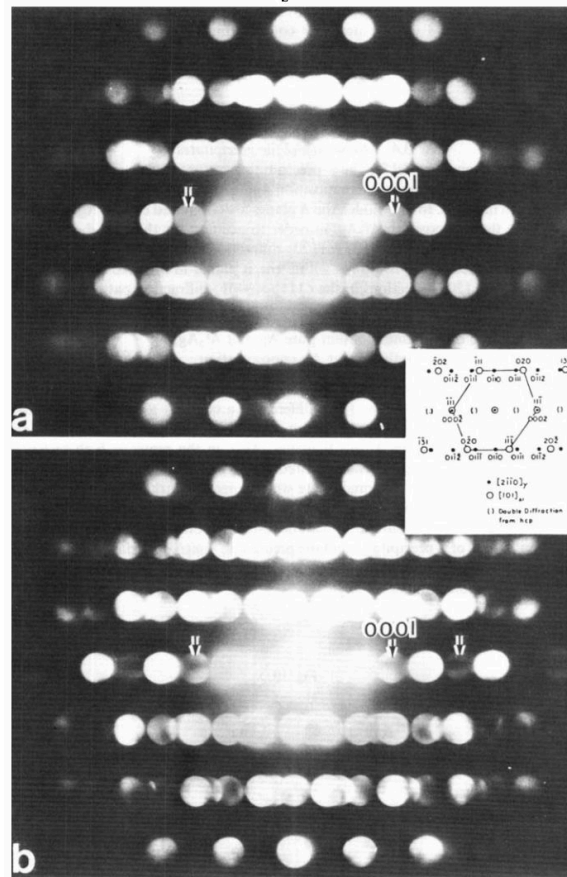


Fig. 2.19 Two  $\langle 110 \rangle_{\text{Al}} // \langle 11\bar{2}0 \rangle_{\gamma}$  CBED patterns obtained from  $\gamma$  precipitates. The  $000L$ ,  $L=\text{odd}$ , precipitate reflections in (a) display strong uniform intensities, indicating that they are allowed, while the same reflections in (b) contain G-M lines, indicating that they are kinematically forbidden. Reprinted from Ref.[69] with permission from Taylor & Francis.

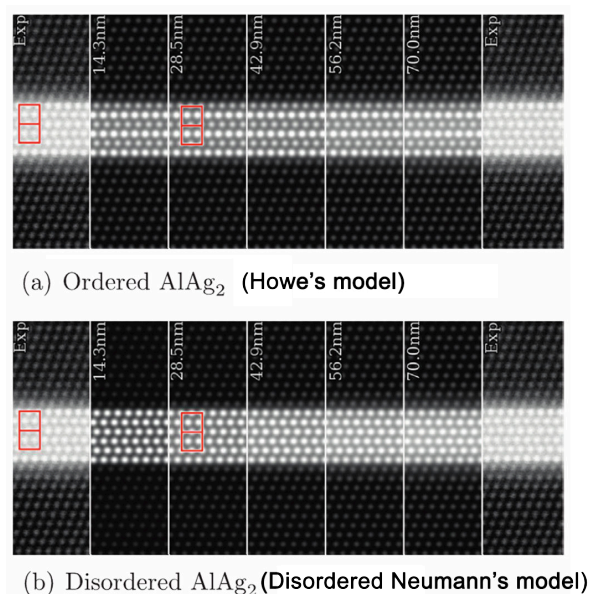


Fig. 2.20 HAADF-STEM images and simulations for (a) ordered and (b) disordered  $\gamma'$  precipitates. The recorded image (labelled “Exp”) is compared with simulations for foil thicknesses of 14–70 nm. The red outline indicates a single HCP unit cell. From Ref.[70], reprinted by permission from Elsevier.

(CBED) and high-resolution TEM [69, 71, 72]. Convergent beam electron diffraction was performed to determine the space group. The  $\pm 000L$  reflections,  $L=\text{odd}$ , were found to be indeed kinematically forbidden, but they could also be generated from double diffraction<sup>4</sup>. In Howe’s observation, Fig. 2.19, the  $\pm 0001$  reflections of some precipitates were cut by Gjønnes-Moodie lines<sup>5</sup> while some were not, indicating that the long-range order along the basal planes was not evident for every precipitate. The space group was still determined to be  $P6_3/mmc$  from CBED experiments on extracted  $\text{Ag}_2\text{Al}$  plates, same as that of the Neumann’s model. However, Howe’s high-resolution TEM and image simulations seem to support the composition of  $\text{Al}_2\text{Ag}$  and pure Ag on alternating basal planes [69]. HAADF-STEM imaging, which provides strong Z contrast, can disclose the chemical order of Ag and Al unambiguously. Fig. 2.20 compares the experimental image with image simulations of the Howe’s model and the disordered Neumann’s model; the long-range order was not observed [70]. Scanning CBED performed across a  $\gamma'$  precipitate (see Fig. 2.21) also shows extinction of the  $\pm 0001$  reflections [70]. From this, we may conclude that the  $\gamma'$  phase has a

<sup>4</sup>Double diffraction spots are caused by extra reflections due to multiple and dynamic scattering of the electron beam through several crystals. The scattering vectors of the extra reflections are linearly composed by those of each crystal.

<sup>5</sup>A Gjønnes-Moodie (G-M) line is where the diffraction is forbidden both kinematically and dynamically: a dark line cutting through the centre of a kinetically forbidden but dynamically arisen reflection.

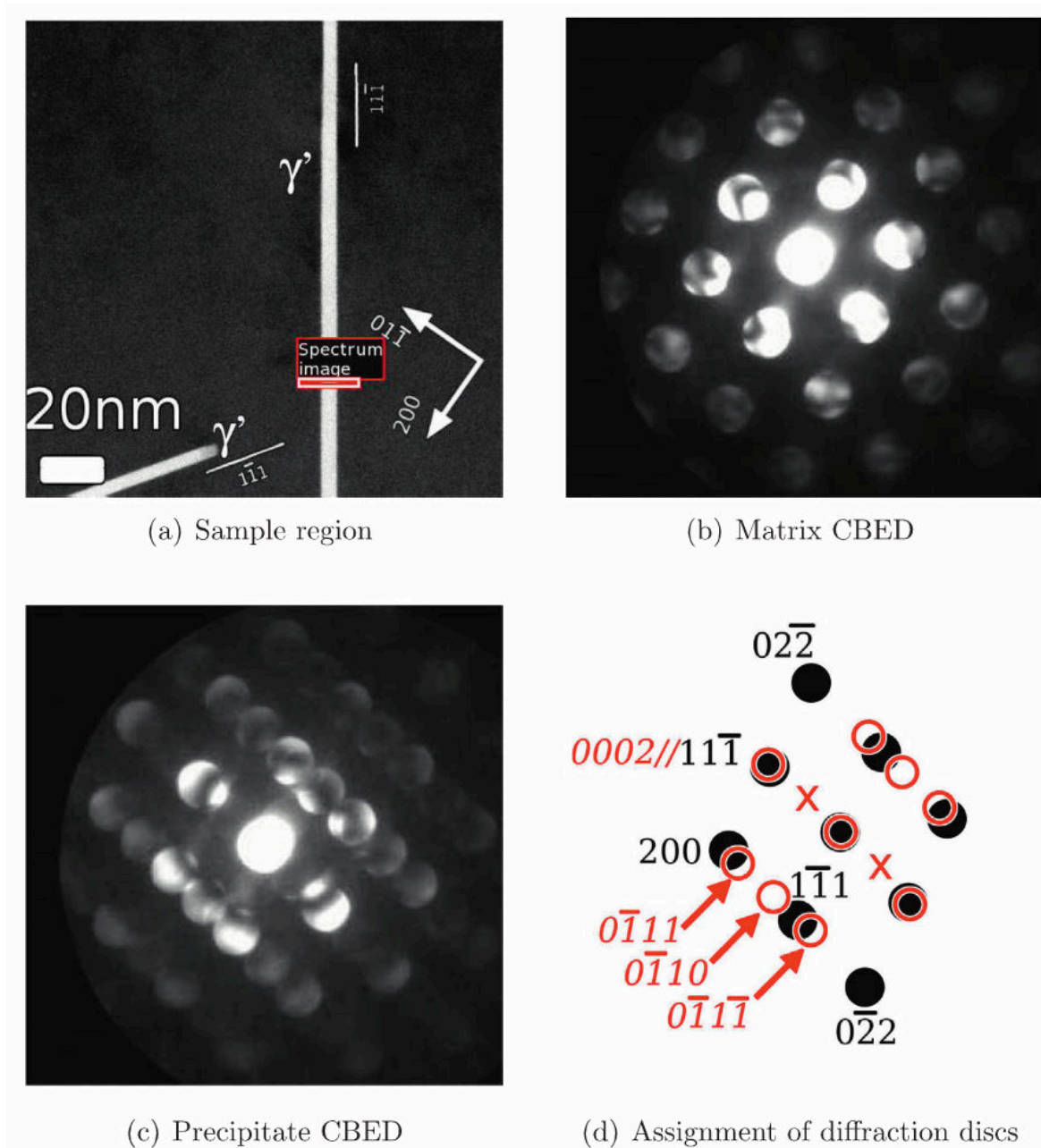


Fig. 2.21 Convergent beam electron diffraction patterns of a  $\gamma'$  precipitate. (a) A HAADF-STEM image of the region of interest. (b) The CBED pattern for the matrix adjacent to the precipitate. (c) A CBED pattern from the  $\gamma'$  precipitate. The main diffraction discs are assigned in (d). Filled and open circles indicate matrix and precipitate reflections, respectively. Note the absence of diffraction intensity in the  $\pm 0001$  positions (labelled "x" in (d)). From Ref.[70], reprinted by permission from Elsevier.

composition of  $\text{Ag}_2\text{Al}$  on each basal plane. However, it would be still interesting to know why the  $\pm 0001$  reflections appear in Nicholson & Nutting's and Howe's diffraction experiments. In addition, the previous TEM studies viewing along the  $\langle 110 \rangle_{\text{Al}}$  direction cannot examine the short-range order within the basal planes as prescribed in the Neumann's model. Diffusive X-ray diffraction experiments [73] and first-principles calculations [74] reported that the  $\gamma$  phase has an order-disorder transformation at  $126^\circ\text{C}$ . A detailed HAADF-STEM is needed to investigate the nature of short-range order, particularly in a  $\langle 11\bar{2} \rangle_{\text{Al}}$  direction where the Neumann's model is distinguishable from the disordered one.

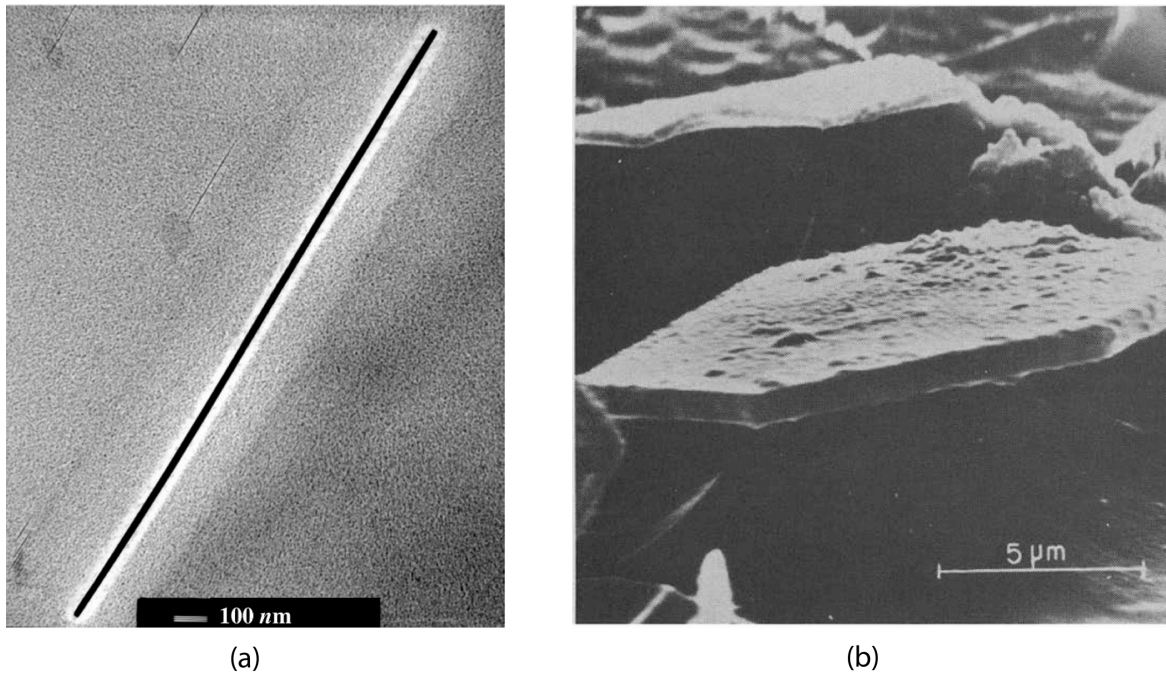


Fig. 2.22 (a) TEM image of an HCP  $\gamma'$  precipitate viewed edge-on along  $\langle 110 \rangle_{\text{Al}}$ . From Ref. [75], reprinted by permission from Elsevier. (b) SEM image of an  $\text{Ag}_2\text{Al}$  precipitate in a deeply etched Al matrix after ageing at  $410^\circ\text{C}$  for 430 h, elucidating its characteristic hexagonal shape. From Ref. [76], reprinted by permission from Elsevier.

The FCC-HCP phase transformation associated with  $\gamma'$  phase formation is a classic example of precipitation. When embedded within the matrix,  $\gamma'$  precipitates have a hexagonal plate geometry, Fig.2.22, and share the following orientation relationship with the Al matrix:

$$\{111\}_{\text{Al}} \parallel \{0001\}_{\gamma'} \text{ and } \langle 110 \rangle_{\text{Al}} \parallel \langle 11\bar{2}0 \rangle_{\gamma'}$$

The broad interface ( $\{111\}_{\text{Al}} \parallel \{0001\}_{\gamma'}$ ) shows excellent coherency between the close-packed planes of FCC and HCP, while the edge interface ( $\{11\bar{2}\}_{\text{Al}} \parallel \{1\bar{1}00\}_{\gamma'}$ ) is semicoherent. The transformation from FCC to HCP changes the stacking sequence of close-packed planes from ABCABC to ABABAB, Fig. 2.11. On close-packed planes, Fig. 2.23, there

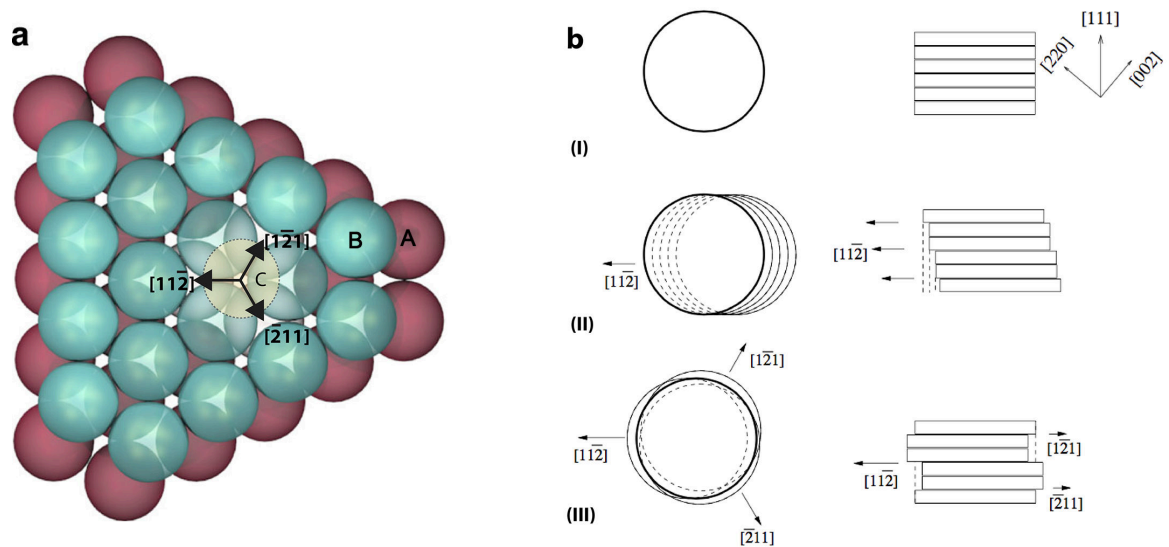


Fig. 2.23 Schematic illustration of the shape-change accompanying the nucleation of an HCP phase in an FCC matrix. (a) Atomic model showing three Burgers vectors of  $1/6\langle 112 \rangle$  on the close-packed planes to transform FCC (ABCABC stacking) to HCP (ABAB stacking) viewed in a  $\langle 111 \rangle$  direction. (b) I: shown as a series of stacking disks on  $\{111\}$  habit planes, each representing a single close-packed layer; II: the precipitate is sheared in one direction, resulting in a considerable shape change of  $\sim 0.35$ , and consequently high shear strain energy; III: the precipitate are sheared through three Shockley partial dislocations and achieves self-accommodation. Reprinted from Ref. [15, 77] with permission from Taylor & Francis and J. M. Rosalie.

are three equivalent Shockley partial dislocations ( $\vec{b} = a/6\langle 11\bar{2} \rangle_{\text{Al}}$ ) that accomplish the FCC-HCP transformation. An embedded  $\gamma'$  precipitate phase requires each one of the partial dislocations equally and periodically to minimise the shear strain. For instance, if only one type of Shockley partial dislocation is used, the macroscopic shape change is equal to the shear of that dislocation, which is significant  $\sim 35\%$ . But the usage of all three partial dislocations in equal number gives no overall shape change. Furthermore, only every three partials can achieve such strain cancellation. The discrete nature of shear strain as a function of the thickness imposes a considerable barrier for  $\gamma'$  nucleation, which was estimated to be of the same magnitude as the interfacial energy for one unit cell of  $\gamma'$  phase [78]. Moreover, Al has a particularly high stacking fault energy [79], which means HCP precipitates generally nucleate with great difficulty. As the stacking fault energy of Ag is one magnitude lower than Al, the segregation of Ag to the stacking faults yields a pathway for the FCC-HCP transformation [80]. The difficult  $\gamma'/\gamma$  nucleation inevitably results in a low precipitate density. As a consequence, Al-Ag alloys have poor mechanical performance [77].

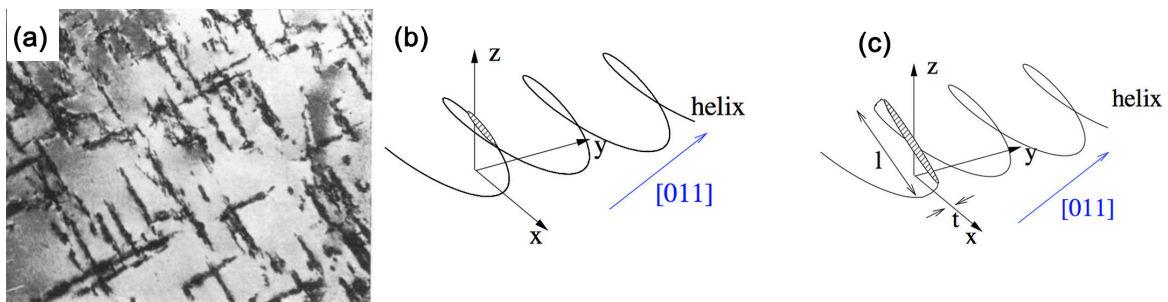


Fig. 2.24  $\gamma'$  precipitation on helical dislocations. (a) TEM image showing the microstructure of an Al-16 wt.% Ag (equivalently Al-4.5 at.% Ag) sample aged at 160°C for 1 day after water quenching from 520°C. From Ref. [54], reprinted by permission from Elsevier. (b and c) Schematic diagrams describing the nucleation and growth of  $\gamma'$  on a helical dislocation. The helical dislocation has Burgers vector  $\vec{b}=1/2\langle 110 \rangle$  and helical axis of  $\langle 110 \rangle_{\text{Al}}$ . The loop dissociates into two Shockley partial dislocations with a narrow stacking fault separating them. The absorption of silver on the stacking fault leads to the formation of  $\gamma'$ . The length of the  $\gamma'$  precipitate,  $l$ , however, is limited by the diameter of the helix. From Ref. [78], p. 11 with permission from J. M. Rosalie.

Because of the intrinsic difficulty of the FCC-HCP transformation,  $\gamma'$  precipitates predominantly nucleate on defects. Not surprisingly, the morphologies and distributions of defects control that of precipitates. Nicholson and Nutting found that quenching introduces helical dislocations, which absorb silver and degenerate into several long and narrow stacking faults [54].  $\gamma'$  nucleation takes place via the dissociation of a unit dislocation into two Shockley partial dislocations:

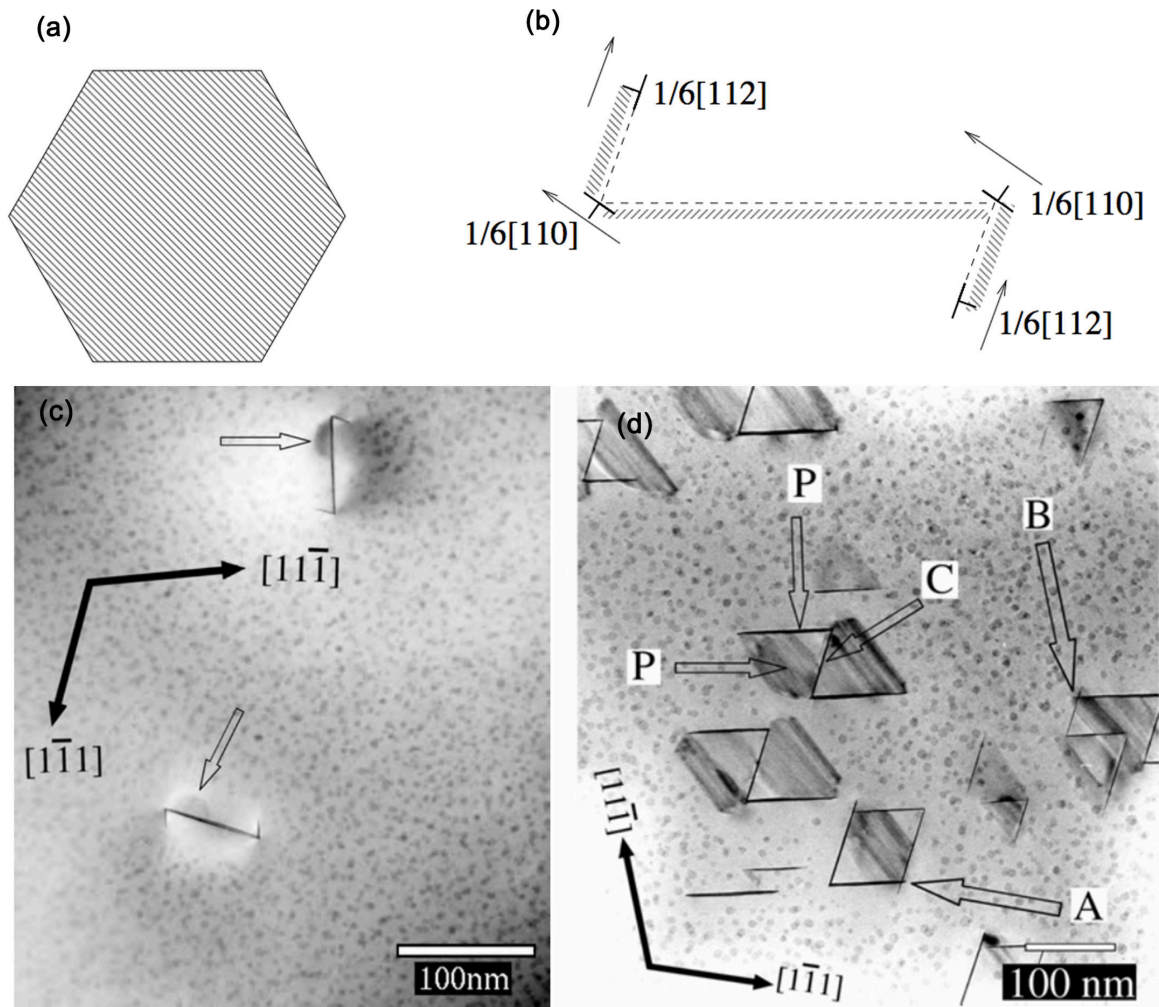


Fig. 2.25 (a) Hexagonal Frank dislocation loop viewed along a  $\langle 111 \rangle_{Al}$  direction. (b) The dissociation of a Frank dislocation loop into Shockley partial dislocations and Lomer–Cottrell dislocations, viewed along a  $\langle 110 \rangle_{Al}$  direction. Taken from Ref. [78], p. 10. (c) The  $\gamma'$  precipitate assemblies at the early stage of ageing (0.5 h at 200°C for an Al-1.7 at.%Ag alloy), where the arrows indicate the peripheral precipitate with diffuse contrast in addition to the central precipitate. From Ref. [78], p. 49. (d) The  $\gamma'$  assemblies after ageing at 200°C for 8 h for an Al-1.7 at.%Ag alloy, where peripheral precipitates (labelled P) are comparable with the centre precipitate (labelled C). Tilting experiments showed that the apparent overlap of precipitates at points A and B was an effect of projection. From Ref. [81], p. 49, 51, 138 reprinted with permission from J. M. Rosalie.

$$1/2[110] \rightarrow 1/6[121] + 1/6[2\bar{1}\bar{1}],$$

which creates a stacking fault in between the two Shockley partial dislocations and satisfies Frank's Energy Criterion <sup>6</sup>. The associated  $\gamma'$  precipitates are lath-shaped on  $\{111\}_{\text{Al}}$  planes with  $\langle 110 \rangle_{\text{Al}}$  as the axis of the helix. The growth of  $\gamma'$  precipitates, however, is limited by the size of the helix as shown in Fig 2.24. Nicholson and Nutting also noted the existence of Frank dislocation loops as the nucleation sites for individual  $\gamma'$  precipitates [54]. In contrast, Rosalie *et al* [78] found the hexagonal Frank dislocation loops ( $\vec{b} = \langle 111 \rangle$ ) were the main quenched-in defects and helices were rare. A Frank dislocation loop is decomposed into Shockley partial dislocations ( $\vec{b} = 1/6\langle 112 \rangle$ ) and Lomer-Cottrell dislocation ( $\vec{b} = 1/6\langle 110 \rangle$ ) via:

$$1/3[111] \rightarrow 1/6[110] + 1/6[112],$$

which results in stacking faults between Shockley partial dislocations; the Lomer-Cottrell dislocations are located at the junctions of stacking faults. This leads to precipitate assemblies as shown in Fig 2.25. The precipitate assemblies are composed of  $\gamma'$  plates on the equivalent  $\{111\}_{\text{Al}}$  planes impinging each other, forming a cage geometry shown in Fig 2.25. Alloy compositions could cause the different observations of Nicholson & Nutting's (Al-4.5 at.%Ag) and Rosalie's (Al-1.68 at.%Ag) experiments, but this should be doubted and tested. It is interesting that although the helices and Frank dislocation loops assist  $\gamma'$  nucleation, they may eventually limit the  $\gamma'$  precipitate growth.

If not bound by the apparent obstacles such as helical dislocations and Frank dislocation loops as mentioned above, the growth of  $\gamma'$  is a textbook precipitate kinetics problem (see Fig. 2.22 for example). Before soft impingement (caused by overlapping of the solute depletion field around precipitates), the growth of  $\gamma'$  can be modelled satisfactorily with volume diffusion kinetics but with an aspect ratio away from equilibrium [76]. The equilibrium ratio is 2.7, but the one from experimental observation is usually above 100 [76]. In short, the thickening is inhibited. When the growth of an individual  $\gamma'$  precipitate is examined closely during an *in situ* TEM experiment [82], the thickening kinetics was found to be clearly discrete rather than continuous as predicted by analytical diffusion equations. Based on the *in situ* TEM observations, Laird and Aaronson [49] proposed a ledge mechanism in which both the coherent and the semicoherent/incoherent interfaces of precipitates advance by ledges. A ledge is a "step raiser" on an otherwise flat precipitate surface, see Fig. A.6 and Fig. 2.27. While the ledge velocity is controlled by diffusion kinetics, the nucleation of the ledge, however, is determined by the interfaces themselves. For a  $\gamma'$  precipitate specifically,

<sup>6</sup>Frank's Energy Criterion states that dissociation is favourable if the elastic strain energy of the reactant dislocations is larger than that of the product dislocations, i.e.  $\vec{b}_1 \rightarrow \vec{b}_2 + \vec{b}_3$ , if  $b_1^2 > b_2^2 + b_3^2$ .

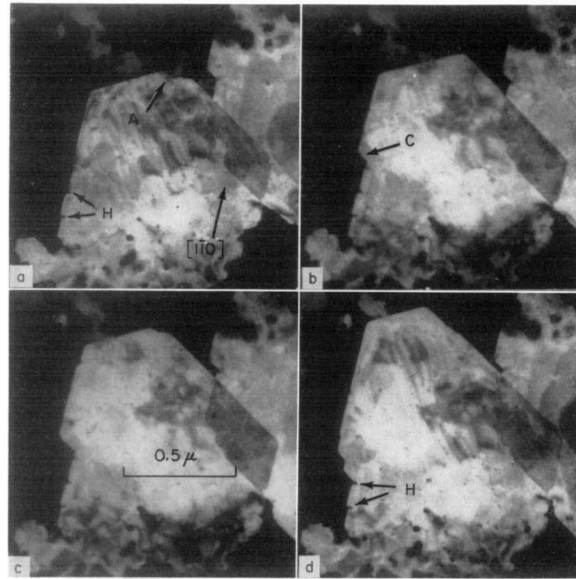


Fig. 2.26 The lengthening of a  $\gamma'$  embedded within a TEM foil through the ledge mechanism while *in situ* annealed at 350°C. The electron beam direction was parallel to  $\langle 111 \rangle_{\text{Al}}$ . Reprinted from Ref. [49] with permission from Elsevier.

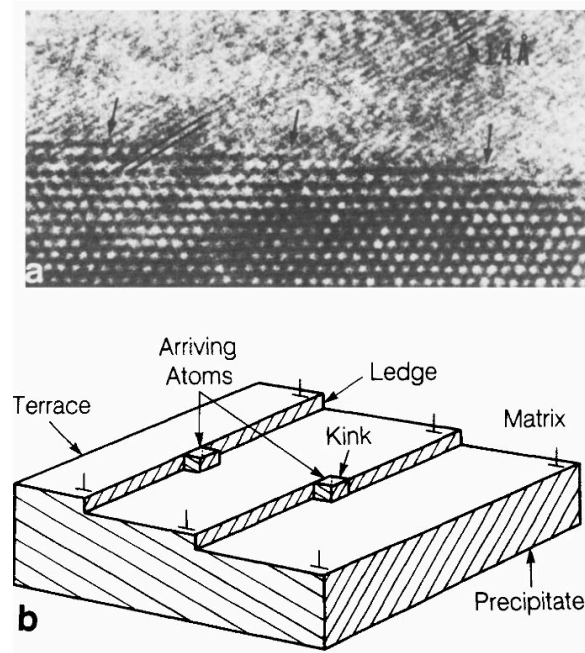


Fig. 2.27 (a) TEM image showing a series of single-atom ledges migrating on the coherent interfaces of a  $\gamma'$  precipitate. (b) Atomically smooth solid-solid interface with atoms represented by cubes, illustrating the terrace-ledge-kink mechanism growth. Reprinted from Ref. [69] with permission from Taylor & Francis.

the lengthening is achieved by the gliding of Shockley partial dislocations at the semicoherent interfaces, while the thickening depends on the initiation of new partial dislocations on the coherent interfaces, Fig. 2.27. On coherent facets, building a new ledge is not favourable due to the increased area of high energy semicoherent facets. The fewer the ledges that can form, the lower the interfacial mobility. Thus, the coherent interfaces of  $\gamma'$  move much more slowly than the semicoherent interfaces. And the aspect ratio increases quickly at the early stage of ageing and converges to a constant value much larger than equilibrium. A quantitative prediction of the non-equilibrium growth (i.e. early stage growth) is a challenge. For a long time, the interfacial mobility has been treated as a fitting parameter. Recently, Finkenstatdt and Johnson [83] developed a non-equilibrium kinetics model to explain the time-dependent aspect ratio. Their growth model involves new dendrite ledge formation which is associated with a nucleation energy barrier. The interfacial energy term contributes to the barrier and influences the kinetics substantially. Whether the model is a true description of growth remains to be examined: in this work [83], the interfacial energies were calculated from the simple combination of FCC and HCP phases. In addition, the shear strain energy was not considered, which dominates the early stage of  $\gamma'$  precipitate growth. But this treatment makes use of the long-standing assumption that the interfacial mobility is related to the interfacial energy.

A deep understanding of phase transformations requires a careful examination of the interfacial structures. Recently, Ag atoms were found to segregate at the coherent interfaces of early stage  $\gamma'$  precipitates [85]. Fig. 2.28 compares the experimental STEM images with simulations, where the monolayer segregation model shows a good match with experiments. Precipitate thicknesses of 1-13 unit cells of  $\gamma'$  phase were found without systematic absence. The segregation is apparent for  $\gamma'$  precipitate with 1-3 unit cells, suggesting that the thickening does not lack solute at the early stage. The excess of Ag at the coherent precipitate-matrix interfaces is a clear evidence of interface controlled growth. The semicoherent interfaces should theoretically consist of three sets of Shockley partials periodically to minimise shear strain. There are two  $30^\circ$  partial dislocations and one  $90^\circ$  partial dislocation relative to a viewing direction of  $\langle 110 \rangle_{\text{Al}}$ . Doing a Burger vector analysis of the entire precipitate suggested that the ratio between the number of  $30^\circ$  partial dislocations to the  $90^\circ$  partial dislocations is 2:1 [69], as predicted by theory. Locating individual dislocations at the precipitate edge, however, is difficult in an HRTEM image because of the Moiré fringes (the interference pattern due to the overlapping of different crystals) and varying contrast (due to dynamic electron scattering) [84]. Clear HRTEM imaging of interfaces is difficult in a sample thicker more than 10 nm. Interestingly, TEM experiments showed that the semicoherent interfaces have a saw-tooth pattern repeating every 6 layers (see Fig. 2.29(a)). A Recent



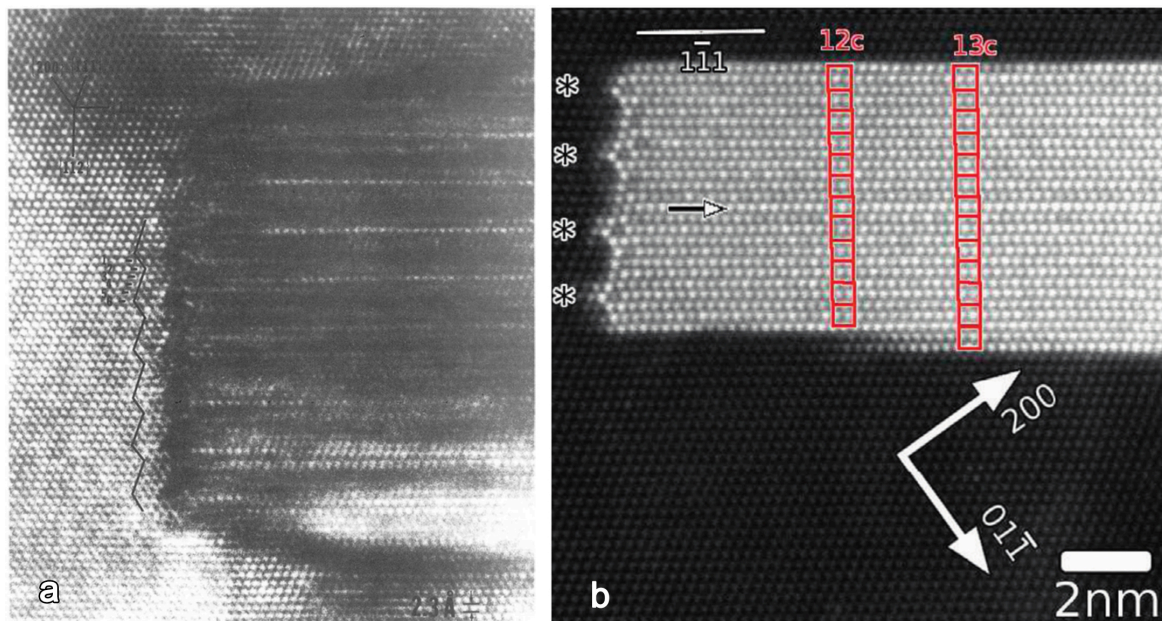


Fig. 2.29 High-resolution TEM image showing the saw-tooth semicoherent interface, as indicated by lines and arrows. Reprinted from Ref. [84], p.234 with permission from J. M. Howe. HAADF-STEM image showing periodic Ag depletion at the saw-tooth interface, as indicated by asterisks. Reprinted from Ref. [70] with permission from Elsevier.

HAADF-STEM study revealed a saw-tooth interface with Ag depleting at one atomic column every 6 layers (see Fig. 2.29(b)), echoing the periodicity associated with commensuration of the FCC and HCP structures [85]. There clearly exists an interplay between solute and interfacial defects, which remains to be characterised and explained.

Previous studies have computed the interfacial energies of the HCP  $\gamma'$  phase embedded in FCC Al using analytical approximations and the first-principles calculations. The analytical approach assumed the energies are determined by the nearest neighbour bond breaking at interfaces [86]. The predicted Wulff construction gives an almost equiaxial and faceted geometry, which means the  $\gamma'$  phase should precipitate homogeneously like GP zones, rather than on dislocations as observed in experiments [86]. This discrepancy suggests that the atomic interaction at the interface may extend beyond the nearest neighbours. First-principles calculations can handle complicated electronic interactions by solving many-body quantum mechanics. The size of the atomic model used in the previous study [87], however, is too small to yield reliable results without a strong boundary effect for the heterophase interface. In addition, the detailed interfacial structures and chemistries were not discovered at the time of the previous calculations (see Fig. 2.28 and Fig. 2.29). The interfacial energies, therefore, have to be re-evaluated with the experimentally informed atomistic structures. This is one of the main aims of this thesis.

### 2.2.1.3 Predicted Phases and Phase Diagrams

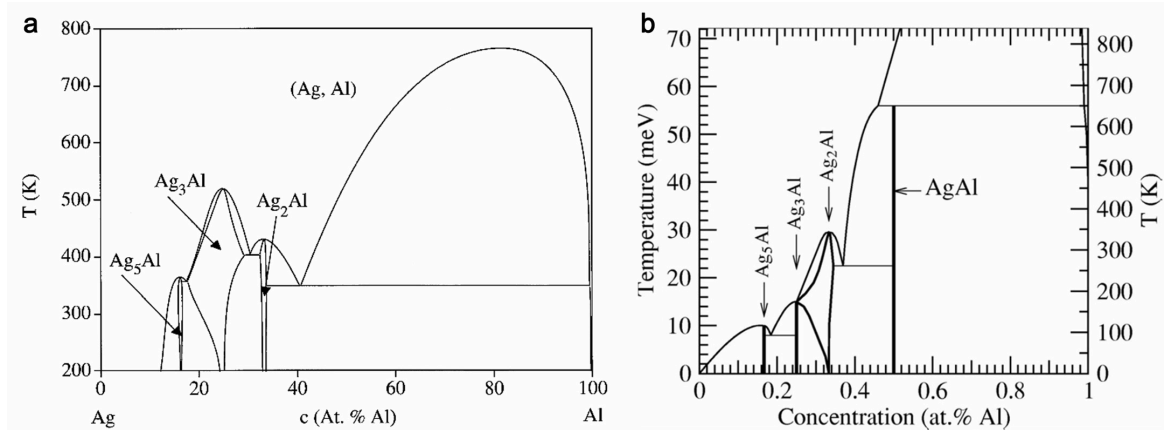


Fig. 2.30 First-principles calculated composition-temperature phase diagram for (a) the FCC-based structure, reprinted from Ref. [58] with permission from Elsevier; and (b) the HCP-based structure in the Ag-Al system, reprinted from Ref. [74] with permission from American Physical Society.

First-principles calculations were used to study the thermodynamics of the Al-Ag system. One particular method called the cluster expansion method calculates the energetics of solute clusters in the matrix with different configurations using DFT. The DFT-calculated energetics are expanded as a basis set to any possible configurations. A stable phase is taken as the configuration with the lowest energy for a given composition and temperature, which constructs the composition-temperature phase diagram. However, the calculated phase diagrams [58, 74], Fig. 2.30, are very different from the one determined experimentally, Fig. 2.12. Interestingly, several structures with the composition of AgAl were predicted by cluster expansion [74, 88]. For FCC-based structures (see Fig. 2.31(a)), a super-lattice of bi-layered AgAl stacking along  $\langle 110 \rangle_{\text{FCC}}$  was found to be a low energy state [88]. For HCP-based structures (see Fig. 2.31(b)), the bi-layered AgAl phase was predicted to be an equilibrium ground state, which has a chemical stacking along  $\langle 11\bar{2}0 \rangle_{\text{HCP}}$  [74]. These structures have not been observed in experiments. However, these theoretical studies hint at a phase diagram richer than that previously known. Our work (Chapter 4 & 5) confirmed an AgAl phase indeed exists but with an atomic structure different from those two predictions.

## 2.2.2 Multi-element Aluminium Alloys with Ag Additions

Though binary Al-Ag alloys only have limited applications, Ag is a popular microalloying element in aluminium alloys. A small amount of Ag (from 0.1 at.% to 0.5 at.%) was found to exert dramatic improvements on the mechanical properties, thermal stability and

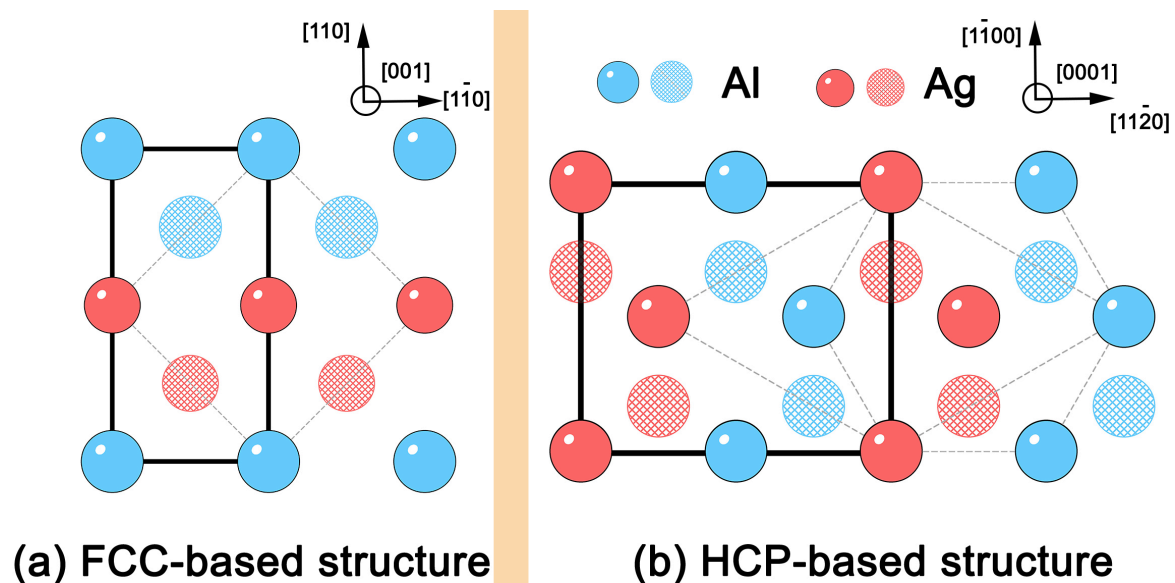


Fig. 2.31 Predicted AgAl phases with (a) FCC-based structure [88] and (b) HCP-based structure [74]. Black solid lines indicate the unit cells of the predicted AgAl phases with the prescribed chemical stacking, while grey dashed lines indicate the cubic or trigonal/hexagonal unit cell of the original FCC and HCP structures. Solid and dashed circles indicate atoms at different heights along the viewing directions.

stress-corrosion cracking (SCC) resistance of aluminium alloys [18, 19]. This effect is widely seen in different aluminium systems, particularly in high-strength alloys for advanced aerospace and defence applications [4]. The underlying mechanisms, however, seem to vary from case to case. In some systems, Ag incorporates within existing precipitate phases and accelerates their formation. But in others, Ag segregates at the precipitate-matrix interfaces, which changes the precipitation behaviour and occasionally modifies the type of phase that forms. This section reviews Ag micro-alloyed aluminium alloys, focusing on the modified microstructures and mechanical properties because of Ag additions.

First, it is important to note that the microalloying effect of Ag often requires the addition of Mg. In fact, Mg and Ag have a strong interaction even in the simplest form. The binary **Al-Mg** alloys (5xxx series) are non-heat treatable alloys with good weldability and corrosion resistance particularly adapted for marine applications. These alloys have characteristics that should result in an ageing response in principle: the Mg solubility is up to 18.6 at.% at the eutectic temperature of 450°C but only 3-4 at.% at 200°C and 2.1 at.% at 100°C [9]. Though the supersaturation is sufficient theoretically, there is virtually no ageing response for alloys with Mg content less than 5 at.%. Only when Mg content is increased to 10 at.% is age hardening noticeable with the precipitations of GP zones,  $\beta'$  and  $\beta$  phases [9]. In addition, the pre-strained condition (T8 treatment) gives no enhancement in age hardening.

The reason for such poor ageing response is the fact that the solvus line of GP zones is below ambient temperature for Mg content less than 5 at.%. Even with high Mg content up to 10 at.%, age hardening is still not significant. However, trace additions of Ag can improve the age hardening considerably, with precipitation of firstly, a quasicrystal phase [89, 90], then the T phase [91] and the equilibrium  $\beta$  phase. The T8 treatment enhances the age hardening for Ag-microalloyed Al-Mg alloys, in contrast to the binary Al-Mg alloys. This is possible due to the strong interaction between Ag and defects that provides heterogeneous nucleation sites.

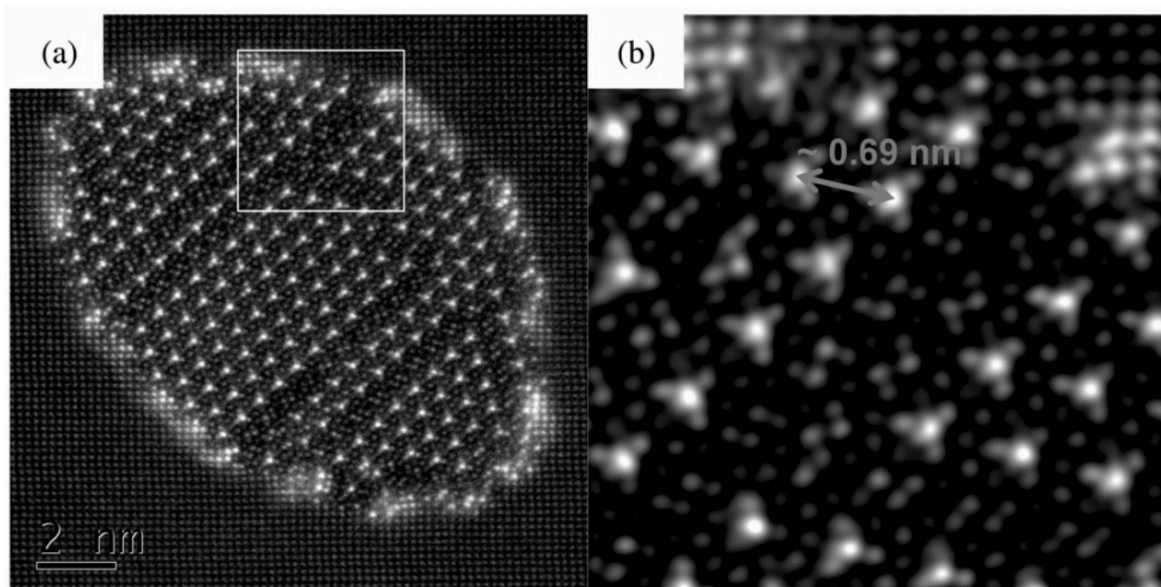


Fig. 2.32 HAADF-STEM showing the cross-section of an Ag-containing  $\beta'$  precipitate in an Al-Mg-Si-Ag alloy. The white box delimits an area shown enlarged in (b), where the anti-phase boundary and periodicity of Ag occupancies are indicated. Reprinted from Ref. [92] with permission from Taylor & Francis.

**Al-Mg-Si** alloys (6xxx series) are middle strength heat treatable alloys with good weldability and resistance against corrosion and stress-corrosion cracking. They are mainly processed via extrusion, in contrast to rolling for Al-Mg plates. Thus, the alloying contents cannot be very high for the sake of the extrusion speed. The phase transformations in Al-Mg-Si alloys are probably the most complicated in aluminium systems, with the sequence going from solute clusters and GP zones to the  $\beta''$ ,  $\beta'$  and  $\beta$  phases [9]. Additions of Ag replace (partially or fully) one of three Si-containing atomic columns in the  $\beta'$  phase. As shown in Fig. 2.32, the Ag networks form a specific pattern with different domains and anti-phase boundaries [92]. The Ag occupancy at Si sites was also observed in  $\beta''$  phase during the earlier stage of ageing [96]. Additions of Cu are beneficial by forming the precipitate phases

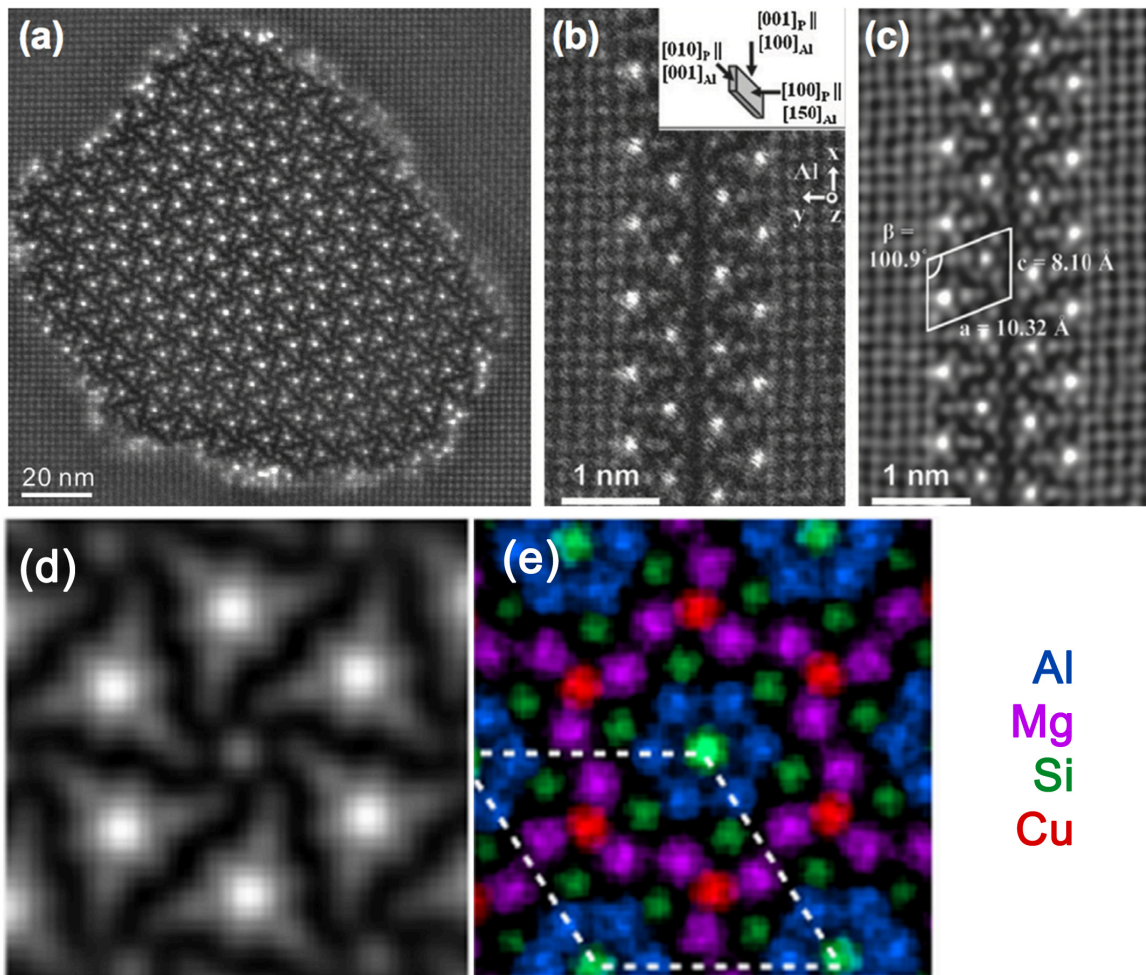


Fig. 2.33 (a) HAADF-STEM image showing the cross-section of a Q phase precipitate in an Al–Mg–Si–Cu alloy. Reprinted from Ref. [93] with permission from Elsevier. (b) Original and (c) Fourier-filtered HAADF-STEM images showing the cross-section of a C phase precipitate in an Al–Mg–Si–Cu alloy. Image courtesy: M. Fiawoo. Atomic-resolution (d) ADF and (e) EDS images of a Q phase, using non-rigid registration and symmetry average techniques to correct non-linear distortion. Reprinted from Ref. [94] with permission from Elsevier.

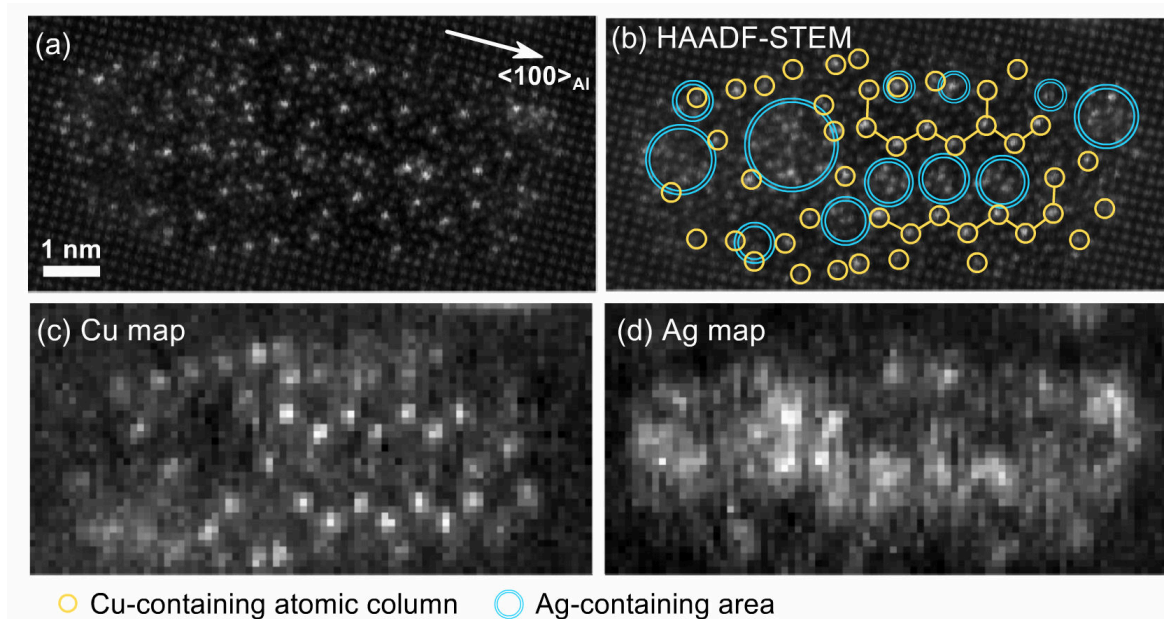


Fig. 2.34 (a) and (b) HAADF-STEM images of the cross-section of a  $Q'$  phase precipitate in an Al-Mg-Si-Cu-Ag alloy, taken respectively before and during the STEM-EELS acquisition. (c) and (d) EELS elemental maps of Cu and Ag. The locations of Cu atomic columns are indicated by yellow circles while areas rich in Ag are indicated by blue circles as marked in (b). Reprinted from Ref. [95] with permission from Elsevier.

C and Q [93, 94]. Compared with the C and Q phase in quaternary Al-Mg-Si-Cu alloys (see Fig. 2.33), Ag additions modify their structures into C and  $Q'$  phases in Al-Mg-Cu-Si-Ag alloys (see Fig. 2.34 and Fig. 2.35). Electron energy loss spectroscopy imaging showed that the Ag distribution includes various atomic columns within the precipitate phases with no apparent order, while Cu is largely confined to specific columns [95]. Interestingly, in contrast to the Cu segregation at the coherent interface of a C plate ( $(100)_C \parallel (150)_{Al}$ ), Ag atoms segregate at the edge interface ( $(001)_C \parallel (100)_{Al}$ ) which has a large misfit strain with the aluminium matrix, Fig. 2.35(a). The reason for Ag distribution within these phases is still largely unknown. One of the main research direction in 6xxx series is to reduce the Mg and Si alloying content to improve the extrusion speed [17]. Microalloying of Ag, Cu and Ge proves to be promising for this purpose [96].

**Al-Zn-Mg** alloys (7xxx series) are one of the strongest age hardenable aluminium alloys typically used in aerospace applications. But one disadvantage is that they are very susceptible to stress-corrosion cracking [17]. Slow quenching, e.g. air cooling, reduces residual stresses and electro-potential difference throughout the sample, which considerably improves the resistance against stress-corrosion cracking. This treatment, however, allows the time for the solute elements and vacancies to be absorbed in the grain boundaries. Consequently, slow

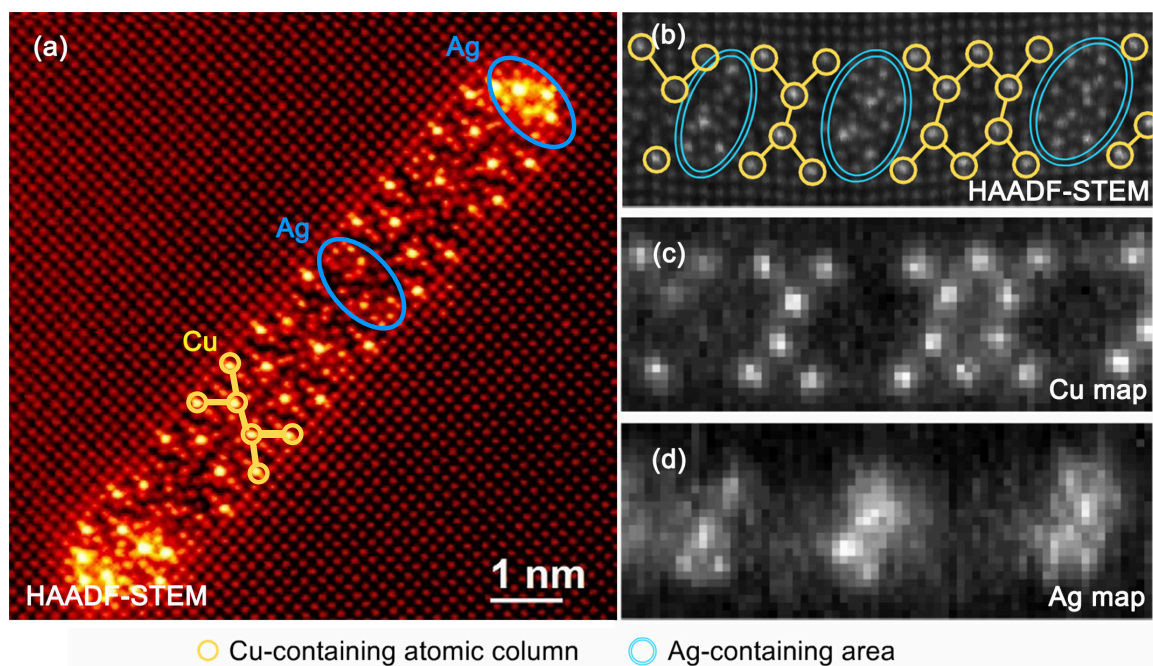


Fig. 2.35 (a) and (b) HAADF-STEM images of the cross-section of a *C* precipitate phase in an Al-Mg-Si-Cu-Ag alloy, taken respectively before and during the STEM-EELS acquisition. (c) and (d) EELS elemental maps of Cu and Ag in areas marked in (a). The location of Cu atomic columns and areas rich in Ag are marked in (b). Cu columns in a *C* phase are connected by lines. Reprinted from Ref. [95] with permission from Elsevier.

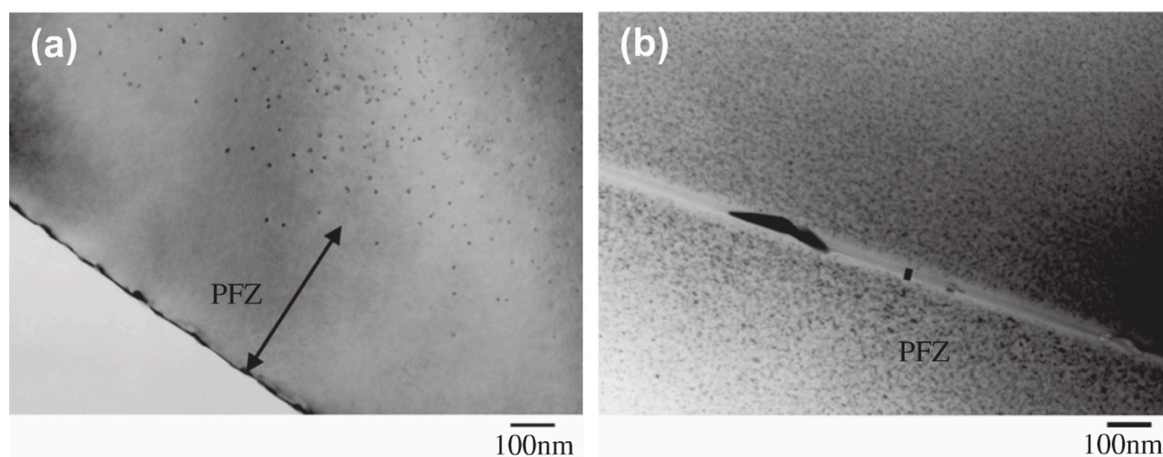


Fig. 2.36 TEM images of the vicinity of grain boundaries in the (a) Al-Zn-Mg ternary and (b) Al-Zn-Mg-Ag alloys aged at 160°C for 1 hr. Reprinted from Ref. [97] with permission from Elsevier.

quenching limits the ageing response. This phenomenon is known as quenching sensitivity [17]. A duplex ageing designed the T73 temper was developed to address the stress-corrosion cracking problem, which involves first ageing at low temperature for dense nucleation of GP zones and secondary ageing at high temperature for  $\eta'/\eta$  precipitation from those pre-existing GP zones. The alloy tensile strength for T73 temper is lowered than that for T6 temper, for example by 15% for 7075 alloys; but the resistance against stress-corrosion cracking is greatly improved [17]. Another complex heat treatment called retrogression and re-ageing has been developed, targeting the stress-corrosion cracking resistance similar to that of the T73 condition and tensile properties expected of the T6 condition. Furthermore, additions of Ag dramatically reduce the precipitate-free zone as shown in Fig. 2.36, due to its strong interaction with defects and solute elements [97]. As a result, the conflicted balance between stress-corrosion cracking susceptibility and quenching sensitivity is resolved. In addition, Ag microalloying promotes precipitation and refines the microstructure of Al-Zn-Mg alloys as well, especially when added with Cu [98]. Atom probe tomography [99] and positron annihilation lifetime spectroscopy (PALS) [100] studies found that Ag is present within all precipitate phases in Al-Zn-Mg, including GP zones,  $\eta'$  and  $\eta$  phases, and assists their formation. The exact location and role of Ag within those phases are still unknown.

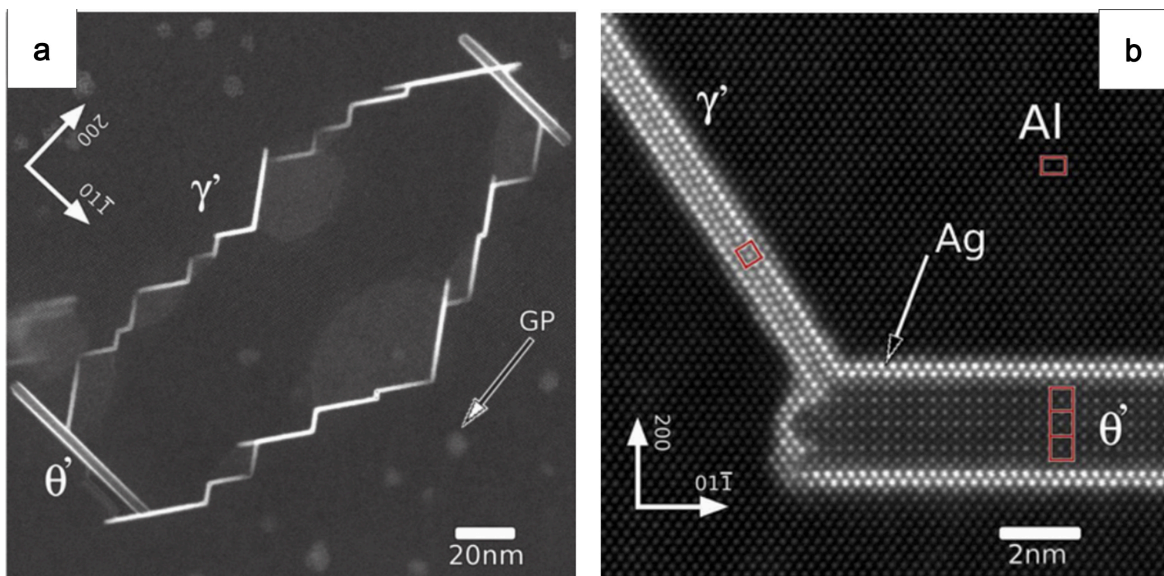


Fig. 2.37 HAADF-STEM showing precipitate assembly formed on the dislocations loops on  $\{110\}_{\text{Al}}$  planes. (a) Low-magnification image showing two  $\theta'$  precipitates formed at the end of the assemblies with zig-zag  $\gamma'$  precipitates in between. (b) High-magnification showing bi-layer Ag segregation to  $\theta'$  precipitate interfaces. Reprinted from Ref. [85] with permission from Elsevier.

**Al-Cu** alloys (2xxx series) are high-strength aluminium alloys with particularly good strength and machinability, making them suitable for construction and transportation applications. Historically, the phase transformation mechanisms in the Al-Cu system have been studied in greater detail than any other aluminium alloy series. Additions of Ag do not stimulate the ageing response of the binary Al-Cu alloys [36]. The quenched-in dislocation loops are on  $\{110\}_{\text{Al}}$  planes in Al-Cu-Ag alloys, in comparison to  $\{111\}_{\text{Al}}$  planes in binary Al-Ag alloys [78]. As Ag interacts more strongly with lattice defects than with Cu, the  $\{110\}_{\text{Al}}$  dislocation loops are enriched with Ag, which promotes  $\gamma'$  phase formation but delays Cu enriched phases. As shown in Fig. 2.37,  $\theta'$  precipitates were found to form at the end of the  $\{110\}_{\text{Al}}$  dislocation loops with  $\gamma'$  assemblies in between [85]. Ag also decorates both the coherent and semicoherent interfaces of  $\theta'$  by two atomic layers [85], Fig. 2.37. The segregation was suggested to lower the interfacial energies of  $\theta'$  phase [85], but this remains to be confirmed with atomistic calculations.

**Al-Cu-Mg** alloys (a major category in the 2xxx series) has a renowned history back to Alfred Wilm in 1906, marking the discovery of age hardening. The precipitate phases in this ternary system depend on the Cu:Mg ratios – low ratios result in the metastable Z phase and the equilibrium T ( $\text{Al}_6\text{CuMg}_4$ ) phase while high ratios are associated with the metastable  $\theta'$  phase and the equilibrium  $\theta$  ( $\text{Al}_2\text{Cu}$ ) phase. The metastable  $S'$  phase and the equilibrium S ( $\text{Al}_2\text{CuMg}$ ) phase are always present for Cu and Mg composition  $> 0.2$  at.% [4]. Traces of Ag in Al-Cu-Mg alloys are responsible for a dramatic improvement in age hardening, not only promoting precipitate nucleation but also changing the type of precipitate phase. Specifically, additions of Ag suppress the  $S'/S$  phases and promote the  $\Omega$  phase, Fig. 2.8. A rational reason for the performance improvement is that  $\Omega$  precipitates are plates with large aspect ratios on  $\{111\}_{\text{Al}}$  planes, which makes them more effective for strengthening than S phase according to the Orowan equation. In addition, the  $\Omega$  phase has good thermal and mechanical stabilities, which gives outstanding creep and fatigue resistance. Early TEM studies yielded evidence that Ag segregates at the coherent interfaces of the  $\Omega$  phase [102, 103]. Field ion microscopy [104, 105] and atom probe tomography [35, 37] suggested that Ag clusters with other solute elements (particularly Mg) at the start of ageing. Ag-Mg clusters initially do not have well-defined geometry but quickly favour  $\{111\}_{\text{Al}}$  planes. After the absorption of Cu,  $\Omega$  nuclei form on  $\{111\}_{\text{Al}}$  planes and eject Ag and Mg to the precipitate-matrix interfaces [35]. Positron annihilation lifetime spectroscopy (PALS) also suggested that Ag binds with Mg, Cu and vacancies during ageing [106]. But there has been much debate on the detailed interfacial structure: whether Ag-Mg interfacial segregation is one or two atomic layers. Early atom probe tomography suggested a monolayer segregation [35] but STEM suggested double layers segregation [20] (see Fig. 2.8). Recent aberration-corrected STEM

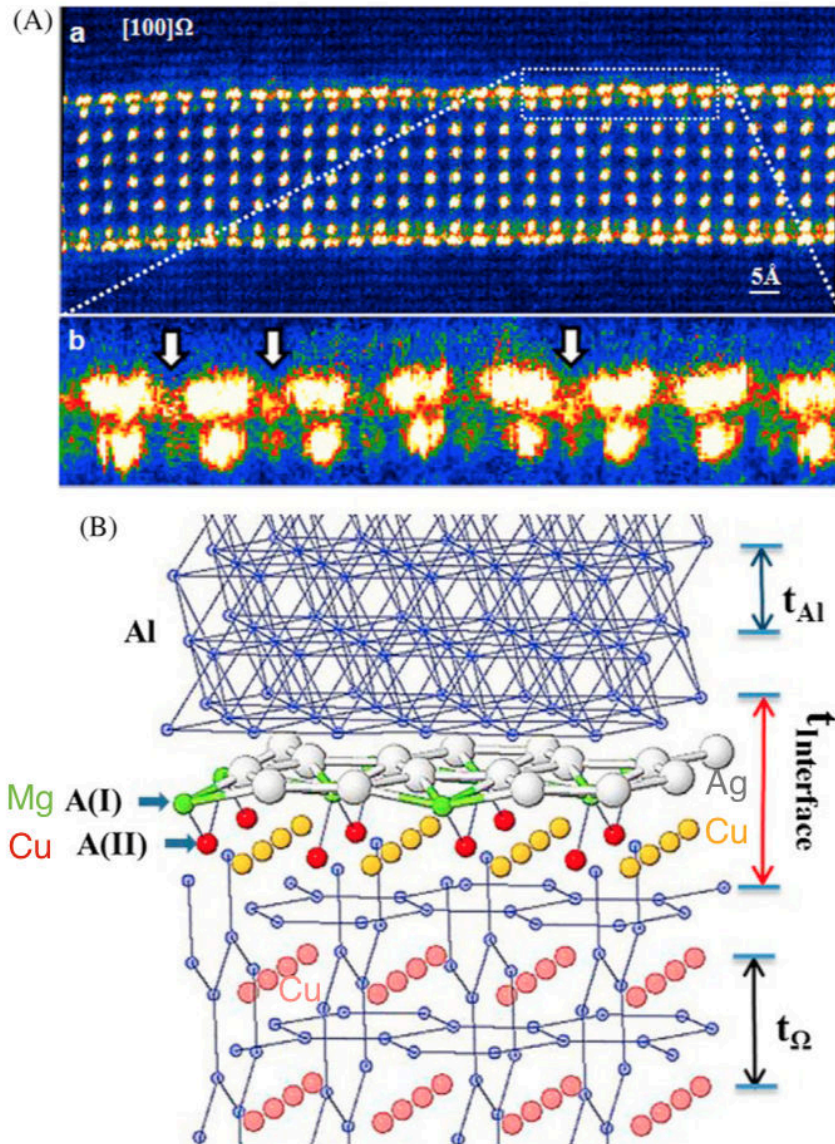


Fig. 2.38 Segregation of a single layer of Ag atoms at the  $\Omega$ /matrix interface. Atoms of Ag, Mg, Cu, and Al are coloured in white, green, red/yellow/orange, and blue, respectively, in the schematic diagram. Adapted from Ref. [13] with permission from Elsevier.

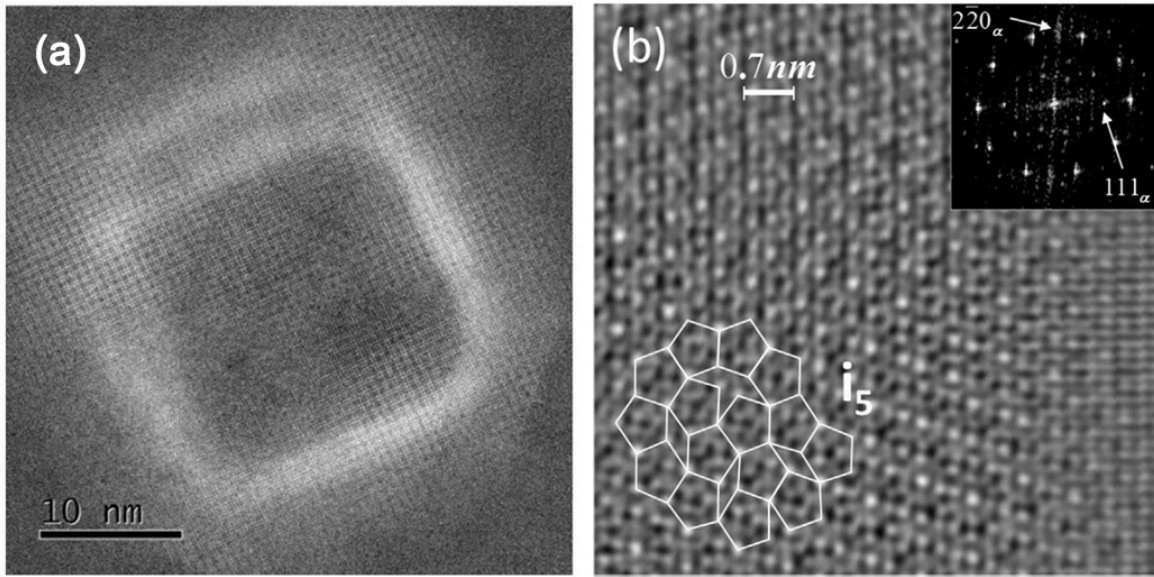


Fig. 2.39 (a) HAADF-STEM images showing the cross-section of the Z phase along  $\langle 100 \rangle_{Al}$  in a base Al-Mg-Cu alloys. (b) HAADF-STEM images showing icosahedral quasi-crystalline of Z phase along  $\langle 112 \rangle_{Al}$  in an Ag-added alloy. Reprinted from Ref. [101] with permission from Elsevier.

[13] confirmed that the interface indeed has a special kind of double layer: hexagonal Ag networks sit at the outmost interface in contact with the Al matrix, while Mg is located at the honeycomb centre of every six Ag atoms. They seem to be on the same layer, but the Mg layer is slightly inwards to the  $\Omega$  phase than Ag layer, which is followed by a Cu layer, as shown in Fig. 2.38. For alloys with high Cu:Mg ratios where the  $\theta'$  phase exists, Ag segregates to their interfaces similar to that in Al-Cu-Ag alloys [107]. For alloys with low Cu:Mg ratios where the T phase exists, additions of Ag trigger a fine precipitation of T phase and Z phase [101]. As shown in Fig. 2.39, the Z phase has a rod geometry with a square cross-section similar to that of the T phase. Electron diffraction patterns showed that the Z phase (cubic system,  $a_Z=19.9\text{\AA}$ ) and T phase (cubic system,  $a_T=14.2\text{\AA}$ ) have an immediate relationship with their lattice parameters as  $a_Z=\sqrt{2}a_T$  [101]. Viewed in a  $\langle 112 \rangle_{Al}$  direction, the Z phase has similar clusters to those of the T phase but with a local 5-fold symmetry, suggesting that Z phase is a quasicrystal version of T phase [101]. How Ag additions help Z phase formation is still unknown. But this behaviour is not totally unexpected since Ag also helps quasicrystal phase formation in binary Al-Mg alloys.

**Al-Cu-Li** alloys (some belong to the 2xxx series, some belong to the miscellaneous 8xxx series) were initially developed for military aircraft but abandoned later due to the low toughness. The coherent  $\delta'$  ( $Al_3Li$ ) phase nucleates homogeneously, which is spherical, shareable and not very effective for precipitation strengthening. But this is only part of the

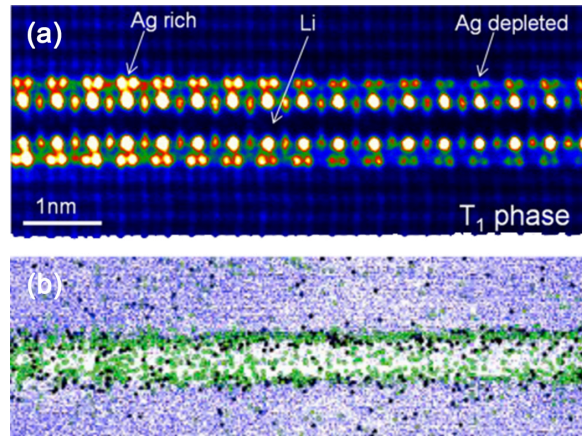


Fig. 2.40 (a) HAADF-STEM images showing Ag segregation to the  $T_1$  phase along  $\langle 112 \rangle_{Al}$  in an Al-Cu-Li-Mg-Ag alloy. Reprinted from Ref. [46] with permission from Elsevier. (b) Atom probe map showing segregation of silver atoms in the  $T_1$ /matrix interface in alloy AA2198 (Al-Cu-Li-Mg-Ag-Zr), where green and black dots represent magnesium and silver atoms respectively. Reprinted from Ref. [108] with permission from Elsevier.

problem; the main problem is the intergranular fracture that results in low toughness. Na and K impurities, which present in Al-Li alloys by 3–10 ppm using conventional casting, cause grain boundaries embrittlement (Ref.[17], pp. 209-218). In other alloys without Li, this is less of a concern as Si reacts with these impurities into innocuous particles. However, for Li-containing aluminium alloys, Si preferentially reacts with Li, which not only reduces the alloying content for precipitation but lets the harmful alkali impurities at large. It took decades to reduce the alloying impurities below 1 ppm using vacuum melting and refining. Then, promoting the shear-resistant  $T_1$  precipitates on  $\{111\}_{Al}$  planes became the main task. The  $T_1$  phase has a hexagonal crystal structure, thus the associated phase transformation mechanisms can be expected to be similar to that of  $\gamma'$  phase in the Al-Ag system. Essentially, the significant shear strain  $\sim 35\%$  imposed by Shockley partial dislocations suppresses precipitate nucleation. Thus, the pre-strained condition is helpful for  $T_1$  formation. Besides the T8 treatment (see Sec. 2.1.3), co-additions of Mg and Ag promote  $T_1$  precipitate formation as well. As shown in Fig. 2.40, atom probe tomography [108] and recent scanning transmission electron microscopy [46] have found that Ag and Mg segregate at the coherent  $T_1$ /matrix interfaces, similar to that of the  $\Omega$  phase in Al-Cu-Mg-Ag alloys. The lengthening of  $T_1$  precipitates is remarkable that often they can penetrate the entire grain. Their thickening, however, is prohibited, which leads to excellent thermal stabilities, especially with microalloying of Ag and Mg. Now, the  $T_1$ -containing alloys are known as one of the strongest aluminium alloys for critical applications, such as the fuel tank of the space shuttle and the current spacecrafts like Curiosity and Orion (see Fig. 1.2).

In general, Ag participates in different precipitate phases or segregates at various precipitate-matrix interfaces, covering almost the entire range of heat treatable aluminium alloys. Previous atom probe and electron microscopy studies have shown that Ag clusters prefer  $\{111\}_{\text{Al}}$  planes during ageing. However, what drives Ag to cluster before the formation of a precipitate phase is still a mystery. Moreover, how the early-stage clustering of Ag modifies the nucleation of precipitates is largely unknown. An accurate description of solute clustering is essential to address one of the most intriguing questions in Al alloys: why do minor additions of Ag play a crucial role in precipitation in a wide variety of Al alloy systems [36]? Atomic-scale studies on precipitate interfaces have progressed quickly in recent years with the aid of modern characterisation and modelling techniques, particularly transmission electron microscopy together with first-principles calculations. In the following section, we will explain why such combination is an effective strategy for precipitation studies.

## 2.3 Characterisation and Modelling Strategies

Modern precipitation studies require accurate information of atomic structures and chemistries at specific sites, i.e. precipitate interfaces and lattice defects, which narrows down the choice of characterisation methods. X-rays diffraction is the most widely used method for crystal structure determination. It is advantages in terms of the cost, data collection time and well-established analysing method. Modern metallurgy studies often use X-ray diffraction to determine the volume fraction of certain phase of interest. In fact, X-ray diffraction is the first method that confirmed the existence of a nanometre-sized precipitate phase (GP zone) in an Al-Cu alloy [5, 6]. However, X-ray diffraction usually yields the averaged structural information of a bulk sample, similar to most of the other diffraction techniques. There are scanning probe X-ray, but the spatial resolution is well above 10 nm [109].

Atom probe tomography offers extensive site-specific information about 3D chemical composition at near atomic resolution (usually around 1-3Å in depth and 3-5Å laterally) [110]. However, atom probe tomography is not accurate enough in terms of crystallographic information. For instance, although atom probe tomography is useful in the study of solute segregation on dislocations, it is impossible to extract the Burgers vector of a dislocation. In addition, atom probe tomography only surveys a very small volume of a material. The sites of interest may not always be included by destroying a very sharp sample tip.

Transmission electron microscopy is a versatile tool that combines imaging, diffraction and spectroscopy. Various regions of a sample can be navigated with the access to accurate crystallography and chemistry of specific sites. Thus, TEM has a long history used for metallurgy research, especially in characterising lattice defects and precipitate phases [111].

Now, aberration-corrected TEM can even reach sub-Å resolution [112]. However, TEM also has many limitations due to the nature of transmitting electrons. For instance, a TEM image is a 2D projection of the 3D microstructure [113]. Not only the overlapping of geometries complicates the image interpretation, but also the Moiré fringes due to the overlapping of lattices and the alternating contrast due to dynamic scattering of electrons (Ref.[16], pp. 389-402). In addition, the high energy electron beam could damage the area of interest, which may even change the lattice structure and composition (Ref.[16], pp. 53-68). TEM can only examine a small thin area anyway compared to the bulk alloy; one should check whether the characterisation is representative of the overall microstructure. In addition, successful TEM characterisation requires a high level of skills for experiments and interpretations.

Thanks to the previous studies, we have a good knowledge of the precipitate phases in the Al-Ag system, which are uniformly distributed with a well-defined plate or spherical geometries; the phases are also stable under the electron beam. Various techniques like electron tomography, image and diffraction simulations can be implemented to ensure a reliable image interpretation. We chose high angle annular dark field scanning transmission electron microscopy (HAADF-STEM) mode in TEM that yields a contrast directly related to the atomic number of elements. The Z-contrast imaging of STEM simplifies image interpretation compared to the phase contrast imaging of high-resolution TEM. Energy dispersive X-ray spectroscopy (see Fig. 2.33) and electron energy loss spectroscopy (see Fig. 2.34 and Fig. 2.35) can be integrated during HAADF-STEM acquisition that inform the site-specific chemistry. With those advantages, the application of STEM becomes increasingly popular for metallurgy, particularly in the precipitate studies as reviewed. Hence, we chose STEM (including aberration-corrected STEM) as the characterisation tool for this project.

Computational modelling is required to obtain accurate energetics associated with different phases to understand their formation. With increasing system size approached to any realistic materials, modelling has to make necessary simplifications to avoid the otherwise expensive computational cost. For instance, it is almost impossible to predict the behaviour of millions of atoms from the many quantum mechanics. The analytical approach aims to understand precipitation from classical thermodynamics and kinetics. Besides manual calculations, commercial software like *Calphad<sup>TM</sup>* and *Thermo – Calc<sup>TM</sup>* also perform phase field simulations with a comprehensive thermodynamics database for common phases. The ultimate goal is to predict the existence and development of different phases and compare with experimental results. However, many parameters described in precipitation equations have well-defined physical meanings but cannot be easily accessed experimentally. The most important one is interfacial energy, which is very sensitive in controlling the kinetics

but often not known sufficiently accurately [14]. For example, an analytical estimation of interfacial energy (based on bond breaking assumption) was attempted for  $\gamma'$  ( $\text{Ag}_2\text{Al}$ ) phase [86], but the results did not agree with experimental observations. As a consequence, those parameters act as phenomenological factors for fitting the experimental results. With fine-tuning, reasonable or non-reasonable values can be obtained with which one must be cautious. Nevertheless, the analytical approach gives a basic and useful understanding of the precipitation process.

The atomistic approach treats the matter as a collection of individual atoms that goes beyond continuum models. Density functional theory (DFT) is a first-principles method that solves many-body quantum mechanics for a given atomic configuration. DFT is recognised as one of the most accurate and robust methods for atomistic materials simulations. However, DFT is computationally demanding that cannot be applied to study the dynamics of a large system. In contrast, semi-empirical potential methods (e.g. embedded atom method (EAM)) are less accurate but require less computational resources in simulating the dynamics of interfaces and defects. Precipitate interfaces and defects may have very different structures and chemistries from bulk phases, which is often beyond the description of the analytical approach. Hence, we chose atomistic calculations (DFT and EAM in particular) to understand their atomic mechanisms.

The strengths of TEM and DFT at the atomic scale bring out the best in each other: TEM provides accurate atomic models, while DFT gives reliable energetics. The combination of TEM and DFT is a powerful strategy for alloy precipitate studies, which becomes increasingly popular in recent years. For example, this strategy was used for resolving many classic precipitation problems, including the precipitate structure of  $T_1$  phase [45], the interfacial structures of the  $\theta'$  phase [11, 12] and the  $\Omega$  phase [13] as reviewed previously. In addition, DFT calculations were shown to agree well with TEM experiments in terms of atomic positions and energetics of different phases in various studies, including mapping the strain field near a precipitate  $\beta''$  phase in an Al-Mg-Si-Cu alloy [114] and revealing the periodic chemical segregations at defects like twin boundaries in Mg alloys [115]. Besides many papers, the Al-Ag alloy system has been the topic of at least four PhD theses using either TEM [78, 84] or DFT [116, 117]. This study combines TEM and atomistic calculations to explore the atomic mechanisms of precipitation in the Al-Ag system with their principles and implementations detailed in Chapter 3.

## 2.4 Summary and Research Scope

Aluminium alloys are light and strong because their mechanical properties are significantly improved by strengthening precipitates. Microstructures with a fine distribution of precipitates are desired for optimum performance. But the diffusional phase transformations underlying precipitation are usually associated with a significant energy barrier that governs phase nucleation and growth. Traditionally, the alloy microstructure is manipulated with processing, during which defects, such as vacancies and dislocations, are intentionally introduced to promote precipitation. In addition, defects accumulate during the servicing of alloy components under thermal and mechanical loadings, which threatens the metastable microstructures in alloys. However, the interactions between pre-existing phases and defects are largely unknown. Such understanding is critical in determining alloy stabilities against environmental degradation. It is our aim to investigate the role of defects during phase transformations in the textbook Al-Ag alloy system. In particular, we developed new processing schemes that demonstrate the concept of stimulating phase transformations on pre-existing metastable phases by introducing defects. Using this method, a new precipitate phase and new precipitation behaviours are reported in Chapter 4.

Microalloying is a practical way of manipulating precipitation behaviour. The Orowan equation relates the orientation of a precipitate phase to its strengthening effect, which suggests precipitate phases on the close-packed  $\{111\}_{\text{Al}}$  planes are most effective for strengthening. But the orientation relationship is already determined by the interfacial energies of an embedded precipitate. According to thermodynamics and kinetics equations, interfaces govern various precipitation behaviours such as nucleation and growth. If possible, engineering the interfacial structures is a novel approach to manipulate alloy properties. In practice, micro-additions of Ag modify the precipitate interfacial structures in many aluminium systems, assisting the formation of  $\Omega$  phase and  $T_1$  phase on the close-packed planes in some of the strongest aluminium alloys. However, it is not clear why Ag prefers the close-packed planes during clustering in aluminium alloys. In addition, it is not understood how the clustering of Ag modifies the type of precipitate phases. The detailed atomic structure of the newly found phase  $\zeta$  (AgAl) is characterised in Chapter 5. DFT calculations are used to understand the clustering behaviours of Ag atoms in the aluminium matrix, which explains the phase transformations in the binary alloy system and gives insight into the Ag-microalloyed aluminium alloys.

The binary Al-Ag alloy system is a textbook system to study precipitation. Its FCC-HCP transformation mechanism is well established. In particular, the pioneering studies investigated  $\gamma'$  precipitate growth in detail, which leads to the development of the ledge growth theory. However, there are still mysteries about the interfacial structures of the  $\gamma'$  phase:

the coherent interface has Ag segregation and the semicoherent interface has a saw-tooth morphology. In addition, the detailed structure of  $\gamma'$ - $\gamma'$  precipitate junctions has not been examined. In order to understand the importance of interfaces during phase transformations, it is necessary to re-examine the FCC/HCP interfacial structures of  $\gamma'/\gamma$  precipitates. Chapter 6 will focus on characterising the atomic structures, chemistry and defects at the interfaces of  $\gamma'/\gamma$  precipitates. DFT calculations are used to understand the solute distribution and the energetics associated with different interfaces. Beside the interfacial structure characterisations and calculations, we will discuss how different interfaces give rise to different precipitation behaviours.

# Chapter 3

## Research Methods

This chapter details the methods and techniques used in this study. The preceding chapter has reviewed the fundamentals of precipitation, highlighting the importance of interfaces and defects during phase transformations. The binary Al-Ag system has inspired many phase transformation insights in the pioneering studies [10]. This study inherits their legacy with modern characterisation and computation techniques.

This chapter classifies methods into three parts:

1. Section 3.1 describes the details of alloy fabrication, including the casting, rolling and heat treatment conditions. Beyond the conventional heat treatments, we developed a new scheme that introduces defects to pre-existing phases and triggers phase transformations. After processing, the sample foils were prepared by electropolishing for the following TEM characterisation.
2. Section 3.2 concerns the application and analysis of scanning transmission electron microscopy (STEM). An extensive array of advanced microscopy techniques was implemented in this study, including aberration correction, *in situ* annealing, electron tomography, energy dispersive X-ray spectroscopy, image and diffraction simulation, mapping of atomic positions and displacements.
3. Section 3.3 describes the application of the atomistic calculations and structural analysis. This study used density functional theory (DFT) calculations and embedded atom method (EAM) calculations with their working principles and implementation details documented. In addition, this section also introduces the common neighbour analysis for local structure identification and the dislocation extraction algorithm for dislocation identification.

### 3.1 Alloy Fabrication, Treatments and Processing

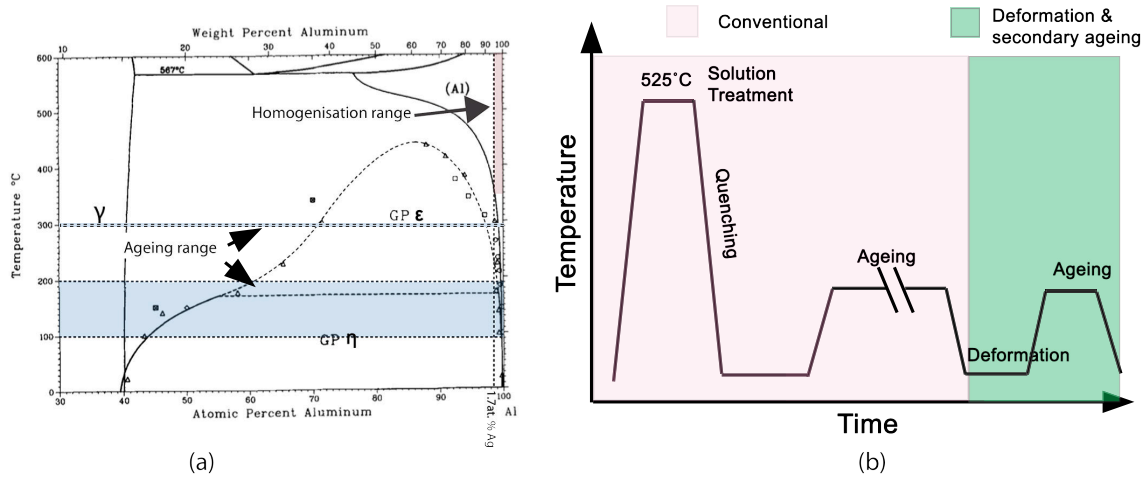


Fig. 3.1 (a) Selection of heat treatment temperatures in reference to the Al-Ag phase diagram, adapted from Ref. [52] with permission from Springer. (b) Schematic diagram illustrating the conventional processing (involves solutionising, quenching and ageing) and the new scheme (deform the pre-aged alloys and perform secondary ageing).

The alloy composition used in this work was Al-1.68 at.% Ag, as cast from high-purity aluminium (Cerac alloys, 99.99% purity) and silver (AMAC alloys, 99.9+%). The pure metals were melted in air at 700°C in a graphite crucible, stirred and poured into graphite-coated steel moulds. The compositions were measured by inductively coupled plasma atomic emission spectrometry, showing very low levels of impurities [78]. The cast ingots were homogenised at 525°C for 7 days, then hot- and cold-rolled to 0.5 mm alloys sheets. (Courtesy: one ingot was cast by Julian M. Rosalie and another ingot was cast by Xiang Gao.)

The heat treatment selection is critical for generating the desired microstructure. For the given composition of Al-1.68 at.% Ag, a temperature range above  $\sim 400^\circ\text{C}$  is needed to fully dissolve the solute in the matrix as shown in Fig. 3.1(a). 525°C was chosen as the solid solution temperature to generate sufficient quenched-in defects. The ageing temperatures both above and below 170°C were examined to study the ordering of GP zones  $\eta$  and  $\epsilon$ . The ageing temperature at 300°C, above the solvus line of GP zones, was used to investigate the  $\gamma$  precipitation directly from the solid solution without the influence of GP zones.

For the conventional heat treatments, the samples were in the form of disks 3 mm in diameter and 0.5 mm in thickness, punched from an alloy sheet after rolling. They were solutionised at 525°C for 30 min in a nitrate salt bath and quenched to room temperature. Different quenching media, including water, oil, and air were tested to manipulate the

quenched-in vacancy concentration before ageing. Then the samples were aged at 100°C, 200°C and 300°C in an oil bath for a range of times (from 30 min to 7 days). We have also aged the alloys at 160°C and 180°C, from 1 hr to 5 days, to study the microstructures just above and below the  $\eta - \varepsilon$  transition temperature.

We developed two processing schemes to introduce defects to pre-aged alloys. In both cases, the alloys were first processed by the conventional treatments (i.e. solid solution at 525°C for 30 min, quenched in oil, aged at 200°C for 7 days). Then, defects were introduced to samples either in the bulk or nano-scale forms. The nanoscale treatment involved secondary ageing of the TEM foil (with a thickness of 10~200 nm). The bulk treatment deformed the aged alloy sheet by 5~7% using cold rolling and disks were punched from them. A secondary ageing at 200°C was performed for those disks for a short amount of time (from 2 min to 30 min). Fig. 3.1 (b) illustrates the treatments in a schematic diagram.

The TEM specimens were made by mechanically grinding the disks to about 100  $\mu\text{m}$  and electro-polishing them in a 67% methanol-33% nitric acid mixture at -25°C and 13 V with a current average of 200 mA.

## 3.2 Transmission Electron Microscopy

We should not, therefore, blame those scientists today who did not believe in electron microscopy at its beginning. It is a miracle that by now the difficulties have been solved to an extent that so many scientific disciplines today can reap its benefits.

---

*Ernst Ruska*  
*Nobel Lecture, 1986*

Transmission electron microscopy (TEM) is a type of microscopy that probes electrons transmitting through an ultra-thin sample. The prime reason for using electrons rather than light for imaging is the resolution limit, which is determined by the wavelength. Louis de Broglie (1924) revealed the wave nature of matter, such as electrons, suggesting that high-energy particles can have a wavelength much smaller than light does [118]. It shows the potential of using the electron as the illumination source, with the wavelength tunable by the accelerating voltage. The concept was soon confirmed by Davisson and Germer (1927) with the electron diffraction experiment [119]. Knoll and Ruska (1932) developed the idea

of electron microscopy into reality [120]. The resolution of electron microscopy quickly surpassed that of light microscopy within a year. After a development of more than 80 years, TEM becomes one of the most efficient and versatile characterisation tools in many fields, including materials science and biology.

The optical system of TEM is complex but its working principles are not significantly different from those of a light microscope. Electrons are emitted from the electron gun and accelerated a energy typically ranging from 100 to 300 keV. Various electromagnetic lenses and apertures are used to manipulate the electrons, including beam intensity and coherency, probe size, shape and convergence angle [16]. The electrons interact with the materials strongly, requiring the sample to be ultra-thin (tens or hundreds of nanometres). A rich amount of information is generated during the interaction enabling the characterisation of the crystallography and chemistry of the material. High-resolution transmission electron microscopy (HRTEM) produces the lattice image with the interference of electron waves [16]. It is known as phase contrast imaging, in comparison to diffraction contrast imaging that selects specific diffracted electron beam(s) to generate the image [16].

Scanning transmission electron microscopy (STEM) is a mode in electron microscopy that combines the concepts of scanning electron microscopy with transmission electron microscopy. This technique focuses the electron beam to a very fine probe to scan across the sample in a raster pattern [121]. The electron signals are collected according to their scattering angles. A high angle annular dark field (HAADF) detector collects the electrons scattered at high angles, mostly inelastic in nature, that are sensitive to the atomic number of the element. A bright field (BF) detector collects the direct and low-angle scattered electrons, mostly elastic in nature, that generates a phase contrast image similar to that of a TEM BF image [122]. HAADF- and BF-STEM signals can be obtained simultaneously. Energy dispersive X-ray spectroscopy (EDXS) and electron-energy-loss-spectroscopy (EELS) can be easily incorporated during the scanning that probe the site-specific chemistry.

Considering the de Broglie wavelength and relativity, 200/300 keV electrons have a wavelength of 2.51/1.97 pm travelling at 69/78% speed of light. The theoretical resolution limit of electrons allows a resolution much finer than an atom. However, it is not possible to manufacture a perfect electromagnetic lens. In addition, the electronic and mechanical stabilities of a microscope considerably influence the final resolution. As Ernst Ruska said, it is a miracle that these difficulties have been solved to the current extent of reaching a sub-Å resolution. In particular, the development of aberration correction is significant, being not just a milestone in the field of electron microscopy but a boost for materials science [112].

The following sections describe the microscopes, aberration corrections and various microscopy techniques implemented in this study.

### 3.2.1 Microscopes and Imaging Conditions

Table 3.1 Microscopes and their imaging conditions used in the present study.

Microscopes	Probe Convergence Semi-Angle (mrad)	Probe Size (Å)	Spherical Aberration (mm)	Collection Semi-angle (mrad)	
				BF	HAADF
JEOL 2100F	10	2	1	15	65-185
FEI F20	9.3	2	1.2	15	41-220
FEI Titan <sup>3</sup> 80-300	15	1.2	<0.001	15/40	55-200

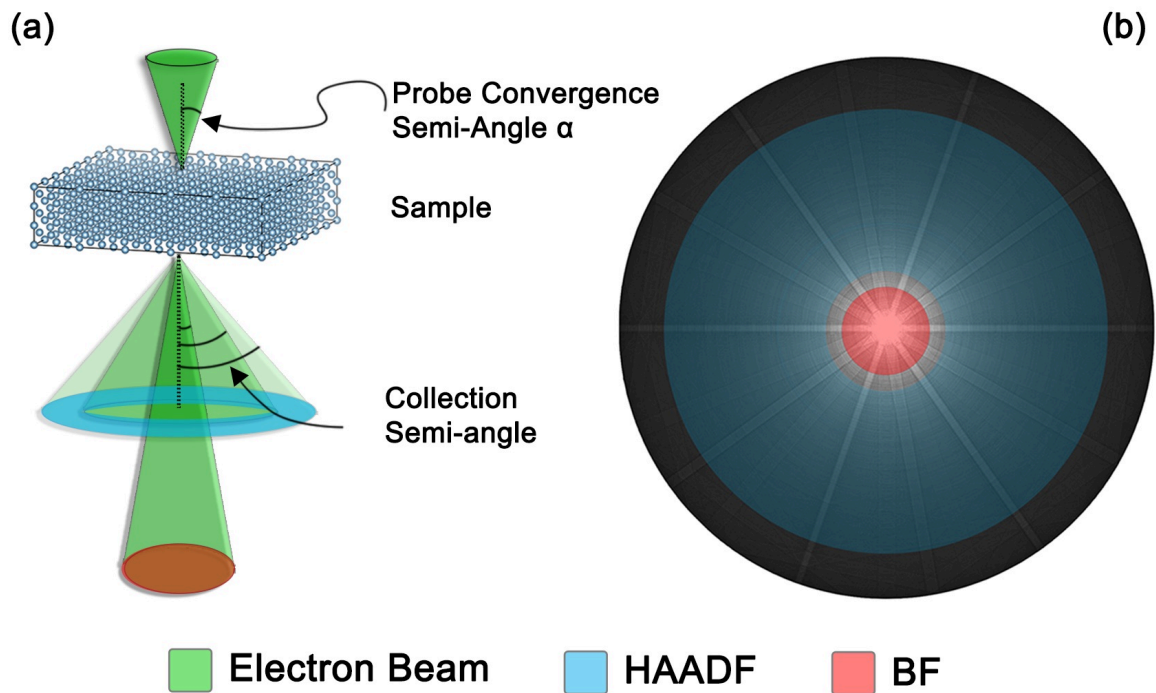


Fig. 3.2 (a) Schematic diagram illustrating the semi-convergence angle of an electron probe and collection semi-angles for the bright field (BF) and high-angle annular dark-field (HAADF) in scanning transmission electron microscopy (STEM). (b) A diffraction pattern demonstrates the angular coverage of BF (40 mrad) and HAADF (55-200 mrad) detectors used in the Titan<sup>3</sup> FEGTEM.

The alloy microstructure and precipitate atomic structures were characterised by transmission electron microscopy. In particular, HAADF-STEM was performed to exploit the

large difference in the atomic numbers between Ag and Al. Preliminary investigations of the microstructures were carried out on a JEOL JEM 2100F field-emission gun transmission electron microscope (FEGTEM) and an FEI Tecnai G<sup>2</sup> F20 Super-Twin lens FEGTEM. Higher resolution imaging was conducted in a dual-aberration-corrected FEI Titan<sup>3</sup> FEGTEM. The detailed imaging conditions are listed in Table. 3.1.

### 3.2.2 Aberration Correction for Scanning Transmission Electron Microscopy

The resolution in the STEM is determined by the size of the probe. For a perfect lens, we might expect all rays emerged from a single point object P to be brought back to a single point image  $P'$  at its Gaussian image plane [16], Fig. 3.3 (a). The ideal resolution is thus only limited by diffraction as:

$$d_d = 1.22 \frac{\lambda}{\alpha}, \quad (3.1)$$

where  $d_d$  is the diffraction limit,  $\lambda$  is the wavelength and  $\alpha$  is the convergence semi-angle. However, neither the lens is perfect nor the source is a point within an electron microscope. The initial Gaussian diameter of the electron gun is given as:

$$d_g = \frac{2}{\pi} \left( \frac{i}{\beta} \right)^2 \frac{1}{\alpha}, \quad (3.2)$$

where  $i$  is the beam current,  $\beta$  is the brightness. For an electromagnetic lens in practice, the most significant imperfection is spherical aberration  $C_s$ . This is illustrated in Fig. 3.3(a) with the diameter of minimum confusion disk as:

$$d_s = 0.5C_s\alpha^3. \quad (3.3)$$

The combination of those three limits the practical resolution. As shown in Fig. 3.3(b), the resolution drops above a critical convergence semi-angle, mainly due to spherical aberration. A condenser aperture is used to select that critical convergence semi-angle to exclude severe aberrations. This can be revealed in a ronchigram, which is a convergent beam electron diffraction disk on an amorphous material with a flat centre corresponds to an infinite magnification of real space and the warped surroundings due to aberration. A small aberration gives a large flat centre to be included by the condenser aperture, hence, a large convergence angle to form a small probe, Fig. 3.3(c).

A small electron probe suffers from aberration beyond spherical aberration. The aberration function  $\chi(\theta, \varphi)$  gives the difference between a perfect planar wave and the actual

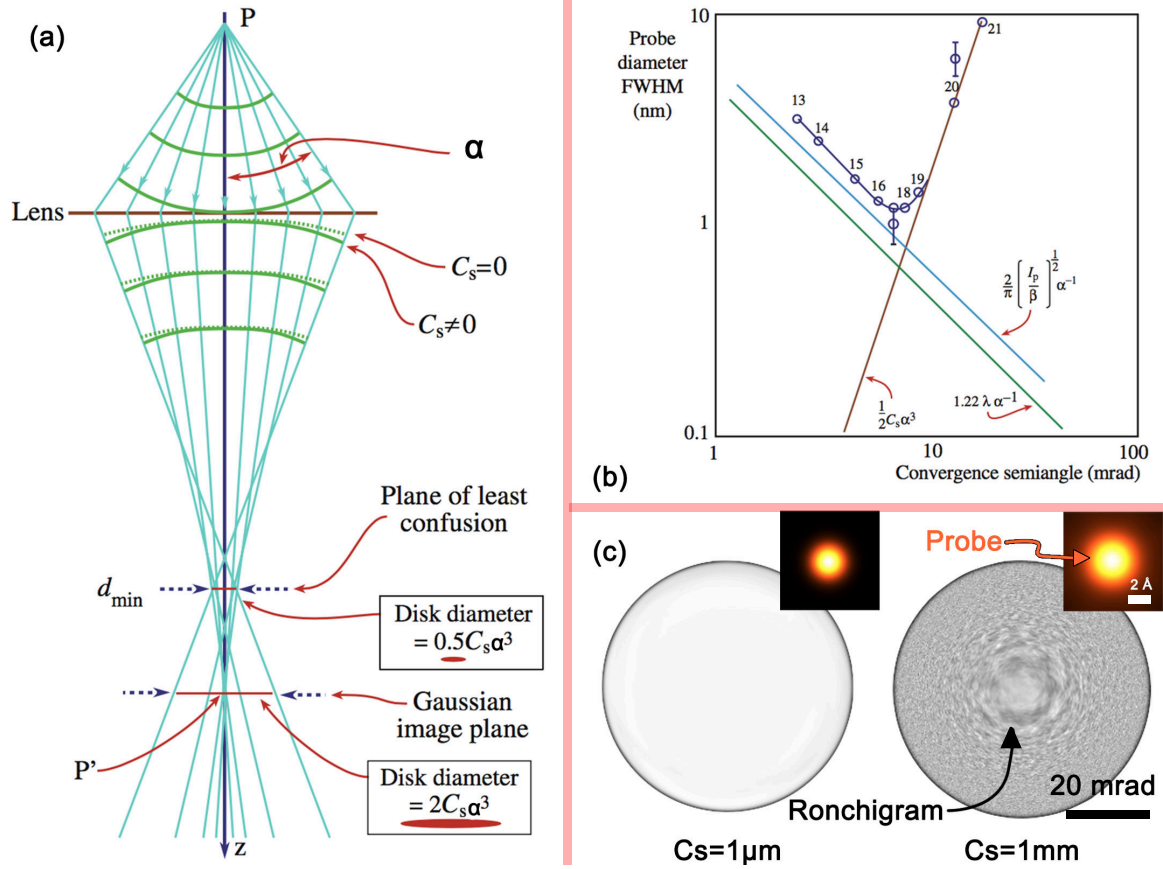


Fig. 3.3 (a) Ray diagram illustrating spherical aberration, which causes deviation from the perfect wavefront. As a result, the rays will not come back to a single point in the Gaussian image plane, instead, they form a disk. The smallest disk along the optical axis is formed at the plane of least confusion. Reprinted from Ref. [16], p. 103 with permission from Springer. (b) The contributions from the diffraction limit, source size and lens spherical aberration to the probe size as a function of the convergence semi-angle, reprinted from Ref. [16], p. 84 with permission from Springer. (c) Ronchigrams and probes with spherical aberrations of  $1\ \mu\text{m}$  and  $1\ \text{mm}$  (with  $0.7\ \text{\AA}$  source radius and no other aberrations), simulated by the Dr. Probe light software [123] with kind license from J. Barthel.

wavefront as a function of diffraction angle  $\theta$  and azimuthal angle  $\varphi$ :

$$\begin{aligned} \chi(\theta, \varphi) = & \frac{1}{2}A_1\theta^2\cos(2\varphi - \varphi_{A_1}) + \frac{1}{2}C_1\theta^2 \\ & + \frac{1}{3}A_2\theta^3\cos(3\varphi - \varphi_{A_2}) + B_2\theta^3\cos(\varphi - \varphi_{B_2}) \\ & + \frac{1}{4}C_3\theta^4 + \frac{1}{4}A_3\theta^4\cos(4\varphi - \varphi_{A_3}) + S_3\theta^4\cos(2\varphi - \varphi_{S_3}) + \dots, \end{aligned} \quad (3.4)$$

where  $A_1$ ,  $C_1$ ,  $A_2$ ,  $B_2$ ,  $C_3$ ,  $A_3$  and  $S_3$  are second-order astigmatism, defocus, third-order astigmatism, coma, spherical aberration, fourth-order astigmatism and star aberration respectively. To overcome aberrations, two classes of methods are developed: (a) image processing of data acquired by through focal series or holography; (b) more robustly, hardware that generates negative aberrations to correct those induced by lenses, or aberration correctors.

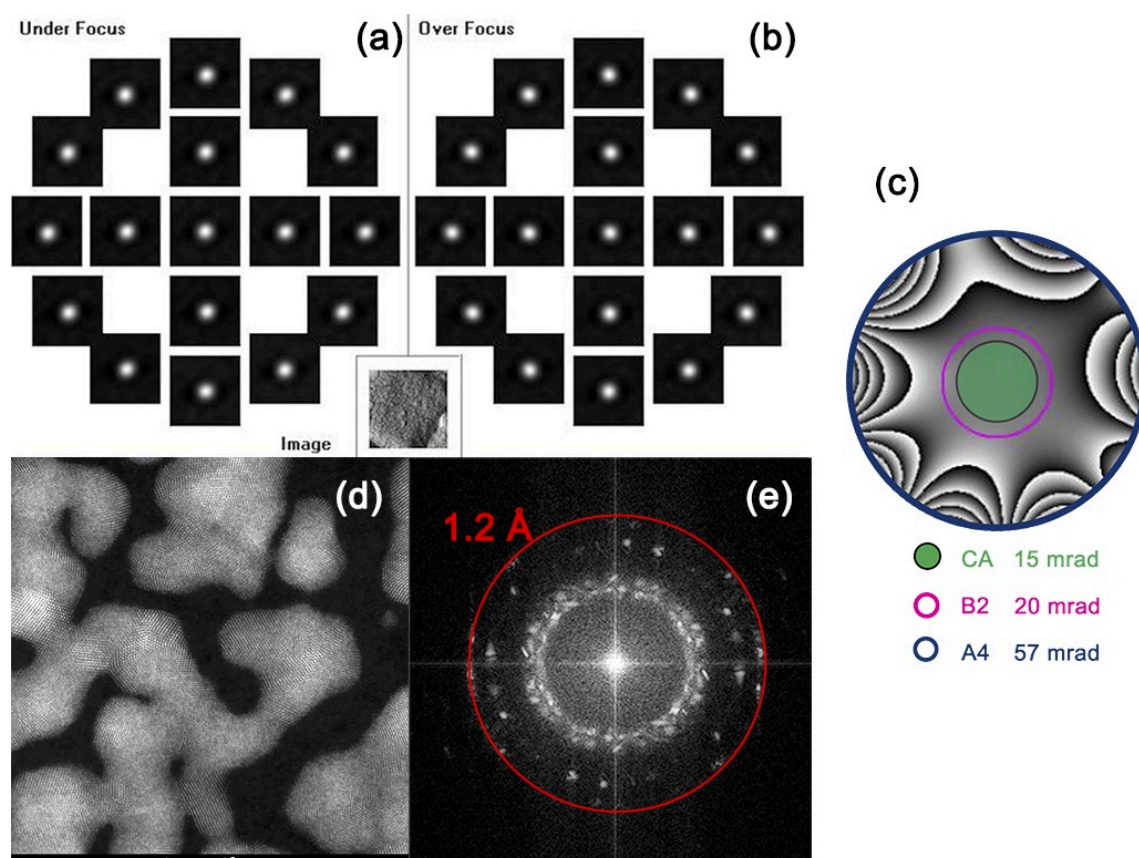


Fig. 3.4 (a-b) Zemlin tableau for measurement of aberration coefficients. It consists of an initial STEM image and deconvoluted under- and over-focused probe shapes obtained at different incident directions with a given tilt angle. (c) Phase plate calculated from aberration measurements and condenser aperture (CA) applied. In this particular case, B2 aberration limits the  $\pi/4$  phase shift at 20 mrad, A4 aberration limits the  $12\pi$  phase shift at 57 mrad, and the condenser aperture with a convergence semi-angle of 15 mrad is applied. (d) HAADF-STEM of gold nano-particles captured after aberration correction and (e) its fast Fourier transform (FFT) showing the frequencies up to  $0.83 \text{ \AA}^{-1}$ , or equivalently  $1.2 \text{ \AA}$  resolution in real space, were obtained.

Correcting all those aberrations requires accurate measurements first. The procedure used on the FEI *Titan*<sup>3</sup> 80-300 follows the Zemlin tableau method, as detailed below. The measurements and corrections are performed on a standard cross-grating specimen, which consists of gold nano particles. The sample is first brought to the eucentric height, where

under- and over-focused images are taken to deconvolute the probe shapes at zero beam tilt.  $A_1$  and  $C_1$  aberrations are calculated from the deconvoluted probe shapes and corrected to be better than  $\pm 10$  nm. Then, the electron beam is tilted and rocked in a hollow cone that probes the aberrations in different directions. As shown in the Zemlin tableau, Fig. 3.4 (a-b), the azimuth is changed by  $-30^\circ$  (clockwise) at each step for the outer circle with a radius of  $\theta$ , and  $-90^\circ$  for the inner circle with a radius of  $\frac{1}{2}\theta$ . The tilting angle of the electron beam needs to be above the targeted convergence angle of the probe. The aberrations up to the third order are measured and corrected. As shown in Fig. 3.4(c-e), the resolution is about 1.2 Å using a condenser aperture with a convergence semi-angle of 15 mrad.

### 3.2.3 *In situ* Scanning Transmission Electron Microscopy

The *in situ* annealing experiments were conducted to capture phase transformations in time. Samples were aged in the JEOL 2100F using a Gatan 652 double-tilt heating holder at different temperatures (100°C, 150°C and 200°C) for various times ranging from 3 min to 120 min. In these experiments, samples were imaged either during *in situ* annealing or after cooling down to room temperature. A Gatan Digital Micrograph script was written to automatically acquire STEM images with user input parameters. We used a probe dwell time of 30  $\mu$ s and a scan size of 512 $\times$ 512 pixels for each frame, with an interval time of 20 s between each frame. The recording usually started 10 min after *in situ* annealing began, giving the time to correct the drift and the reorientation of the sample due to heating.

### 3.2.4 Electron Tomography

Imaging in TEM can sometimes be misleading due to the nature of transmission: the two-dimensional TEM image is a projection of a three-dimensional object, which is particularly true for microstructures consisting of complicated geometries. To gain the full picture, tomography<sup>7</sup> restores the 3D structure from a series of 2D projections at different angles [113]. The theory of tomography was developed by Radon in 1917 [124], and then first applied by Bracewell in radio astronomy [113]. Tomography finds applications in many fields, like computerised tomography (CT) in hospitals and electron tomography in materials science.

Radon theory describes the transformation between an object in the real space  $f(x, y)$  and its projections in all different angles  $Rf$  [113]. The projection collects the intensity of the object along a particular direction  $L$  by a line integral. The Radon transformation sums up all

<sup>7</sup>The word “tomography” originates from the Greek “tomos” – to slice.

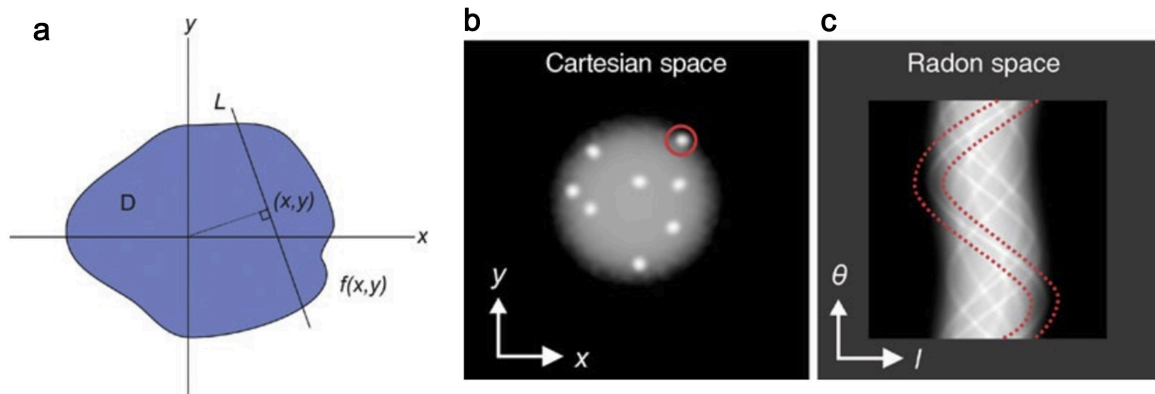


Fig. 3.5 (a) The Radon transformation defines the projection of an object  $D$  in Cartesian space  $(x,y)$  through the line integral  $L$  (in all possible angles). (b-c) Demonstration of Radon transformation, for an object over a full range of tilt  $\theta \pm 180^\circ$ . The circled point in the Cartesian space becomes a sinusoidal line in Radon space, as indicated by dashed lines. The amplitude of the line in  $l$  is a function of its distance from the centre of the volume. Reprinted from Ref. [113], p.345 with permission from Springer.

possible  $L$  as:

$$Rf = \int_L f(x,y) ds, \quad (3.5)$$

where  $ds$  is the unit length of  $L$ , Fig. 3.5(a). By calculating the intensity in terms of projection angles and distances from the origin, the objects in the Cartesian space can be converted into the Radon space, Fig. 3.5(b-c). According to the “projection slice theorem”, the fast Fourier transform (FFT) of each 2D projection is a central section through the Fourier transformation of the object in that direction. This theorem informs two things: (1) a reconstruction method by summing all FFTs of projections in the reciprocal space and performing inverse Fourier transformation; (2) a missing wedge of information because we have limited access to high angles within the electron microscope [113]. This missing wedge, together with the number of projections and noise level, limits the ultimate resolution of a reconstruction. Equivalent to the reconstruction in the reciprocal space, back-projection restores the object in real space, Fig. 3.6. As the name suggests, it simply projects the intensity back to the object space at their projection angles. However, assuming we have a uniform sampling of spatial frequencies in the recorded 2D images and the knowledge of the “projection slice theorem”, this method over-samples the low-frequency profiles but under-samples the high-frequency details, Fig. 3.6(b). An easy correction to the radial sampling problem is to apply radially weighted filter [113]. It is intuitive that the reconstructed object should generate the same re-projections as the inputs projections. The reality, in contrast, is very different. Simultaneous iterative reconstruction technique (SIRT) compares the differences

in all projections simultaneously (between the experimental images and re-projected images) and improves in each iteration. SIRT is proven to be stable and robust [113], which was chosen as the reconstruction method in our study.

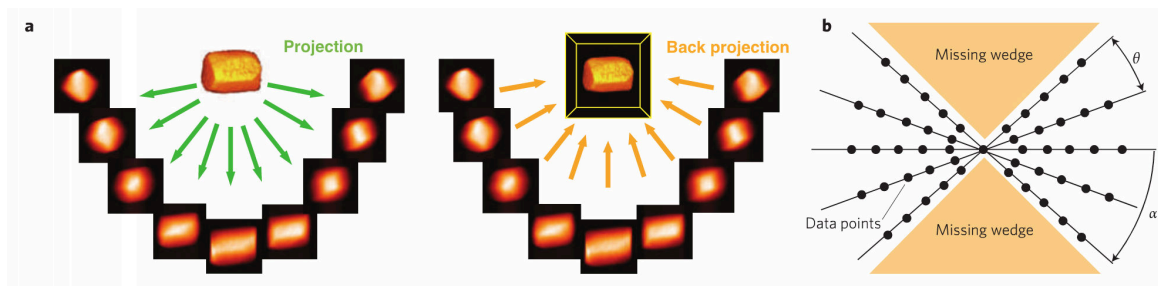


Fig. 3.6 (a) Illustration of the two-stage tomography process with (left) acquisition of an ensemble of images (projections) about a single tilt axis and (right) the back-projection of these images into 3D object space. (b) Representation in Fourier space of the ensemble of projections, indicating the undersampling of high-spatial-frequency information and the missing wedge of information brought about by a restricted tilt range.  $\theta$  is the tilt increment between successive images and  $\alpha$  is the maximum tilt angle. Reprinted from Ref. [125] with permission from Nature.

STEM tomography was carried out following the approach of Midgley and Weyland [126]. The STEM tilt series experiments were performed in the Tecnai F20 under the image condition as detailed in Table 3.1 but with a halved collection angle to improve the signal-to-noise ratio. Specifically, the collection semi-angle was 7.5 mrad for the BF-STEM and 20.5-110 mrad for the annular dark field (ADF) STEM respectively. A Fischione model 2020 single-tilt axis high-tilt sample holder was used, acquiring BF- and ADF-STEM images  $2^\circ$  per tilt from the maximum negative tilting angle ( $\sim -70^\circ$ ) to the maximum positive tilting ( $\sim 70^\circ$ ). The movement of the holder, as well as the optic axis, were pre-calibrated using standard cross-grating specimen with gold nano-particles. Both low and high magnifications tilt series were performed to cover the field of view from few micrometres to tens of nanometres. The pixel size of each frame was  $2048 \times 2048$  with an exposure time of 48 s. The data collection was performed using the FEI Xplore3D software, implementing automatic re-centring (pre-acquisition tracking of the area of interests) and re-focusing. Though the Tecnai F20 has a relatively small convergence semi-angle that the depth of focus is generally not an issue, all tilt series were taken at thin regions to avoid the problem. As the tomography theory assumes intensities increase monotonically with densities, only ADF-STEM was used for reconstruction. ADF-STEM data were aligned and reconstructed using the code programmed in IDL 6 [126]. The data were first binned by four times to  $512 \times 512$  pixels per frame for alignment. The background was normalised by setting vacuum intensity to zero. Shift alignment was carried out using sequential cross-correlation with a band-pass

filter corresponding to the size range of the precipitates. Then, manual corrections were performed to fix small shifts. Axis alignment was fine-tuned by interactive minimisation of arcing in the reconstruction [126]. Finally, the shift and rotation axis alignments determined in the binned data were applied back to the original data with full pixels. The aligned data were reconstructed using SIRT with 30 iterations, segmented and visualised in Amira 6. The segmentations of voxel and isosurface were performed by manually adjusting the threshold value in such way that the profiles of reconstructed microstructure matched with the original ADF-STEM images.

### 3.2.5 Energy Dispersive X-ray Spectroscopy

Compositional analysis was performed on the JEOL 2100F and the Tecnai F20 using energy-dispersive X-ray spectroscopy (EDXS). The JEOL 2100F has a JEOL 50 mm<sup>2</sup> Si(Li) detector with ultra-thin window. The Tecnai F20 has a Bruker XFlash 6120T 30 mm<sup>2</sup> silicon drift windowless detector. The composition measured by EDXS across the sample thickness is contributed by the Ag-enriched precipitate and the Al matrix. The precipitates examined in this study have a roughly spherical geometry. Thus, the diameter of a precipitate in the electron transmission direction was approximated to be equal as its averaged diameter on the HAADF image. The thickness of the specimen in the vicinity of a precipitate was determined by comparing on-zone position-averaged convergent-beam electron diffraction (PACBED) of the surrounding matrix [127] obtained experimentally and calculated PACBED patterns with the Bloch wave method in the JEMS software [128]. The PACBED patterns used for comparison were taken in Titan at 300 KeV with the corresponding simulation. Because on-zone PACBED requires fine sample tilting for each precipitate on FEI F20 and JEOL 2100F without misaligning the optics. Even after onerous sample tilting, we found that small misorientation (<1 mrad) is hardly avoidable. In contrast, on-zone PACBED can be easily achieved with a beam tilt in Titan via positioning a smaller condenser aperture (30 mm, 10 mrad) without interfering the condenser aperture used for imaging (i.e. 50 mm, 15 mrad). Thus, after the EDXS and PACBED experiments on F20 and 2100F, the PACBED experiments were performed again in Titan for each precipitate in the same region. The accuracy of the PACBED thickness measurements was  $\pm 2$  nm as demonstrated in Ref. [129]. Note that PACBED can only measure the thickness of crystalline materials that does not include the thin amorphous oxide film on top and bottom surfaces of a sample. The sample was tilted away from its zone axis to the optimum angle for EDXS detection, also to avoid strong dynamical diffraction conditions. A position-averaged EDXS spectrum was taken at the centre of each precipitate over a  $3 \times 3$  nm<sup>2</sup> area in order to remove the effect of local chemical inhomogeneity. A schematic diagram of the method is illustrated in Fig. 3.7.

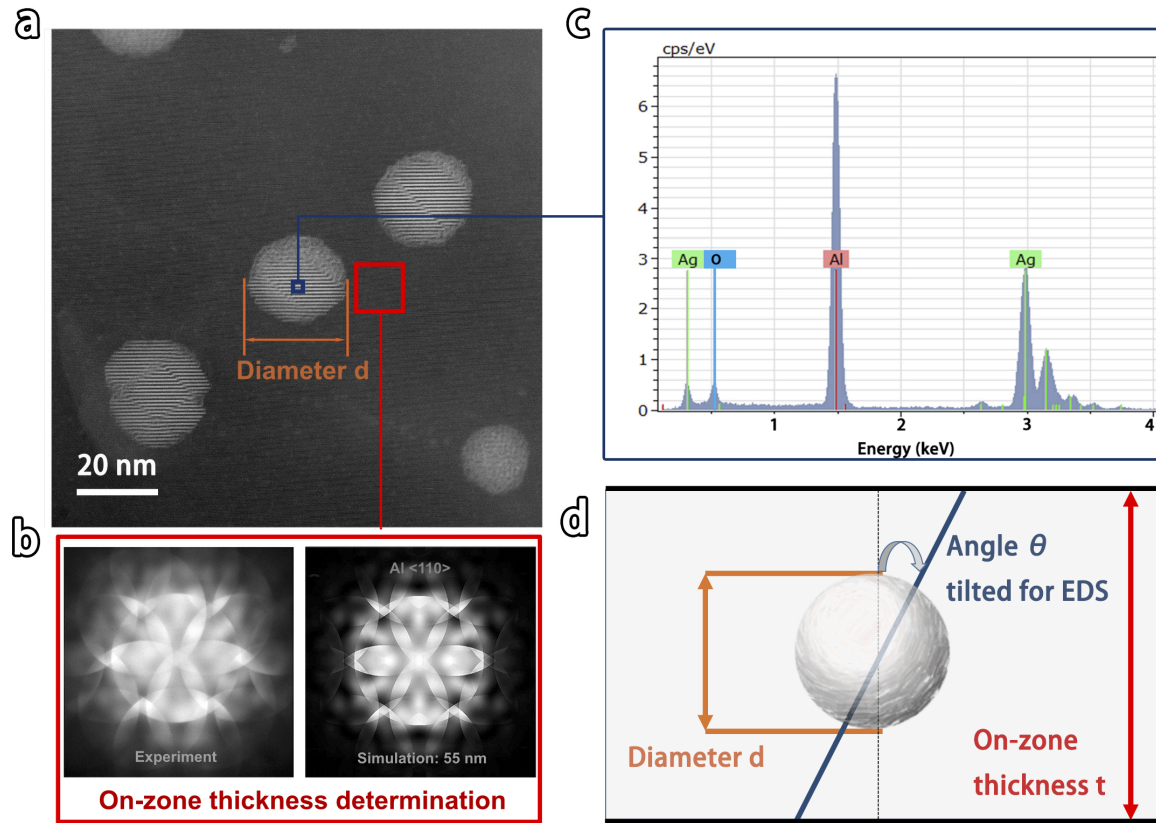


Fig. 3.7 Compositional analysis for an embedded, spherical precipitate by energy-dispersive X-ray spectroscopy (EDXS). (a) HAADF-STEM image showing the measurements of a precipitate. The diameter of a precipitate,  $d$ , in the electron transmission direction was estimated by its averaged size on the HAADF-STEM image. The electron beam was parallel to  $\langle 110 \rangle_{\text{Al}}$ . (b) The thickness,  $t$ , in the vicinity of a precipitate was determined by comparing an on-zone position-averaged convergent beam electron diffraction (PACBED) pattern of its surrounding matrix with simulations (Titan, 300 KeV). (c) A position-averaged spectrum was taken at the centre of the precipitate and the composition was quantified by the software supplied with TEM, using the Cliff-Lorimer ratio method. The sample was tilted away from its zone axis to the optimal angle for EDXS detector and avoiding strong dynamical diffraction conditions (the electron channelling would be problematic otherwise). We ignored the thin oxide film on the sample surface. (d) A schematic diagram illustrating the parameters needed for determining the composition as written in the Eq. 3.7.

Starting from the Cliff-Lorimer equation,

$$\begin{aligned} \frac{C_{\text{Ag}}^{\text{dect}}}{C_{\text{Al}}^{\text{dect}}} &= k_{\text{Ag-Al}} \cdot \frac{I_{\text{Ag}}^{\text{dect}}}{I_{\text{Al}}^{\text{dect}}} \\ &= \frac{C_{\text{Ag}}^{\text{prec}} \cdot d}{C_{\text{Al}}^{\text{prec}} \cdot d + (t - d)}, \end{aligned} \quad (3.6)$$

we can deduce the composition of an embedded precipitate as follows:

$$C_{\text{Ag}}^{\text{prec}} = \frac{C_{\text{Ag}}^{\text{dect}} \cdot t}{d \cdot \cos\theta}, \quad (3.7)$$

where  $C^{\text{prec}}$  is the deduced composition of the precipitate,  $C^{\text{dect}}$  is the measured composition,  $k_{\text{Ag-Al}}$  is the Cliff-Lorimer k-factor between Ag and Al,  $I^{\text{dect}}$  is the detected characteristic intensities for quantification,  $t$  is the thickness of the matrix near the precipitate,  $d$  is the diameter of the precipitate and  $\theta$  is the tilting angle difference between that for the thickness determination and the EDXS detection. We checked the k-factor by measuring the composition of the as-water-quenched sample, as the theoretical value stored in the quantification software may easily vary by  $>10\%$  [130]. The measured composition of 1.8 at.% to 2.0 at.% Ag across the sample is in good agreement with the alloy composition (Al-1.68 at.% Ag). Although errors of the deduced compositions arising from neglecting the geometrical X-ray absorption and fluorescence remain, these errors were found not to be significant for a thin foil: according to mass-energy X-ray absorption calculations [131], about 2% of the major characteristic X-ray for Ag ( $L_{\alpha}=3$  KeV) is absorbed by the Al matrix for a 100 nm-thick sample, Fig. 3.8. Thus, the results should still be comparable between precipitate phases. Furthermore, the composition of one of the phases (GP zone  $\varepsilon$ ) is already known from the phase diagram [52] and many previous experiments (see for example Ref.[61]).

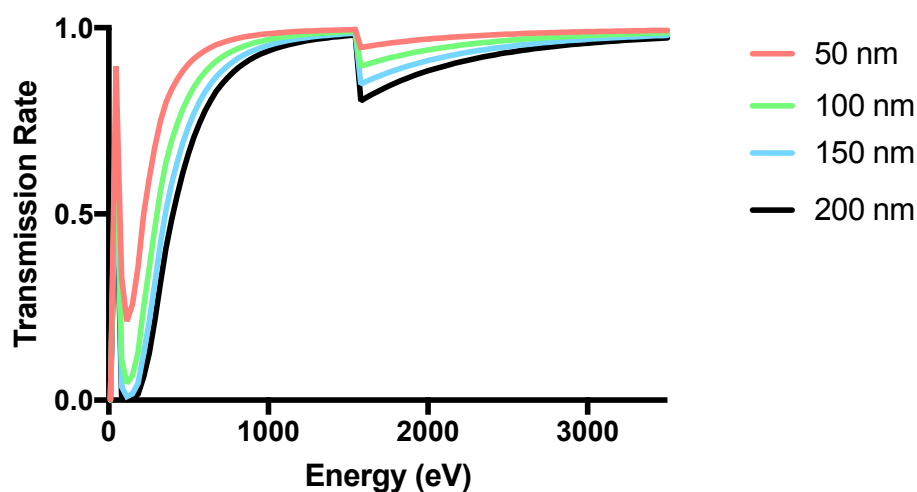


Fig. 3.8 Calculated X-ray transmission spectrum for Al with different thicknesses [131], showing the absorption of Ag characteristic peak  $L_{\alpha}=3$  KeV is negligible in a thin Al foil ( $\sim 2\%$  for 100 nm or  $\sim 5\%$  for 200 nm).

### 3.2.6 Image and Diffraction Pattern Simulations

Computer simulation is necessary for quantitative interpretation of images and diffraction patterns in electron microscopy. The reason is simple: being a charged particle, an electron is scattered very strongly by matters and usually for multiple times. The multiple scattering brings the dynamic nature of electron diffraction. In addition, electrons are likely to lose energy during the multiple scattering by exciting phonons or ionising atoms. Thus, it is not straightforward to interpret the contrast quantitatively. There are two simulation approaches that explicitly account for the dynamic scattering: (a) the Bloch wave method, derived in Bethe's original attempt [132] to interpret Davisson-Germer electron diffraction experiment [119], and (b) the multislice method, pioneered by Cowley and Moodie [133].

Electrons are travelling fast in TEM ( $\sim 78\%$  speed of light for the 300 KeV electrons). Their wave functions should be solved by the Dirac equation to include relativistic effects. However, the Dirac equation is difficult to work with. It has been shown that the Schrödinger equation with the relativistically corrected mass and wavelength of electron yields accurate results within the typical energy range of electron microscopy [134]. The Schrödinger equation is listed for the scattering of fast electrons as:

$$-\frac{\hbar^2}{2m}\nabla^2\psi(x,y,z) - eV(x,y,z)\psi(x,y,z) = E\psi(x,y,z), \quad (3.8)$$

where  $\hbar$  is the reduced Plank constant,  $m$  is the particle mass,  $\nabla^2$  is the second derivative in terms of position,  $V(x,y,z)$  is the atomic potential that varies with positions in space,  $\psi(x,y,z)$  is a solution of the wave function and  $E$  is the kinetic energy of the incident beam (determined by the accelerating voltage of the electron gun).

The Bloch wave method supposes the electron waves are scattered by the periodic atomic potentials, which inherit the symmetry of the crystal. According to the Bloch theorem, the periodic potential  $V(\vec{r})$  is expanded as a 3D Fourier series as:

$$V(\vec{r}) = \sum_g V_g \exp[2\pi i \vec{g} \cdot \vec{r}], \quad (3.9)$$

where  $\vec{g}$  is the reciprocal space vector and  $V_g$  is the potential Fourier coefficient. Similarly, the electron wave solution  $\psi(\vec{r})$  has the same crystal periodicity and is a sum of all those Bloch waves as:

$$\psi(\vec{r}) = \sum_i c_i \exp[2\pi i \vec{k}_i \cdot \vec{r}] \sum_g C_g^i \exp[2\pi i \vec{g} \cdot \vec{r}], \quad (3.10)$$

where  $i$  is the index of a Bloch wave,  $c_i$  is the coefficient of  $i$ th Bloch wave that contributes to the overall solution and  $C_g^i$  is the coefficient of reflection  $\vec{g}$  in  $i$ th Bloch wave. Substituting

Eq. 3.9 and Eq. 3.10 into Eq. 3.8, we can get the high-energy electron diffraction equation as:

$$2KS_gC_g + \sum_h V_{gh}C_h = 2K_n\gamma C_g, \quad (3.11)$$

where  $K$  is the incident wave number inside the crystal defined as  $K^2 = k_0^2 + V_0$  with  $k_0$  defined as the incident wave number in the vacuum.  $S_g$  is the excitation error defined as  $S_g = (K^2 - (K + g)^2)/2K$ .  $K_n$  is the wave number in the surface normal direction  $\vec{n}$  defined as  $K_n = \vec{k} \cdot \vec{n}$ . Detailed derivation can be found in Ref. [135]. Eq. 3.11 can be written in matrix form to solve the eigenfunctions and eigenvalues associated with  $C_g$  of all reflections in all Bloch states. After resolving the incident wave at the entrance surface with  $t = 0$ , the wave solution inside the crystal at thickness  $t$  can be found by applying the scattering matrix  $S = C \exp[2\pi i \gamma^j t] C^{-1}$  to the incident wave function. The intensity of a particular Bragg beam can be obtained by taking the modulus square of the wave function for that reflection. The Bloch wave calculations were performed in the JEMS software [128] to simulate the convergent beam electron diffraction patterns for thickness determination. The calculations were performed for Al in both  $\langle 110 \rangle_{\text{Al}}$  and  $\langle 11\bar{2} \rangle_{\text{Al}}$  directions with sample thicknesses ranging from 20 nm to 200 nm with a step size of 2 nm, using a semi-convergence angle of 10 mrad and 96 electron beams.

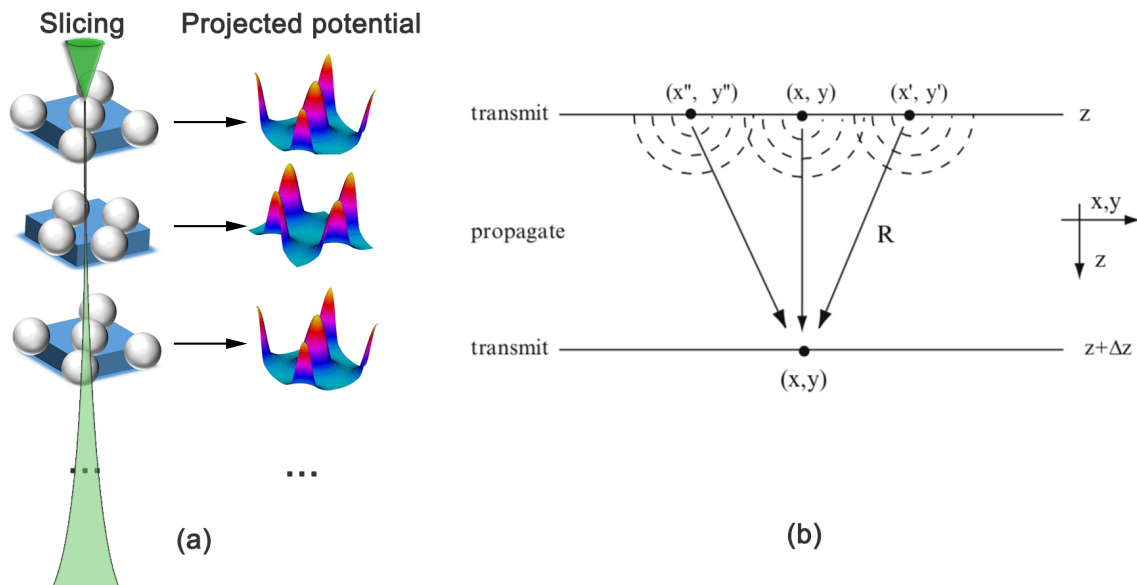


Fig. 3.9 (a) Schematic diagram demonstrating the projection of atomic potentials within each finite slice. (b) Schematic diagram demonstrating the propagation of electron wave from one slice to the next. The wavefront at the depth  $Z$  is scattered by the projected atomic potentials and emits a spherically outgoing wave, which contributes to the wave front of the next slice. Reprinted from Ref. [136], p, 138 with permission from Springer.

The intensity in HAADF-STEM is contributed heavily by the phonon-scattered electrons [137]. The construction of phonon (atoms deviating from their equilibrium positions) breaks the periodic potential conditions that underpin the Bloch wave method, making multislice the option for STEM simulations as now described. One can transform this Schrödinger equation to the travelling of the wave along,  $z$ , the beam transmission direction [136]:

$$\frac{\partial \psi(x, y, z)}{\partial z} = \left[ \frac{i\lambda}{4\pi} (\nabla_{xy}^2) + i\sigma V(x, y, z) \right] \psi(x, y, z), \quad (3.12)$$

with  $\nabla_{xy}^2 = \nabla_x^2 + \nabla_y^2$  and the interaction parameter  $\sigma = 2\pi m\lambda/h^2$ . Adapted from Eq. 3.12, the wave function evolves from one slice at thickness  $z$  to the next slice at  $z + \Delta z$  as:

$$\psi(x, y, z + \Delta z) = P(x, y, \Delta z) \otimes T(x, y, z) \psi(x, y, z) + \mathcal{O}(\Delta z^2), \quad (3.13)$$

where  $P(x, y, \Delta z)$  is the Fresnel propagator

$$P(x, y, \Delta z) = \frac{1}{i\lambda\Delta z} \exp\left(\frac{i\pi}{\lambda\Delta z} (x^2 + y^2)\right), \quad (3.14)$$

and the convolution operator ( $\otimes$ ) is defined as:

$$f(\vec{r}) \otimes g(\vec{r}) = \int f(\vec{r}') g(\vec{r} - \vec{r}') dr. \quad (3.15)$$

The convolution of the Fresnel propagator comes from the term  $\frac{i\lambda}{4\pi} \nabla_{xy}^2$  in Eq. 3.12, propagating the wave from one slice to the next, Fig. 3.9(b).  $T(x, y, z)$  is the transmission function:

$$T(x, y, z) = \exp\left(i\sigma \int_z^{z+\Delta z} V(x, y, z') dz'\right), \quad (3.16)$$

which comes from the term  $i\sigma V(x, y, z)$  in Eq. 3.12, projecting the 3D atomic potentials into 2D potentials for each slice, Fig. 3.9(a). Detailed derivation can be found in Ref. [136].

The multislice algorithm divides materials into slices and treats multiple scattering as a repetition of single scattering within each slice. Because atoms are vibrating slowly ( $10^{12} \sim 10^{13}/s$ ), through the eyes of fast travelling electrons, phonons are virtually frozen during the electron transmission [136]. To simulate this effect, atoms are displaced from the equilibrium position with a probability according to the Einstein model <sup>8</sup>:

$$p(\vec{r}) \propto \exp[-(\vec{r} - \vec{r}_0)^2 / 2\langle u^2 \rangle], \quad (3.17)$$

<sup>8</sup>Einstein model treats the atomic vibrations as a set of independent harmonic oscillators with the same frequency.

where  $\langle u^2 \rangle$  is the mean-squared displacement, which relates to the Debye-Waller factor  $B$  as  $B = 8\pi^2 \langle u^2 \rangle$ .

HAADF-STEM simulations were performed using the  $\mu$ STEM software [137], implementing the multislice method with the quantum excitation of phonons to incorporate elastic and inelastic electron scattering. The simulations used the crystal structures optimised by the first-principles density functional theory methods. The supercells were constructed from those crystal structures, tiling around 30 Å in the lateral directions to avoid the “wrap around” error, that is the interference of the probe wave function with itself from the neighbouring supercells. To offer a sufficient angular range for the HAADF detector, the pixel size is determined by the following equation as:

$$pixel\ size = \frac{1}{3} \frac{\lambda}{\theta_{max}}, \quad (3.18)$$

where  $\lambda$  is the electron wavelength (1.97 pm for 300 KeV electron) and  $\theta_{max}$  is the outer angle for HAADF detector ( $\sim 200$  mrad in the *Titan*<sup>3</sup>)<sup>9</sup>. Slicing was selected to go through the centre of each atomic layer in the electron beam direction, which yielded a slice thickness of 1.485 Å in a  $\langle 110 \rangle_{Al}$  direction or 0.825 Å in a  $\langle 11\bar{2} \rangle_{Al}$  direction. To account for the effect of phonons, atoms in each slice were displaced randomly into 40 different configurations according to the probability in the Einstein model. The mean-squared displacement was  $1.033 \times 10^{-2} \text{Å}^2$  for Al and  $0.942 \times 10^{-2} \text{Å}^2$  for Ag at room temperature, calculated from the experimentally fitted polynomials in Ref. [138]. The scattering within each slice was iterated for 20 passes, with a new set of configurations at each pass to average the scattering within each slice. The total sample thickness was modelled from 100 Å to 600 Å. Microscope parameters were matched with the experimental settings of *Titan*<sup>3</sup> as specified in Table 3.1.

### 3.2.7 Quantitative Scanning Transmission Electron Microscopy

The experimental and simulated images were analysed using the ImageJ software. For the relative contrast comparison, the brightness of the simulated images was scaled linearly to the same dynamic range as an experimental image. The contrast was then adjusted to that of the experimental image by modifying the gamma correction value ( $\Gamma$ ). The intensity was given by  $I' = I^\Gamma$ , where  $I'$  is the output intensity, and  $I$  is the input intensity. Except for the brightness and contrast adjustments, no other image manipulation was performed.

For the absolute contrast comparison, we need to characterise the detector, determine the sample thickness in the vicinity of a precipitate and perform multislice calculations.

<sup>9</sup>It is because the sampling frequency is limited by the Nyquist frequency, below which aliasing error shall mix different frequencies and distort the image.

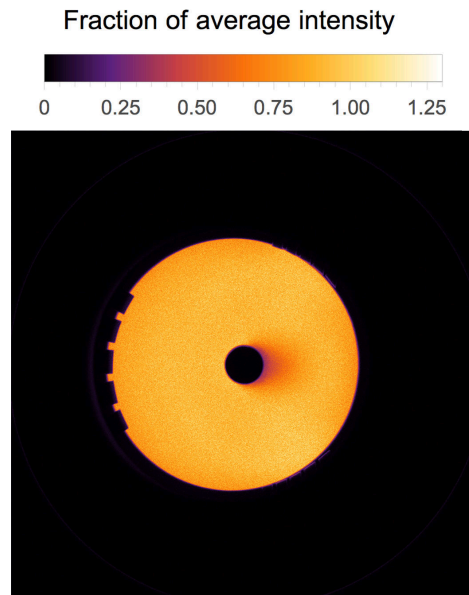


Fig. 3.10 Mapping of the HAADF detector response with the efficiency normalised against the averaged intensity of the active area.

(a) The experimental images were normalised to an absolute scale according to  $I_{norm} = (I_{raw} - I_{dark}) / (I_{det} - I_{dark})$ , where  $I_{norm}$  is the intensity normalised against the incident beam,  $I_{raw}$  is the raw image intensity,  $I_{dark}$  is the dark current of the detector,  $I_{det}$  is the averaged intensity of the detector with the incident beam scanned across the detector in real space without specimen. In order to avoid saturation of HAADF detector, a smaller condenser aperture ( $10 \mu\text{m}$ , convergence semi-angle of 3 mrad) was used for characterising the detector instead of the one for imaging ( $50 \mu\text{m}$ , convergence semi-angle of 15 mrad). The probe intensity difference brought by those two condenser aperture sizes was calibrated in the vacuum with a CCD camera. Fig. 3.10 shows the inhomogeneous response of the HAADF detector in the Titan<sup>3</sup> FEGTEM, which needs to be averaged to compare with the simulations. Care was taken to distinguish the active area of the detector from its physical size. Though detector response is stable, the probe intensity and the imaging amplifier off-set value vary with experiments. Thus, those calibration procedures were performed for each quantitative STEM experiment. (b) The sample thickness was determined in the Al matrix adjacent to a precipitate phase, by comparing an on-zone PACBED pattern with the simulations (via JEMS or muSTEM). The experimental PACBED patterns were recorded using a  $30 \mu\text{m}$  condenser aperture (convergence semi-angle of 10 mrad) and an energy filtered CCD (GIF Quantum filter). An energy slit of 10 eV was centred at the zero-loss peak in the electron energy loss spectrum (EELS) to remove the diffusive diffraction background caused by the inelastic scattering. (c) The thickness determined by PACBED was used as an input for

multislice calculations. Images with different atomic occupancies at the precipitate interface were simulated to determine the interfacial chemistry. The details of multislice simulation were described previously. Both experimental and simulated images were normalised to the incident beam for comparison.

### 3.2.8 Atomic Positions Refinement and Experimentally-informed Model Building

The atomic positions at the interfaces may deviate from that of the bulk. Reconstruction at the interface is common due to the interactions between solute and defects. We applied statistical parameter estimation theory to locate the atomic positions at the interface, as implemented in the software StatSTEM [139]. In the algorithm, Gaussian peaks are fitted atomic positions according to:

$$f_{kl}(\theta) = \xi + \sum_{n=1}^N \tau_n \exp\left(-\frac{(x_k - \beta_{x_n})^2 + (y_l - \beta_{y_n})^2}{2\rho_n^2}\right), \quad (3.19)$$

where  $f_{kl}(\theta)$  is the parametric model for the intensity of the pixel (k,l) at the position  $(x_k, y_l)$ ,  $\xi$  is the background constant intensity,  $\rho_n$  and  $\tau_n$  are the width and height while  $\beta_{x_n}$  and  $\beta_{y_n}$  are the refined coordinates of the  $n$ th Gaussian peak.  $\theta$  is the vector space of unknown parameters to be refined, as a function of  $\beta$ ,  $\rho$ ,  $\tau$  and  $\xi$ . Atomic columns of the different types may have different widths and heights. By minimising the cost function (the least square of difference between experimental images and Gaussian peak models), the 2D coordinates were obtained for each atomic column. The accuracy and precision of this method was examined down to few pm [139].

Building 3D atomic models of complicated structures is always a practical barrier that prevents the microscopy evidence to be implemented in atomistic calculations. The heterophase interfaces in this study involve specific chemistries and dislocations that makes the model building even more formidable. After the 2D atomic column positions were retrieved, we applied the known periodicities of FCC and HCP phases in the viewing direction to build the experimentally-informed 3D interface models. This was achieved by exporting the 2D positions to the software QSTEM Model Builder [140], which can specify independent crystal structures in arbitrary directions with arbitrary 2D outlines. The detailed atomic positions at the interfaces were adjusted from the perfect positions of each phase to the experimentally recorded positions. The models were expanded laterally to reach the periodic boundary condition.

### 3.2.9 Geometric Phase Analysis

Geometric phase analysis (GPA) filters a lattice image according to the peaks in its fast Fourier transform (FFT) and compares that image to a reference lattice to resolve local strain in real space [141]. GPA has demonstrated an excellent spatial accuracy in agreement with classical strain theory [142, 143]. In this study, as the coherent precipitates have a super lattice of FCC aluminium and are coherently embedded within the matrix, the value calculated by GPA reflects the lattice displacements relative to FCC Al. An experimental STEM image with  $1024 \times 1024$  pixels was used as input, where Al matrix away from the precipitate in the same image was used as the reference. The theoretical values of lattice displacements for bulk precipitate phase were calculated by comparing the DFT-optimised structure of precipitate phase (see details in DFT methods) in reference to the DFT-optimised Al lattice parameter using elastic strain calculation [144] in the Ovito software [145]. The lattice parameter values of aluminium obtained from both experimental measurements ( $4.04 \pm 0.05 \text{ \AA}$ ) and DFT optimisation ( $4.05 \text{ \AA}$ ), as the reference for both calculations, were in good agreement. The linear scanning distortion was corrected with a standard gold cross-grating sample before imaging for geometric phase analysis. Because STEM moves the probe in a raster, scanning artefacts arise due to the time delay between measurements and accumulated error in probe position [146]. The noise, usually non-linear in nature due to the external field, is more predominant in the slow scanning direction comparing to the fast scanning direction. The non-linear scanning distortion was corrected with image pairs in orthogonal scan directions using the algorithm described in Ref. [146]. The uncertainties in our GPA results were better than  $\pm 1\%$  after the distortion correction. Note that the atomic size difference between Al and Ag is negligible (about 0.5%). Therefore, our geometric phase analysis is not sensitive to the composition. However, it is sensitive to any structural change larger than 1%. All the calculated images were colourised with the same scale from -7% (contraction) to 7% (extension) for visualisation.

### 3.3 Atomistic Calculations

The fundamental law necessary for the mathematical treatment of a large part of physics and the whole of chemistry are thus completely known, and the difficulty lies only in the fact that application of these laws leads to equations that are too complex to be solved.

---

*Paul A. M. Dirac*  
*Quantum Mechanics of Many Electron*  
*System, 1929*

All materials properties (except nuclear irradiation) are determined by their electronic structures. In quantum mechanics, we assume that all the information about a quantum state is described by wave functions [147]. The eigenstate of a wave and the associated eigenenergy are prescribed by the Schrödinger equation as follows:

$$\left[-\frac{\hbar^2}{2m}\nabla^2 + V(\vec{r})\right]\psi_i(\vec{r}) = \varepsilon_i\psi_i(\vec{r}), \quad (3.20)$$

where  $\hbar$  is the reduced Plank constant,  $m$  is the particle mass,  $\nabla^2$  is the second derivative in terms of position,  $V$  is the potential, which varies with particle position  $\vec{r}$  in space,  $\psi_i(\vec{r})$  is one eigenfunction and  $\varepsilon_i$  is the associated energy. The left side is the Hamiltonian operating on wave function that involves the kinetic energy and the potential energy; the right side is the eigenenergy of the wave function, so this is a typical linear algebra problem. Any state observable in the system is a linear combination of the eigenfunctions with associated weights. However, solving the Schrödinger equation is not easy because of particle interactions. For instance, let one atom has a number of  $N$  electrons, each not just interacts with the nuclei but between themselves. Due to the nature of fermion, two electrons cannot occupy the same quantum state, known as the exchange interaction (or Pauli exclusion principle) [148, 149]. The movement of one electron is inevitably influenced by the presence of all other electrons, known as correlation interaction [150, 151]. The exchange-correlation interactions of electrons suggest that the kinetic energy term and effective potential energy term have many-body effects. The analytical solution to any many-electron element beyond hydrogen is fundamentally difficult. Any practical material has many of them. Putting more atoms in a

box adds the inter-atomic interactions to a new level of complexity. The wave function is practically unsolvable.

The following sections describe the atomistic calculations and structure analyses used in this study. In particular, density functional theory is the first-principles method that solves many-body quantum mechanics, which is used for calculating accurate energetics. Embedded atom method is the semi-empirical method that involves a first-principles calculated or experimentally fitted potential, Newtonian mechanics and molecular thermodynamics, which is often used for studying the dynamics of many-body systems.

### 3.3.1 Density Functional Theory

Density functional theory (DFT) tackles many-body quantum mechanics by electron density functionals. A functional is a function of another function. In this case, the functional is the variations of the system properties (i.e. energy) against the spatial distribution of electron density; hence, the method is known as density functional theory. The ground state energy and electronic structures are obtained via the Hohenberg-Kohn theorem [152]:

1. The wave function is uniquely determined by the electron density.
2. The ground state electron density is the one that minimises the wave function energy and hence determines all the ground state properties.

Solving the wave function from the electron density perspective uses the Kohn-Sham equation [153]:

$$\left[-\frac{\hbar^2}{2m}\nabla^2 + V_{Eff}(\vec{r})\right]\psi_i(\vec{r}) = \epsilon_i\psi_i(\vec{r}), \quad (3.21)$$

$$V_{Eff}(\vec{r}) = V_{Ex}(\vec{r}) + V_H(\vec{r}) + V_{XC}(\vec{r}), \quad (3.22)$$

that involves the kinetic term and the effective potential term similar to that in the Schrödinger equation. The effective potential is composed of the external potential  $V_{EX}(\vec{r})$  that includes the ion-ion Coulomb interaction and electron-ion Coulomb interaction, the electron-electron Coulomb interaction  $V_H$  (Hartree term) and the exchange-correlation effect  $V_{XC}$ . Rather than directly solving the Schrödinger equation, DFT simplifies the problem by searching for the electron density that yields the lowest energy, as long as those quantities are uniquely related. The wave function is solvable if the electron density is known. Meanwhile, the electron density is determined by wave function as  $n=\Psi^* \cdot \Psi$  [147]. Their relationship implies the density functional theory is a self-consistent calculation to solve the many-body quantum mechanics [153].

The essence of density functional theory is solving the Kohn-Sham equation with a self-consistent electron density [154]. Thus, the workflow is iterative as shown in Fig. 3.11. Though the formalism of DFT has been proven to be exact, the practice has to approximate the exchange-correlation interactions because the exact expressions are unknown. Historically, the first tempt is local density approximate (LDA) [155, 156], using local homogeneous electron gas with simple analytical expressions to solve the Kohn-Sham equation. The success of LDA was overwhelming that excited the development of *ab-initio* materials simulation [157]. However, LDA is not a true representation of electron density. For instance, localisation means a large gradient of electron density, hence an overestimated kinetic energy. As a consequence, LDA usually has an over-binding problem with an underestimated bond length and an overestimated bond energy. General gradient approximation (GGA) takes the gradient of the charge density into consideration. As a more semi-localised functional, GGA usually gives better ground state structures and energies than LDA [158]. Meta-GGA [159] and hybrid method [160] exist but are less commonly used due to their computational costs.

Selecting the right exchange-correlation functional is crucial for DFT calculations. Besides the density approximations mentioned above, one has to decide how to sample the electron density: in the real space or the reciprocal space? For the real space sampling, localised orbitals method treat electrons in their orbitals, which is advantageous for large systems as the computation complexity scales linearly with the system size,  $N$ , as  $O(N)$ . However, the localisation sacrifices the accuracy. In addition, choosing the basis sets of the orbitals is not trivial that their completeness and superposition errors are not guaranteed [161]. For the reciprocal space sampling, the plane wave method is a natural choice according to the Bloch theorem. The detailed electronic structure in the real space can be easily explored with the high-frequency waves in the reciprocal space, though the computation complexity scales with the system size as  $O(N^3)$ . It is because the atomic potentials perturb increasingly when approaching to the core. As a result, those nodal functions require a large basis set of waves to construct. Given a significant computation effort, however, the core electrons do not contribute to the bonding and hence most of the materials properties [162]. Thus, using pseudopotentials is a common practice that only fits the potential beyond the selected "core radius" and neglects the core. The core electrons are pre-calculated in an atomic environment and kept "frozen" for further calculations. Historically, norm-conserving pseudopotential [163] and ultrasoft pseudopotential [164] were used. However, those pseudopotential schemes were found to be problematic if the atomic environment in an actual calculation deviates away from the reference where the potentials were constructed [165]. This problem inspired the development of the plane augmented wave method (PAW) [166, 167]. PAW approximates the potential with the pseudopotential handling the valence electrons and exact potentials

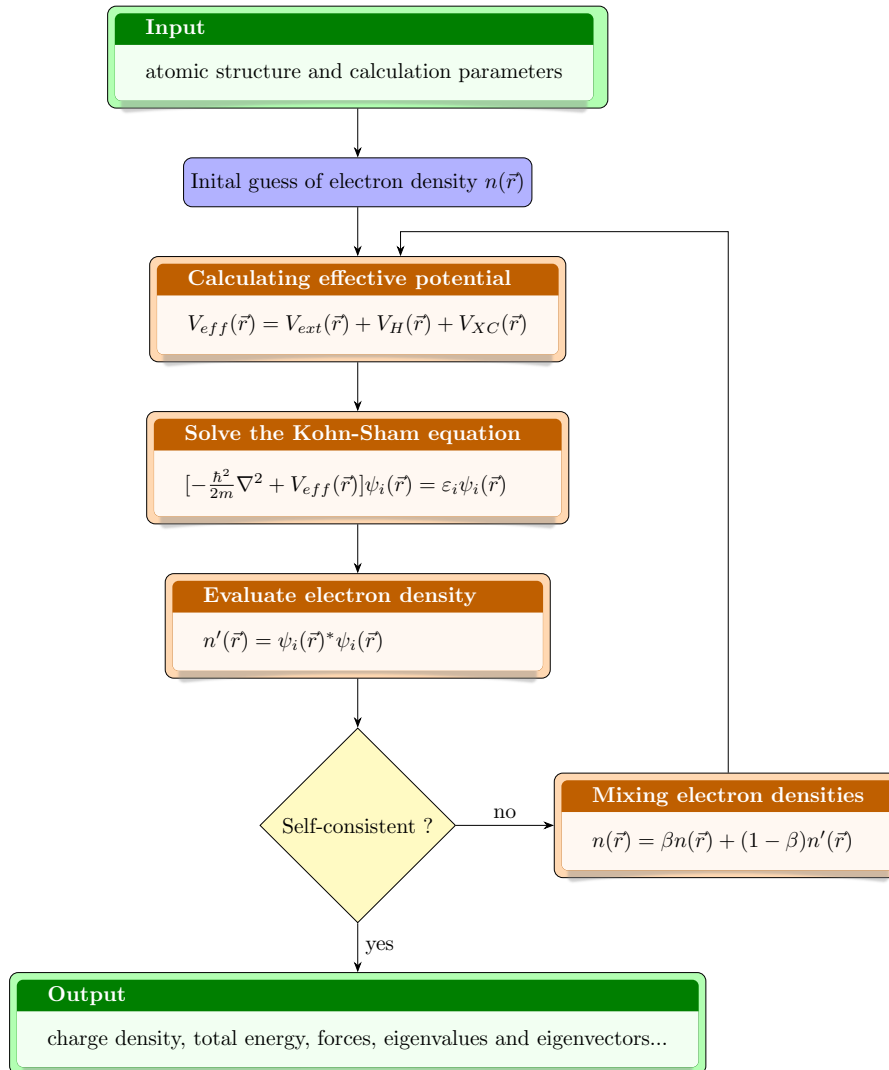


Fig. 3.11 The workflow of density functional theory calculations. At first, a trial density  $n(\vec{r})$  is proposed with the input atomic structures, which is used to construct the effective potential  $V_{eff}(\vec{r})$ . The Kohn-Sham equation is solved with the effective potential, which yields the wave function  $\psi_i(\vec{r})$  and the corresponding energy  $E_{tot}[n(\vec{r})]$ . As long as the electron density  $n'(\vec{r})$  calculated from the wave function does not converge with the input  $\rho(\vec{r})$ , the procedure is continued with the mixed electron density as the new input and loop again. When the two electron densities are self-consistent, the calculation is finished with the output quantities.

handling the core electrons [167]. Recently, the DFT community has examined the reliability of the Perdew-Burke-Ernzerhof (PBE) exchange-correlation density functional for various elements [168], showing a good agreement in different code implementations. In particular, PBE-PAW is highly efficient with an accuracy comparable with the result from all-electron scheme [168].

In a practical DFT calculation, the computation parameters need to be wisely chosen to balance the accuracy and efficiency. For plane-wave DFT calculations, they determine the sampling in the Brillouin zone (BZ): the primitive cell in the reciprocal space [154]. There are several things to be considered:

(a) As the quantum state is uniquely related to the charge density, a great deal of the calculations is about evaluating the charge density in the real space via integral in the reciprocal space as:

$$\bar{n} = \frac{V_{cell}}{(2\pi)^3} \int_{BZ} n(\vec{k}) d\vec{k}, \quad (3.23)$$

where  $V_{cell}$  is the volume of the primitive cell in the real space. Numerically, the integration is simplified as the sum of discrete points, known as k-points, as:

$$\int_{BZ} n(\vec{k}) d\vec{k} \approx \sum_{j=1}^n C_j n(\vec{k}), \quad (3.24)$$

where  $C_j$  is the coefficient for the  $j$ -th k-point. Therefore, for a calculation of a cubic crystal with  $M \times M \times M$  k-points, the more k-points are, the more accurate results will be, though with an increased computational cost. However, one can save some cost by considering the fact that crystals have symmetries. It means that we can evaluate a reduced portion of the zone – known as the irreducible Brillouin zone (IBZ) – to represent the entire BZ [154].

(b) There are two different approaches to distribute the k-points in BZ: the Monkhorst-Pack method [169] and gamma method [154]. The difference between them is gamma method always includes the origin of the BZ as the  $\Gamma$  point. In contrast, only odd k-points in the Monkhorst-Pack method include the  $\Gamma$  point. The difference is important when sampling the IBZ with even k-point mesh for a hexagonal lattice, in which case the Monkhorst-Pack method results in non-equally distributed k-points in BZ after the rotation symmetry operation [154].

(c) Metals have a sharp Fermi surface that separates the occupied and unoccupied electron states [154]. The discontinuous function brings a complication for k-point sampling at the Fermi surface. A number of methods have been developed to solve this problem. For example, the smearing method smears the step function into a smooth function with a smearing factor [170]. The tetrahedron method defines a set of tetrahedra that fill the reciprocal space according to the discrete k-points [171]. The values within each tetrahedron are interpolated for integration. The smearing method is fast for structure relaxations, while the tetrahedron method yields accurate results for energy calculations.

(d) According to the Bloch theorem, the solution to the Schrödinger equation for a crystal has the form of [154]:

$$\psi_{\vec{k}}(\vec{r}) = \exp[i\vec{k} \cdot \vec{r}] \phi_{\vec{k}}(\vec{r}), \quad (3.25)$$

where  $\phi_{\vec{k}}(\vec{r})$  has the same periodicity as the crystal structure, which can be expanded as:

$$\phi_{\vec{k}}(\vec{r}) = \sum_{\vec{g}} C_{\vec{g}} \exp[i\vec{g} \cdot \vec{r}], \quad (3.26)$$

where  $\vec{g}$  is the reciprocal lattice vector. Combining Eq. 3.25 and Eq. 3.26, the wave function is expressed as:

$$\psi_{\vec{k}}(\vec{r}) = \sum_{\vec{g}} c_{\vec{k}+\vec{g}} \exp[i(\vec{k} + \vec{g})\vec{r}]. \quad (3.27)$$

Evaluating the wave function at each position in the real space involves summing all possible  $\vec{G}$  in the reciprocal space, which is computationally expansive. The kinetic energy for the wave function in Eq. 3.27 has a simple form as:

$$E_{kinetic} = \frac{\hbar^2}{2m} |\vec{k} + \vec{g}|^2. \quad (3.28)$$

The solution is largely characterised by low energy waves. Thus, it allows us to truncate the infinite summation with a threshold energy, known as the energy cut-off [154] as:

$$E_{cut} = \frac{\hbar^2}{2m} g_{cut}^2, \quad (3.29)$$

$$\psi_{\vec{k}}(\vec{r}) = \sum_{|\vec{k}+\vec{g}| < g_{cut}} c_{\vec{k}+\vec{g}} \exp[i(\vec{k} + \vec{g})\vec{r}]. \quad (3.30)$$

Note that the Bloch wave theorem is universal in both electron diffraction simulation in Section. 3.2.6 and in density functional theory calculation presented here. They all include a finite number of electron beam reflections or energy cut-off for the calculation efficiency. The only difference is that the electron diffraction simulation does not include the exchange-correlation effects: (I) it treats the crystal potential as a superposition of independent atoms; (II) the fast electron is scattered by such potential without exchanging or correlating with the electrons belong to atoms. In contrast, density functional theory has to include the exchange-correlation effects to yield accurate energy calculations or electronic structures.

There are other parameters that are beyond short description here. But in general, one needs to check the convergence of the k-points and energy cut-off for accurate and efficient DFT calculations.

In this study, DFT calculations were performed using the Vienna *Ab initio* Simulation Package (VASP) [172]. We used the potentials supplemented with the VASP, constructed from the generalised gradient approximation of Perdew, Burke, and Ernzerhof (GGA-PBE) [158] using the projector augmented wave (PAW) method [166, 167]. Geometrical relaxations were performed to optimise the supercells until Hellmann-Feynman forces were less than 0.01 eV/Å, using Methfessel-Paxton method [170] with a smearing factor of 0.05 eV. All lattice parameters and all internal coordinates were optimised if not stated otherwise. Single-point energy calculations were performed using tetrahedron method with Blöchl corrections [171]. K-points in the Brillouin zone were sampled using the gamma method. The convergence of the relevant energy differences with respect to energy cut-off (500 eV), k-point sampling ( $\sim 2000/\text{atom}^{10}$ ) and supercell size (separation  $\approx 2$  nm for non-periodic structures) was better than 1 meV/atom. Fig. 3.12 shows the convergence tests for FCC Al and Ag and HCP  $\text{Ag}_2\text{Al}$ .

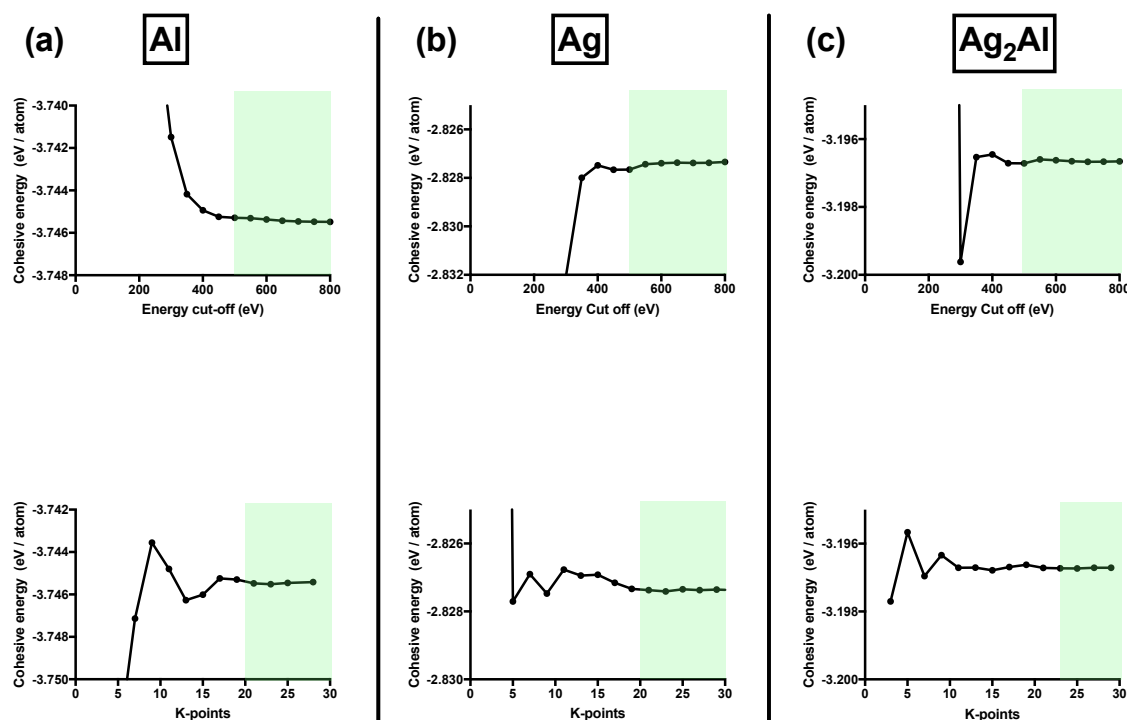


Fig. 3.12 Cohesive energy as a function of energy cut-off and k-point sampling for (a) Al, (b) Ag and (c)  $\text{Ag}_2\text{Al}$ , where green shaded regions indicate a good convergence ( $\ll 1$  meV/atom) with the selected energy cut-off (500 eV) and k-points ( $\sim 2000/\text{atom}$ ).

The formation energies of different phases are given relative to the energy of FCC Al and Ag in the ground state. For the Al-Ag system with  $n$  Ag atoms and  $m$  Al atoms, the

<sup>10</sup>The 4-atom unit cells of FCC Ag and Al were sampled with  $20 \times 20 \times 20$  k-points; the value was scaled linearly for other systems. Note that our k-points are over-sufficient which can be reduced in a future study.

Table 3.2 Lattice parameters and energetics of different phases in the Al-Ag alloy system.

Phase	Lattice Parameters (Å)			Cohesive Energy (eV/atom)		Formation Energy (eV/atom)	
	Experiment	Previous DFT	This work	Previous DFT	This work	Previous DFT	This work
Al	4.046 <sup>a</sup>	4.039 <sup>d</sup> , 3.98 <sup>f</sup>	4.050	-3.748 <sup>d</sup>	-3.745	0	0
Ag	4.079 <sup>a</sup>	4.161 <sup>d</sup> , 4.02 <sup>f</sup>	4.161	-2.832 <sup>d</sup>	-2.827	0	0
Ag <sub>2</sub> Al	a=2.858 <sup>b</sup> c=4.607 <sup>b</sup>	a=2.922 <sup>d</sup> , 2.850 <sup>e</sup> c=4.618 <sup>d</sup> , 4.546 <sup>e</sup>	a=2.890 c=4.600	-3.208 <sup>d</sup>	-3.209	-0.071 <sup>d</sup> , -0.121 <sup>e,f</sup>	-0.075
AgAl	a=2.88 <sup>c</sup> c=27.35 <sup>c</sup>	N/A	a=2.97 c=26.88	N/A	-3.331	N/A	-0.044

- a. X-ray measurements, taken from Ref. [173].  
b. X-ray measurements, taken from Ref. [68].  
c. Our HAADF-STEM measurements [174].  
d. PBE-GGA calculations, taken from Materials Genome Project [175].  
e. Ultrasoft-LDA calculations, taken from Ref. [176].  
f. Ultrasoft-LDA calculations, taken from Ref. [87].

formation energy is defined as:

$$E_{\text{F}}^{\text{nAg+mAl}} = E_{\text{tot}}^{\text{nAg+mAl}} - nE_{\text{atom}}^{\text{Ag}} - mE_{\text{atom}}^{\text{Al}} \quad (3.31)$$

Where  $E_{\text{F}}^{\text{nAg+mAl}}$  is the formation energy of certain structure,  $E_{\text{tot}}^{\text{nAg+mAl}}$  is the total energy of the system,  $E_{\text{atom}}^{\text{Ag}}$  and  $E_{\text{atom}}^{\text{Al}}$  are the energy per atom for FCC Ag and Al lattices respectively. The formation energy per Ag atom  $E_{\text{F}}^{\text{Ag}}$  is defined as:

$$E_{\text{F}}^{\text{Ag}} = E_{\text{F}}^{\text{nAg+mAl}} / n. \quad (3.32)$$

The defect energy of Ag in solid solution was calculated by an isolated Ag substitutional point defect in an Al supercell containing 108 atoms, giving a substitutional defect energy of 0.09 eV, in reasonable agreement with previous calculations of 0.02 eV using the local density approximation (LDA) [88]. The formation energies of Ag clusters, including di-atom clusters and tri-atom clusters, were also calculated using a 108-atom Al supercell with Ag substitutions in different configurations. Planar Ag-Al structures were modelled using tetragonal or trigonal supercells in which the precipitates were surrounded above and below by Al (representing the infinitely wide two-dimensionally coherent Ag plane(s) surrounded by Al matrix), containing the equivalent of 20-24 atomic planes ( $\{001\}_{\text{Al}}$ ,  $\{110\}_{\text{Al}}$  or  $\{111\}_{\text{Al}}$ ). Sufficient numbers of Al atomic layers were used to simulate the effect of an infinitely large Al matrix. The newly discovered  $\zeta$  phase was investigated by assuming each bilayer was pure Ag or Al, which resulted in a composition of AgAl. The embedded  $\gamma'$  phase and  $\zeta$  phase were calculated by the sandwiched structure of AgAl with the Al matrix using the supercell

as described above. The bulk  $\gamma'$  phase was calculated using the model by Neumann [68] with lattice parameters constrained to experimental measurements [70]. The bulk phases of Al, Ag,  $\zeta$  (AgAl) and  $\gamma$  (Ag<sub>2</sub>Al) were fully optimised; their calculated lattice parameters and formation energies were consistent with previous experiments [68, 69], calculations [88, 176] and database of Materials Genome Project [175], see Table 3.2. In particular, Materials Genome Project used the same exchange-correlation functional (PBE-GGA) as this study and similar calculation parameters (energy cut-off of 520 eV and k-point  $\sim 1000/\text{atom}$ ) that make the results comparable (energy differences  $< 5 \text{ meV/atom}$ ).

### 3.3.2 Embedded Atom Method

The embedded atom method (EAM) approximates the energy of a group of atoms by their separations from neighbour atoms with an inter-atomic potential [177]. The inter-atomic potential includes (1) an embedding term that embeds atom with the electron cloud, and (2) a pair-wise term that accounts for the interaction between two or more atoms as follow:

$$E_{tot} = \sum_i E_i, \quad (3.33)$$

$$\sum_i E_i = F_i(\bar{\rho}_i) + \frac{1}{2} \sum_{j(j \neq i)} \phi_{ij}(R_{ij}), \quad (3.34)$$

where  $E_{tot}$  is the total energy of the system,  $E_i$  is the energy of atom  $i$ ,  $F_i$  is the embedding potential as a function of electron density,  $\bar{\rho}_i$  is the superposition of electron density at the site of atom  $i$ ,  $\phi_{ij}$  is the pair wise potential between atom  $i$  and  $j$ , and  $R_{ij}$  is the distance that separates them. Symmetries of  $s$ ,  $p$ ,  $d$ ,  $f$  electrons were added to the modified embedded atom method (MEAM), which gives the angular dependency to the inter-atomic potentials [178]. EAM is particularly useful for studying defects in the metallic system [177].

In this study, EAM has been used to study the evolution of dislocation loops and precipitate interfaces, which was implemented in Large-scale Atomic/Molecular Massively Parallel Simulator (LAMMPS) [179]. We used the DFT-fitted inter-atomic potential of Al-Ag specified in Ref. [180]. For dislocation loops, the modelling cell consists of a rectangular box with periodic boundary conditions, filed with FCC Al-1.7 at.% Ag (by random replacement). The box had a size of  $99\text{\AA} \times 98\text{\AA} \times 80\text{\AA}$ , in  $[11\bar{2}]_{\text{Al}}$ ,  $[111]_{\text{Al}}$  and  $[1\bar{1}0]_{\text{Al}}$  respectively, containing 31360 atoms. A vacancy disk of trigonal shape and hexagonal shape were drilled at the centre of the box, on  $\{111\}_{\text{Al}}$  planes to simulate the Frank dislocation loop ( $\vec{b} = 1/3\langle 111 \rangle$ ). The initial vacancy disk with over 100 vacancies can generate a reliable structure [181]. For precipitate interfaces, the modelling cell consists of a rectangular box with periodic boundary conditions, filed with FCC Al and HCP Ag<sub>2</sub>Al phases with atomic positions determined by

HAADF-STEM experiments. Energy and force relaxations were performed for each structure to study the evolution of dislocation loops and precipitate interfaces. The crystal structures were recognised with common neighbour analysis [182], explained in Section. 3.3.3. Dislocation analysis was performed using dislocation extraction algorithm [144], explained in Section. 3.3.4. Both common neighbour analysis and dislocation extraction algorithm were implemented in the Ovito software [145].

### 3.3.3 Local Structure Identification

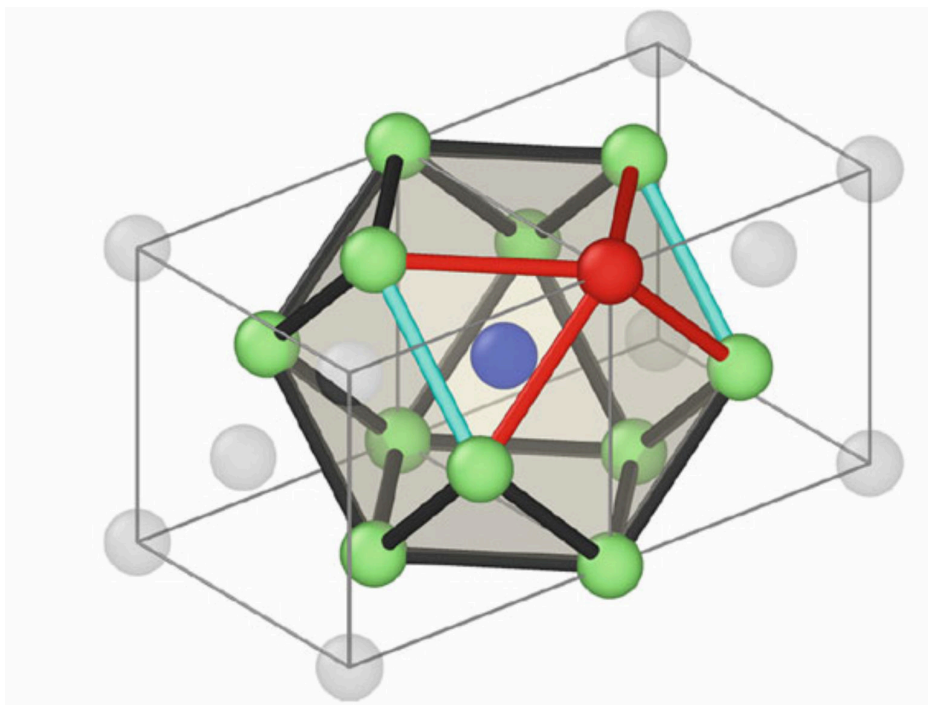


Fig. 3.13 Illustrating the common neighbour analysis index for the FCC structure. Each FCC atom has 12 nearest neighbours (coloured in green) and every neighbour has 4 bonds (coloured in red) to other neighbours of the central atom. Those 4 bonded neighbour-neighbour atoms have 2 bonds connecting between them (coloured in light blue), and the maximum length of those two bonds is 1. Reprinted from Ref. [183], p.327 with permission from Springer.

Understanding the atomic mechanisms of phase transformations requires identification of the local, atomic-level structures. In other words, we need to know the classification of atoms during phase transformations. This requires an algorithm to distinguish different phases and lattice defects. Usually, contentious order parameters like centrosymmetry parameter are used to evaluate the local arrangement of atoms. However, they become problematic when different structures are mapped to the same value [183]. Discrete order parameters were

developed to solve this problem and a popular choice is the common neighbour analysis employed in this study.

Common neighbour analysis characterises the topology of local bond networks for each atom and its neighbour atoms. The local bond networks are defined by atoms within a cut-off distance. For close-packed structures (FCC and HCP), this cut-off distance is chosen to be the half-way between the first and the second nearest neighbours atoms. For each atom, a triplet index  $(n_{cn}, n_b, n_{lc})$  is computed, with

- $n_{cn}$ : the number of common neighbour between the central atom and its neighbour atoms,
- $n_b$ : the number of bonds between the common neighbour atoms,
- $n_{lb}$ : the number of bonds in the longest continuous chain of bonds between the common neighbour atoms

As shown in Fig. 3.13, FCC atoms have 12 neighbours yielding the same index of (4, 2, 1) [183]. In contrast, HCP atoms have 6 neighbours with the index of (4, 2, 2) and 6 neighbours with the index of (4, 2, 1) [183]. Using the common neighbour analysis, we can systematically distinguish between FCC and HCP structures in complicated structures.

### 3.3.4 Dislocation Identification

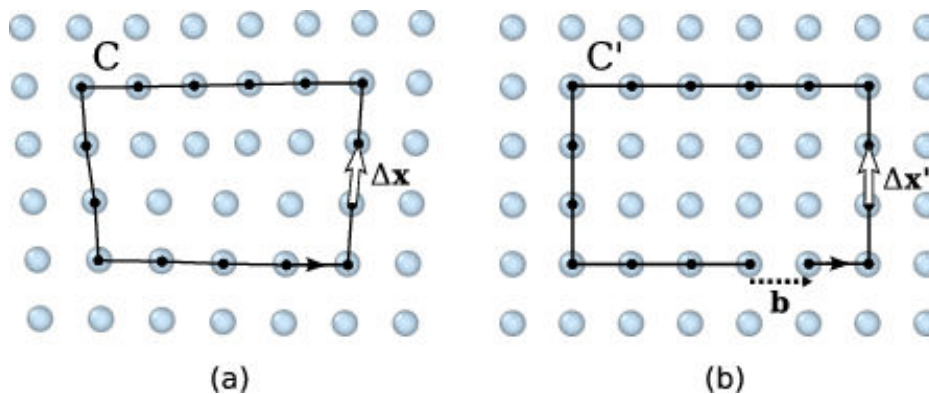


Fig. 3.14 Burgers circuit method to identify a dislocation and its associated Burgers vector. A closed circuit around a dislocation in (a) is mapped to the perfect crystal in (b). The closure failure defines the Burgers vector. Reprinted from Ref. [183] p.331 with permission from Springer.

As reviewed in Chapter 2, dislocation plays a critical role during the FCC-HCP phase transformations in Al-Ag alloys and many other precipitation systems in general. It is

important to identify the positions of dislocations and their associated Burgers vectors. Traditionally, this is done by constructing Burgers circuit [184] on 2D lattice images obtained from high-resolution electron microscopy or atomistic calculations. As shown in Fig. 3.14, dislocation is essentially a failure of closing the Burgers circuit when mapping the vector loop  $C$  in the dislocated crystal to the vector loop  $C'$  in the perfect crystal. The Burgers vector of the dislocation is thus defined as:

$$\vec{b} = - \sum_{C'} \Delta \vec{X}'. \quad (3.35)$$

However, it is tedious to manually construct Burgers circuit for each atom. Human intuition is needed to identify dislocated regions from perfect crystals. For complicated heterophase interface, this intuition is prone to errors. Therefore, we used the dislocation extraction algorithm [144] to systematically identify dislocations in experimentally-informed interface models (see Section. 3.2.8).

The core task of dislocation extraction algorithm is guiding the construction of Burgers circuit efficiently [183]. In other words, the algorithm should be able to distinguish the dislocated region and calculate the associated Burgers vector. The classification of perfect crystal and defected crystal is assisted by common neighbour analysis described earlier. The calculation of Burgers vector is performed by Delaunay tessellation, which connects the discrete lattice points in space such that no point is inside the circumcircle/circumsphere of any tessellation (triangle for 2D lattice, tetrahedron for 3D lattice) [183].

As shown in Fig. 3.15(a-c), common neighbour analysis identified atoms at the dislocation core (coloured in black), which are excluded from perfect tessellation [183]. An interface mesh is constructed as the boundary between the perfect region and defected region, which encloses defects in the crystal. Trial Burgers circuits are constructed on the interface mesh to measure the Burgers vector by summing the ideal lattice vectors defined in tessellation. The algorithm tests all possible circuits up to a prescribed maximum length in the order of increasing circuit length until a non-zero Burgers vector is found. Then this circuit length is used to discover the rest of the dislocation line by sweeping the circuit along the interface mesh, shown in Fig. 3.15(d). An 1D dislocation line is then located by calculating the centre of mass for each circuit. The maximum circuit length is in place to prevent the algorithm missing any dislocation details like kinks and junctions.

In summary, this chapter describes a combination of state-of-art techniques – including alloy processing, electron microscopy and atomistic calculations – to study phase transformations in the Al-Ag system.

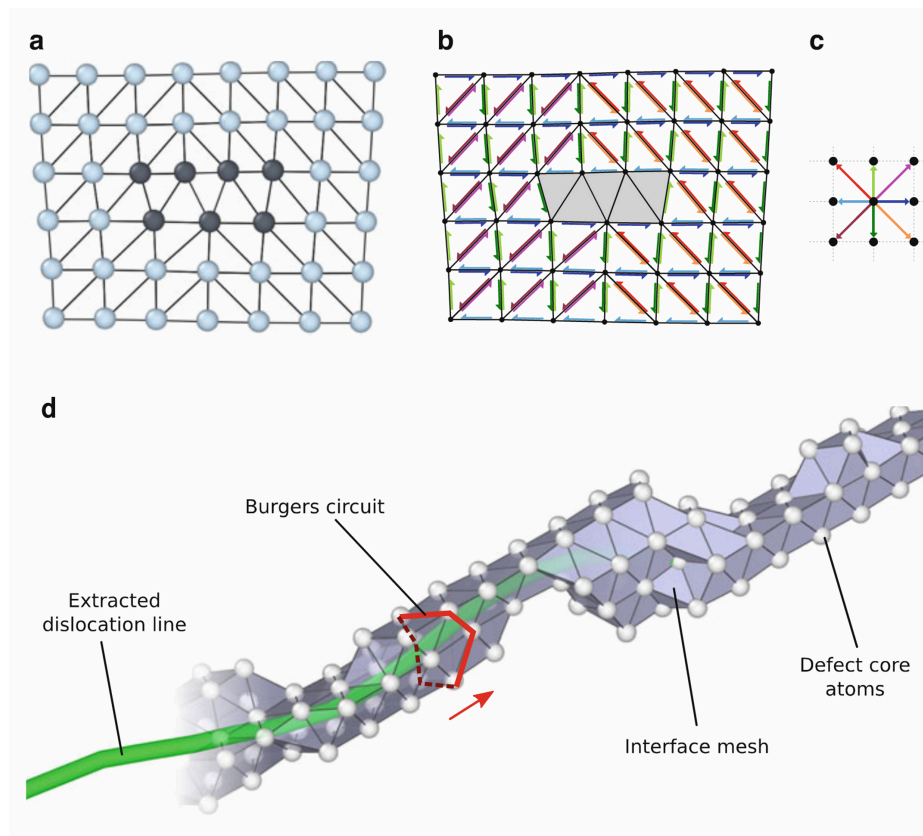


Fig. 3.15 Illustration of dislocation extraction algorithm. (a) Delaunay tessellation of a dislocated crystal with the core atoms coloured in black, as identified by common neighbour analysis. (b) Delaunay tessellation is highlighted by coloured arrows indicating the corresponding perfect lattice vectors. The grey region indicates the defected crystal which cannot map to the perfect reference lattice in (c). (d) Sweeping of the Burgers circuit in a step-wise manner – triangle by triangle on the interface mesh – resolves the continuous dislocation line. Reprinted from Ref. [183] p.333,334 with permission from Springer.

# Chapter 4

## Modifying Phase Transformation Pathways through the Interaction Between Defects and Pre-existing Phases

### 4.1 Introduction

In the preceding review, it was highlighted that defects often assist phase transformations in terms of both diffusion and structural transformations. In particular, the FCC-HCP transformation requires the dissociation of defects into Shockley partial dislocations for the formation of  $\gamma'$  phase in Al-Ag alloys. Thus, defects are added deliberately via thermal and mechanical processing prior to or during artificial ageing to promote precipitation. In addition, defects also trigger precipitation in the supersaturated solute solid matrix during fatigue – known as dynamic precipitation. However, our current knowledge of the interactions between defects and pre-existing precipitate phases are highly limited. This chapter examines defects in an Al-Ag alloy and their role during phase transformations. Specifically, we used HAADF-STEM to characterise alloy microstructures under different ageing conditions. We accidentally found a rare layer-structured phase within a GP zone  $\epsilon$ . An in-situ annealing experiment of a pre-aged TEM alloy foil surprisingly reproduced this ordered structure from pre-existing GP zones. This unusual phenomenon inspired us to develop a bulk processing scheme to confirm the proposed mechanism of defect-induced phase transformation, which is relevant to the thermomechanical processing in manufacture industry and the durability of alloy components during their servicing. This study demonstrated that defects can be manipulated to tailor the precipitation behaviours and even change the transformation pathways in the classic Al-Ag alloy system.

This chapter begins with the microstructure overview obtained from conventional heat treatments in Section. 4.2.1, which involves the precipitate phase  $\gamma'$  and GP zones  $\epsilon$ . Section. 4.2.2 describes the geometries of the  $\gamma'$  precipitate assemblies with electron tomography and atomistic simulations. Section. 4.2.3 describes GP zones in the as-quenched state and during ageing with different heat treatments.

In Section. 4.3, defects were introduced in alloys with nanoscale and bulk processing, where large GP zones were in place as a pre-existing phase. Section 4.3.1 describes the nanoscale treatment by *in situ* annealing of the thin TEM foils. Section 4.3.2 describes the bulk treatment through deforming the pre-aged alloys and performing secondary ageing. A new ordered phase was found in both approaches.

Part of the results in this chapter was published in Ref. [174].

## 4.2 The Microstructure of Conventional Heat Treatments

### 4.2.1 Overview

An Al-1.68%Ag alloy aged at 200°C for times varying from as-quenched to 15 days exhibited the microstructure expected from previous studies [77]: finely distributed Ag-enriched coherent precipitates known as GP zones and sparsely distributed  $\gamma'$  precipitates. Fig. 4.1(a) shows a typical view of the alloy quenched in water and aged at 200°C for 2 h. The  $\gamma'$  precipitates were present in the shape of structured assemblies, in agreement with previous findings [77]. Fig. 4.1(b) confirms that  $\gamma'$  precipitates have an ABAB... stacking embedded in the FCC aluminium matrix with ABCABC... stacking. The  $\gamma'$  precipitates displayed the expected orientation relationship of  $\{111\}_{\text{Al}} \parallel \{0001\}_{\gamma'}$  and  $\langle 110 \rangle_{\text{Al}} \parallel \langle 11\bar{2}0 \rangle_{\gamma'}$  with an exceptionally good lattice matching with aluminium [69, 185]. Fig. 4.1(c) shows chemical inhomogeneity within the GP zones  $\epsilon$ , where the darker columns correspond to Ag depletion in Al. This observation is consistent with earlier X-ray [62] and STEM results [186] that showed Ag depletes in the core and enriches in the shell. However, the detailed structure of  $\epsilon$  can be considered as a “sponge-like” distribution of Ag, rather than the simple model with one core as proposed previously [62]. These GP zones  $\epsilon$  are likely the growth product of small Ag clusters. Fig. 4.1(d) shows that small Ag enriched clusters with few atoms readily existed in the as-quenched state due to decomposition, in agreement with work published over 50 years ago [53].

Ageing the alloy below the  $\eta$ - $\epsilon$  transition temperature revealed GP zone  $\eta$  with homogeneous Ag distribution and  $\gamma'$  precipitate assemblies which agree with previous studies [61]. In contrast, ageing the alloy at 300°C (above the GP zone solvus at Al-1.7 % Ag) only

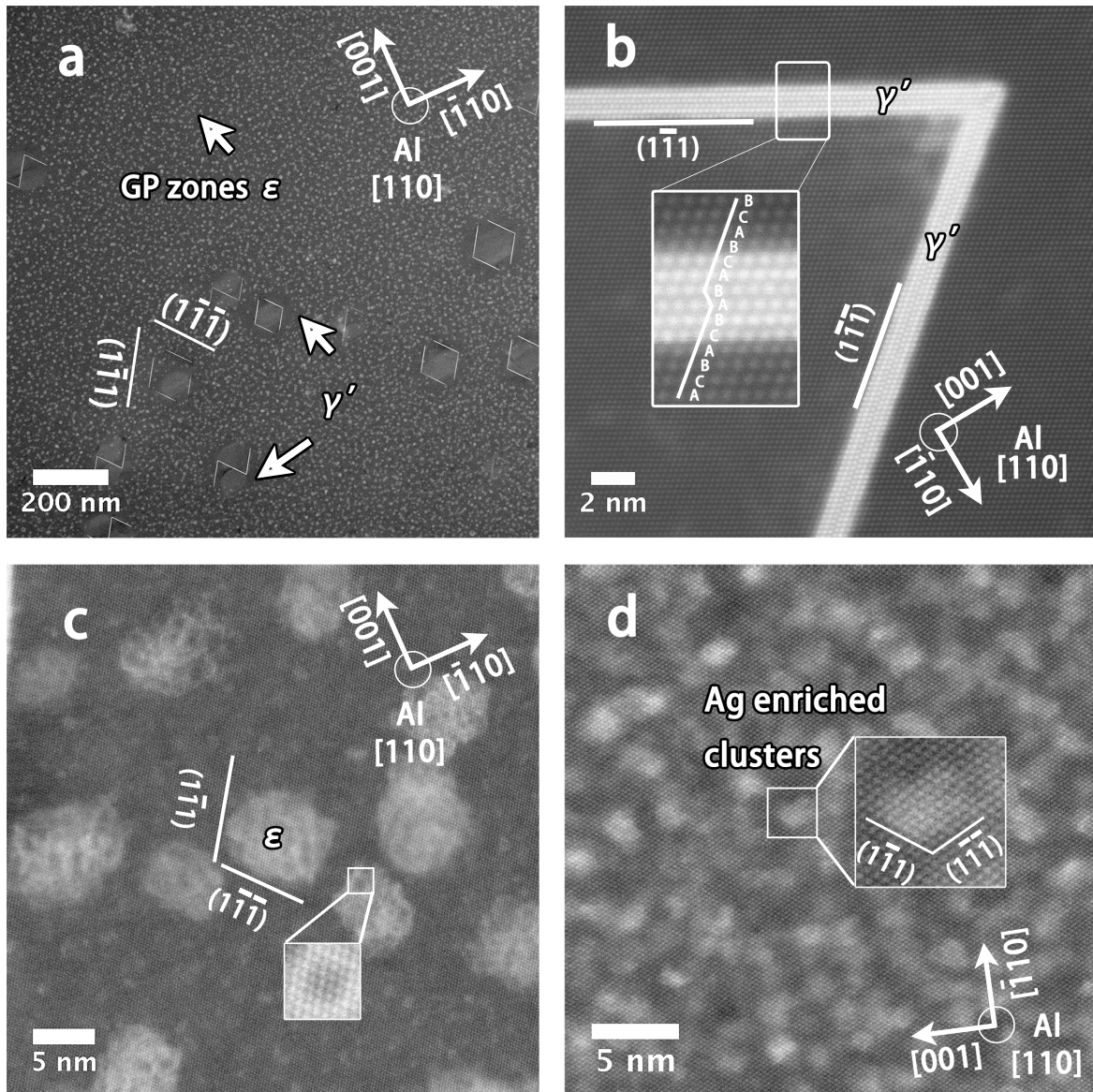


Fig. 4.1 HAADF-STEM images of the typical microstructure for Al-1.68 at.% Ag aged 2 h at 200°C after water quenching. (a) Low magnification image of  $\gamma'$  precipitate assemblies and GP zones; (b) high magnification image showing a  $\gamma'$  precipitate with the enlarged inset illustrating the characteristic stacking fault associated with a HCP precipitate (AB... stacking) embedded within the FCC matrix (ABC... stacking); (c) high magnification images showing the  $\epsilon$  GP zones with the enlarged inset show the Ag depletion area inside a GP zone. (d) High magnification image of small Ag clusters formed in the as-water-quenched state. The electron beam is parallel to  $\langle 110 \rangle_{\text{Al}}$ .

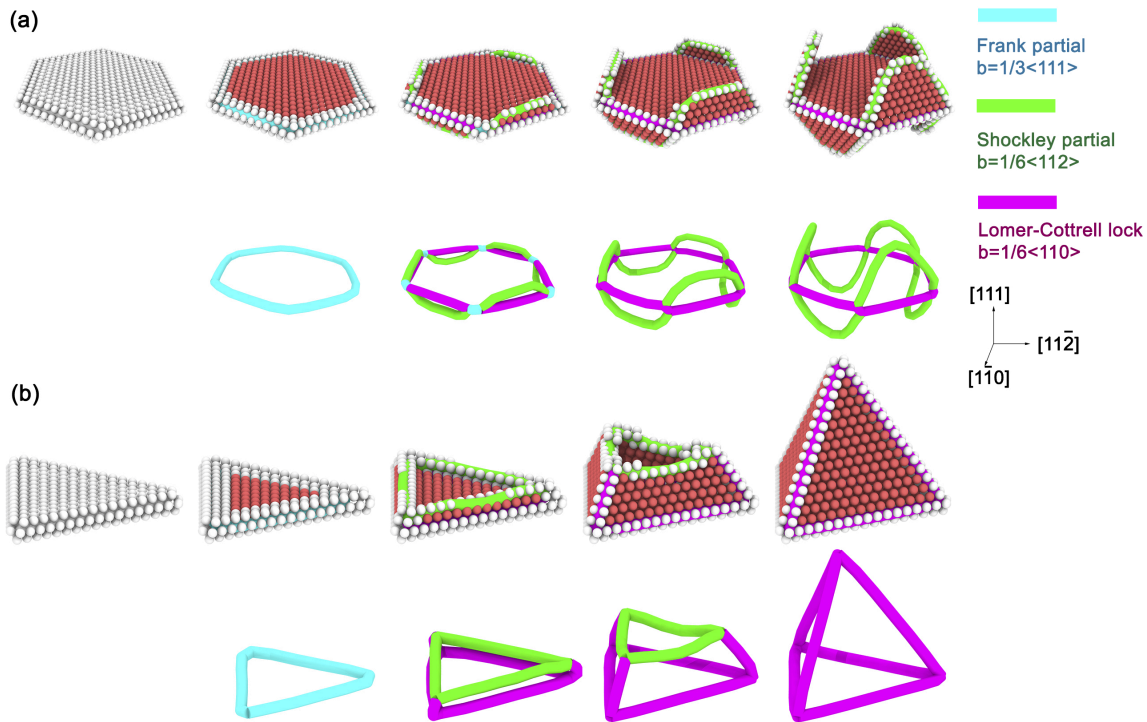


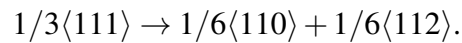
Fig. 4.2 Simulations of dislocation reaction for Frank dislocation loops ( $\vec{b} = 1/3\langle 111 \rangle$ ) in an Al-Ag alloy. (a) Formation of stacking fault quasi-bi-tetrahedron from a hexagonal vacancy disk. (b) Formation of stacking fault tetrahedron from a trigonal vacancy disk. The local crystal structure was recognised by common neighbour analysis [145]. Atoms at FCC sites were deleted for visualising the defect structure, while atoms at HCP sites were coloured in red, and atoms with the coordinate number other than 12 were coloured in white. The Frank partial dislocations were coloured in blue, the Shockley partial dislocations were coloured in green and Lomer-Cottrell dislocations were coloured in purple, as computed by the dislocation extraction algorithm [144].

displayed quenched-in Ag clusters and large individual  $\gamma'$  precipitate plate which agrees with Ref. [75]. Since those observations are well-recorded in the literature [61, 84, 187], we will concentrate on the microstructure obtained by 200°C ageing in the following sections.

#### 4.2.2 Nucleation and Growth of $\gamma'$ Precipitate Phase

Previous TEM studies [78] using dark field imaging ( $\vec{g} \cdot \vec{b}$  analysis) showed that the  $\gamma'$  precipitate assemblies heterogeneously nucleate on the quenched-in Frank dislocation loop ( $\vec{b} = 1/3\langle 111 \rangle$ ). The detailed dislocation reaction associated with the assembly nucleation is now explained with the embedded atom method (EAM) simulations. A supercell of Al-1.7 at.%Ag in solid solution was constructed by randomly replacing Al with Ag according to the composition. The hexagonal and trigonal vacancy disks were constructed by removing

atoms on the close-packed planes. These two structures were optimised with EAM using a semi-empirical potential at 0 K. As shown in Fig. 4.2, the collapse of the vacancy disks on the close-packed plane gave rise to the Frank partials ( $\vec{b} = 1/3\langle 111 \rangle$ ). This process changed the atomic stacking from FCC to HCP, which formed the central HCP plate. However, the Frank partial dislocations were found to be not stable as associated with a larger strain energy that they dissociated into the sessile Lomer-Cottrell dislocations ( $\vec{b} = 1/6\langle 110 \rangle$ ) and glissile Shockley partial dislocations ( $\vec{b} = 1/6\langle 112 \rangle$ ) via:



The Shockley partial dislocations cross-slipped to new close-packed planes while Lomer-Cottrell dislocations locked the junction between the central HCP plate and the peripheral HCP plates. There was only one intrinsic stacking fault (relative to the FCC matrix) for each HCP plate that determined the minimum thickness of  $\gamma'$  precipitate during nucleation. The final geometry of the assembly depends on the initial shape of Frank dislocation loop. For a hexagonal loop, Fig. 4.2(a), it evolved into a stacking fault quasi truncated bi-tetrahedron with seven stacking fault plates: one hexagonal plate in the centre and three peripheral plates facing up and alternating three plates facing down. Such quasi truncated bi-tetrahedron displays a hexagonal symmetry (point group:  $\bar{3}2/m$ ), which is the highest point symmetry in the trigonal system [188]. The trigonal loop developed into a stacking fault tetrahedron (point group: 332), Fig. 4.2(b). The results presented therein Al-Ag alloys agree with the previous molecular dynamics study of Frank dislocation loops in pure Ag [188].

The atomic mechanisms of dislocation reaction determine the precipitation geometry evolution during ageing the alloy. Fig. 4.3(a) shows an electron tomography reconstruction of the microstructure after ageing at 200°C for 2 hr. Most of the precipitate assemblies were indeed truncated bi-tetrahedron, such as one highlighted in the centre of the reconstruction. The peripheral plates were fully developed into a hexagonal shape that impinged each other and completed the truncated tetrahedron geometry. Interestingly, the corners of the geometry were still open as triangular “windows”. This complicated geometry can be visualised as the combination of two truncated tetrahedra with one sharing facet and 60° relative rotation, see Fig. 4.3(a).

The tetrahedron assemblies, in contrast, were less common with two examples in Fig. 4.3(a) and (c). This is because the defect formation energy associated with the trigonal loop is much higher than the hexagonal loop [188]. Examination of the early stage microstructure revealed that the peripheral plates were still in development, as highlighted with green arrows in Fig. 4.3(b). The driving force for the peripheral plate developments is the formation of HCP precipitate phase that lowers the system enthalpy. The excellent agreement

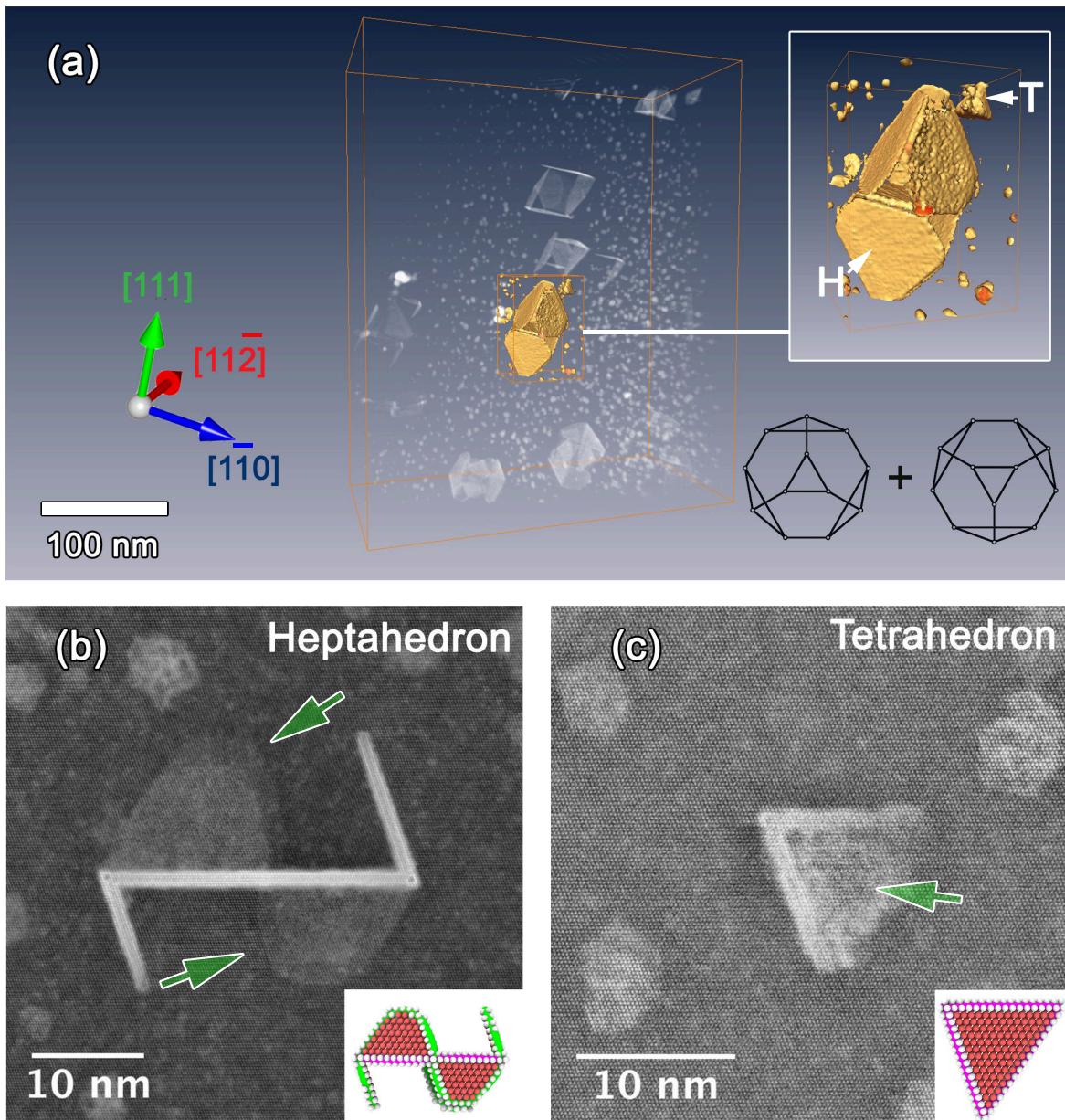


Fig. 4.3 The topology of the  $\gamma'$  precipitate assemblies. (a) Electron tomography of the microstructure in an Al-1.68 at.% Ag aged 2 h at 200°C after water quenching. The precipitate assemblies in the centre of the reconstructed volume are highlighted by rendering the isosurface, showing a truncated bi-tetrahedron assembly labelled as BT, and a tetrahedron assembly labelled as T in the image. The geometry of a truncated bi-tetrahedron is illustrated with two truncated tetrahedron (one facing up, one facing down) with 60° rotation. (b-c) Comparing the precipitate assemblies between the early stage microstructure (aged at 200°C for 30 min) and the simulations viewed along a  $\langle 110 \rangle_{\text{Al}}$  zone axis. The green arrows indicate the precipitate plates tilting  $\pm 60^\circ$  from the viewing direction.

between the simulations and the experiments consolidates our proposed atomic mechanisms for the heterogeneous nucleation of  $\gamma'$  precipitate assemblies on Frank dislocation loops.

The evolution of the  $\gamma'$  precipitate phase was examined as a function of time at 200°C. Fig. 4.4 shows the precipitate assemblies were gradually replaced by large individual  $\gamma'$  plates, which grew in both length and thickness directions. Chapter 6 will characterise the interfacial structures of the  $\gamma'$  plates in details.

The precipitate assemblies, in contrast, **did not coarsen** throughout the ageing time. Fig. 4.5 shows the precipitate assemblies remained the same thickness by comparing the microstructures of ageing at 200°C for 30 min and 24 hr. The precipitate thickening was completely stopped. This is counter-intuitive given our current understanding of precipitation kinetics (Appendix A). Interestingly, the precipitate-precipitate junctions were associated with Ag depletion without exception. The detailed structures and chemistries of those junctions will be investigated in Chapter 6.

### 4.2.3 Nucleation and Growth of GP Zones $\epsilon$

In Al-Ag alloys, Al clusters form during quenching without further ageing, which is different from most heat-treatable aluminium alloys [17]. We manipulated the morphology of the quenched-in Ag clusters with different quenching media. Fig. 4.6 shows the water-quenched and oil-quenched samples did not display a well-defined GP zone shape. In contrast, the air-quenched Ag clusters had a truncated octahedron geometry with sharp  $\{111\}_{\text{Al}}$  and  $\{002\}_{\text{Al}}$  facets. The formation of the faceted geometry is due to minimising the interfacial energy during Ag clustering, known as Wulff construction (Appendix A). Slow quenching gives the time for Ag atoms and vacancies to diffuse, which results in a state close to equilibrium. With few quenched-in defects in oil- and air-quenched samples, the microstructures during ageing were very different from the water-quenched sample with sufficient defects, Fig. 4.7. For instance, the water-quenched samples had  $\gamma'$  precipitate assemblies nucleated on Frank dislocation loops. But the oil-quenched and air-quenched alloys only showed GP zones  $\epsilon$ . This distinct contrast demonstrated the non-equilibrium nature of precipitation. With a depletion of defects, the FCC-HCP phase transformation was suppressed.

In the water quenched samples, there were more types of quenched-in defects than merely vacancies and Frank dislocation loops. Fig. 4.8 (a-b) shows the atomic resolution HAADF-STEM images of a void embedded in a GP zone  $\epsilon$  in both  $\langle 110 \rangle_{\text{Al}}$  and  $\langle 110 \rangle_{\text{Al}}$  directions. Reconstructed from a HAADF-STEM tilt series, electron tomography revealed the core-shell structure had a truncated octahedron void in the centre (about 5 nm in diameter) surrounded by Ag enriched  $\epsilon$  phase. The overall core-shell structure was about 8 nm in diameter, larger than the nearby GP zones  $\epsilon$  with sizes of 2~5 nm. Besides the interactions with the GP zones

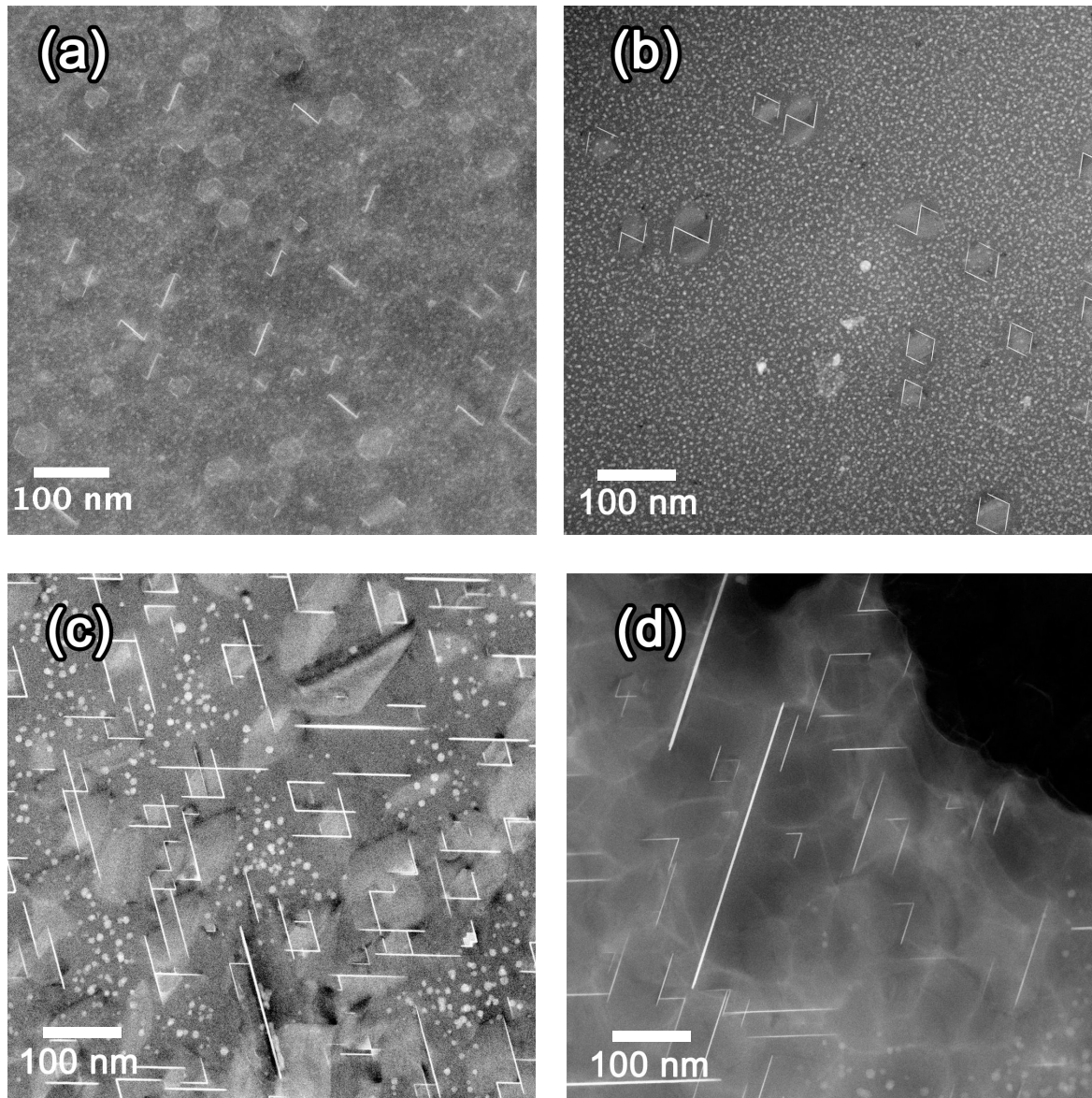


Fig. 4.4 Evolution of the microstructure while ageing at 200°C as a function of time: (a) 30 min, (b) 2 hr, (c) 4 hr, (d) 24 hr. The  $\gamma'$  precipitate assemblies and GP zones are replaced by large individual  $\gamma'$  plate. Electron beam along a  $\langle 110 \rangle_{Al}$  zone axis.

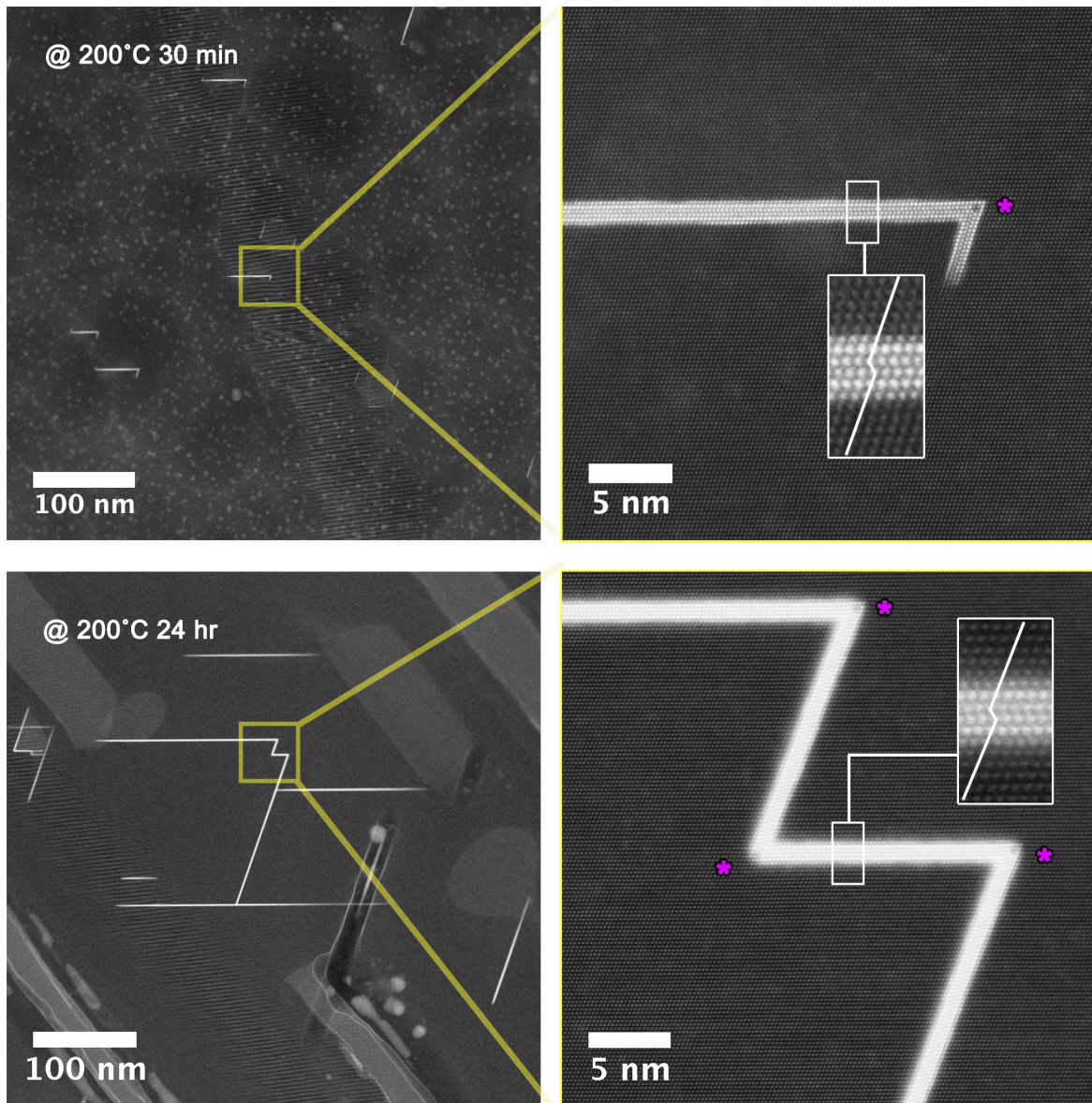


Fig. 4.5 Low and high magnification HAADF-STEM images showing the  $\gamma'$  precipitate assemblies after ageing at 200°C for (a-b) 30 min and (c-d) 24 hr. The Ag depletions precipitate-precipitate junctions are highlighted with purple asterisks. The inset images show the thicknesses of the  $\gamma'$  precipitates are the same with 1 stacking fault for both ageing conditions. The electron beam is parallel to  $\langle 110 \rangle_{Al}$ .

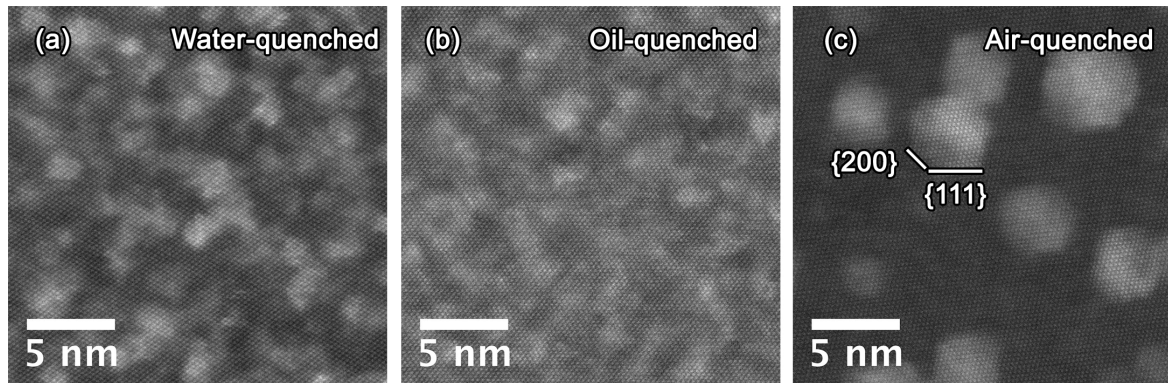


Fig. 4.6 The as-quenched Ag clusters obtained by quenching the alloy in different media: (a) water; (b) oil and (c) air. The electron beam is parallel to  $\langle 110 \rangle_{Al}$ .

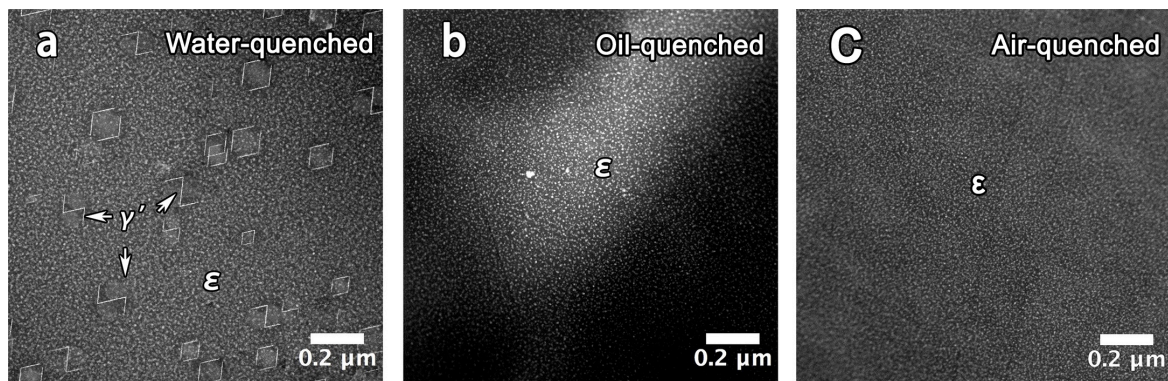


Fig. 4.7 Low magnification HAADF-STEM images showing the microstructure for Al-1.68 at.% Ag aged 2 h at 200°C after quenched in (a) water, (b) oil and (c) air from the solid solution temperature at 525°C. The differences in the microstructures between those conditions are caused by the quenched-in vacancies and defects that provide heterogeneous nucleation sites for  $\gamma'$  precipitates. The electron beam is parallel to  $\langle 110 \rangle_{Al}$ .

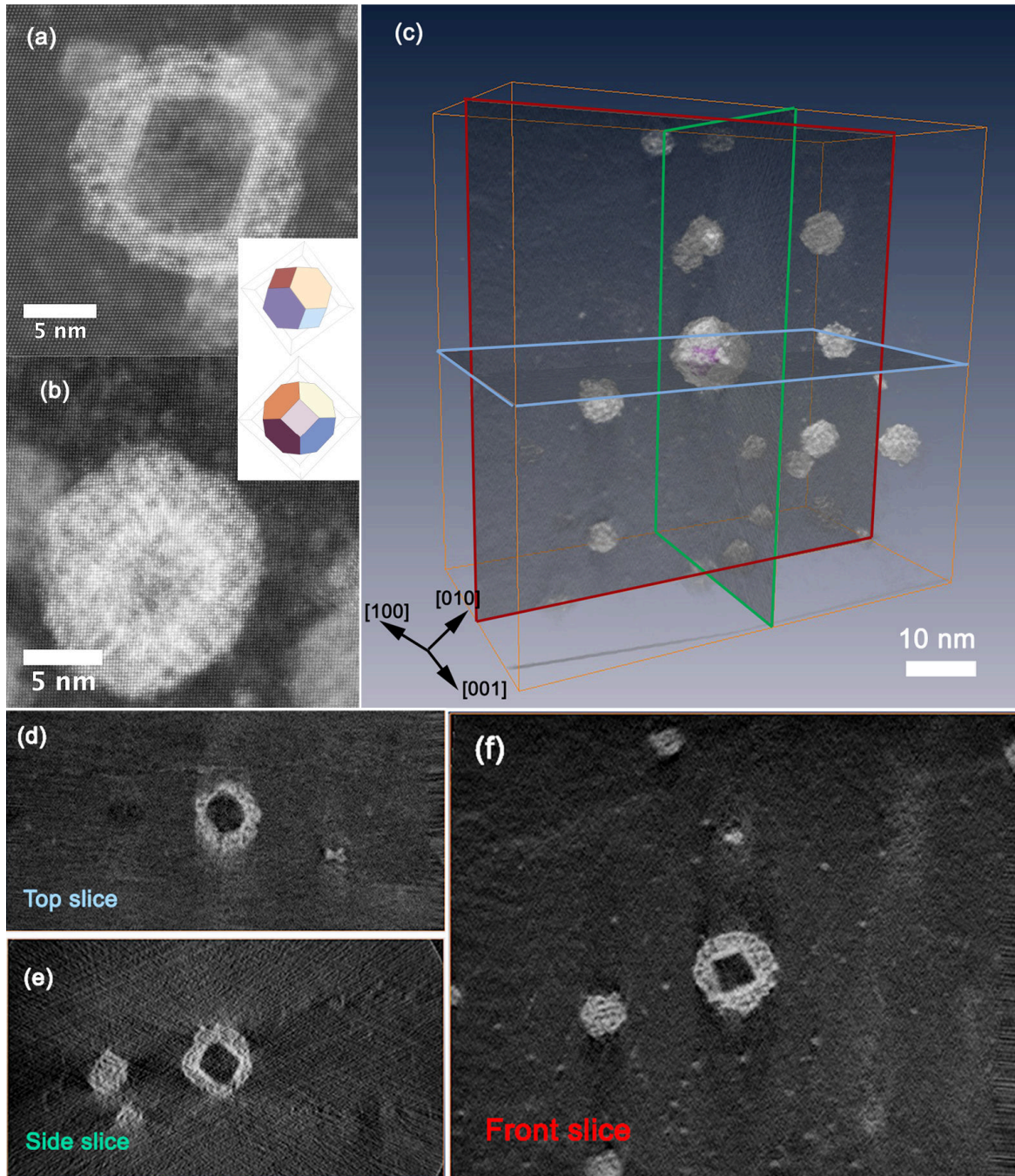


Fig. 4.8 Atomic resolution HAADF-STEM of the core-shell structure of a void embedded with a GP zone  $\epsilon$ , viewed along (a)  $\langle 110 \rangle_{Al}$  and (b)  $\langle 100 \rangle_{Al}$  directions. The truncated octahedron geometries in those directions are shown as insert images at the corner. (c-f) Electron tomography of a void and surrounding GP zones  $\epsilon$  with orthogonal slices at the centre. The sample was water-quenched and aged at 200°C for 2 h.

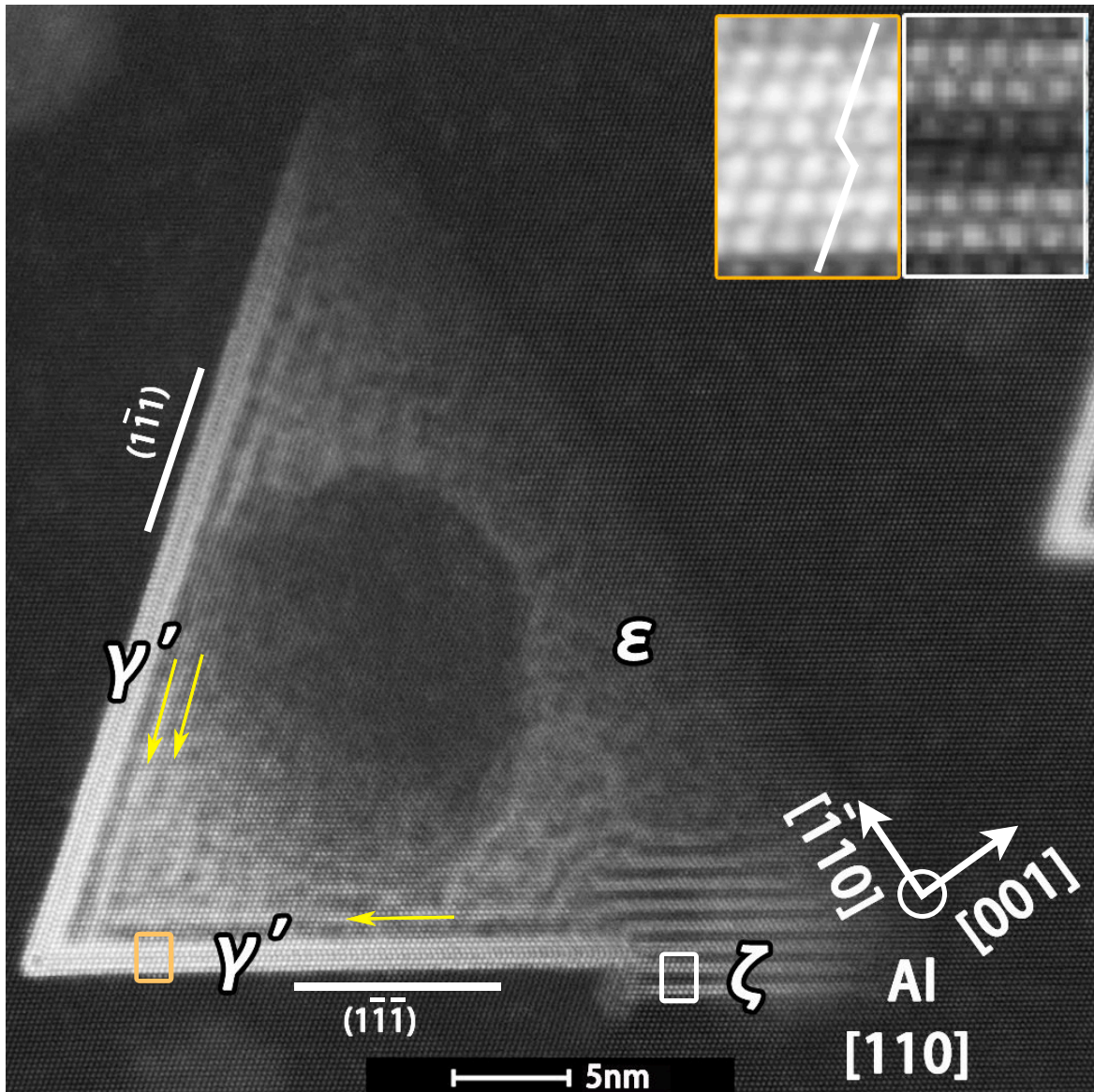


Fig. 4.9 HAADF-STEM image of the rare occurrence of a  $\gamma'$  assembly nucleated inside a GP zone with Ag depletion. The single stacking fault associated with the  $\gamma'$  phase is shown in the enlarged orange-framed insert image. The formation of  $\gamma'$  introduces partial ordering on the coherent interface of  $\gamma'$  plate, as indicated by yellow arrows. There is a fully ordered structure  $\zeta$  at the tail of the  $\gamma'$  assembly, as shown in the enlarged white-framed image. The electron beam is parallel to  $\langle 110 \rangle_{\text{Al}}$ . Image courtesy: Laure Bourgeois.

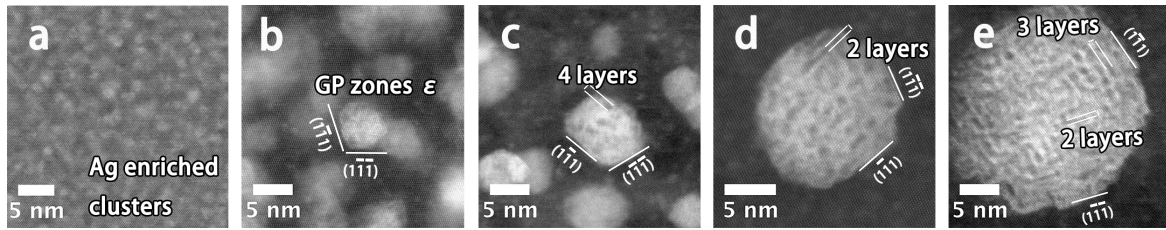


Fig. 4.10 HAADF-STEM images of GP zones aged at 200°C after quenching in oil for various ageing times: (a) as-oil-quenched (b) 1 h; (c) 2 h; (d) 24 h; (e) 7 days. The ordering of Ag solute becomes increasingly defined on the  $\{111\}_{\text{Al}}$  planes while the width of the Ag depletion remains about two to four  $\{111\}_{\text{Al}}$  layers. The electron beam is parallel to  $\langle 110 \rangle_{\text{Al}}$ .

$\epsilon$ , voids seem to facilitate phase transformations within GP zones as well. As voids shrink with the ageing time [189], the released vacancies may trigger the FCC-HCP transformation. Fig. 4.9 shows a GP zone developed Ag depletion inside and formed  $\gamma'$  assemblies at its edges. The Ag depletion region could originate from a collapsed void. Interestingly,  $\gamma'$  precipitates induced Ag ordering at their coherent interfaces as indicated by yellow arrows. In addition, we found a fully ordered region of Al and Ag as highlighted in the enlarged view. This ordered structure was exceedingly rare according to our observations, which is possibly due to the low density of voids. However, it inspired us as a possible new phase within the Al-Ag system, with a new pathway manipulated by defects. We name the structure as  $\zeta$  for the following experiments and analysis.

The chemical inhomogeneities within GP zones  $\epsilon$  developed gradually by diffusion of Ag atoms in the aluminium matrix. Fig. 4.10(a-c) shows  $\epsilon$  GP zones were more homogeneous at the early stage of ageing in the oil quenched samples than those in the water quenched samples. Fig. 4.10(c-e) shows that the Ag distributions on  $\{111\}_{\text{Al}}$  planes became increasingly ordered, while the widths of the Ag depletion regions remained relatively constant at about two to four  $\{111\}_{\text{Al}}$  layers. This unique behaviour will be explained with first-principles calculations in Chapter 5. The purpose of oil quenching was to reduce the quenched-in vacancy concentration to suppress the formation of  $\gamma'$  thus preserve the growth of GP zones, as shown in Fig. 4.7. This process enabled us to obtain large GP zones with diameters up to 25 nm that were subsequently used as a pre-existing phase in the following nanoscale and bulk treatments.

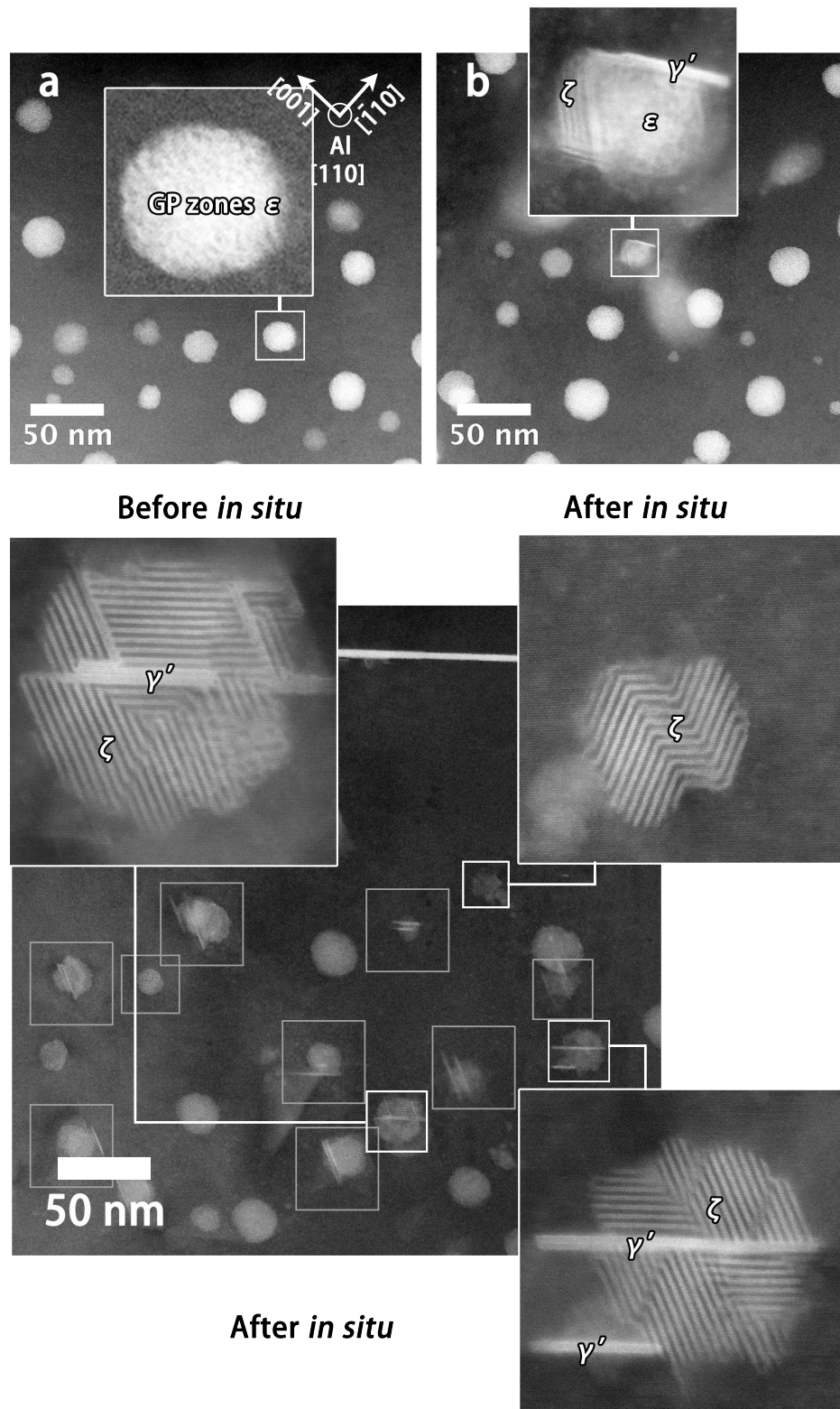


Fig. 4.11 HAADF-STEM images of the microstructure before and after *in situ* annealing at 200°C for 3 min. The original sample is oil quenched and aged at 200°C for 7 days. (a) Before *in situ* annealing, where the enlarged image shows the GP zone before transformation; (b) after *in situ* annealing, where the enlarged image shows the GP zone shown in (a) now containing  $\gamma'$  precipitates; (c) after *in situ* annealing in a different area from (a), where the enlarged images show several examples of the transformed GP zones with a layered structure, while other transformed GP zones are indicated with grey frames. The electron beam is parallel to  $\langle 110 \rangle_{\text{Al}}$ .

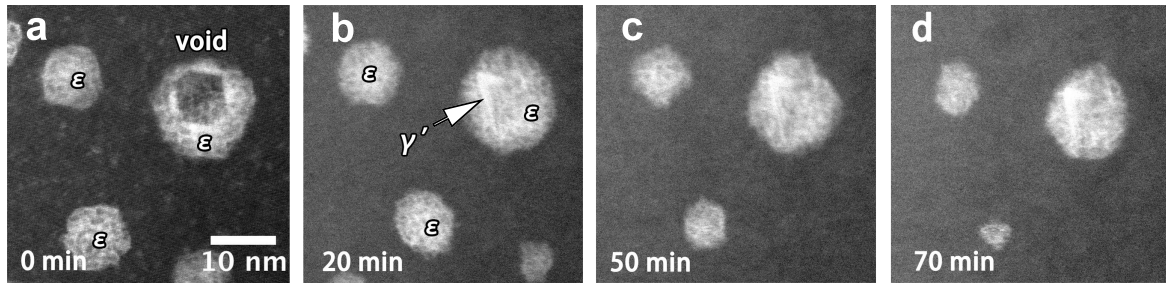


Fig. 4.12 HAADF-STEM images showing the shrinkage of small GP zones during *in situ* annealing at 200°C. The embedded void collapsed within a GP zone  $\epsilon$  that resulted in the nucleation of a small  $\gamma'$  precipitate assembly. The original sample was water quenched and aged at 200°C for 2 h. The electron beam is parallel to  $\langle 110 \rangle_{\text{Al}}$ .

### 4.3 Defects-induced Phase Transformations on Pre-existing Phases

#### 4.3.1 Nanoscale Processing: *In-situ* Annealing

Ageing the ultra-thin TEM samples demonstrated new transformations on pre-existing GP zones. Fig. 4.11 shows the microstructure change of the alloy containing large GP zones after 7 days ageing at 200°C before and after the secondary ageing within the electron microscope. A transformation occurred within a GP zone  $\epsilon$  after a short time (3 min) annealing at 200°C, as shown in Fig. 4.11(a-b). This transformation did not occur for every GP zone, and the density was not uniform across the sample. Fig. 4.11(c) shows a different area of the same sample with a much higher density of the transformed GP zones and a clear layered structure inside (see insets), reproducing the minor presence of  $\zeta$  phase in Fig. 4.9 on a large scale.

We tested different *in situ* annealing temperatures (100°C, 150°C and 200°C) and samples with different GP zones sizes. The results indicated that the transformation needs large GP zones and a relatively high annealing temperature ( $\geq 150^\circ\text{C}$ ). Interestingly, Fig. 4.12 shows that small GP zones actually shrunk during *in situ* annealing, as a result of Ag diffusion to the sample surface. In addition, the void embedded within a GP zone  $\epsilon$  collapsed to assist the formation of  $\gamma'$  precipitate, which confirms our previous hypothesis of the transformations assisted by shrinking voids. In order to examine the potential effect of electron irradiation on phase transformations, we performed *in situ* annealing experiments without the electron beam. Results in Fig. 4.13 show that, without the interaction with the electron beam, newly formed layered structure  $\zeta$  and  $\gamma'$  precipitates were still found.

The phase transformations are possibly induced by a vacancy flux during *in situ* annealing. Because a vacancy is more likely to form on the surface than the bulk. The difference in

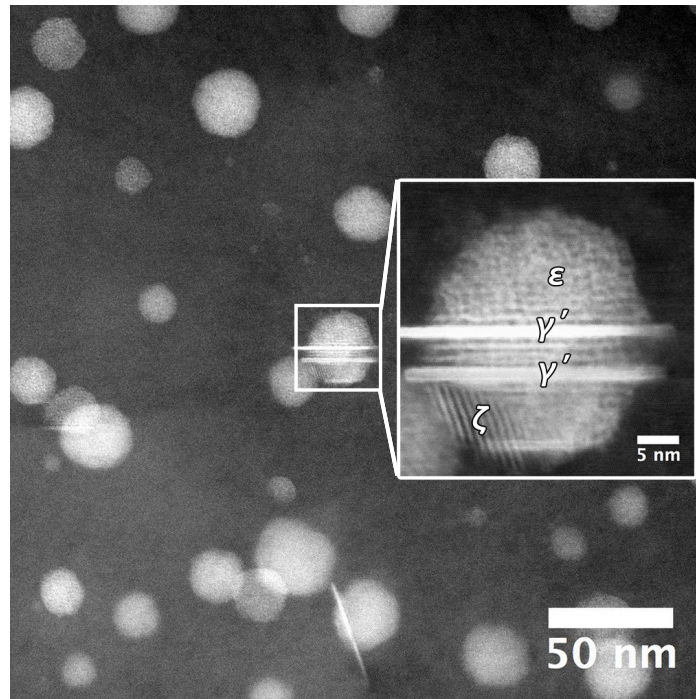


Fig. 4.13 HAADF-STEM images showing the  $\zeta$  phase and  $\gamma'$  phase were found in a sample *in situ* annealed at 200°C for 3 min without beam irradiation during *in situ* annealing. The original sample was oil quenched and aged at 200° for 7 days. The electron beam is parallel to  $\langle 110 \rangle_{Al}$ .

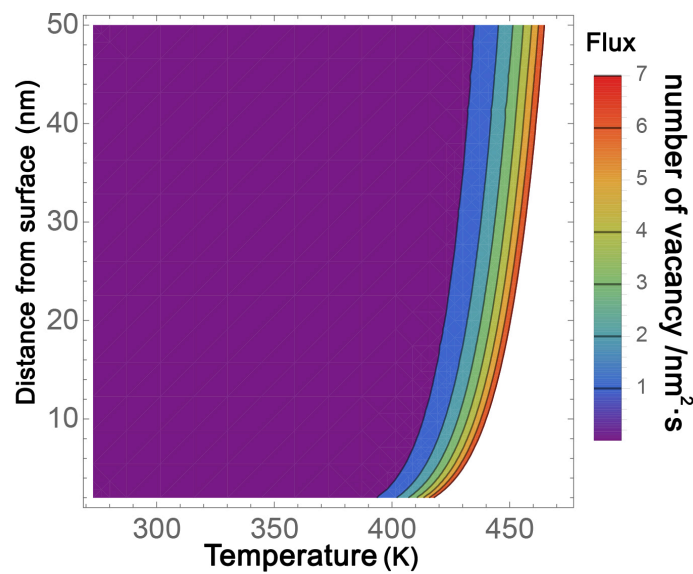


Fig. 4.14 Vacancy flux from the surface as a function of temperature and distance for a thin aluminium foil.

vacancy concentration leads to a flux. Based on Fick's law, the flux equation can be derived as:

$$\frac{dn}{dt} = \frac{D}{r\Omega} (e^{\frac{-E_{vs}}{kT}} - e^{\frac{-E_v}{kT}}) e^{\frac{-E_m}{kT}}, \quad (4.1)$$

where  $\frac{dn}{dt}$  is the vacancy flux (number of vacancy per second),  $D$  is the aluminium diffusivity ( $1.76 \times 10^{13} \text{ nm}^2/\text{s}$  [190]),  $\Omega$  is the atomic volume of aluminium ( $16.6 \text{ \AA}^3$ ),  $r$  is the distance from the surface,  $E_{vs}$  is the vacancy formation at the surface,  $E_v$  is the vacancy formation energy of bulk aluminium (0.65 eV [191]),  $E_m$  is the vacancy migration energy in aluminium (0.65 eV [191]),  $k$  is the Boltzmann constant,  $T$  is the temperature. The vacancy formation energies for pure aluminium surfaces of different crystallographic planes were calculated by the first-principle calculations [192], which are indeed much lower than that in the bulk. However, aluminium TEM foils are always covered with a thin amorphous alumina and possibly Ag oxides for the Al-Ag alloys; an accurate estimation of  $E_{vs}$  for this amorphous surface is beyond the scope of this study. Thus, we chose  $E_{vs}=0.5$  eV as a dummy parameter since the exact value should not change the quality of our results. As shown in Fig. 4.14, the vacancy flux rises exponentially with temperature, which is significant for temperature above  $\sim 120^\circ\text{C}$  (or 393 K). This result agrees with our experimental observations that transformations occur with an *in situ* temperature above  $100^\circ\text{C}$ .

### 4.3.2 Bulk Processing: Deformation and Secondary Ageing

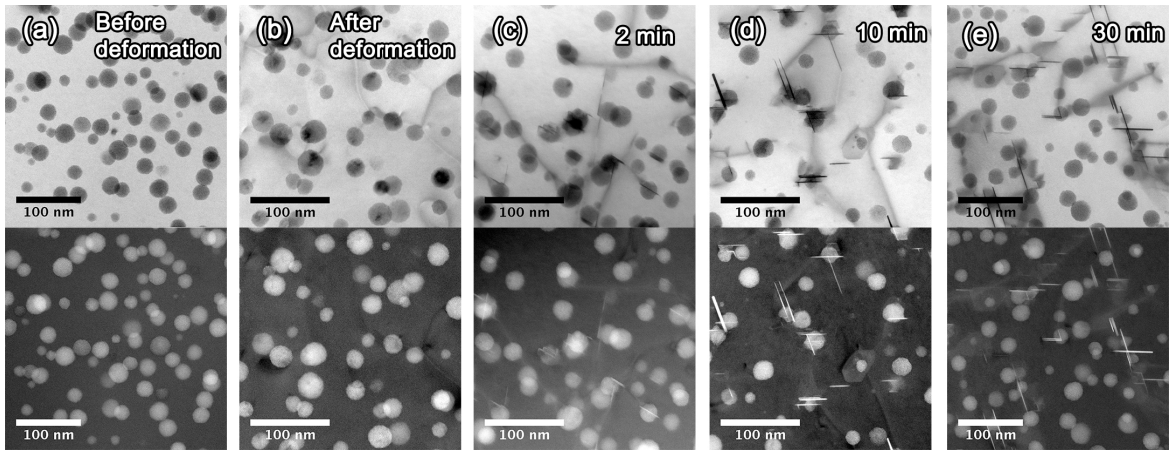


Fig. 4.15 BF- and HAADF-STEM images showing the microstructures during different stages of the bulk processing scheme. (a-b) The microstructure before and after deformation, with dislocation line visible in the BF image. (c-e) The microstructure as a function of secondary ageing time at  $200^\circ\text{C}$ . The original sample is water quenched, aged at  $200^\circ\text{C}$  for 7 days. The electron beam is parallel to  $\langle 110 \rangle_{\text{Al}}$ .

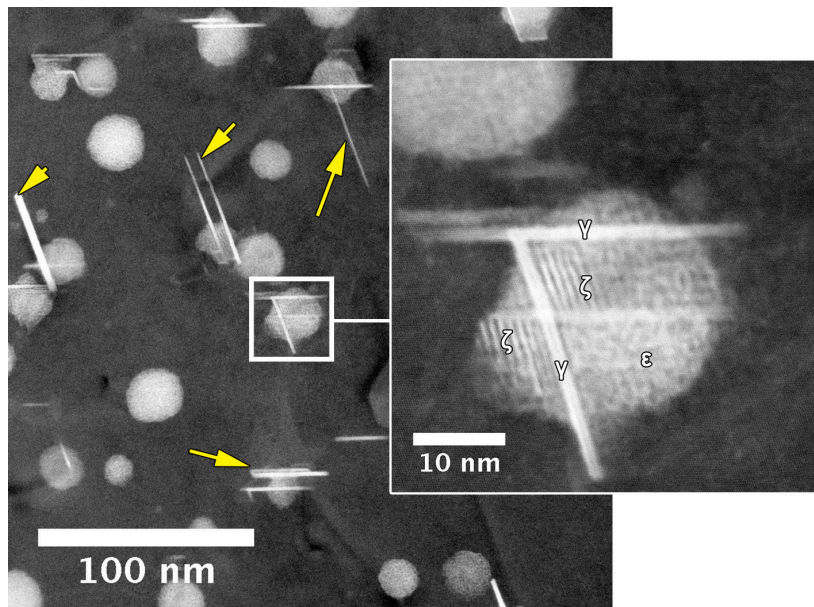


Fig. 4.16 HAADF-STEM image showing the ordered structure  $\zeta$  was also found with the bulk treatment. The sample is water quenched, aged at 200°C for 7 days, deformed by 7% and aged at 200°C for 10 min. The electron beam is parallel to  $\langle 110 \rangle_{Al}$ .

The bulk treatment introduced defects directly by deforming the alloy, followed by the secondary ageing. Fig. 4.15(a-b) compares the microstructures before and after deformation, showing dislocations were introduced by deformation. Fig. 4.15(c-e) show the microstructure evolution as a function of time while the secondary ageing at 200°C. The  $\gamma'$  precipitate plates predominantly nucleated from GP zones with the assistant of dislocations. The precipitate plates grew in length and thickness directions unless they formed junctions that impinged each other. In addition, Fig. 4.16 shows the  $\zeta$  phase was also found with the bulk treatment. The density of the new ordered phase obtained by bulk treatment was lower than that obtained by nanoscale treatment, but it was much higher than that obtained by conventional heat treatments.

Small deformation was specifically chosen to generate dislocations with relatively low density and high mobility to be captured by GP zones. Fig. 4.17(a-b) shows the gliding of a dislocation that cut through GP zones within 20 s, as highlighted with yellow arrows. Fig. 4.17(c-d) show the formation of  $\gamma'$  precipitate plates within GP zone on a dislocation line. High-density dislocations, in contrast, form a dislocation network that acts as a barrier to the dislocation movement, which is known as the origin of work hardening [21]. We tested the high dislocation density condition with 70% deformation and secondary ageing at 200°C, Fig. 4.18. The preliminary results showed that the GP zones were severally elongated after large deformation, similar to the microstructure processed by the equal-channel angular

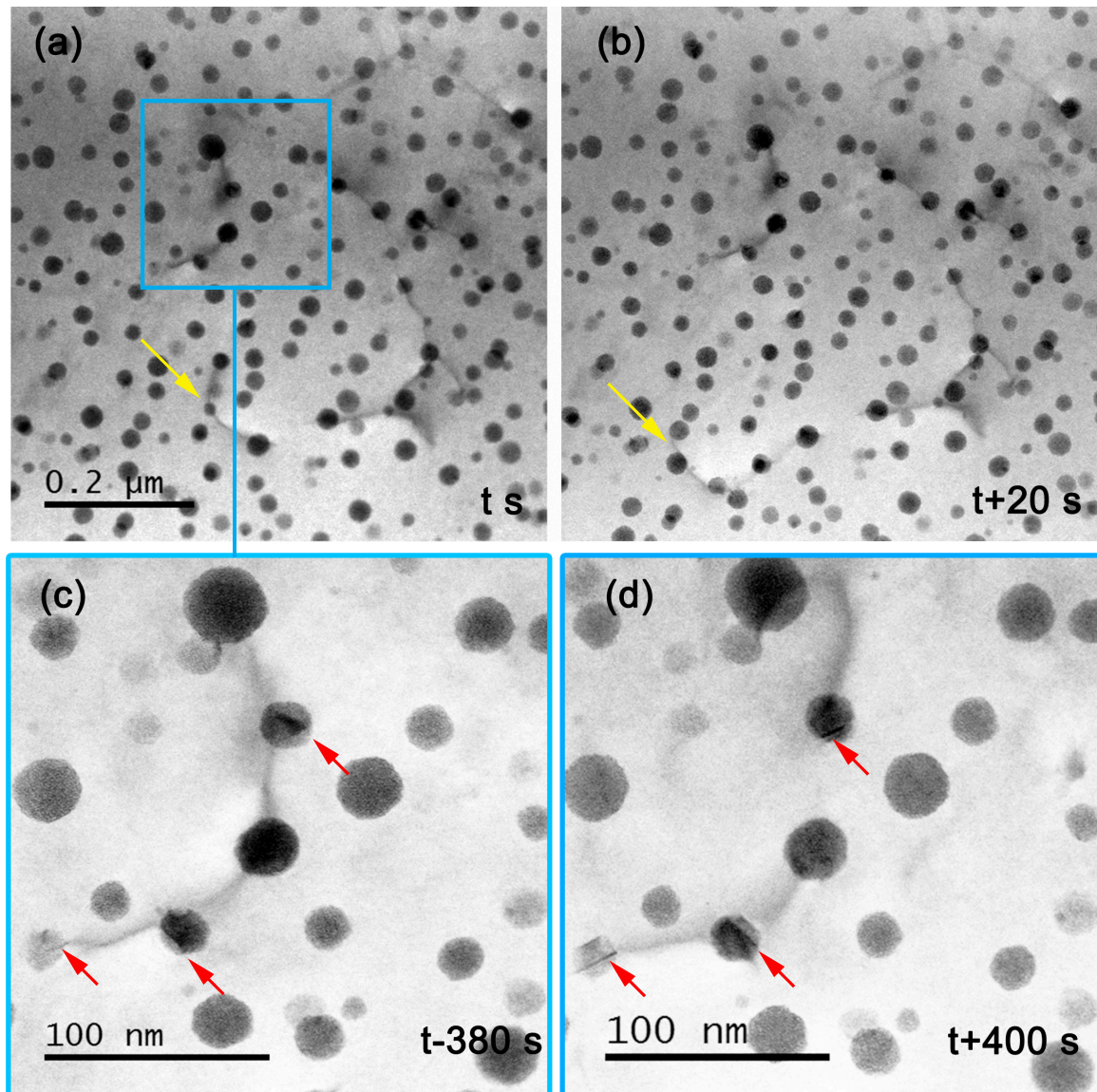


Fig. 4.17 BF-STEM images showing the gliding of dislocations and formation of  $\gamma'$  precipitate plates during *in situ* annealing at 150°C. (a-b) The gliding of a dislocation within 20 s, with the position of the dislocation indicated by yellow arrows. (c-d) Formation of  $\gamma'$  precipitate plates within GP zone  $\epsilon$  on a dislocation line as indicated by red arrows. The original sample was water-quenched, aged at 200°C for 7 days and deformed by 7% by cold rolling. The electron beam is parallel to  $\langle 110 \rangle_{\text{Al}}$ .

pressing (see Fig. 2.15) [50]. The  $\gamma'$  precipitates nucleated from the matrix, instead of forming inside the GP zones as seen in the small deformation condition. The ordered structure  $\zeta$  was not found for those severely deformed samples. More systematic studies are

needed to investigate the relationship between the extent of deformation and the resulting microstructure.

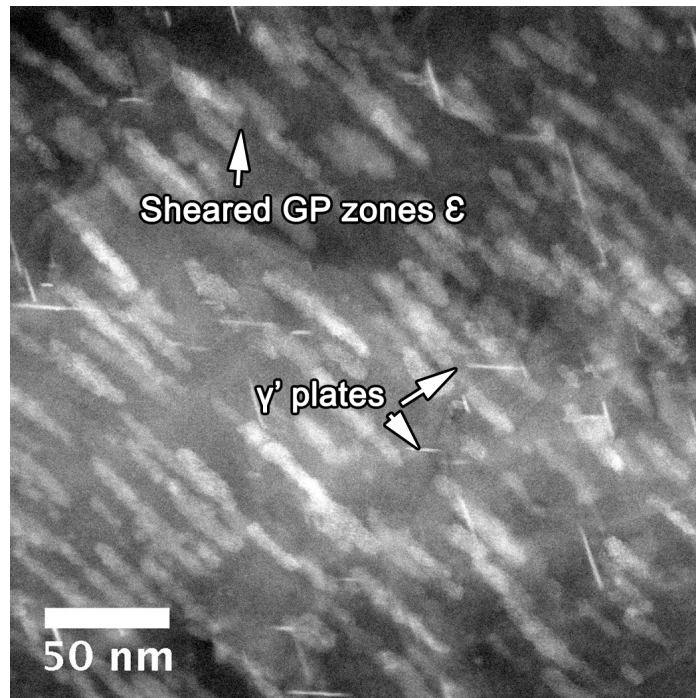


Fig. 4.18 HAADF-STEM images showing the shearing of GP zones by large deformation and nucleation of  $\gamma'$  precipitate plates in the matrix. The original sample was oil-quenched, aged at 200°C for 24 hr and deformed by 70%, secondary aged at 200°C for 10 min. The electron beam is parallel to  $\langle 110 \rangle_{\text{Al}}$ .

## 4.4 Discussion

Defects are critical for phase transformations – they lower the critical transition barrier and triggers the transition pathways. The nature of defects, as a consequence, directly determines the precipitation behaviours. For instance,  $\gamma'$  precipitate phase heterogeneously nucleates on the Frank dislocation loops and forms a topologically structured assembly, Fig. 4.3. The atomic mechanisms associated with the assemblies formation was illustrated with atomistic dislocation reaction simulation, Fig. 4.2. According to Frank's Energy Criterion [21], the Frank dislocation loop decomposes into Shockley partials and Lomer-Cottrell to lower the strain energy. The topology of the decomposed loop acts as a template for  $\gamma'$  precipitate phase nucleation. Interestingly, the precipitate-precipitate junctions are associated with Ag depletions but the mechanisms are still not understood. Such understanding is important to explain the impingement of the assemblies growth during ageing, as shown in Fig. 4.5. In

contrast, individual  $\gamma'$  precipitate plates without junction were found to coarsen continuously. Voids were also found as quenched-in defects, and together with GP zones  $\varepsilon$ , they form a core-shell structure: a truncated octahedron vacuum core and Ag enriched shell. This may be due to the favourable interaction between Ag and vacancies during clustering [9, 24]. Voids, however, are not thermally stable in aluminium that they shrink during ageing [189], while GP zones  $\varepsilon$  keep growing. The released defects may lead to the formation of  $\gamma'$  assemblies and a new ordered structure  $\zeta$  within a GP zone, as shown in Fig. 4.9. The  $\zeta$  structure has a fully ordered structure on the close-packed planes, which has not been reported in Al-Ag alloys. Given the rare existence, we asked ourselves whether such structure is a non-repeatable accident – since the Al-Ag system is well-established – or an actual precipitate phase. Moreover, even it is an actual phase, the significance is negligible with such low density.

Once the importance of defects was realised, we manipulated the microstructure with different quenching rates and hence different amount of quenched-in defects. The variation of quenched-in defects resulted in different morphologies of the as-quenched Ag clusters, Fig. 4.6, and completely different microstructures during ageing, Fig. 4.7. Slow quenching reduced the quenched-in defects, like Frank dislocation loops, and suppressed the  $\gamma'$  precipitation. The size of GP zones  $\varepsilon$  increased with ageing time, while the ordering of Ag on  $\{111\}_{\text{Al}}$  planes became increasingly clear. Large GP zones  $\varepsilon$  with local ordering acted as a pre-existing, metastable phase for the next step heat treatment.

The sequence of introducing defects during phase transformations is important. There are a wide variety of heat treatment codes (see Ref. [4]), but most of them introduce defects prior to ageing by thermal and/or mechanical treatments. The philosophy of our treatment is annihilating defects first to suppress phase transformations while preserving the growth of metastable phases. Then we introduce defects with secondary ageing to trigger phase transformations on pre-existing phases. This idea was demonstrated in both the nanoscale and the bulk treatments. In particular, the hidden  $\zeta$  structure was revealed by manipulating the transformation pathways with defects. The  $\zeta$  phase appears to be a fully ordered structure on  $\{111\}_{\text{Al}}$  planes, in comparison with the pre-existing phase GP zone  $\varepsilon$  with partial ordering. The  $\varepsilon$ - $\zeta$  phase transformation is diffusional in nature, the kinetics of which depends on the vacancy concentration.

For the nanoscale treatment, often the reaction within the thin TEM specimen differs from that in the bulk, both due to the surface effect and the electron irradiation. Electron irradiation indeed can substantially lower the energy barrier for vacancy diffusion, as we quantitatively measured in our recent study of *in situ* annealing of voids in aluminium [189]. However, according to our *in situ* annealing experiment without the electron beam,  $\zeta$  and  $\gamma'$

were still found to form within GP zones, Fig. 4.13. This demonstrates that electron beam irradiation is not responsible for those transformations. When considering surface effects, there is a depth dependency of the vacancy formation energy at the Al surface [192]. In general, a vacancy has a lower formation energy at the surface than in the bulk, which leads to a vacancy flux from the surface to the bulk. Diffusion calculations using Fick's law (Eq. 4.1) suggested that such a vacancy flux can be significant for an ultra-thin sample at a temperature higher than 100°C (see Fig. 4.14), as was the case for *in situ* annealing experiments. The fact that small GP zones shrink during *in situ* annealing is an indication of such vacancy flux, Fig. 4.12. The induced vacancies are also likely to be the source for Shockley partial dislocations, which is required for  $\gamma'$  formation within GP zones  $\epsilon$ . The oil quenched samples with large GP zones after long ageing times are depleted of vacancies. When vacancies are induced to mediate solute diffusion, those large GP zones with the local ordering of Ag on  $\{111\}_{\text{Al}}$  planes act as a template for  $\zeta$  formation.

For the bulk treatment, the introduced defects are clearly dislocations. Such dislocations, most likely to be the perfect dislocation ( $\vec{b} = 1/2\langle 110 \rangle_{\text{Al}}$ ) for FCC crystals [21], can be decomposed into two Shockley partial dislocations (one leading and one trailing) via

$$1/2\langle 110 \rangle = 1/6\langle 211 \rangle + 1/6\langle 12\bar{1} \rangle.$$

Stacking fault forms in the region between the leading and trailing partial dislocations that changes the local structure from FCC to HCP. Such dislocation decomposition is suppressed in the matrix because of the high stacking fault energy associated with aluminium. As a result, dislocations glide in the matrix until trapped by GP zones, as shown in Fig. 4.17. Within the GP zones, however, the stacking fault energy is significantly reduced with the enrichment of Ag [87]. The stacking fault region between the leading and trailing dislocations leads to the formation of HCP  $\gamma'$  precipitate during the secondary ageing. In addition, dislocations may cross-slip between the close-packed planes that form  $\gamma'$  assemblies, Fig. 4.16. Unlike the assemblies nucleated on the Frank dislocation loop in Fig. 4.3, the topology of newly formed assemblies is not fully impinged by precipitate plates. Thus, the  $\gamma'$  precipitate plate may grow in both length and thickness as indicated by arrows in Fig. 4.16. Beside the decomposition of dislocations, vacancies can also be generated during ageing. For instance, the climbing of dislocations and gliding of dislocation jogs release vacancies during their movement [21]. Those vacancies may facilitate the ordering of Ag on  $\{111\}_{\text{Al}}$  planes within GP zones  $\epsilon$ , which enables the  $\zeta$ - $\epsilon$  transformation.

The defects-induced phase transformations should not just provide theoretical insights to precipitation in a simple system but may bear practical significance. In engineering applications, defects are generated all the time during the servicing of alloys, i.e. under the thermal and mechanical loading or even sometimes irradiation. As Chapter 2 reviewed,

the microstructure in alloys is usually dominated by the metastable phases because the equilibrium phases are not effective for strengthening. Those two conditions are the exact requirements of our proposed treatments, namely, defect induced phase transformation on pre-existing metastable phases. Thus, it is plausible that those phenomena happen in many engineering applications. For instance, the under-aged alloys are known to offer a higher fatigue strength than the peak-aged and over-aged alloys, even with a lower tensile strength [4]. The reason is thought to be dynamic precipitation during fatigue, which states the formation of precipitates in the solid-enriched matrix on dislocations that blocks the crack propagation with newly formed precipitates. Despite preliminary studies (see Ref. [4]), the mechanisms of dynamics precipitation are poorly understood. It is because the dynamic precipitation theory was built on previous studies measuring the precipitate densities during cyclic loadings. However, phase transformations may occur in pre-existing phases but not yet investigated in detail. Depending on the nature of the pre-existing phase, dislocations either cut through the phase that results in shearing, or bypass the phase that leaves a dislocation loop. In both cases, the movement of dislocations creates defects for the pre-existing phase. As reviewed in Chapter 2, diffusional phase transformations may include a structural change from one crystal structure to another [193], which requires the dissociation of dislocations to accomplish the transformation. Well-known examples are the shear partials ( $\vec{b} = a/2\langle 100 \rangle_{\text{Al}}$ ) for  $\theta'$  phase in Al-Cu alloys [8], Shockley partials for the  $T_1$  phase in Al-Cu-Li alloys [45] and for  $\gamma'$  phase in Al-Ag alloys [82]. It is important to note that the critical step during diffusional phase transformation is the structural transformation. For instance, with a depletion of defects, GP zones  $\varepsilon$  can grow into a significant size without the FCC-HCP transformation. From our observations, dislocations are trapped by coherent GP zones (probably also vacancies but they are not visible) that transform the metastable phase into  $\gamma'$  phase and sometimes a new precipitate phase  $\zeta$ . This mechanism is not just limited to Al-Ag alloys, but should be applicable for other precipitation systems with their transformation triggers by defects. For example, the same treatments were applied to the metastable  $\theta''$  phase in Al-Cu alloys and an unreported precipitate phase was found as well (paper to be submitted). The concept presented here hopefully points out a direction to revisit the phase transformations in classic alloy systems. One should also examine the phase transformations during the servicing of alloy components to confirm this mechanism in practice.

## 4.5 Conclusions

Defects provide heterogeneous sites for phase transformations. Based on the role of defects during precipitation, we developed new heat treatment schemes – for both thin TEM samples

and bulk alloys – to introduce defects to pre-existing phases and trigger phase transformations. In such way, we revealed a new phase and new transformation pathways in the classic Al-Ag system. The main conclusions are as follows:

1. Our simulations explained the atomic mechanisms associated with heterogeneous nucleation of  $\gamma'$  precipitate assemblies on quenched-in defects. The simulated geometries agree with the microstructure observations and electron tomography reconstructions. The  $\gamma'$  precipitate assemblies with such self-impinged geometry do not coarsen with ageing time at 200°C, while individual  $\gamma'$  plates grow both in length and thickness directions. The reason is not yet well understood.

2. Small Ag enriched clusters are formed during the quenching of Al-Ag alloys. The morphology of Ag clusters can be manipulated with different quenching media. Slow quenching annihilates defects and suppresses the FCC-HCP transformation, which preserves the growth of GP zones. The ordering of GP zones  $\epsilon$  with inhomogeneous Ag distribution increases with ageing time.

3. Annealing ultra-thin TEM samples or deforming bulk alloys introduce lattice defects to pre-existing metastable GP zones  $\epsilon$ . Those introduced lattice defects are likely in the form of vacancies and dislocations that trigger new transformation pathways on pre-existing phase. This mechanism may occur during the thermomechanical processing and the servicing of alloy components for engineering applications.

# Chapter 5

## Atomic Structure and Phase Transformations of The Bi-layered Precipitate $\zeta$ Phase

### 5.1 Introduction

The preceding chapter reviewed the phase diagram and the FCC-HCP phase transformation in the Al-Ag system. AgAl phases with FCC and HCP structures were predicted by first-principles calculations but never confirmed in experiments. Using the heat treatment schemes elaborated in Chapter 4, an ordered phase  $\zeta$  with the layered structure emerges from pre-existing GP zones  $\varepsilon$ . This chapter presents the characterisation of the atomic structure and chemistry of the  $\zeta$  phase using scanning transmission electron microscopy (STEM) and energy dispersive X-ray spectroscopy (EDXS). The detailed phase transformations were revealed by the *in-situ* STEM. We also investigated the stability of the  $\zeta$  phase relative to other phases with first-principles calculations.

Section. 5.2 describes the characterisation of the atomic structure of the  $\zeta$  phase by imaging in both  $\langle 110 \rangle_{\text{Al}}$  and  $\langle 112 \rangle_{\text{Al}}$  directions. We proposed a simple AgAl model with alternating Al and Ag bi-layers for the  $\zeta$  phase. Electron tomography in HAADF-STEM mode allowed the reconstruction of a single  $\zeta$  particle, showing different domains. Various electron microscopy techniques were combined with simulations to examine the chemistry and atomic positions of the  $\zeta$  phase.

Section. 5.3 reveals the phase transformation pathways by the *in-situ* STEM. While the overall transformation has been described in Chapter 4, the present section is concerned about the detailed transformation process of individual precipitates. We revealed the time-resolved

$\varepsilon$ - $\zeta$ - $\gamma'$  transformation at relatively high magnification. Those experiments also illustrated the explicit role of defects that modify the transformation pathways.

Section. 5.4 analyses the energetics associated with the transformations of the phases involved. Enthalpies of different solute configurations were calculated by density functional theory, while entropy and strain energies were calculated with classical approximations. Those calculations were performed to explain the unique behaviours of Ag atoms in the aluminium matrix.

Part of the results in this chapter was published in Ref. [174].

## 5.2 Atomic Structure: HAADF-STEM Imaging, Simulation and Analysis

The atomic structure of the  $\zeta$  phase was studied using aberration-corrected HAADF-STEM. Fig. 5.1(a) shows that the ordered phase is clearly distinct from GP zones  $\varepsilon$  or  $\gamma'$  plates. We named this new phase as  $\zeta$ . Specifically, the  $\gamma'$  phase has an ABAB stacking (see orange inset) while the  $\zeta$  phase follows the ABCABC stacking as the FCC Al and GP zone  $\varepsilon$  (see white and green insets). In other words, the  $\zeta$  phase is a coherent precipitate phase without misfit dislocations as shall be demonstrated later. The  $\zeta$  phase exhibits different domains corresponding to different  $\{111\}_{\text{Al}}$  variants, as viewed along a  $\langle 110 \rangle_{\text{Al}}$  direction, Fig. 5.1. Fig. 5.2 shows that Ag can be depleted in some atomic columns within the Ag-enriched bi-layers, as viewed along  $\langle 112 \rangle_{\text{Al}}$  (see yellow arrow in inset). But the depletion has no periodicity, and the overall intensity is quite uniform. After imaging in the  $\langle 110 \rangle_{\text{Al}}$  and  $\langle 112 \rangle_{\text{Al}}$  directions, we conclude that the new phase has a super-lattice structure of FCC Al and consists of alternating Ag-enriched bi-layers and Al-enriched bi-layers on  $\{111\}_{\text{Al}}$  planes.

In many cases,  $\gamma'$  precipitates formed inside GP zones  $\varepsilon$  and introduced Ag depletion at their coherent interfaces ( $\{111\}_{\text{Al}/\varepsilon} \parallel \{0001\}_{\gamma'}$ ). As shown in Fig. 5.3, the widths of the Ag depletion region are about two to three atomic layers. Away from the coherent interfaces of  $\gamma'$  precipitates, Ag enriches and then depletes again in a specific frequency that is similar to the modulation of  $\zeta$ , suggesting these regions are poorly ordered version of  $\zeta$  phase. Yellow arrows indicate such chemical ordering at the  $\gamma'$ - $\varepsilon$  coherent interface using both the new processing schemes, Fig. 5.3, and the conventional heat treatment, Fig. 4.9.

Precipitation of the  $\zeta$  phase accompanied the  $\gamma'$  phase in most cases, but some isolated examples of the  $\zeta$  phase without the  $\gamma'$  phase were also found. As shown in Fig. 5.4, a tilt series was performed for a given  $\zeta$  precipitate. Fig. 5.4(a) shows the  $\zeta$  precipitate

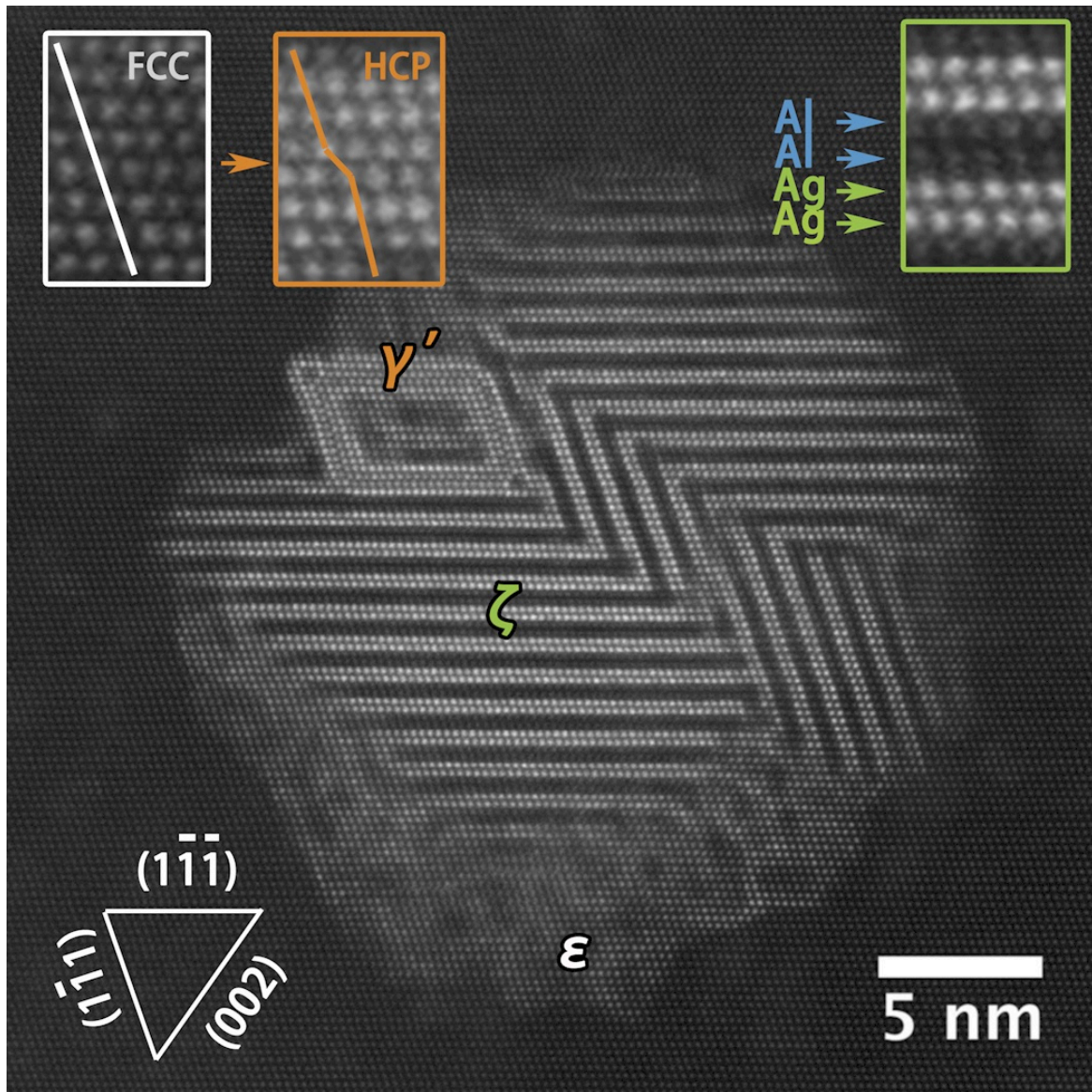


Fig. 5.1 HAADF-STEM images of the bi-layered phase formed on  $\{111\}_{\text{Al}}$  planes and viewed along  $\langle 110 \rangle_{\text{Al}}$ , where the green framed region shows in which the bi-layered phase has an ABCABC stacking as the white framed region of FCC aluminium matrix, while the orange framed region shows the characteristic stacking fault of  $\gamma'$ .

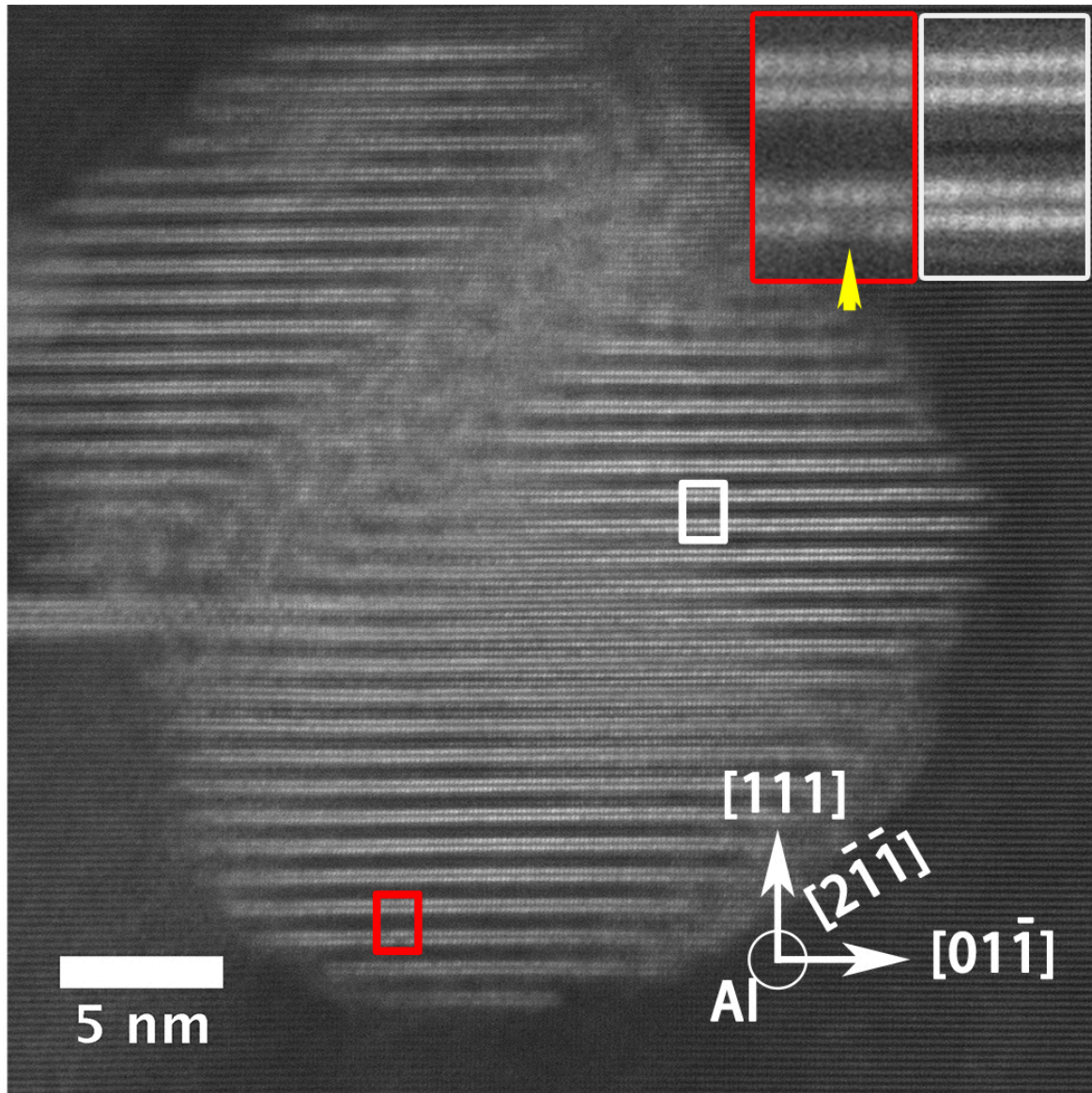


Fig. 5.2 HAADF-STEM images of the bi-layered phase formed on  $\{111\}_{\text{Al}}$  planes and viewed along  $\langle 112 \rangle_{\text{Al}}$ , where the white framed region shows the uniformly enriched Ag layers while the red framed region shows non-uniformly enriched Ag layers as indicated by a yellow arrow. Image courtesy: Laure Bourgeois.

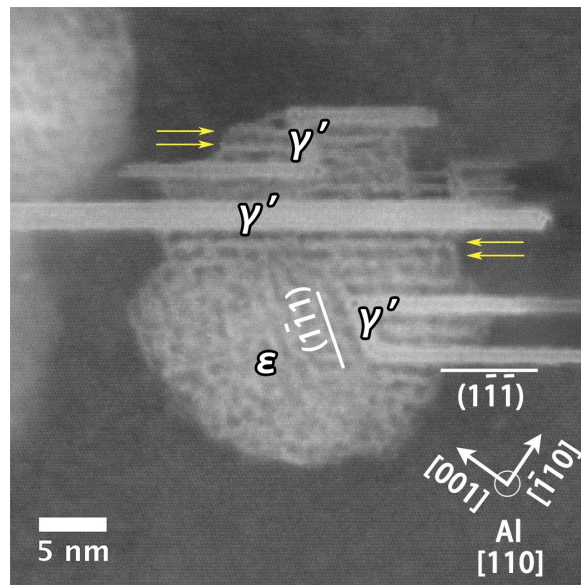


Fig. 5.3  $\gamma'$  plates formed inside a GP zone introducing ordering at their coherent interfaces as indicated by yellow arrows

viewed along the  $\langle 110 \rangle_{\text{Al}}$  zone axis with different domains of  $\{111\}_{\text{Al}}$  bi-layers and their domain boundaries on  $\{001\}$  planes. Fig. 5.4(b-i) shows the tilt series of the same precipitate in an angular range of  $-73^\circ$  to  $64^\circ$ . The layered contrast can be seen in Fig. 5.4(e) and (g), corresponding to the  $\{111\}_{\text{Al}}$  bi-layered variants. Throughout the tilt series, no  $\gamma'$  precipitate is visible. Fig. 5.4(j-k) shows the electron reconstruction based on the tilt series, revealing the  $\zeta$  phase with a domain structure in 3D. It is worth noting that the tilt series did not visit a  $\langle 110 \rangle_{\text{Al}}$  zone axis, but electron tomography (see Fig. 5.4(k)) successfully reconstructed the main features that are comparable STEM image obtained using double-tilt holder along a  $\langle 110 \rangle_{\text{Al}}$  direction, Fig. 5.4(a). In particular, the layered pattern with different domains of the  $\zeta$  phase is visible in the reconstruction, which corresponded to distance smaller than  $5\text{\AA}$ . However, some fine details are missing, which was probably due to small misalignment and limitation of the tilting angles. The drift-corrected tilt series can be found in the Supplementary Movie<sup>11</sup>, revealing the structural difference between the  $\zeta$  phase and surrounding GP zones  $\epsilon$  during tilting.

It is important to characterise the precise chemical composition and crystal structure of the  $\zeta$  phase. However, determining the composition of each layer is challenging for an embedded precipitate, particularly having matrix above and below in the electron beam direction. Thus, we proposed the simplest model in which each layer is pure Al or Ag

<sup>11</sup>Supplementary Materials in Ref. [174]. Link: <https://doi.org/10.1016/j.actamat.2017.04.061>

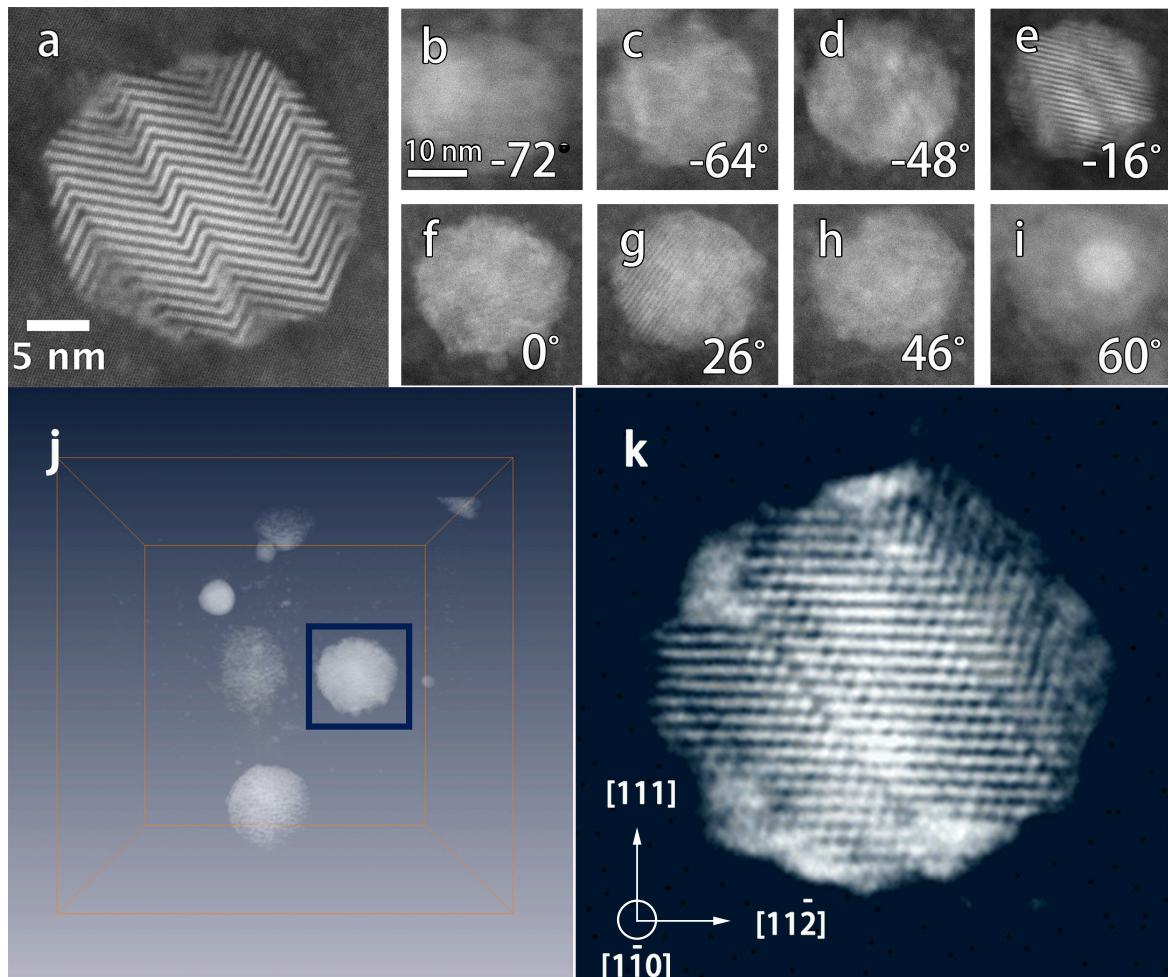


Fig. 5.4 (a) HAADF-STEM images of a bi-layered phase viewed along the  $\langle 110 \rangle_{\text{Al}}$  zone axis, showing domains formed by two variants of  $\{111\}_{\text{Al}}$  bi-layers. (b-i) HAADF-STEM tilt series of the same bi-layered precipitate phase for a tilt range from  $-73^\circ$  to  $64^\circ$ . The tilt angles are as labelled in each image. (j) Electron tomography reconstruction, where the blue-framed precipitate is  $\zeta$  phase while other precipitates are GP zones  $\epsilon$ . (k) An enlarged view of the  $\zeta$  phase along the  $\langle 110 \rangle_{\text{Al}}$  zone axis.

and examined the validity of the model in terms of EDXS analysis, HAADF-STEM image simulations, atomic positions and energetics deduced from first-principles calculations.

We examined 8 different GP zones  $\epsilon$  and 10 different  $\zeta$  precipitates from 3 different grains with sizes ranging from 10 nm to 25 nm and the thickness of each surrounding matrix ranging from 20 nm to 100 nm with two different EDXS systems (see Section. 3.2.5 for EDXS details). The deduced compositions are essentially the same for both GP zone  $\epsilon$  (38 at.% Ag at 200°C) and  $\zeta$  (40 at.% Ag at 200°C) with a small standard deviation between different datasets (3 at.% Ag for each phase). The uncertainties are 6 at.% Ag for each phase when quantified spectrums using the Cliff-Lorimer ratio method. Together with other errors from the K-factor (11%), the thickness (PACBED accuracy and amorphous oxides 4-8%) and the absorption (2-5%) described in Chapter 3, the overall uncertainty is estimated to be  $\sim 20\%$ . Notably, the measured  $\epsilon$  composition is in excellent agreement with previous X-ray results (38 at.% Ag at 200°C) [62] and atom probe tomography (40 at.% Ag at 200°C) [61]. The compositional analysis strongly suggests that the  $\epsilon$ - $\zeta$  transformation involves a minimal chemical change if any, and only rearrangement of the solute atoms within GP zones.

Fig. 5.5 shows an embedded  $\zeta$  phase and nearby Al matrix from a HAADF-STEM image, where both regions had approximately the same thickness. The experimental images were compared with simulated images for bulk  $\zeta$  (AgAl) and Al without matrix (see Section. 3.2.6 for multislice simulation details and Section. 3.2.7 for relative contrast comparisons). The peak positions of Al or  $\zeta$  (AgAl) determined in the experiments and simulations match reasonably well. The shoulders in the experimental intensity profile of  $\zeta$  phase correspond to the Al columns in the AgAl model. In the experimental images, the Al-enriched columns in  $\zeta$  are brighter than the Al matrix. However, it does not necessarily mean there is Ag within those columns, as the simulated images also show the same phenomenon. This means that the recorded intensities corresponding to Al columns actually contain a contribution from the scattering by neighbouring Ag columns. It is hard to preclude the presence of Ag in the Al-enriched columns, but there is a distinct possibility that beam spreading [194] causes the increase in intensity. The matrix above and below the precipitate would result in a lower contrast between the Ag-enriched and Al-enriched layers compared to the model. Besides, the atomic positions of bulk Al differ from that of  $\zeta$  in both experiments and simulations, which distorts the pathways for electron scattering and confounds the projected atomic column positions. The  $\mu$ STEM algorithm takes no account of source size, which limits the ultimate resolution of experimental STEM image compared to simulations. But the HAADF-STEM intensity is dominated by Ag, and hence those effects should not change the validity of our results. We are still exploring quantitative STEM to determine the exact composition of an embedded  $\zeta$  phase.

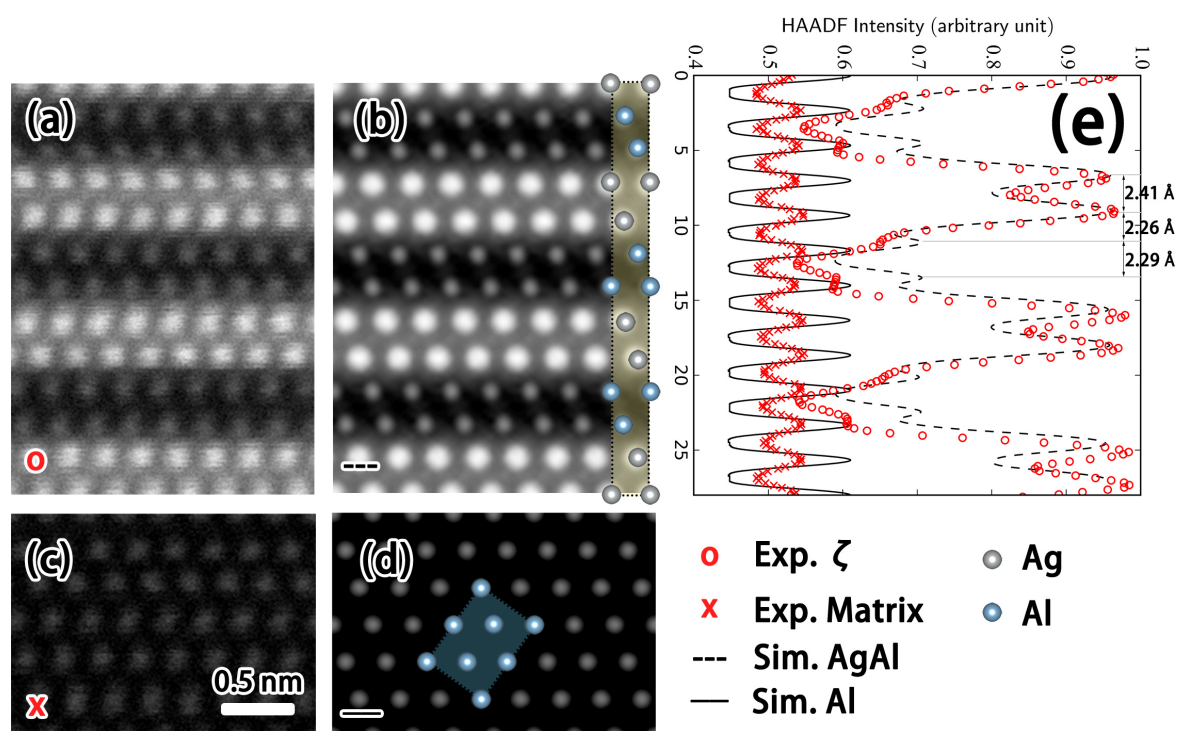


Fig. 5.5 Atomic-resolution HAADF-STEM images obtained from experiments and simulations for a  $\zeta$  precipitate: (a) raw image section of embedded  $\zeta$  precipitate; (b) simulated image of bi-layered AgAl [thickness: 30 nm] with the atomic structure overlaid [grey: Ag, blue: Al]; (c) raw image section of the matrix near the embedded  $\zeta$  shown in (a); simulated image of Al [thickness: 30 nm] with the atomic structure overlaid. (e) The intensity profile of the experimental and simulated images in  $\zeta$  compared to that of the Al matrix. The orientation of the intensity profile is aligned with images (a) and (c). The electron beam is parallel to  $\langle 110 \rangle_{\text{Al}}$ .

Table 5.1 Atomic coordinates of the precipitate  $\zeta$  phase. The listed coordinates are fractional in respect to the simplest trigonal cell with a space group of  $P3$ . It is equivalent to a trigonal cell with a space group of  $R\bar{3}m$  (hexagonal axis) and Wyckoff positions of Ag at (0 0 0.878) and Al at (0 0 0.375). The experimental parameters are  $a_{\text{exp}}=2.88 \pm 0.05 \text{ \AA}$  and  $c_{\text{exp}}=27.35 \pm 0.05 \text{ \AA}$ . The DFT-optimised parameters are  $a_{\text{DFT}}=2.97 \text{ \AA}$  and  $c_{\text{DFT}}=26.88 \text{ \AA}$  for the bulk  $\zeta$  phase and  $a_{\text{DFT}}^{\text{emb}}=2.92 \text{ \AA}$  and  $c_{\text{DFT}}^{\text{emb}}=27.26 \text{ \AA}$  for the embedded  $\zeta$  precipitate phase. The uncertainty in the experimentally determined z coordinates is 0.005.

Site	Experiment			DFT		
	x	y	z	x	y	z
Al(1)	1/3	2/3	0.086	1/3	2/3	0.081
Al(2)	2/3	1/3	0.165	2/3	1/3	0.163
Al(3)	2/3	1/3	0.417	2/3	1/3	0.414
Al(4)	0	0	0.500	0	0	0.496
Al(5)	0	0	0.741	0	0	0.747
Al(6)	1/3	2/3	0.836	1/3	2/3	0.830
Ag(1)	0	0	0	0	0	0
Ag(2)	0	0	0.248	0	0	0.244
Ag(3)	1/3	2/3	0.336	1/3	2/3	0.333
Ag(4)	1/3	2/3	0.580	1/3	2/3	0.577
Ag(5)	2/3	1/3	0.668	2/3	1/3	0.667
Ag(6)	2/3	1/3	0.917	2/3	1/3	0.910

The modulation in the chemical composition by 4 (2 Ag and 2 Al) and the stacking ordering by 3 (ABCABC) require at least 12 close-packed planes to achieve the periodicity of  $\zeta$ , as shown in the atomic structure in Fig. 5.5(b). The bi-layered AgAl model of  $\zeta$  is a trigonal crystal with a space group of  $R\bar{3}m$  (hexagonal axes). The lattice parameters for the bulk  $\zeta$  phase are  $a_{\text{DFT}}=2.97 \text{ \AA}$  and  $c_{\text{DFT}}=26.88 \text{ \AA}$  after DFT optimisation, which agree reasonably well with the experimental measurements for embedded  $\zeta$  precipitates of  $a_{\text{exp}}=2.88 \pm 0.05 \text{ \AA}$  and  $c_{\text{exp}}=27.35 \pm 0.05 \text{ \AA}$ . The embedded  $\zeta$  precipitate calculation gives a much better match with  $a_{\text{DFT}}^{\text{emb}}=2.92 \text{ \AA}$  and  $c_{\text{DFT}}^{\text{emb}}=27.26 \text{ \AA}$ , which means  $\zeta$  precipitates are deformed to accommodate the change in lattice parameters compared with Al. When embedded within the Al matrix,  $\zeta$  is coherent with the matrix displaying an orientation relationship of  $\{111\}_{\text{Al}} \parallel \{001\}_{\zeta}$  and  $\langle 110 \rangle_{\text{Al}} \parallel \langle 100 \rangle_{\zeta}$ . Table 5.1 lists the coordinates of Ag- and Al-containing sites in  $\zeta$ , showing an exceptionally good agreement between experiments and calculations.

Close inspection of the lattice sites reveals that the spacings of the basal planes (including Ag-Ag, Ag-Al and Al-Al) vary along  $\langle 001 \rangle_{\zeta} \parallel \langle 111 \rangle_{\text{Al}}$ . This is further demonstrated in Fig. 5.6 using geometric phase analysis (GPA) of a distortion-corrected HAADF-STEM image in order to map these lattice displacements (see Section 3.2.9 for GPA details). Theoretical displacements of  $\zeta$  relative to Al were calculated based on the DFT-optimised structure of the AgAl model and compared with GPA results in each direction. The effect

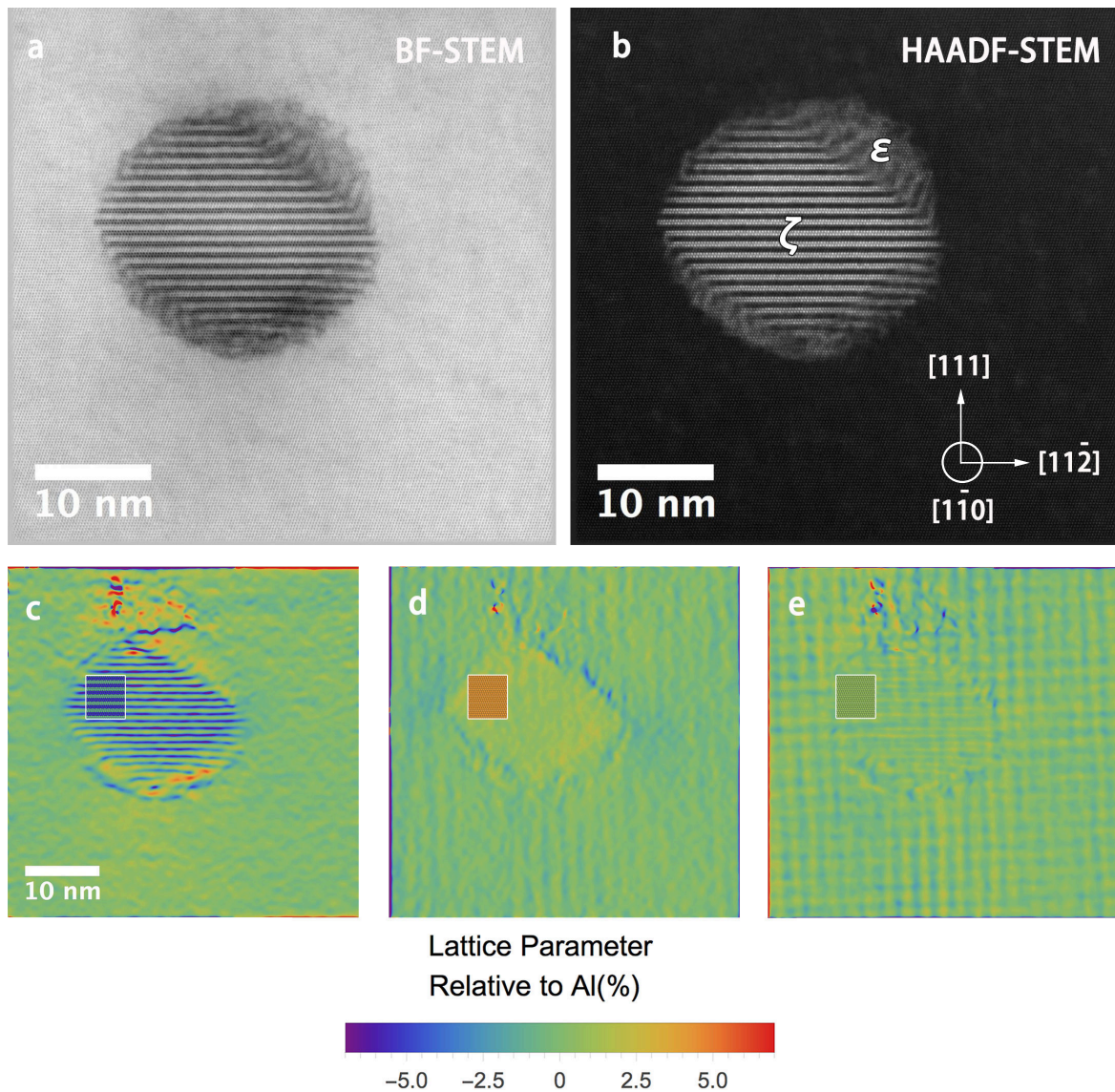


Fig. 5.6 Lattice displacements mapping of a  $\zeta$  precipitate in aluminium. Original (a) BF-STEM and (b) HAADF-STEM images for geometric phase analysis (GPA). The GPA results were compared with simulations based on the DFT-optimised structure of the bi-layered AgAl model (in the white box) in the following directions (c) normal, (d) parallel and (e) sheared with respect to the  $\zeta$  basal planes.

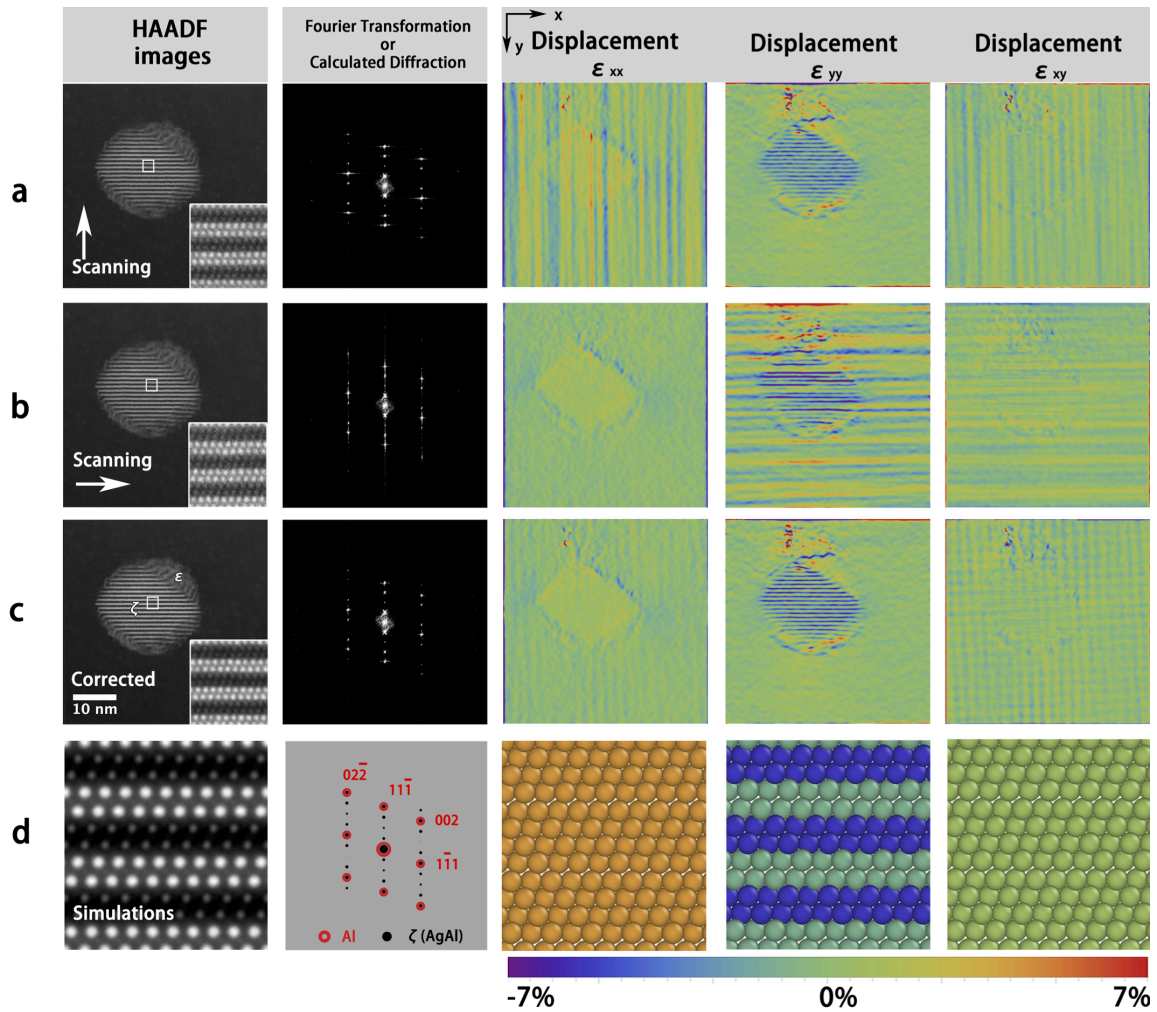


Fig. 5.7 Nonlinear drift correction for geometric phase analysis, in comparison to simulations of bulk AgAl structure. HAADF images (with enlarged inserts), Fourier transform amplitudes and strain field measurements for (a) vertical scan direction, (b) horizontal scan direction, (c) drift-corrected images. (d) Simulations ( $\mu$ STEM and elastic lattice strain calculations) of bulk AgAl structure respectively. The arrows in (a) and (b) indicate the fast scanning directions for each case. The electron beam is parallel to  $\langle 110 \rangle_{\text{Al}}$ . There is noticeable noise in the direction normal to the fast scanning direction as shown in the GPA results, which corresponds to the strikes in Fourier transformations. The kinematic diffraction pattern was calculated by CrystalMaker SingleCrystal software, based on bulk AgAl structure after optimisation by DFT calculations. Red circles highlight the reflections of AgAl that are overlapped with Al (the reflections are indexed).

of scanning noise is demonstrated in Fig. 5.7. Fig. 5.6(c) shows that the displacements in the direction normal to  $\zeta$  basal planes have a clear modulation in both the GPA result and the DFT-optimised structure. Within the  $\zeta$  phase, the local contraction of the lattice is significant at the Al sites as deduced from both GPA and DFT (GPA: -6.5% and DFT:

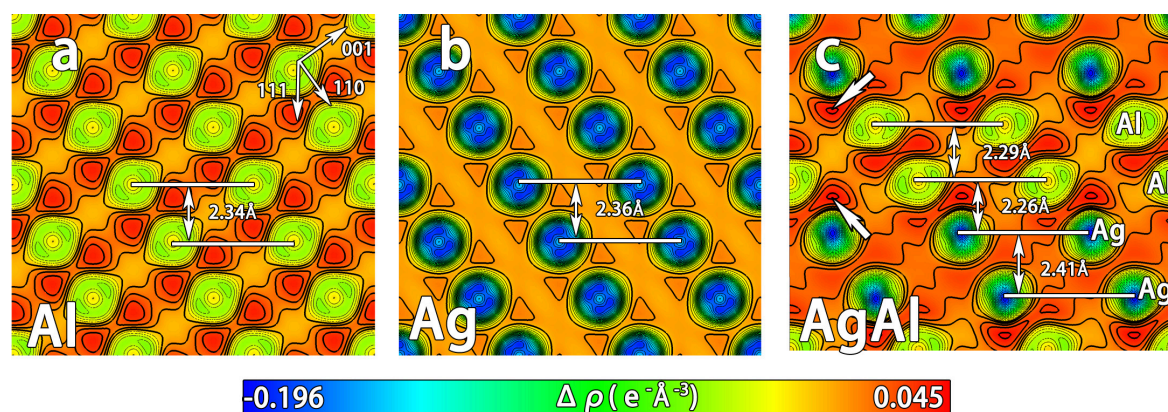


Fig. 5.8 Contour plots of deformed charge density  $\Delta\rho$  on  $\{110\}$  plane section for (a) Al, (b) Ag and (c) proposed AgAl model. Contours are at  $0.01e^{-}\text{\AA}^{-3}$  interval, with the first dark line showing  $\Delta\rho = 0e^{-}\text{\AA}^{-3}$ .

-6.6%), but less at the Ag sites (GPA: 0% and DFT: -1.9%). This remarkable lattice variation between the bi-layers of a  $\zeta$  precipitate is not due to the atomic size difference between Al and Ag; instead, it is a result of different spacings of the basal planes in  $\zeta$  phase. For instance, the inter-planar distance between Al-Ag in  $\zeta$  phase is significantly decreased to 2.26 Å compared to the spacing of 2.34 Å between  $\{111\}_{\text{Al}}$  planes, as shown in Fig. 5.5. DFT calculations of the electronic structures (Fig. 5.8) suggested that the variation in spacing is caused by strong interaction between Al and Ag on the close-packed planes. Fig. 5.8 shows the  $\{110\}$  cross-section of deformed charge densities<sup>12</sup> of pure Al, Ag and AgAl. In AgAl crystal, the charge densities between Al and Ag close-packed planes layers are significantly increased as indicated by white arrows. Specifically, the maximum  $\Delta\rho$  at the tetrahedron centre of Al lattice is  $0.037e^{-}\text{\AA}^{-3}$ , in excellent agreement with previous Wien2K calculation and quantitative CBED experiments [195], while the maximum  $\Delta\rho$  is  $0.014e^{-}\text{\AA}^{-3}$  in Ag lattice and  $0.041e^{-}\text{\AA}^{-3}$  in AgAl lattice. The decreased interplanar spacing between Al and Ag are associated with an increased electron density. The chemical compositions ought to be significantly different between the sequential bi-layers to cause a change of the bond length, which also demonstrates the validity of our model regarding the atomic positions. The experimentally observed displacements are small in the direction along the basal planes of  $\zeta$  (GPA: 0.8% and DFT: 1.8%) in Fig. 5.6(d) and negligible in the shear direction in Fig. 5.6(e), which represents a good agreement between GPA and DFT. Finally, the  $\zeta$  precipitate is coherent within the matrix without any misfit dislocation as evident from the BF-STEM

<sup>12</sup>The deformed charge density  $\Delta\rho$  is defined as  $\Delta\rho = \rho_{total} - \rho_{IAM}$ , where  $\rho_{total}$  is the total charge density and  $\rho_{IAM}$  is the charge density of unbonded atoms in superposition, also known as independent atom model (IAM) [195].

image (see Fig. 5.6(a)). The remaining GP zone  $\varepsilon$  (as labelled in Fig. 5.6(b)) is almost strain-free in all directions, as shown in Fig. 5.6(c-e).

### 5.3 Transformation Pathways: *In-situ* Scanning Transmission Electron Microscopy

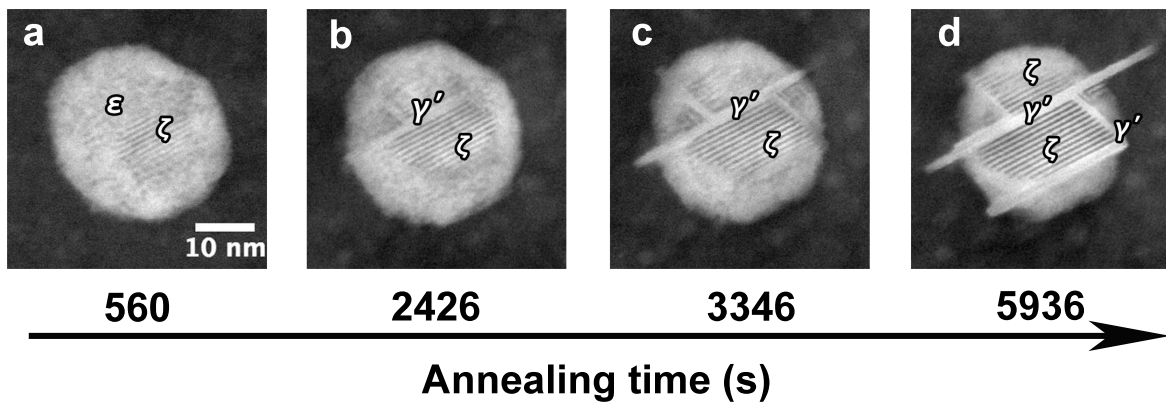


Fig. 5.9 Time-resolved HAADF-STEM images showing the  $\varepsilon$ - $\zeta$ - $\gamma'$  transformation while *in situ* annealed at 150°C. The original sample was oil quenched and aged at 200°C for 7 days. The recording was started 560 s after *in situ* annealing began, giving time to correct drift and reorientation of the crystal due to heating. We should note that the distortions in the images and movie were due to the thermal drift during acquisition. The electron beam is parallel to  $\langle 110 \rangle_{\text{Al}}$ .

The atomic mechanisms associated with phase transformations constitute a cornerstone of modern metallurgy. However, the dynamics of phase transformations are rarely characterised at the atomic scale because of the experimental difficulties in performing such studies. Indeed, studies often focus on the atomic structures before and after phase transformations (for example, against different ageing times), which provides important clues about phase transformations. But this indirect approach may miss many intermediate states. Recently, *in situ* imaging has been successfully applied to resolve many dynamic processes at nano-scale [196]. In the present study, we combined heating in the TEM with an automatic image acquisition script in STEM mode to resolve the *in situ* phase transformations associated with the newly discovered  $\zeta$  phase (see Section. 3.2.3 for details).

Fig. 5.9 shows the microstructure evolution inside a GP zone  $\varepsilon$  during *in situ* annealing at 150°C. The  $\zeta$  phase originated from the local ordering of  $\varepsilon$  and grew in size. Later,  $\gamma'$  assemblies nucleated and grew beside the  $\zeta$  phase, thus resulting in a complicated microstructure

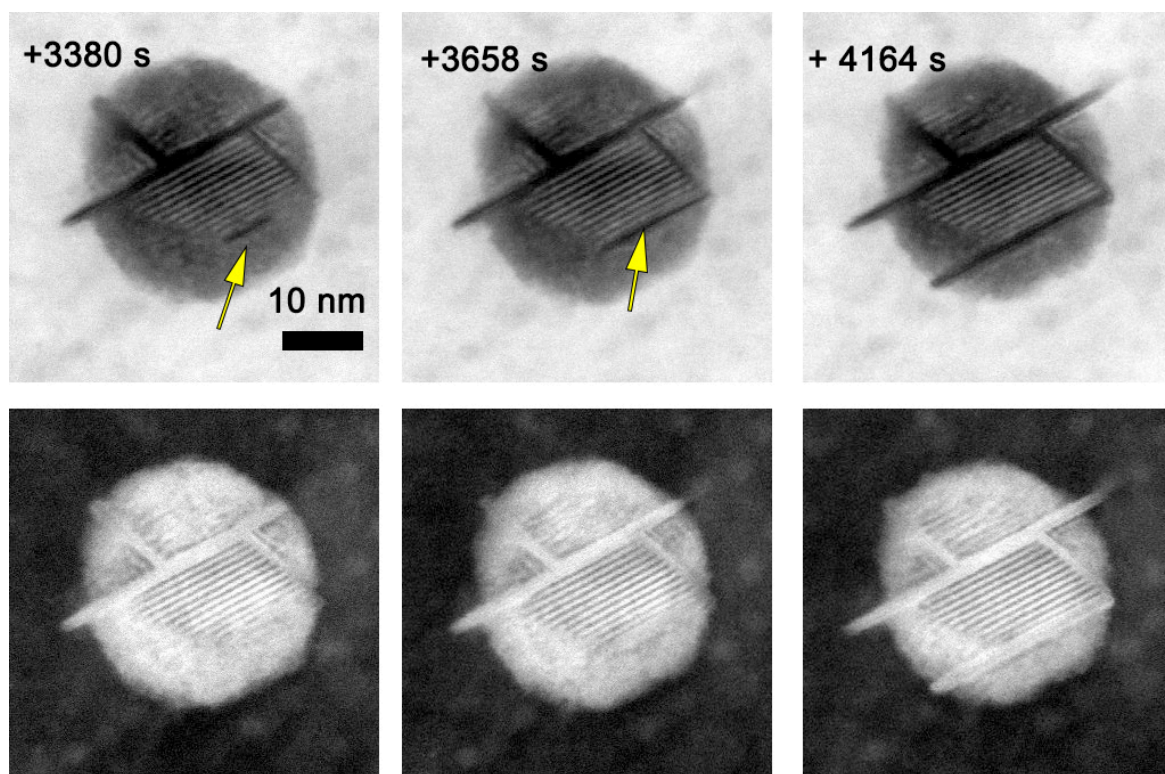


Fig. 5.10 Time-resolved BF- and HAADF-STEM images showing the nucleation of  $\gamma'$  assemblies on defects inside of a GP zone  $\epsilon$ . The nucleation of a stacking fault is indicated by yellow arrows in BF-STEM images.

consisting of the  $\epsilon$ ,  $\zeta$  and  $\gamma'$  phases (see Supplementary Movie<sup>13</sup>). It is worth noting that the contrast change was not simultaneous in BF- and HAADF-STEM images. Fig. 5.10 shows that dark contrast clearly formed inside of a GP zone  $\epsilon$  in BF-STEM images as indicated by yellow arrows. In contrast, there did not have a noticeable change in corresponding HAADF-STEM images. The places where dark contrast initiated in BF-STEM were proven to be the nucleation sites of  $\gamma'$  precipitate phase, suggesting the change of contrast in BF-STEM is related to the formation of stacking faults. It is reasonable to suspect that Ag atoms need time to diffuse from GP zone  $\epsilon$  (38% Ag) to the stacking fault regions where  $\gamma'$  precipitates (67% Ag) were supposed to form. Thus, the contrast change in BF-STEM images was ahead of HAADF-STEM images. However, it is difficult to ascertain the atomic resolution dynamics due to thermal drifting.

The  $\zeta$  phase proved to be relatively robust against electron irradiation and heating, for instance, it survived *in situ* annealing at 150°C for 1.5 hr shown in Fig. 5.9. But the  $\zeta$  phase is a metastable phase in a long run compared to  $\gamma'/\gamma$  phases. This is evident in Fig. 5.11

<sup>13</sup>Supplementary Materials in Ref. [174]. Link: <https://doi.org/10.1016/j.actamat.2017.04.061>

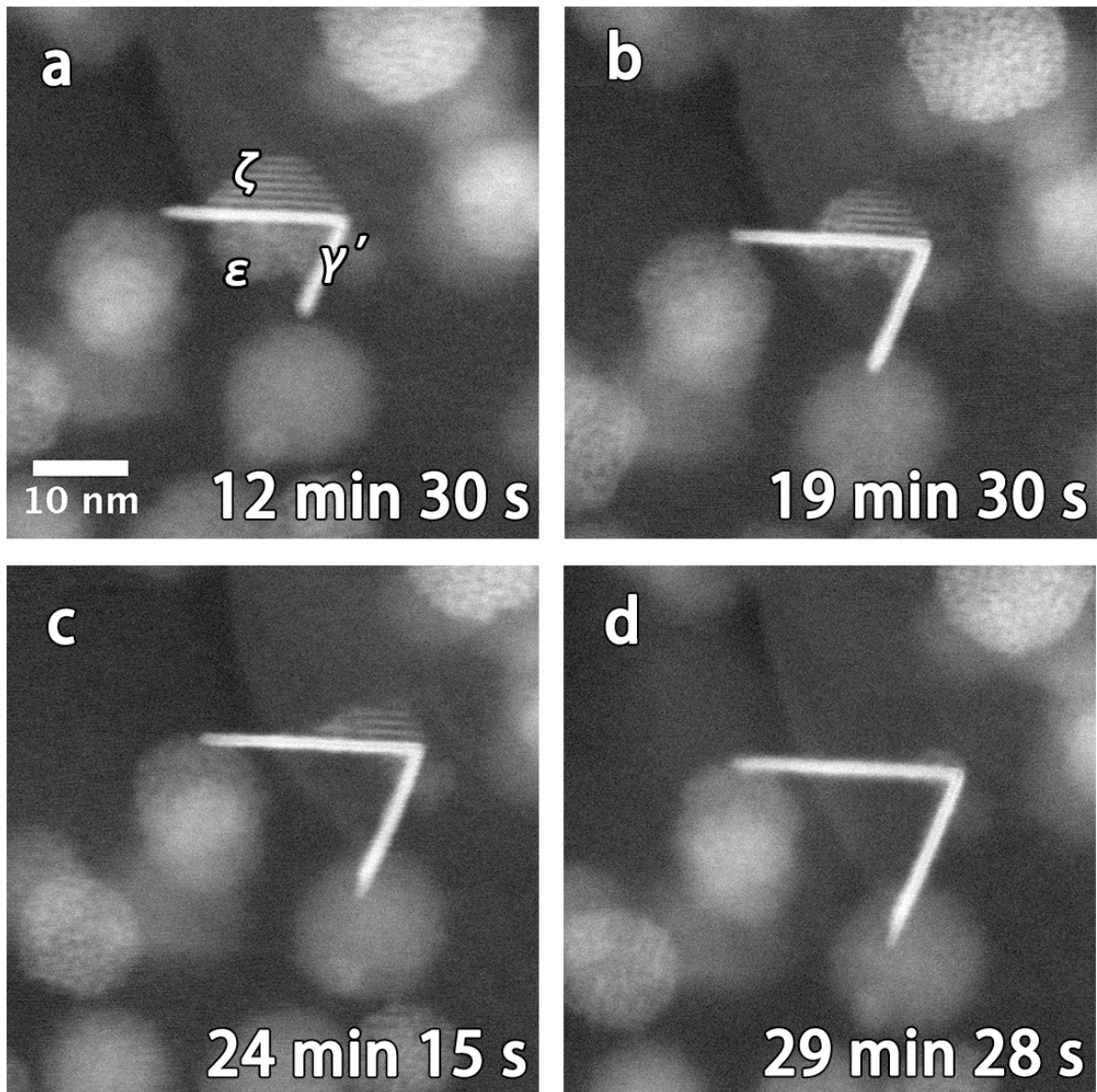


Fig. 5.11 HAADF-STEM images showing the evolution of  $\zeta$  into  $\gamma'$  during *in situ* annealing at 200°C for times as labelled. The original sample was oil quenched and aged at 200°C for 24 h. The electron beam is parallel to  $\langle 110 \rangle_{\text{Al}}$ .

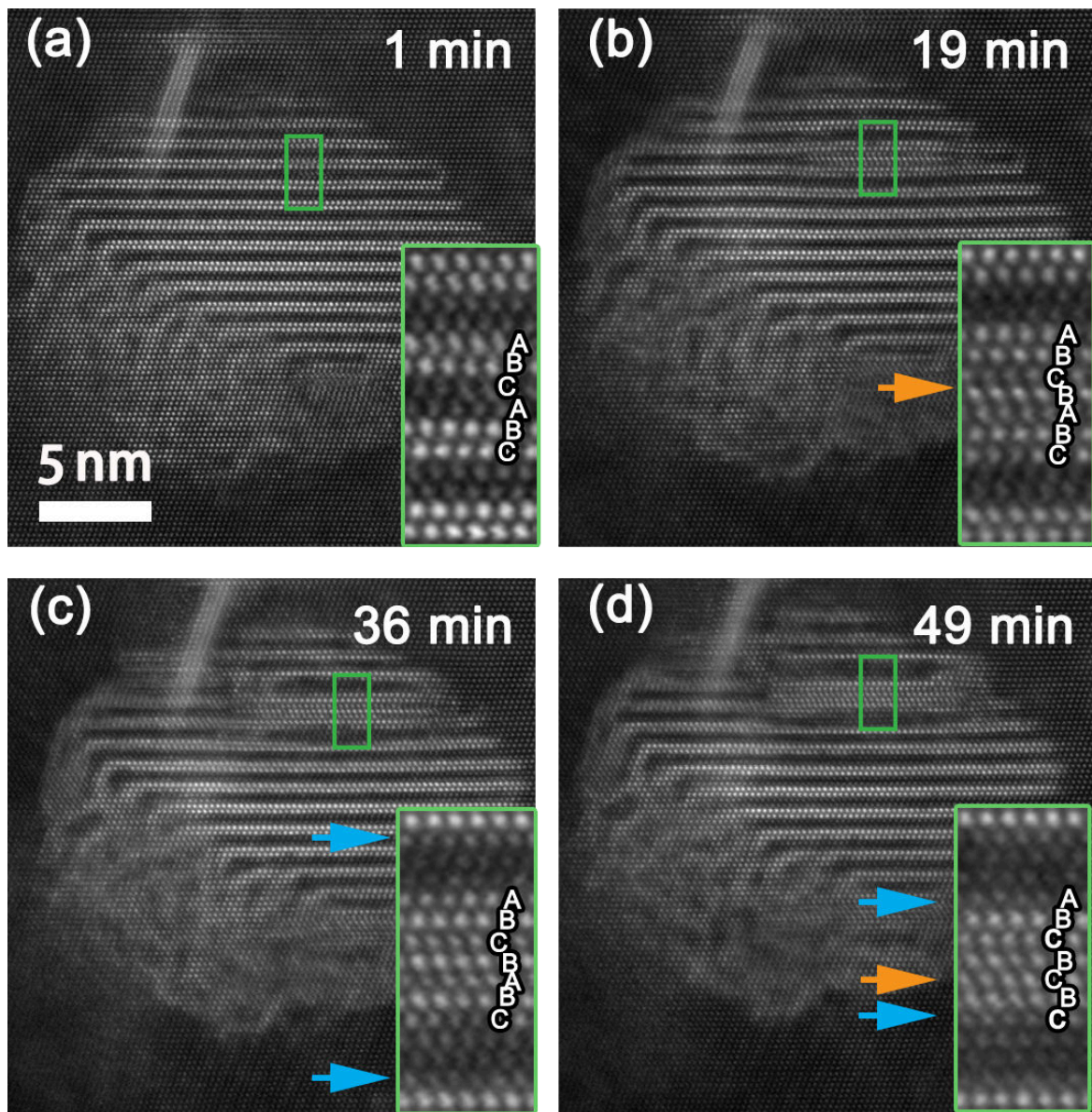


Fig. 5.12 HAADF-STEM images of the  $\zeta$ - $\gamma'$  transformation under electron irradiation at room temperature. The electron beam is parallel to  $\langle 110 \rangle_{Al}$ . The change of stacking is indicated by orange arrows, while the depletion of Ag is indicated by blue arrows.

where the  $\zeta$ - $\gamma'$  transformation during *in situ* annealing was recorded. Fig. 5.11(a) shows both the  $\zeta$  phase and the  $\gamma'$  phase formed inside a GP zone  $\varepsilon$ . Fig. 5.11(b-d) shows that  $\zeta$  and the remaining GP zone shrunk gradually with increasing ageing time until their full dissolution, to the benefit of the growing  $\gamma'$  precipitates. This suggests that Ag atoms diffuse from the metastable phases to the more stable HCP phase which is richer in Ag.

The atomic mechanisms associated with the  $\zeta$ - $\gamma'$  transformation were studied by *in situ* electron irradiation experiments, revealing the explicit role of stacking faults during transformation. The electron beam was scanning with a constantly high current density ( $\approx 5.6 \times 10^5 e^- \cdot nm^{-2} s^{-1}$  in the *Titan*<sup>3</sup>). As shown in Fig. 5.12(a-b), irradiation induced an extrinsic stacking fault between the Al-enriched bi-layers as indicated by an orange arrow (stacking change from ABC-ABC to ABC-B-ABC). The insertion of an extra close-packed plane induced a significant compression strain around the extrinsic stacking faulting in  $[111]_{Al} \parallel [001]_{\zeta}$  direction, Fig. 5.12(b). Meanwhile, the faulted region grew in length and became increasingly enriched in Ag, probably due to the diffusion of Ag atoms from nearby Ag-enriched bi-layers in the  $\zeta$  phase. Fig. 5.12(c) shows that the Ag-enriched bi-layers evolved into Ag-enriched mono-layers indicated by blue arrows. The transformation is accomplished with the extrinsic stacking fault (ABC-B-ABC) replaced by the intrinsic stacking fault (ABC-BC-BC), Fig. 5.12(d).

## 5.4 Thermodynamics: First-principles Calculations, Strain Energy and Entropy

The clustering process during the decomposition of the solid solution is governed by the energy of different solute configurations and the barriers between them. To understand the clustering of Ag in Al, we calculated the formation energy of various Ag clusters by DFT as summarised in Table 5.2. The solid solution is not energetically stable, with a defect energy of 89 meV/Ag atom, which drives the solid solution to decompose. For bi-atom Ag clusters, the nearest neighbours along  $\langle 110 \rangle_{Al}$  are preferred compared with the second nearest neighbours along  $\langle 001 \rangle_{Al}$ . A tri-atom cluster on either  $\{110\}_{Al}$  or  $\{111\}_{Al}$  planes is almost as stable as segregated Al and Ag in bulk. The calculated formation energy of Ag monolayer aggregation on  $\{111\}_{Al}$  is -65 meV/Ag atom, which is significantly lower than for Ag on the other low-index crystallography planes. This energy is substantial, given the thermal energy at 200°C is 40 meV. Not surprisingly,  $\{111\}_{Al}$  planes become the basal planes for the metastable  $\zeta$  phase and the equilibrium  $\gamma'/\gamma$  phases.

Table 5.2 DFT calculations for the preference of Ag clustering in Al matrix.  $E_F^{\text{Ag}}$  is the formation energy per Ag atom. The 1<sup>st</sup> nearest neighbour stands for two Ag atoms in the nearest neighbour configuration in a  $\langle 110 \rangle_{\text{Al}}$  direction in FCC Al lattice. Similarly, the 2<sup>nd</sup> nearest neighbour is two Ag atoms next to each other in a  $\langle 001 \rangle_{\text{Al}}$  direction.

Number of Ag Atoms	Configurations	$E_F^{\text{Ag}}$ (meV)
1 Ag (Solid Solution)	N/A	89
2 Ag	1 <sup>st</sup> nearest neighbour	44
	2 <sup>nd</sup> nearest neighbour	99
3 Ag	$\{001\}_{\text{Al}}$	27
	$\{110\}_{\text{Al}}$	-1
	$\{111\}_{\text{Al}}$	-1
Ag plane	$\{001\}_{\text{Al}}$	431
	$\{110\}_{\text{Al}}$	66
	$\{111\}_{\text{Al}}$	-65

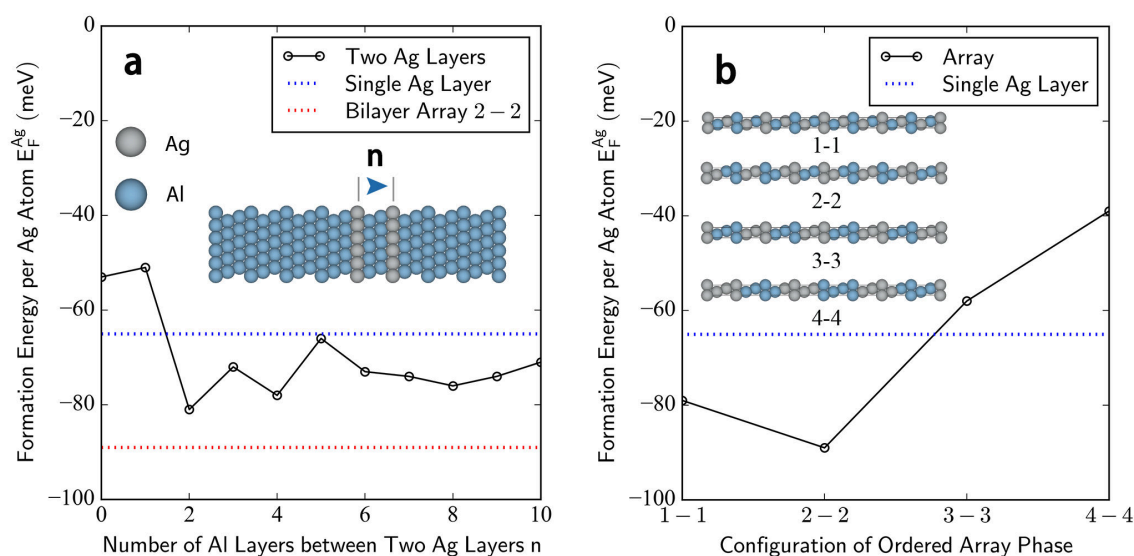


Fig. 5.13 DFT calculations illustrating the preference of  $\{111\}_{\text{Al}}$  planes for Ag aggregation in aluminium. (a) The energetics of two Ag  $\{111\}_{\text{Al}}$  planes separated by a varying number “ $n$ ” of Al planes as shown in the schematic diagram. (b) Energetics of different periodic arrays with a composition of AgAl. For instance, “1-1” means the modulation of one Ag layer and one Al layer as shown in the schematic diagram.

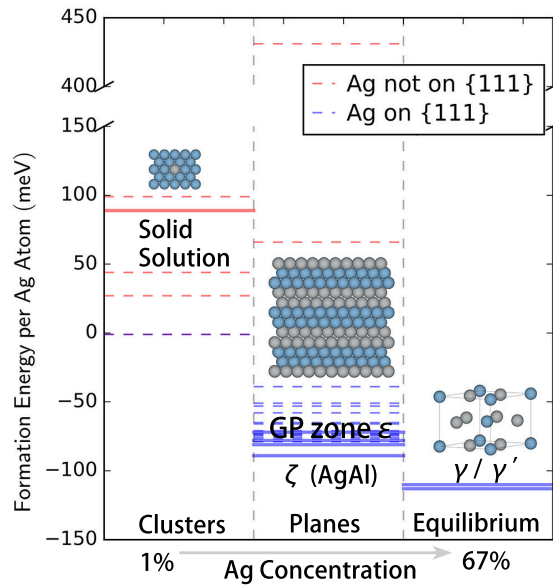


Fig. 5.14 Energetics of Ag clustering from the solid solution to the equilibrium  $\gamma$  phase. Different configurations of Ag on  $\{111\}_{\text{Al}}$  planes are shown in blue while configurations of Ag clustering on other crystallographic planes are shown in red. The phases in the transformation sequence are highlighted with a bold unbroken line with their corresponding names and atomic structures, while other configurations calculated are shown as dashed lines.

With Ag placed on  $\{111\}_{\text{Al}}$  planes, we investigated the preferential distance between two Ag layers in aluminium. A series of calculations were performed with varying Al layers between two Ag layers as shown in Fig. 5.13. Interestingly, a distance ranging from two to four  $\{111\}_{\text{Al}}$  Al layers between the two Ag layers is favourable, as a closer spacing yields a considerably higher energy state. The lowest energy structure corresponds to two Al layers between two Ag layers. The energy is further lowered when Ag layers are assembled according to a periodic layered array as shown in Fig. 5.13(b). For a fixed composition of AgAl and ABCABC stacking, the bi-layered array is the most stable, which demonstrates the validity of our model for the  $\zeta$  phase from an energetics perspective. As summarised in Fig. 5.14, each phase transformation is accompanied by a decrease in energy. From clusters containing only a few atoms to the equilibrium phase  $\gamma$ , the Al-Ag system lowers its energy by ordering Ag solute on  $\{111\}_{\text{Al}}$  planes in the Al matrix. The formation energy of the complex GP zone  $\epsilon$  is about 72–81 meV/Ag atom, as approximated by the energy range of layered Ag aggregation with favourable spacings. The formation energy of the new phase  $\zeta$  (AgAl) is 89 meV/Ag atom, the lowest in terms of ordered Ag planes on  $\{111\}_{\text{Al}}$  prior to the FCC-HCP transformation, which agrees with our *in situ* observations (see Fig. 5.11).

The enthalpy difference between the GP zone  $\epsilon$  and the  $\zeta$  phase is as little as 8–17 meV/Ag atom. The free energy difference between those two phases should be even smaller: the strain

energy and configurational entropy do not favour the  $\varepsilon$ - $\zeta$  transformation. Specifically, GP zones  $\varepsilon$  are coherent with almost no strain in the Al matrix, as evident in Fig. 5.6. In contrast,  $\zeta$  precipitates are still coherent but displaying alternating strain along  $\langle 111 \rangle_{\text{Al}}$  directions according to our experiments and simulations (see Fig. 5.7), which gives  $\zeta$  precipitates a higher strain energy comparing to GP zones  $\varepsilon$ . Based on elastic theory for a spherical precipitate with anisotropic strain, the strain energy contribution  $E_e$  of an embedded  $\zeta$  precipitate is estimated using the following equation:

$$E_e = \mu \delta^2 V, \quad (5.1)$$

where  $\mu$  is the shear modulus, which is assumed to be the same for both the  $\zeta$  precipitate and aluminium matrix;  $\delta$  is the averaged strain along  $\langle 001 \rangle_{\zeta} \parallel \langle 111 \rangle_{\text{Al}}$ , given the strains in other directions are negligible. Here we assume that Poisson's ratio is 1/3 for both the matrix and the precipitate.  $V$  is the atomic volume of  $\zeta$ , *i.e.* the ratio of the unit cell volume and the number of atoms within the cell. The strain energy is estimated to be 3 meV/atom, or 6 meV/Ag atom with the composition of AgAl. Also, GP zones  $\varepsilon$  have a higher configurational entropy due to the chemical inhomogeneities, in contrast to a well-ordered phase like the  $\zeta$  phase. The entropy of GP zones  $\varepsilon$  is difficult to estimate given their complex and disordered structure, but the value should be in between that for a well-ordered phase and a well-mixed alloy using the equation

$$\Delta S_{\text{mix}} = -k_B (X \ln X + (1 - X) \ln(1 - X)), \quad (5.2)$$

where  $\Delta S_{\text{mix}}$  is the mixing entropy of the binary alloy,  $k_B$  is the Boltzmann constant,  $X$  is the composition of the binary alloy. For GP zones  $\varepsilon$  with the composition of Al-40 at.%Ag, the configurational entropy is  $0.67 k_B/\text{atom}$ . In practice, the Bragg-Williams approximation of Eq. 5.2 overestimates the configurational entropy as it neglects any ordering. The short range and long-range order can be incorporated into the equation by considering the probabilities of bonds between Al-Al, Ag-Ag and Al-Ag [197]. According to thermodynamics, such probabilities can be calculated based on the bond energies, usually between nearest neighbours. The bond energies are assumed to be constant while the bond fractions are varying for different configurations, no matter whether solute atoms are isolated or clustered. This simplification violates our DFT calculations that Al-Ag bond is unstable in solid solution but the bond becomes stable when Ag atoms are placed on  $\{111\}_{\text{Al}}$  planes with surrounding Al close-packed planes. An accurate 3D reconstruction of the chemical distribution from the tilt series should be useful for the direct measurement of ordering. New numerical computation techniques need to be used for the purpose of entropy estimation. Nevertheless,

the contribution from configurational entropy must be small during phase transformations in the Al-Ag system, as it would otherwise prevent any kind of ordering and phase separation. We have not considered vibrational entropy in this study.

## 5.5 Discussion

The bi-layer phase first reported herein is a new phase in the Al-Ag system. We propose to name it the  $\zeta$  phase, by analogy with the patterned skin of the zebra. HAADF-STEM images revealed the Ag ordering on  $\{111\}_{\text{Al}}$  planes, starting from a small cluster to a large GP zone (see Fig. 4.10). The positive defect energy of Ag in aluminium is consistent with previous calculations [24] that explains the driving force for the decomposition [53]. For comparison, Au has almost an identical size to Ag, yet Au displays a very negative defect energy in Al [33]. It is the electronic difference between Ag and Au in aluminium that leads to completely different clustering and precipitation behaviours, either in the binary alloys [33][this work] or when they are added to Al-Cu alloys [31, 85]. Our DFT calculations illustrate the preference of Ag aggregation on  $\{111\}_{\text{Al}}$  planes in Al-Ag binary alloys, which also occurs at the early stage of ageing in Al-Cu-Mg-Ag alloys [37, 104] and Al-Cu-Li-Mg-Ag alloys [198]. During ageing,  $\{111\}_{\text{Al}}$  planes enriched in Ag within GP zones  $\varepsilon$  begin to move away from each other and form Ag depletion regions as shown in Fig. 4.10. The ordering of Ag clearly increases with ageing time, while the depletion width remains about two to four  $\{111\}_{\text{Al}}$  layers. The unique clustering behaviour can be understood from our DFT calculation that Ag prefers to be on  $\{111\}_{\text{Al}}$  planes but not with the  $\{111\}_{\text{Al}}$  planes close to each other (see Fig. 5.13). The favourable spacing is around two to four Al  $\{111\}_{\text{Al}}$  planes, which is in excellent agreement with our experiments. The chemical ordering within GP zones  $\varepsilon$  develops faster in the water-quenched sample than the oil-quenched sample, because more quenched-in vacancies are present to mediate diffusion at the early stage of ageing. Ag also needs diffusion in the late stage of ageing to transform the mid-range order exhibited by GP zones  $\varepsilon$  to the long-range order exhibited by the bi-layered  $\zeta$  phase. The requirements of vacancies at different ageing stages inspired us to manipulate thermal and mechanical histories of alloys.

The free energy landscape can reveal the transformation pathways between different phases. But based on DFT alone, one cannot rationalise the difference in  $\zeta$  phase formation between conventional heat treatments and *in situ* annealing experiments. After considering the strain energy and the entropy contribution, there is almost no energy difference between GP zone  $\varepsilon$  and the  $\zeta$  phase. But the rearrangement of Ag atoms associated with the  $\varepsilon$ - $\zeta$  transformation is expected to have a high energy barrier. Therefore, the local energy minimum

state of  $\zeta$  is hardly visited during precipitation in Al-Ag alloys. However, the experimental fact that GP zones  $\varepsilon$  transform to the  $\zeta$  phase and eventually  $\gamma'$  phase demonstrates that the free energy of  $\zeta$  phase is indeed lower than that of  $\varepsilon$  phase. It means that their thermal and mechanical histories must be taken into account to understand different phase transformation pathways. We may appreciate this phenomenon by considering that the  $\zeta$  phase evolves through the chemical ordering of GP zone  $\varepsilon$  on  $\{111\}_{\text{Al}}$  with the assistance of induced defects.

Our *in situ* STEM microscopy revealed many intermediate steps during phase transformations that couldn't otherwise be accessed. The existence of the  $\zeta$  phase is associated with new phase transformation pathways that gives a more gradual change in terms of the chemical compositions and atomic structures. A  $\zeta$  precipitate (50 at.% of Ag in the AgAl model) develops from the increased local ordering of a GP zone  $\varepsilon$  (38 at.% of Ag at 200°C) before transforming into HCP  $\gamma'/\gamma$  (67 at.% Ag). Fig. 5.9 and Fig. 5.11 clearly show that  $\zeta$  is an intermediate phase between GP zone  $\varepsilon$  and  $\gamma'$ . The absence of shear in  $\zeta$  minimises the energy barrier for its formation, which restricts  $\gamma'$  nucleation [81]. Previous calculations also have shown that pure Ag layers lower the stacking fault energy in Al [80], which may offer a pathway for a  $\zeta$  to  $\gamma'$  transformation. As shown in Fig. 5.9 and Fig. 5.12, stacking faults are critical for the nucleation of a  $\gamma'$  phase. However, some questions are still open regarding the relationship between  $\zeta$  and  $\gamma'$ . Although our electron tomography indicated that  $\zeta$  can form independently from  $\gamma'$  (See Fig. 5.4), the two metastable phases were generally seen in association with one another (Fig. 5.9, 5.11). We have seen  $\zeta$  absorbed by an existing  $\gamma'$  assembly in Fig. 5.11, instead of initiating new  $\gamma'$  precipitates. In contrast, electron irradiation experiments revealed the direct  $\zeta$ - $\gamma'$  transformation at the atomistic level in Fig. 5.12. The energy barrier associated with the  $\zeta$ - $\gamma'$  transformation has not been calculated yet but should be feasible in a future study. In the currently available Al-Ag phase diagram [52], there is no intermediate phase in the composition range between  $\text{Ag}_2\text{Al}$  and Al except the metastable GP zones. Several possible structures with the composition of AgAl were predicted using cluster expansions of DFT results [74, 88]. However, all predictions either have HCP stacking rather than the FCC stacking displayed by  $\zeta$  phase [74], or have FCC stacking but with bi-layers aligned in  $\langle 110 \rangle_{\text{Al}}$  directions [88] (see Fig. 2.31). The large periodic size of  $\zeta$  along  $\langle 001 \rangle_{\zeta} \parallel \langle 111 \rangle_{\text{Al}}$  means such structures are difficult to predict via the cluster expansion method. This points out the importance of atomic resolution electron microscopy for providing critical structural information for atomistic calculations.

The  $\zeta$  phase in the Al-Ag system has structural similarities with layered Ag segregations to precipitate interfaces in various aluminium alloys. They have a deeper connection regarding the transformation mechanisms as well. It is very interesting that Al-Ag alloys have a

poor mechanical performance but numerous aluminium alloys with a minor addition of Ag constitute the strongest and most thermally stable series [17]. Taking the famous example of Al-Cu-Mg-Ag alloys, the  $\Omega$  phase is responsible for their outstanding mechanical performance and thermal stability [17]. The  $\Omega$  phase can be considered as a distorted  $\theta$  ( $\text{Al}_2\text{Cu}$ ) on  $\{111\}_{\text{Al}}$ , which is originally body-centred tetragonal forming on  $\{100\}_{\text{Al}}$  planes [199, 200]. To reorient Cu atoms from  $\{100\}_{\text{Al}}$  planes to  $\{111\}_{\text{Al}}$  planes, Mg is essential to minimise the misfit of the  $\Omega$  phase along its c-axis, which can be as large as -9.3% matching half unit cell of the  $\Omega$  phase with multiples of  $\{111\}_{\text{Al}}$  d-spacing [13]. Indeed, the  $\Omega$  phase has not been found in Al-Cu or Al-Cu-Ag alloys [85], and only very few  $\Omega$  precipitates appear in Al-Cu-Mg alloys where the dominant precipitate phase is the S phase [17]. However, this fact, as well as our unpublished DFT calculations [201], suggest Mg itself does not have much tendency to drive the segregation of Cu atoms on  $\{111\}_{\text{Al}}$  planes. As we have shown above, Ag prefers to aggregate on  $\{111\}_{\text{Al}}$  planes in aluminium (see Table 5.2). Furthermore, Ag and Mg are known to interact strongly with each other [36]. The addition of Ag attracts Mg to the  $\{111\}_{\text{Al}}$  planes, which greatly promotes the  $\Omega$  phase and suppresses the S phase. This is evident by the existence of a monolayer of Ag associated with a mono-layer of Mg at the coherent interface of  $\Omega$ -Al; such interfacial phase can independently exist at the early stages of precipitation [13]. Precipitates nucleate from solute clusters, and hence the determination of the location of the clusters is important. As Ag decomposes quickly from the solid solution and interacts strongly with other solute elements and quenched-in vacancies, the preference of Ag aggregation provides a special kind of heterogeneous nucleation site. The nucleation sites are strongly biased on  $\{111\}_{\text{Al}}$  planes, thus giving Ag the ability to modify subsequent precipitation. Interestingly, Ag also aggregates on  $\{0001\}$  planes in Mg ( $\{0001\}/\{111\}$  planes are the close-packed planes in HCP/FCC), stimulating precipitation in magnesium alloys [202, 203]. It is not the purpose of this work to unify the microalloying mechanisms of Ag in aluminium, but we hope the present study on the Al-Ag binary system may provide a useful reference for the phase transformations of complicated aluminium alloys containing Ag. Particularly, the preference of specific crystallographic planes for Ag aggregation may shed light on its microalloying effects in aluminium.

## 5.6 Conclusion

We performed scanning transmission electron microscopy to characterise the atomic structure of  $\zeta$  phase and associated phase transformations. The energetics of Ag clustering within aluminium were studied by density functional theory. The main conclusions are as follows:

1. We discovered a new precipitate phase which we named  $\zeta$  in the Al-Ag system. The  $\zeta$  phase is an intermediate precipitate phase between GP zone  $\varepsilon$  and  $\gamma'/\gamma$  phases in the Al-Ag precipitation sequence. The structure of  $\zeta$  is characterised by the long-range order of bi-layers enriched in Al and Ag on alternating  $\{111\}_{\text{Al}}$  planes. The  $\zeta$  phase is coherent and displays alternating lattice displacements relative to the aluminium matrix in  $\langle 111 \rangle_{\text{Al}}$ . The composition of  $\zeta$  is close to AgAl.

2. The detailed  $\varepsilon$ - $\zeta$ - $\gamma$  transformations were revealed by *in situ* scanning transmission electron microscopy. The  $\zeta$  phase originates from the local ordering of GP zones  $\varepsilon$  on  $\{111\}_{\text{Al}}$  planes. The ordering of Ag atoms leads to both  $\zeta$  phase and  $\gamma'$  phase. In particular, the formation of the  $\zeta$  phase is often in association of the  $\gamma'$  phase. The  $\zeta$ - $\gamma'$  transformation is initiated by stacking faults.

3. The fast decomposition from the solid solution can be explained by the positive defect energy of Ag atoms in the aluminium matrix. The chemical inhomogeneities within GP zones  $\varepsilon$  is caused by Ag aggregation on  $\{111\}_{\text{Al}}$  planes with favourable spacing. The fast decomposition and the preferred close-packed planes for aggregation are intrinsic properties of Ag in aluminium. Those properties provide heterogeneous nucleation sites on  $\{111\}_{\text{Al}}$  planes when Ag is microalloyed in aluminium alloys and fundamentally influence precipitation.

# Chapter 6

## Interfacial Structures of the HCP Precipitate $\gamma'/\gamma$ Phases

### 6.1 Introduction

Precipitation takes place through nucleation and growth, which are accompanied by the formation and migration of heterophase interfaces between matrix and precipitates. Appendix A reviews the importance of interface during phase transformations in terms of thermodynamics and kinetics. However, little is known about the atomic mechanisms of interface motion even for the simplest phase transformations. Textbooks [10, 15] often choose the  $\gamma$  precipitate in Al-Ag alloys as an example of simple precipitate-matrix interfaces. Yet a previous TEM study [84] and a recent STEM study [70] demonstrated a far greater complexity than expected: the coherent interface has Ag segregation and the semicoherent interface is saw-toothed (see Fig. 2.29). In particular, the dislocation structure cannot be determined at the saw-tooth semicoherent interface. Thus, it is the purpose of this chapter to characterise the interfacial structures of  $\gamma'/\gamma$  precipitates with atomic-resolution STEM and resolve the interfacial dislocations. We also estimated the associated interfacial energies using first-principles calculations. In Chapter 4, we found that individual  $\gamma'$  plates grow with increasing ageing time while  $\gamma'$  assemblies resist coarsening (Fig. 4.5). These mysterious precipitation behaviours can be rationalised through the atomic-scale structures of the interfacial dislocations. This chapter also explores the complicated coupling between defects and chemistry confined at interfaces, which gives new insights into the atomic mechanisms of solid-state precipitation.

Section. 6.2 presents a characterisation of the coherent interface of  $\gamma'/\gamma$  precipitates. Ag segregation at the coherent interface was confirmed by comparing STEM experiments and

multislice image simulations. The driving force for Ag segregating at the coherent interface was explained by first-principles calculations of embedded  $\gamma'$  precipitates with different thicknesses.

Section. 6.3 presents a characterisation of the semi-coherent interface of  $\gamma$  precipitates. The saw-tooth interface was explained with interfacial energy calculations. In addition to the one reported in Ref. [70], a new type of semicoherent interface was discovered. The atomic positions of each individual column were determined at the interfaces, which gave reliable models for atomistic calculations. A dislocation extraction algorithm was used to analyse those models and revealed the dislocation structures at interfaces. We proposed an interfacial dislocation reaction model that may explain the occurrence of both types of interfaces.

Section. 6.4 presents a characterisation of the  $\gamma$  precipitate-precipitate junctions. These junctions were found to introduce the coupling between defects and chemical segregations. *In situ* experiments revealed the role of the interfacial dislocations during precipitate growth.

The results in this chapter are not yet published.

## 6.2 The Coherent Precipitate-Matrix Interface

The broad interface of  $\gamma'$  precipitates has an excellent coherency with the aluminium matrix, matching the close-packed planes between HCP and FCC ( $\{0001\}_{\gamma'} \parallel \{111\}_{Al}$ ). For the HCP  $\gamma'$  phase, the nearest neighbour distance is 2.89Å within the close-packed planes and the close-packed planes spacing is 2.30Å. For comparison, those two distances for FCC Al are 2.85Å and 2.33Å respectively, leading to 1.4% strain on the close-packed planes and -1.3% strain normal to the close-packed planes. A previous STEM study showed that a mono-layer of Ag segregates at the coherent interface; this Ag-rich layer has the FCC stacking outside of the thin HCP  $\gamma'$  precipitate [70]. But the reason behind the Ag segregation is yet to be resolved. This section focuses on characterising the interfacial chemistry and calculating the associated energetics. Fig. 6.1 shows the microstructure of  $\gamma'$  precipitates at an early and a late stage of ageing, viewing along the  $\langle 110 \rangle_{Al}$  directions. Blue arrows indicate the mono-layer Ag segregation as reported in Ref. [70] (see Fig. 2.28 for comparison). However, apart from this known segregation, a close inspection of the next layer inside the precipitate also showed Ag segregation, as indicated by red arrows. As shown in Fig. 6.1(b) and the corresponding line profile, the intensity is higher at the interface than the centre of precipitate, suggesting that the Ag composition at this layer is higher than that of  $\gamma'$  phase ( $Ag_2Al$ ). Fig. 6.2 shows the precipitate at different stages of ageing, as viewed in a  $\langle 112 \rangle_{Al}$  direction. It is clear that interfacial Ag segregation is far more pronounced for  $\gamma'$  precipitates with

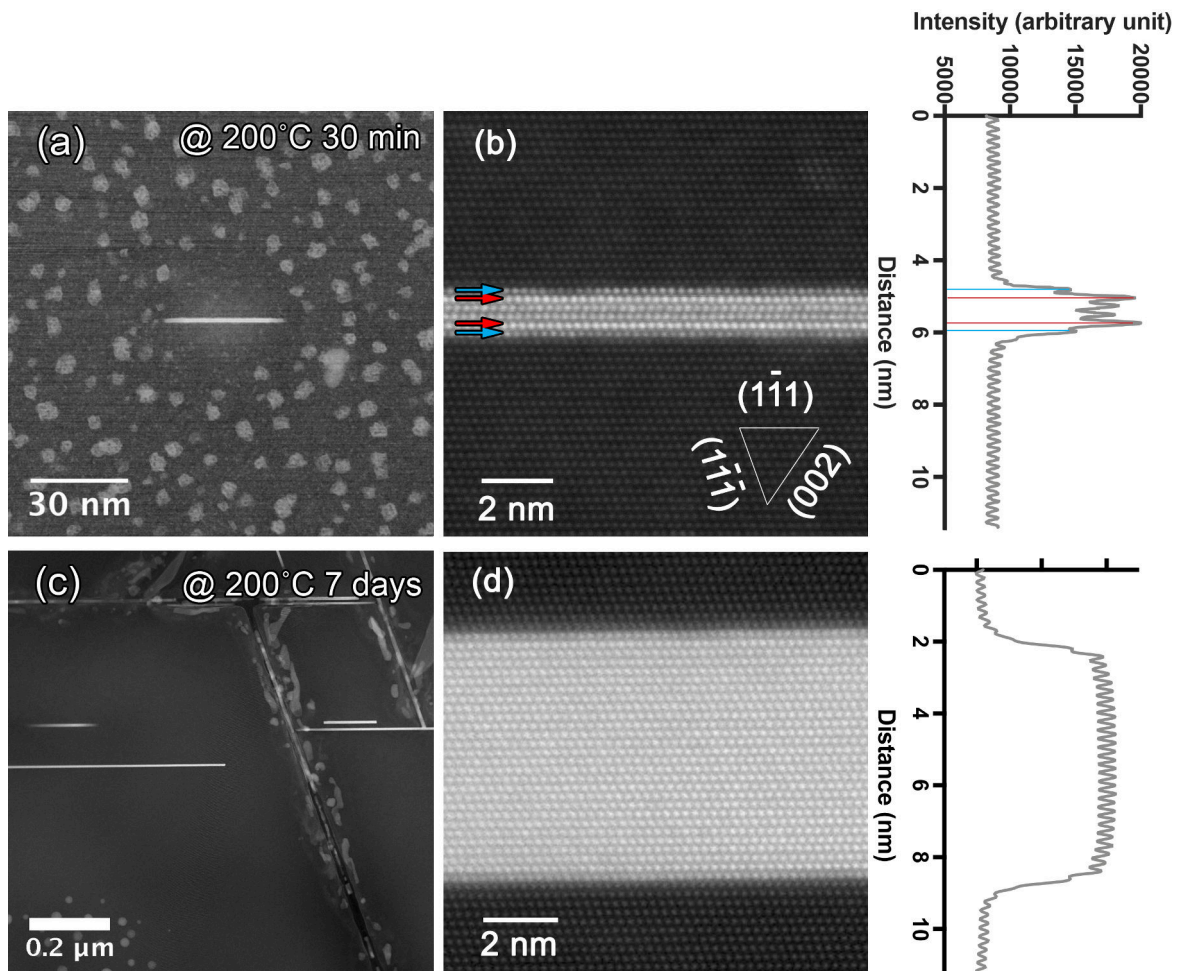


Fig. 6.1 HAADF-STEM images of  $\gamma'$  coherent precipitate-matrix interface viewed in a  $\langle 110 \rangle_{\text{Al}}$  direction. (a-b) Low magnification and high magnification images of the alloy aged at  $200^\circ\text{C}$  for 30 min, where blue arrows indicate the Ag segregation as reported in [70] while red arrows indicate the Ag segregation found in this study. (c-d) Low magnification and high magnification images of the alloy aged at  $200^\circ\text{C}$  for 7 days, where the interfacial Ag segregation was not clear. Intensities across the precipitates are plotted for both high magnification images.

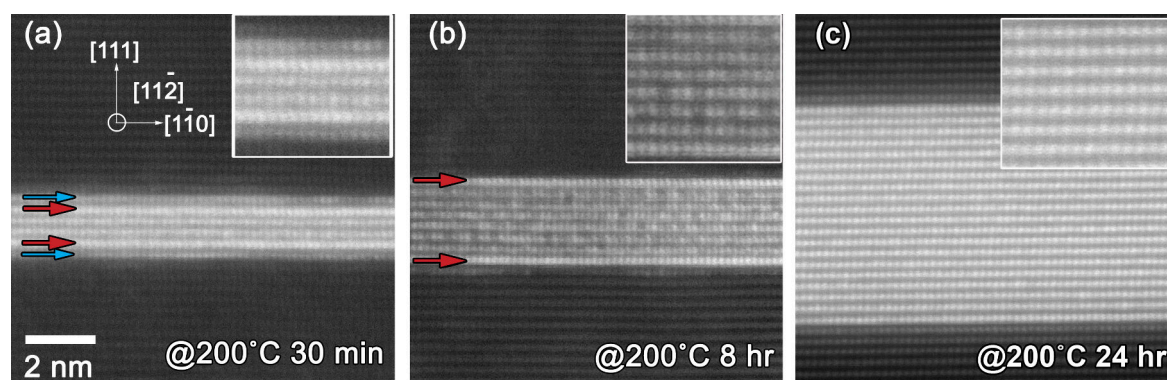


Fig. 6.2 HAADF-STEM images of the  $\gamma'$  coherent precipitate-matrix interface viewed in a  $\langle 112 \rangle_{\text{Al}}$  direction. The alloy aged at 200°C for (a) 30 min, (b) 8 hr and (d) 24 hr, where the blue arrows indicate the Ag segregation as reported by previous authors in [70], while the red arrows indicate the Ag segregation identified in this study.

a small thickness than precipitates with a large thickness. For more than 100 precipitates examined, this observation was consistent when viewing in both directions.

Image simulations were performed to compare the contrast of the same precipitate with and without interfacial Ag segregation. Fig. 6.3(a-c) shows a brighter contrast with the interfacial layers occupied by 100% Ag compared to  $\text{Ag}_2\text{Al}$  (66% Ag) in a  $\langle 110 \rangle_{\text{Al}}$  direction. This result qualitatively agrees with the experiments. Quantitative STEM studies are still on-going to determine the exact composition at the coherent interface. The simulation of the  $\gamma'$  precipitate in a  $\langle 112 \rangle_{\text{Al}}$  direction also demonstrates a similar effect and gives additional opportunity to examine the short-range order of the  $\gamma$  phase on its close-packed planes. As shown in Fig. 2.18, in the Neumann's model, each Al atom is surrounded by 6 Ag atoms on the close-packed planes. There are two variants, corresponding to two different orientation along  $\langle 112 \rangle_{\text{Al}}$ . Simulations were performed for both  $\langle 112 \rangle_{\text{Al}}$  variants and for the thinnest (1 unit-cell thick<sup>14</sup>) embedded  $\gamma'$  precipitate with pure Ag interfacial segregation. The ordering in Neumann's model shown in Fig. 6.3(c-d) was not observed in experiments in Fig. 6.2(a). Although Fig. 6.2(b) shows some inhomogeneity of the Ag distribution inside the  $\gamma'$  precipitate, the column contrast was largely uniform throughout different ageing time at 200°C. A mixed model with random occupancy of  $\text{Ag}_2\text{Al}$  yields a better match with experiments as shown in Fig. 6.3(e). We, therefore, conclude that the  $\gamma'/\gamma$  phase does not possess the regular short-range order suggested by the Neumann's model at 200°C. However, precipitates aged at a lower temperature (i.e. 100°C) should be examined, as an order-disorder

<sup>14</sup>We followed the convention that the  $\gamma'$  precipitate thickness is structurally defined by the HCP stacking instead of by the chemical composition [78]. It is because different interfacial segregations may cause ambiguity to the thickness definition. In this structure definition, the precipitates shown in Fig. 6.1(b) and Fig. 6.2(a) are 1 unit-cell thick.

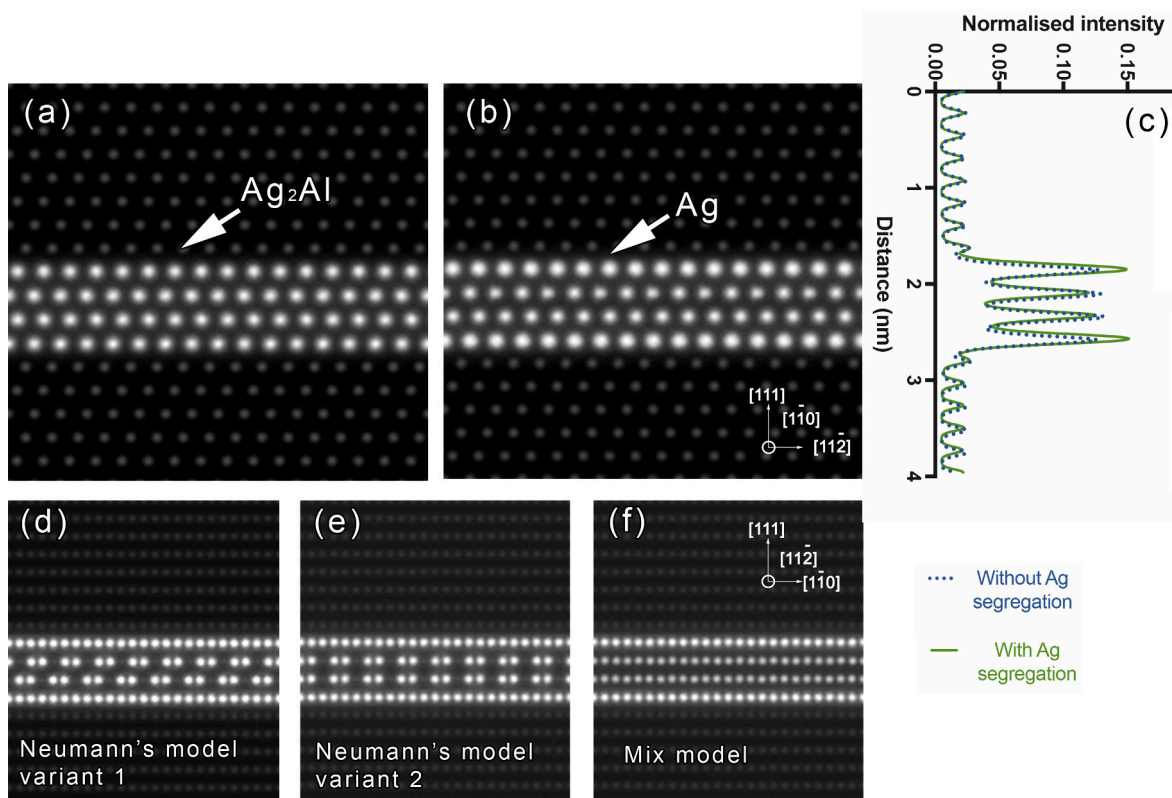


Fig. 6.3 Simulated HAADF-STEM images of an embedded  $\gamma'$  precipitate. (a) Precipitate with and (b) without interfacial Ag segregation, as viewed in a  $\langle 110 \rangle_{\text{Al}}$  direction. (c) Plots of intensities across the precipitates with and without interfacial Ag segregation shown in (a-b). (d-f) Two variants of the Neumann's model and the randomly mixed model for a precipitate with interfacial Ag segregation, when viewed in a  $\langle 112 \rangle_{\text{Al}}$  direction.

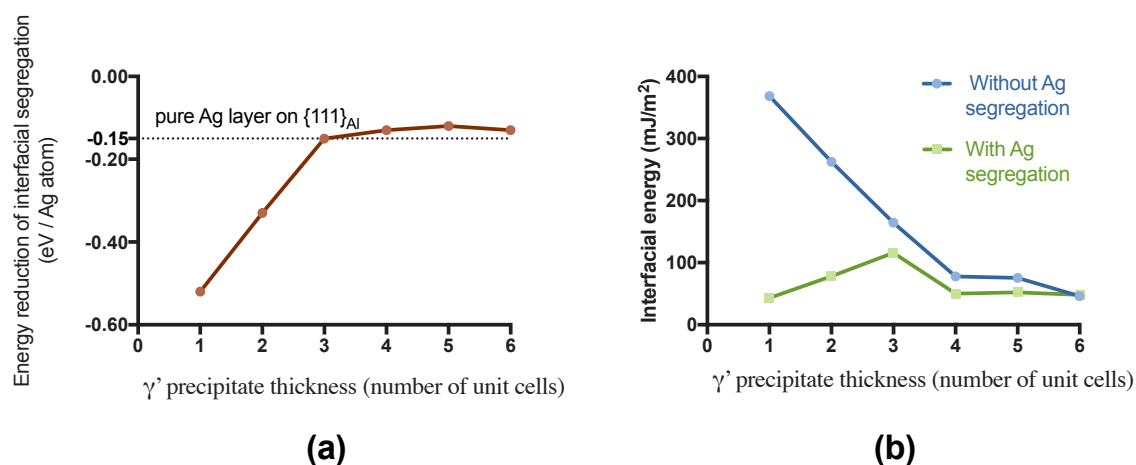


Fig. 6.4 Energetics of Ag segregation at the coherent interface of  $\gamma'$  precipitate as calculated by DFT. (a) Energy reduction associated with interfacial Ag segregation as a function of precipitate thickness, compared to the energy state of Ag in solid solution. The energy of an Ag mono-layer on  $\{111\}_{Al}$  planes (-0.15 eV/Ag atom) is displayed as a dashed line for comparison. (b) The interfacial energies of models with and without interfacial Ag segregation as a function of precipitate thickness.

transition at 124°C has been suggested in previous reports on the basis of diffusive X-ray experiment [73] and first-principles calculations [74].

Our first-principles calculations support interfacial Ag segregation for thin precipitate from an energetics perspective. Fig. 6.4(a) shows the energy reduction associated with Ag segregation at the coherent interface relative to Ag in solid solution. Ag atoms are not stable in solid solution, with a substitutional defect energy of 0.09 eV/Ag atom shown in Table 5.2. In contrast, segregation at the coherent interface significantly reduces the energy by 0.5 eV/Ag atom for the thinnest  $\gamma'$  precipitate. This explains the presence of Ag segregation as shown in Fig. 6.1(a) and Fig. 6.2(a). The energy reduction associated with interfacial Ag segregation quickly decreases with increasing  $\gamma'$  precipitate thickness and converges to 0.13 eV/Ag atom, which is similar to the energy reduction associated with a mono-layer of pure Ag on  $\{111\}_{Al}$  planes in the aluminium matrix. Fig. 6.4(b) shows the interfacial energies for coherent interfaces with and without Ag segregation. For the thinnest embedded  $\gamma'$  precipitate, the interfacial energy is much lower when Ag segregation is present (43 mJ/m<sup>2</sup>) than that without segregation (368 mJ/m<sup>2</sup>). Note that the calculated interfacial energies vary with different  $\gamma'$  thickness. This is not an error but a reasonable result due to the electronic interactions between two adjacent interfaces for a thin precipitate, which is not taken into account in the classical definition of interfacial energy. Calculations for thick  $\gamma'$  precipitates should produce a better value for the “classical” interfacial energy. Indeed, the energy for

with/without Ag segregation is found to converge to almost the same value  $\approx 48\text{mJ}/\text{m}^2$ . Again, the trend in the interfacial energy calculations is consistent with our experimental observations that the interfacial Ag segregation is clear for thin  $\gamma'$  precipitates.

### 6.3 The Semicohherent Precipitate-Matrix Interface

The orientation relationship of the  $\gamma'$  semicoherent interface ( $\{1\bar{1}00\}_{\gamma'} \parallel \{112\}_{\text{Al}}$ ) is preserved with a saw-tooth reconstruction. Previous TEM and STEM studies [70, 84] presented images of the saw-tooth interface morphology but did not explain its formation. Little is known about this interfacial reconstruction. As reviewed in Chapter 2, the semicoherent interface is expected to contain three equivalent Shockley partial dislocations in a periodic fashion to minimise the overall shear strain. However, the atomic dislocation structure is difficult to reveal for such complicated heterophase interface. Those gaps are critical for understanding the fundamental mechanisms that underpin the FCC-HCP phase transformation. Therefore, this section focuses on characterising and analysing the dislocations confined at the  $\gamma'$  semicoherent interface. First-principles calculations were performed to reveal the energetics associated with interfacial reconstruction. Moreover, embedded atom method calculations were performed to reveal the reaction from three equivalent Shockley partial dislocations to a different dislocation structure.

There are two types of saw-tooth semicoherent interfaces. The reported saw-tooth interface was also found in our study as shown in Fig. 6.5(a), here denoted as the Type-I interface. Specifically, this interface is composed of nano-steps parallel to low-index  $\{002\}_{\text{Al}}$  and  $\{111\}_{\text{Al}}$  planes. A close inspection showed that the orientation relationship of  $\{1\bar{1}00\}_{\gamma'} \parallel \{112\}_{\text{Al}}$  was periodically reconstructed by a four-layer step of  $\{10\bar{1}1\}_{\gamma'} \parallel \{111\}_{\text{Al}}$  and a two-layer step of  $\{10\bar{1}1\}_{\gamma'} \parallel \{002\}_{\text{Al}}$  as illustrated in Fig. 6.5(c). The Type-I interface has hexagonal features consisting of 1 column enriched in Al surrounded by 6 columns enriched in Ag at the periodic nano-step ridges, as indicated by white asterisks. This unique chemical distribution was suspected to indicate the core of Shockley partial dislocation in a previous STEM study [70]. Fig. 6.5(b) shows another type of semicoherent interface not reported before, here denoted as the Type-II interface. This interface also displays a saw-tooth morphology and a periodic solute distribution. The top half of the interface (above the white dashed line) had the same  $\{111\}_{\text{Al}}$ - and  $\{002\}_{\text{Al}}$ -steps ratio (4:2) as that of the Type-I interface. However, the bottom half of the interface (below the white dashed line) had a different ratio (5:1) that produced an interface macroscopically tilted away from  $\{112\}_{\text{Al}}$  planes. As shown in Fig. 6.5(b), the Type-II interface has a one-column Ag depletion region near a three-column Ag depletion region, which are periodically spaced along the interface

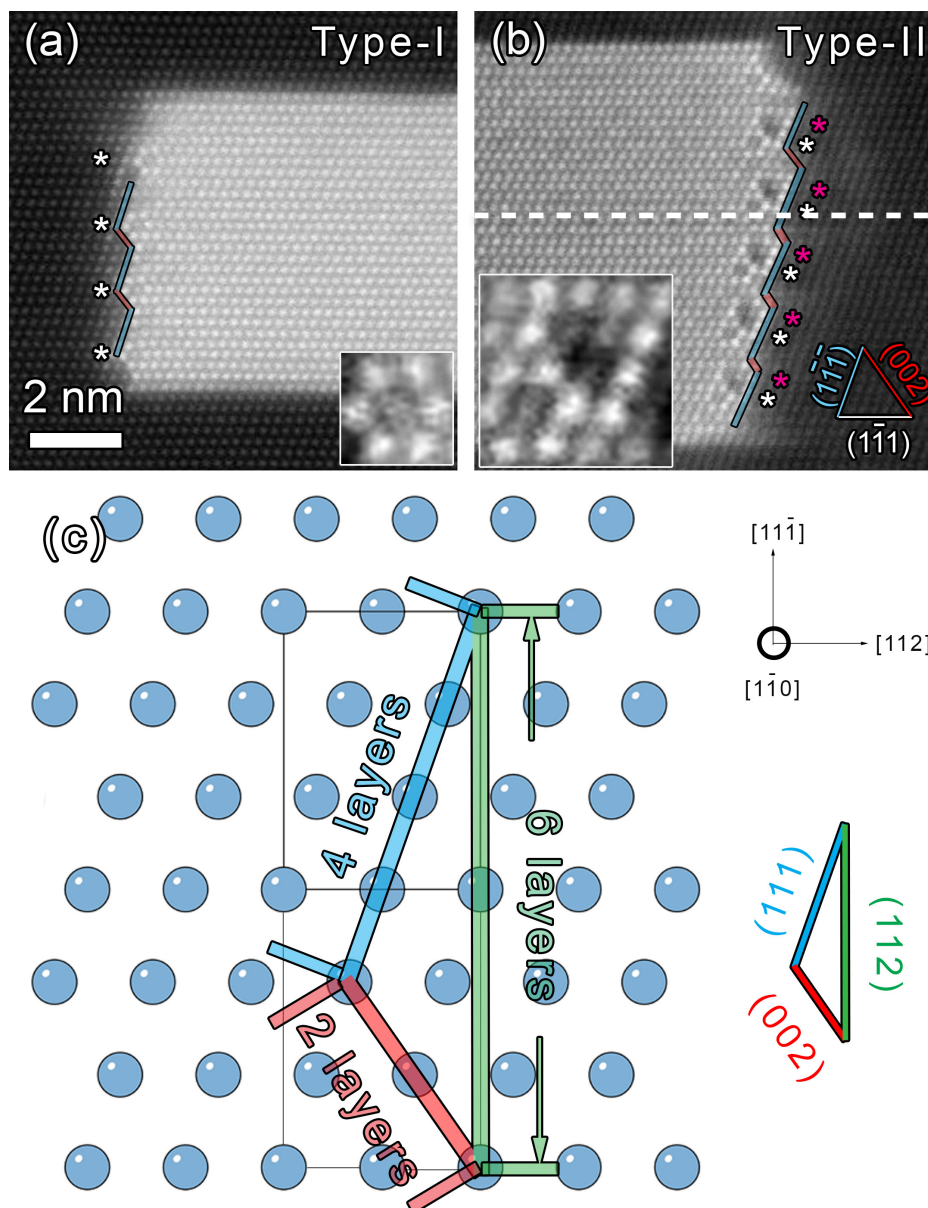


Fig. 6.5 (a-b) Two types of semicoherent interfaces of the  $\gamma'$  precipitate plate. The blue lines indicate steps parallel to  $\{111\}_{Al}$  planes and the red lines indicate steps parallel to  $\{002\}_{Al}$  planes. The white asterisks are near to the 1-column Ag depletion at the ridges of the interface, while the purple asterisks are near to the 3-column Ag depletion. The insets show the enlarged sections of the Ag depletion features at the two types of interfaces. (c) Schematic diagram illustrating the reconstruction of the  $\{1\bar{1}00\}_{\gamma'} \parallel \{112\}_{Al}$  orientation relationship by a four-layer step parallel to  $\{111\}_{Al}$  planes and a two-layer step parallel to  $\{002\}_{Al}$  planes. The electron beam is parallel to a  $\langle 110 \rangle_{Al}$  direction.

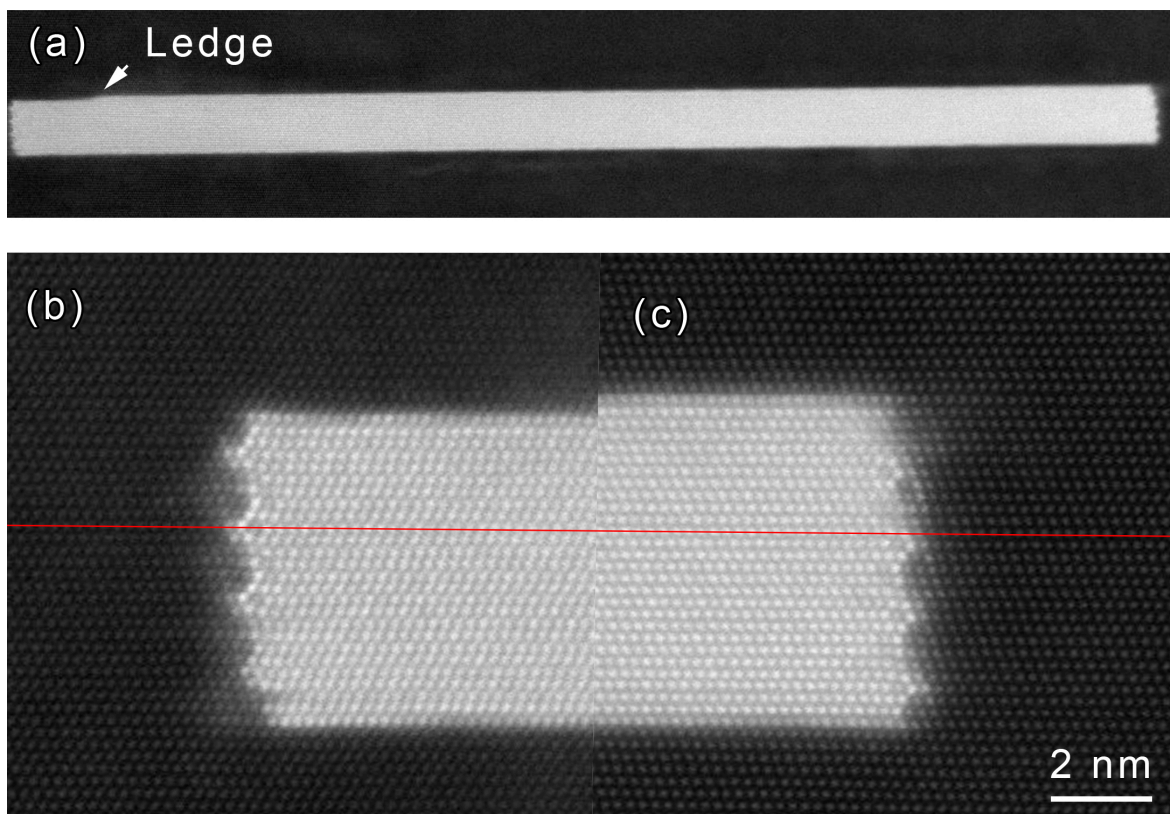


Fig. 6.6 HAADF-STEM images of semicoherent interfaces at two sides of a  $\gamma'$  precipitate. (a) Low magnification image where the arrow indicates a two-layer-thick ledge. (b-c) High magnification images of semicoherent interfaces at both sides, where a red line indicates the same close-packed layer that runs through the precipitate. The electron beam is parallel to a  $\langle 110 \rangle_{Al}$  direction.

every six close-packed planes. The three-column Ag depletion is similar to the pattern at the  $\gamma'$  precipitate-precipitate junctions (see Fig. 4.5). Fig. 6.6 shows that the structure of semicoherent interfaces was the same at different sides of a  $\gamma'$  precipitate plate, but the exact sequence was different. A red line indicates that the locations of the ridges and the associated Ag-depletion features differ between two sides of a precipitate. Note that a ledge was identified in Fig. 6.6(a), which resulted in a two-layered thickness difference between the two sides. Thus, the precipitate did not display a mirror symmetry or a rotation symmetry in a  $\langle 110 \rangle_{\text{Al}}$  direction.

We performed first-principles calculations to deduce the interfacial energies associated with different orientation relationships, including the traditionally considered atomic sharp  $\{1\bar{1}00\}_{\gamma} \parallel \{112\}_{\text{Al}}$  interface and the experimentally observed reconstruction with  $\{10\bar{1}1\}_{\gamma} \parallel \{111\}_{\text{Al}}$  and  $\{10\bar{1}1\}_{\gamma} \parallel \{002\}_{\text{Al}}$  interfaces. As shown in Fig. 6.7(a-c), we used periodic conditions for those orientations relationships along the interfaces and an equal number of atomic planes of Al and  $\text{Ag}_2\text{Al}$  (Neumann's model) normal to the interfaces. All atom positions, as well as the supercell parameters, were fully optimised to obtain the total energy of each structure. The formation energy  $\Delta E^f$  relative to the bulk Al and  $\text{Ag}_2\text{Al}$  (Neumann's model) phases can be written as  $\Delta E^f = E(\text{Al}, \text{Ag}_2\text{Al}) + 2\gamma A$ , where  $E(\text{Al}, \text{Ag}_2\text{Al})$  is the strain energy associated with matching the two phases that scales with the volume and hence the number of atomic planes;  $A$  is the interfacial area and  $\gamma$  is the interfacial energy per unit area, which are constant with varying supercell sizes. Thus, the interfacial energy per unit area for a given interface can be deduced by plotting  $\Delta E^f$  vs  $1/n$  and measuring the slope as shown in Fig. 6.7(e). For the atomically sharp  $\{112\}_{\text{Al}}$  interface, the interfacial energy is  $331 \text{ mJ/m}^2$ , in good agreement with the values obtained from previous experimental estimation ( $350 \text{ mJ/m}^2$ ) [204] and DFT calculations ( $325 \text{ mJ/m}^2$ ) [87]. The interfacial energies for the  $\{111\}_{\text{Al}}$  and  $\{002\}_{\text{Al}}$  interfaces are  $175 \text{ mJ/m}^2$  and  $183 \text{ mJ/m}^2$  respectively. The reconstruction can be expected to have an energetic origin: it is energetically favourable if the sum of the interfacial energies of the steps is lower than that of the sharp  $\{1\bar{1}00\}_{\gamma} \parallel \{112\}_{\text{Al}}$  interface. After computing the interfacial energies per unit area times the associated areas of those nano-steps, Fig. 6.7(d), the reconstruction criterion is simplified as:

$$\gamma_{112} > \frac{1}{\sqrt{2}}\gamma_{111} + \frac{1}{\sqrt{6}}\gamma_{002}, \quad (6.1)$$

where  $\gamma_{112}$  is interfacial energy per unit area associated with sharp  $\{1\bar{1}00\}_{\gamma} \parallel \{112\}_{\text{Al}}$  interface, while  $\gamma_{111}$  and  $\gamma_{002}$  are those associated with  $\{10\bar{1}1\}_{\gamma} \parallel \{111\}_{\text{Al}}$  and  $\{10\bar{1}1\}_{\gamma} \parallel \{002\}_{\text{Al}}$  interfaces respectively. The interfacial energies deduced from our DFT calculations satisfy this energetics-based reconstruction criterion.

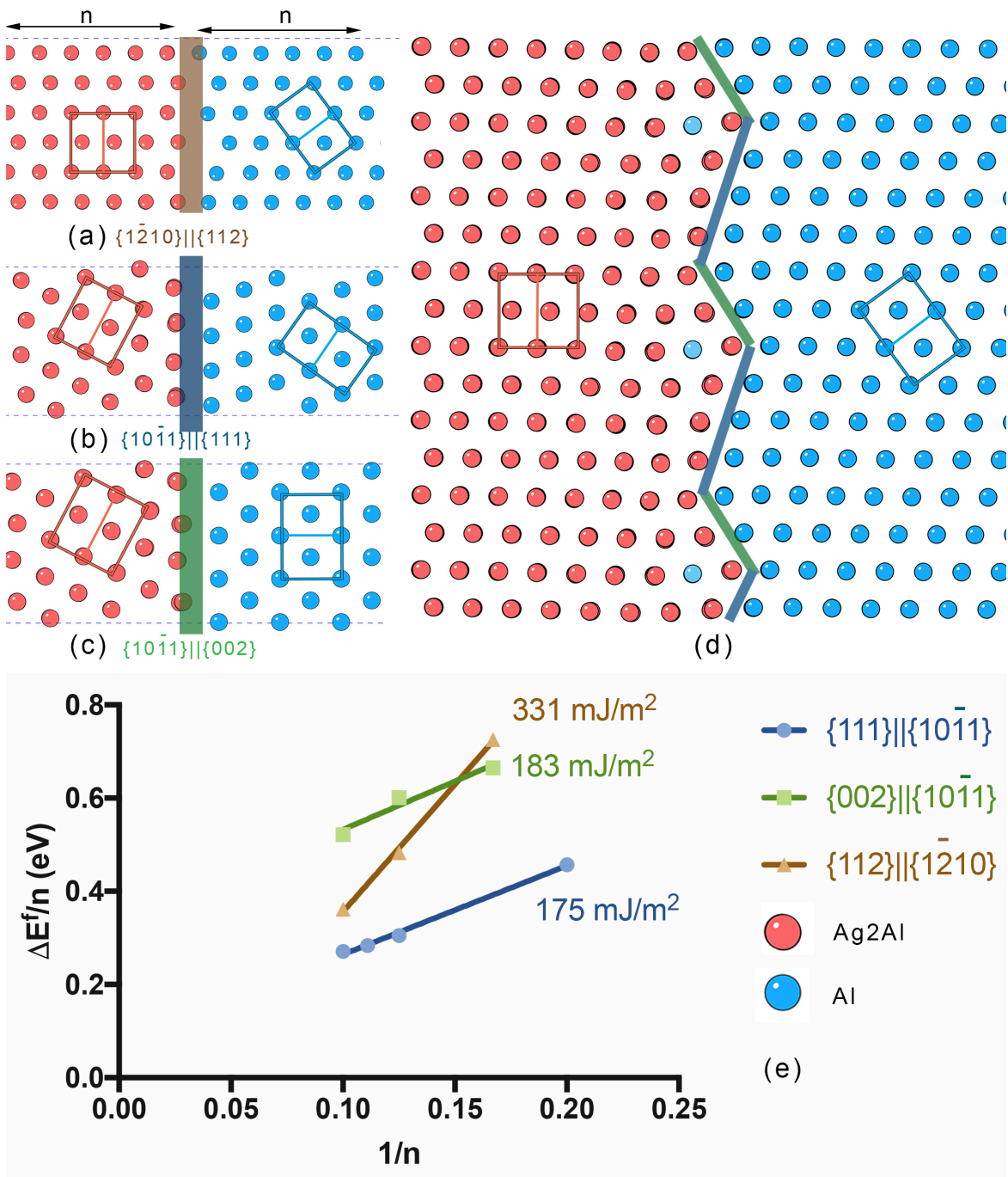


Fig. 6.7 Atomic models of (a)  $\{1\bar{1}00\}_{\gamma} \parallel \{112\}_{\text{Al}}$ , (b)  $\{10\bar{1}1\}_{\gamma} \parallel \{111\}_{\text{Al}}$  and (c)  $\{10\bar{1}1\}_{\gamma} \parallel \{002\}_{\text{Al}}$  interfaces, viewed in a  $\langle 110 \rangle_{\text{Al}}$  direction. Each supercell contains an equal number of atomic layers  $n$  for both FCC Al and HCP Ag<sub>2</sub>Al phases. The crystallographic directions are indicated by the projected unit cell of FCC and HCP phases. (d) Atomic model of  $\{1\bar{1}00\}_{\gamma} \parallel \{112\}_{\text{Al}}$  interface reconstructed by nano-steps parallel to  $\{10\bar{1}1\}_{\gamma} \parallel \{111\}_{\text{Al}}$  and  $\{10\bar{1}1\}_{\gamma} \parallel \{002\}_{\text{Al}}$  planes. (e) Variation of formation energy per plane  $\Delta E^f/n$  vs.  $1/n$  for deducing the interfacial energies.

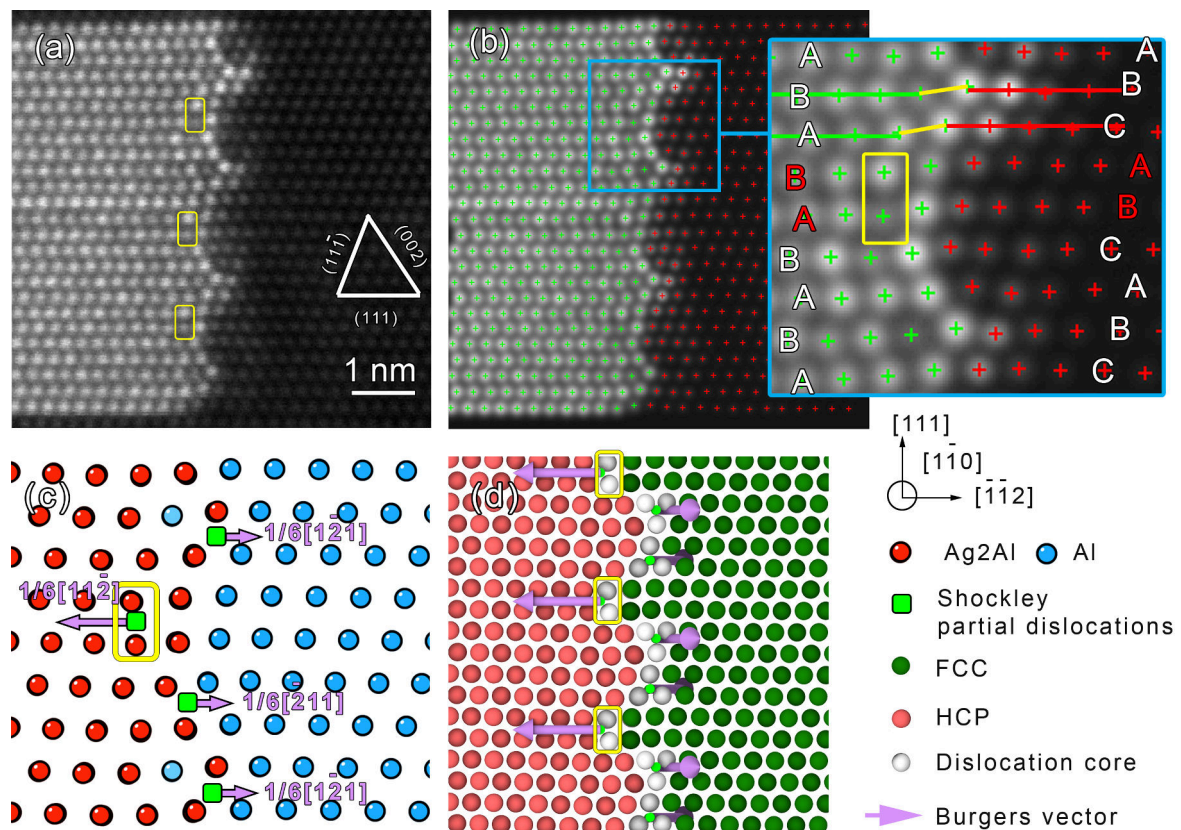


Fig. 6.8 Resolving dislocation structures at the FCC/HCP semicoherent interface. (a) Original HAADF-STEM image of a  $\gamma'$  semicoherent interface (Image Courtesy: Laure Bourgeois, taken from Ref. [70]). (b) Refined atomic column positions by parameter estimation theory as indicated by green and red plus signs. (c) The composition used in the 3D model. (d) Dislocation structure in the 3D model as identified by dislocation extraction algorithm. Three pairs of Shockley partial dislocations are periodically located at the FCC/HCP interface, where red atoms are HCP, green atoms are FCC and white atoms are those at the dislocation cores.

To understand the detailed atomic structure at the FCC/HCP semicoherent interface, parameter estimation theory was applied to locate the precise positions of each atomic column. A 3D model was built based on the experimentally determined 2D positions and the known periodicities of FCC Al and HCP  $\gamma$  (Neumann's model  $\text{Ag}_2\text{Al}$ ) in the  $\langle 110 \rangle_{\text{Al}}$  electron beam direction. Fig. 6.8(a-b) show the original HAADF-STEM image and the refined column positions as highlighted by the green and red plus signs. In the enlarged view in Fig. 6.8(b), it is clear that the FCC/HCP transition region has a shift normal to the close-packed planes as indicated by yellow lines. By comparing the stacking of FCC (ABCABC) with that of HCP (ABABAB), we identified two layers (highlighted in red) that have their stacking exchanged when crossing the FCC/HCP interface. The exchanged stacking results in the atomic column in one close-packed layer aligned on top of the next close-packed layer in the transition zone, as indicated by the yellow rectangular frames on HAADF-STEM images. Fig. 6.8(c) shows the composition map that was used in building the 3D model. By performing a Burgers vector analysis for each atom in the experimentally informed 3D model (see Section. 3.3.4), dislocation extraction algorithm identified three pairs of Shockley partial dislocations periodically located at the FCC/HCP interface, Fig. 6.8. Specifically, a  $90^\circ$  Shockley partial dislocation is located in between the "exchanged" layers as described above, while two  $30^\circ$  Shockley partial dislocations are located above and below the ridges with 1-column Ag depletion. Each Shockley partial dislocation is separated by two layers of close-packed planes as expected. Common neighbour analysis distinguished the FCC and HCP phases correctly (see Section. 3.3.3), which analyses the topology of bonds between the nearest neighbours for each atom. The atoms having the number of nearest neighbour other than 12 are identified as atoms at the dislocation cores. The locations of Shockley partial dislocations and their Burgers vectors are labelled in reference to the composition map in Fig. 6.8 for the ease of understanding.

In addition to the Shockley partial dislocations as described above, we surprisingly found another option of dislocations at the FCC/HCP interface. EAM structure optimisation calculations were performed for a precipitate inside a sufficiently large matrix ( $\approx 40,000$  atoms) by minimising the total energy. As shown in Fig. 6.9(a), the starting structure involves Shockley partial dislocations in three directions located at the FCC/HCP interface. Note that the dislocation directions are opposite at the two sides of the precipitate. The final optimised structure involves a  $90^\circ$  Shockley partial dislocation, a Lomer-Cottrell dislocation and a Hirth dislocation periodically spaced at the interface, Fig. 6.9(b). We propose this is a result of the interfacial dislocation reaction. The two  $30^\circ$  Shockley partial dislocations climb by one close-packed plane towards each other to form a  $90^\circ$  anti-Shockley partial dislocation (with the opposite Burger vector relative to that of  $90^\circ$  Shockley partial dislocation), which then

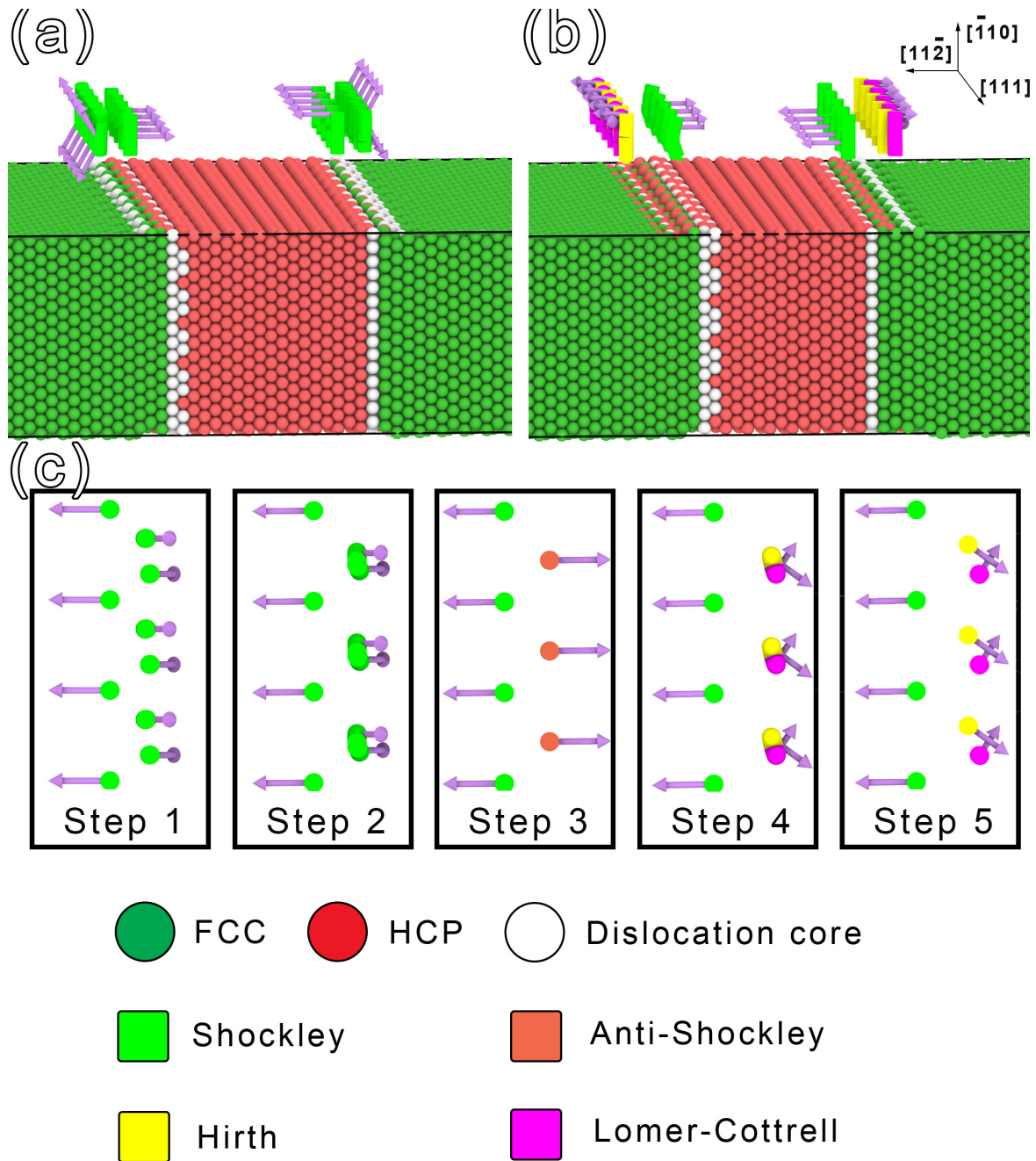


Fig. 6.9 Proposed dislocation reaction at the FCC/HCP semicoherent interface. (a) Input structure viewed near a  $\langle 111 \rangle_{Al}$  direction, where Shockley partial dislocations are periodically spaced along the interfaces. (b) EAM optimised structure viewed near a  $\langle 111 \rangle_{Al}$  direction, where a  $90^\circ$  Shockley partial, a Lomer-Cottrell and a Hirth dislocation are periodically spaced along the interface. (c) Detailed dislocation reaction process during EAM optimisation, viewed in a  $\langle 110 \rangle_{Al}$  direction, where only the Burgers vectors are shown. Step 1 shows the initial structure with three pairs of Shockley partial dislocations. Step 2 shows the climbing of two  $30^\circ$  Shockley partial dislocations. Step 3 shows the combining of two  $30^\circ$  Shockley partial dislocations into a  $90^\circ$  anti-Shockley partial dislocation. Step 4 shows the decomposition of the  $90^\circ$  anti-Shockley partial dislocation into a Lomer-Cottrell dislocation and a Hirth dislocation. Step 5 shows the separation of the Lomer-Cottrell dislocations and the Hirth dislocations to the original positions of the two  $30^\circ$  Shockley partial dislocations.

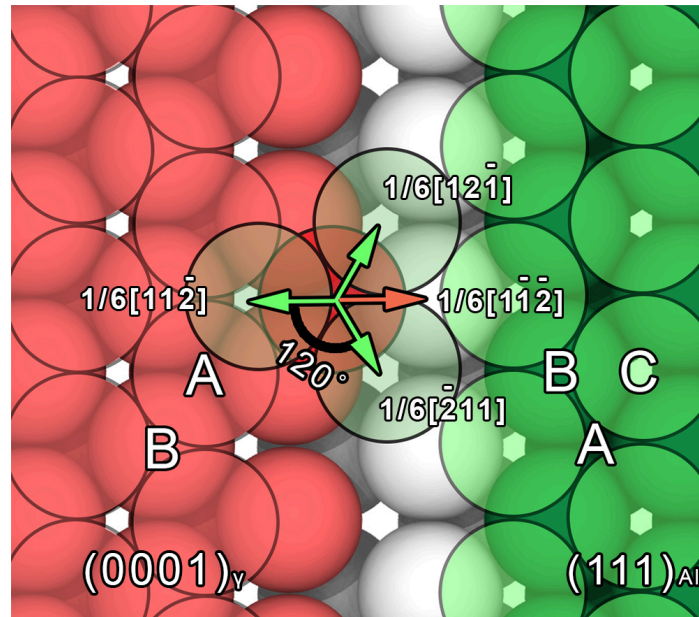


Fig. 6.10 Demonstration of the change of stacking for an atom at the FCC/HCP interface viewed in a  $\langle 111 \rangle_{Al}$  direction. The Burgers vectors of the three Shockley partial dislocations are coloured in green while the Burgers vector of the anti-Shockley partial dislocation is coloured in orange. The accommodation sites of the close-packed layers are labelled as AB/ABC for HCP/FCC respectively.

decomposes into a Lomer-Cottrell dislocation and a Hirth dislocation. The detailed reaction process is demonstrated in Fig. 6.9(c). The spatial relationship of Shockley and anti-Shockley partial dislocations are illustrated on close-packed planes, Fig. 6.10. An atom at the interface on the HCP side (ABAB...) could change its stacking to that of FCC (ABCABC...) along three directions, known as Shockley partial directions (indicated by green arrows). The combination of two  $30^\circ$  Shockley partial dislocations, Fig. 6.9(c), corresponds to a vector addition from a geometric perspective and results in a  $90^\circ$  anti-Shockley partial dislocation (indicated by orange colour). However, this dislocation shifts interfacial atoms from an A site to a B site; the B site is directly on top of the atom of the FCC close-packed plane below. Thus, the  $90^\circ$  anti-Shockley is expected to exhibit a high energy and should not be stable. To appreciate this dislocation reaction at the interface, the spatial relationship of their Burgers vectors was examined in three dimensions. Three Shockley partial dislocations ( $\vec{b} = 1/6\langle 112 \rangle$ ) and the  $90^\circ$  anti-Shockley partial dislocation ( $\vec{b} = 1/6\langle 112 \rangle$ ) are on the close-packed  $\{111\}_{Al} \parallel \{0001\}_\gamma$  planes, Fig. 6.11(a). The Shockley partial dislocations are separated by  $120^\circ$ , while the  $90^\circ$  anti-Shockley partial dislocation is  $60^\circ$  tilted away from the two  $30^\circ$  Shockley partial dislocations that constitute it. After decomposition, the remaining  $90^\circ$  Shockley partial dislocation ( $\vec{b} = 1/6\langle 112 \rangle$ ), the Lomer-Cottrell dislocation

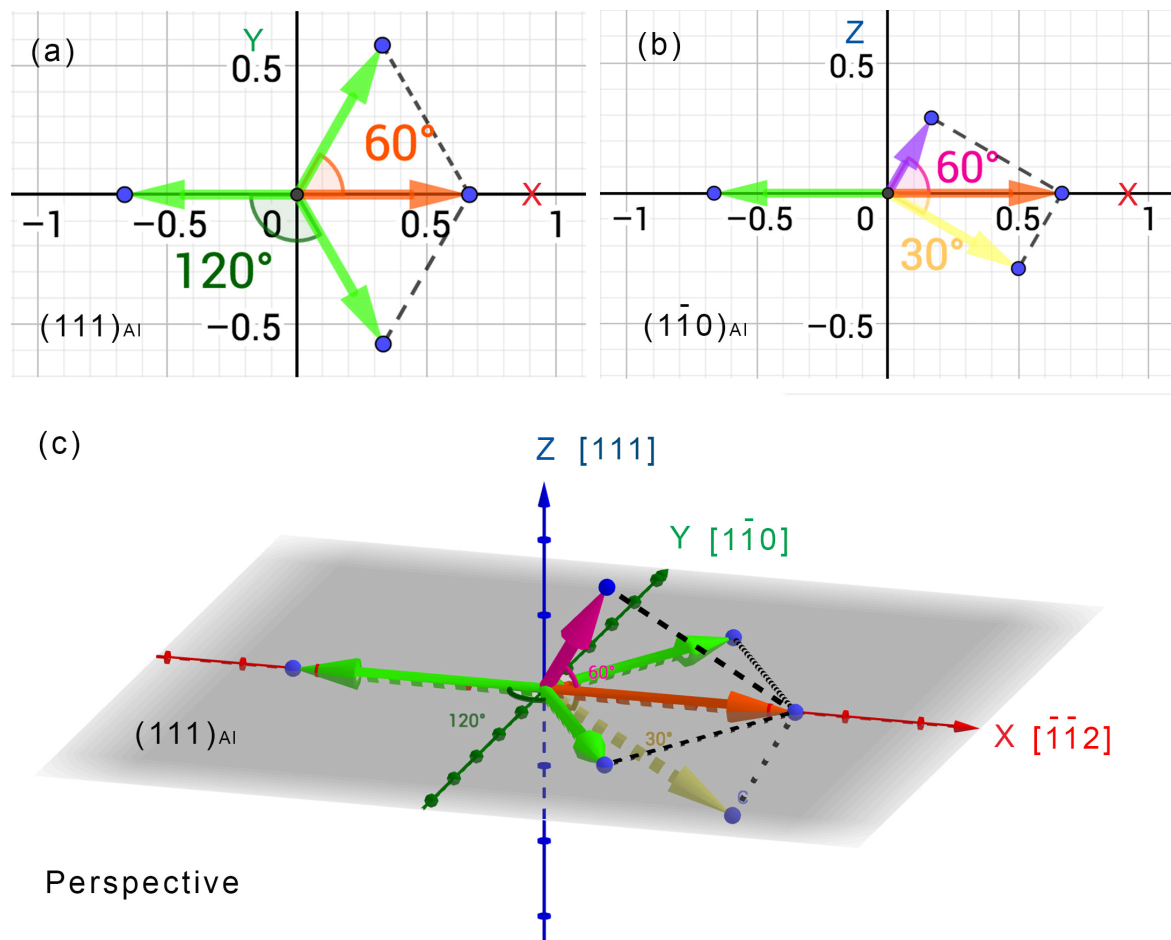


Fig. 6.11 The spatial relationship between Burgers vectors of different dislocations at the FCC/HCP interface. (a) The Shockley partial dislocations (green) before reaction and the metastable anti-Shockley partial dislocation (orange). These vectors are co-planar on  $\{111\}_{Al} \parallel \{0001\}_{\gamma}$  planes. (b) The remaining  $90^\circ$  Shockley partial dislocation (green), Lomer-Cottrell dislocation (purple) and Hirth dislocation (yellow) after the reaction. Those vectors are co-planar on  $\{110\}_{Al} \parallel \{1\bar{2}10\}_{\gamma}$  planes. (c) Perspective view of all Burgers vectors involved in the interfacial dislocation reaction. The lengths of the Burgers vectors are computed from the modulus of vectors ( $|\vec{b}|$ ) times the lattice parameter of aluminium, units in Å.

( $\vec{b} = 1/6\langle 110 \rangle$ ) and the Hirth dislocation ( $\vec{b} = 1/3\langle 001 \rangle$ ) are still co-planar but on the  $\{110\}_{\text{Al}} \parallel \{1\bar{2}10\}_{\gamma}$  planes, Fig. 6.11(b). The Lomer-Cottrell dislocation is tilted by  $60^\circ$  away from the close-packed planes while the Hirth dislocation is tilted by  $30^\circ$ . Note that the Lomer-Cottrell dislocation is perpendicular to the Hirth dislocation, while both are normal to a  $\langle 110 \rangle_{\text{Al}}$  direction.

## 6.4 Precipitate-Precipitate Junctions

The formation of a  $\gamma'$  precipitate requires Shockley partial dislocations to change the stacking from FCC to HCP at the matrix-precipitate interfaces. In Chapter 4, we have shown that  $\gamma'$  precipitate assemblies are constructed from precipitates on different close-packed planes. The associated Shockley partial dislocations react at the precipitate-precipitate junctions. This section examines the atomic structures and chemistries at those junctions and reveals their role in controlling precipitation growth. Fig. 6.12(a-b) shows a precipitate assembly in the binary Al-Ag alloy, which is composed of  $\gamma'$  precipitates on close-packed planes tilted  $70.5^\circ$  relative to each other. Their junctions have three atomic columns depleted in Ag as suggested by the contrast in the HAADF-STEM image. Using the model building software developed by Koch [140], the experimentally-informed 3D structure was built by aligning the column positions of FCC and HCP phases to the refined atomic positions on a HAADF-STEM image. We performed the common neighbour analysis (Section. 3.3.3) and the dislocation extraction algorithm (Section. 3.3.4) for the experimentally-informed 3D structure, which yielded the correct assignment of FCC/HCP phases and the presence of Lomer-Cottrell dislocation at the junction as expected, Fig. 6.12(c). A HAADF-STEM image was simulated based on the experimentally-informed 3D structure to compare with experimental images, Fig. 6.12(d). The precipitates have four atomic layers in thickness with a stacking fault (relative to the FCC Al) in the centre and Ag segregation at the precipitate-matrix interface, as indicated by the dashed lines. The intersection of stacking faults leads to a precipitate-precipitate junction. We followed the right-hand start-to-finish convention around a junction to manually construct the Burgers circuit on the simulated HAADF-STEM image, which can be well approximated as a projection of the 3D structure. The vector analysis from this circuit suggests that such junction consists of a Lomer-Cottrell dislocation ( $\vec{b} = 1/6\langle 110 \rangle$ ). A Lomer-Cottrell dislocation is an edge dislocation. In an edge dislocation, an extra plane is inserted into the crystal, which distorts the arrangement of surrounding planes of atoms. The Lomer-Cottrell dislocation is on the  $(001)_{\text{Al}}$  plane with an extra  $1/6(110)_{\text{Al}}$  plane indicated by the “ $\perp$ ” symbol. However, because of the small magnitude of its Burgers vector, the associated strain is barely measurable in both experimental and simulated images.

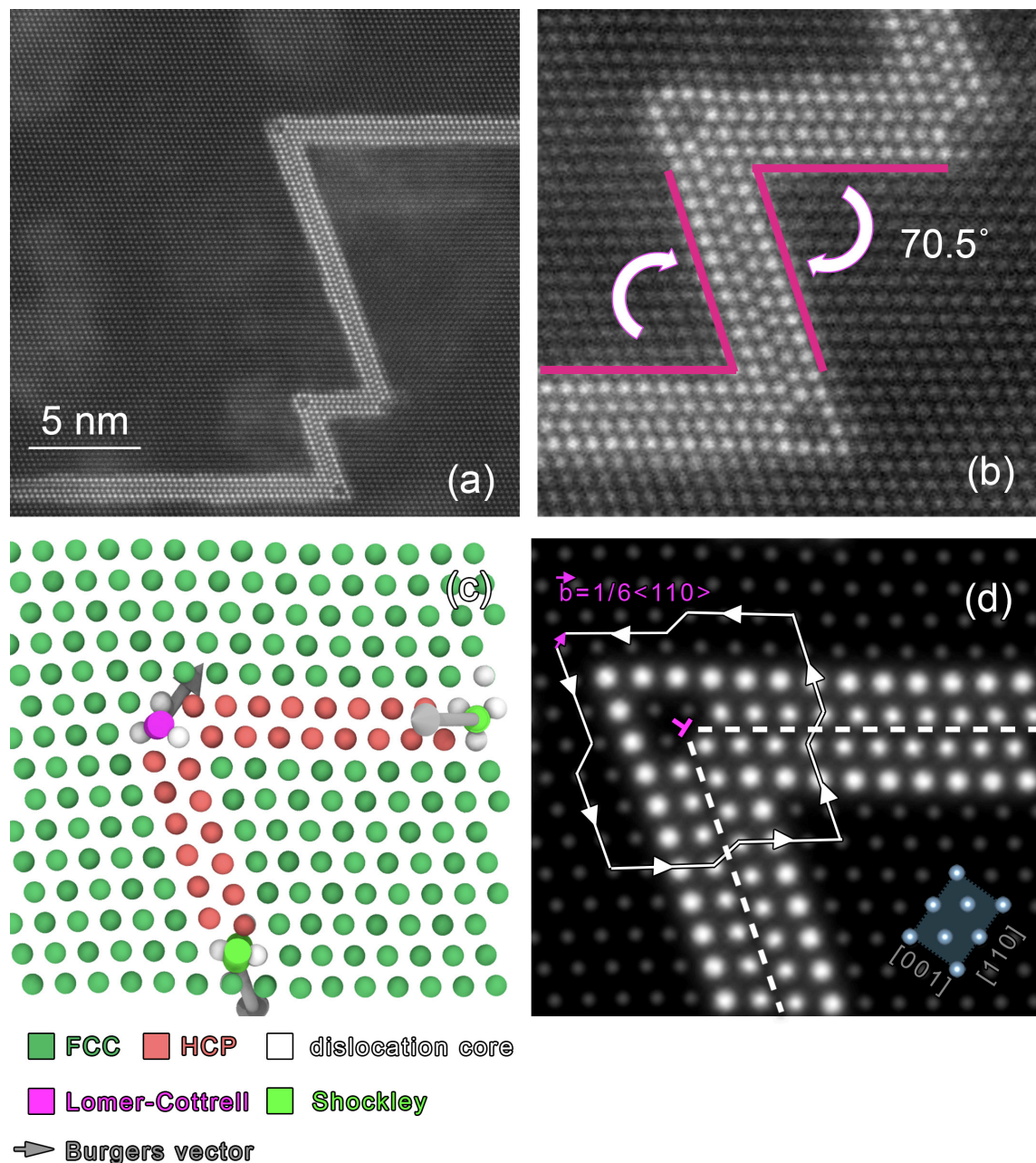


Fig. 6.12 The atomic structure and chemistry of Lomer-Cottrell dislocations at the precipitate-precipitate junctions of  $\gamma'$  phase viewed in a  $\langle 110 \rangle_{\text{Al}}$  direction. (a-b) HAADF-STEM images showing precipitates are on the close-packed planes tilted  $70.5^\circ$  relative to each other. The junctions have three-column Ag depletion at the dislocation cores. The sample was water quenched and aged at  $200^\circ\text{C}$  for 30 min. (c) Dislocation extraction analysis based on the experimentally informed 3D model with the colour representation of the local crystal structures and dislocations as labelled. (d) Simulated HAADF-STEM image with Burgers vector analysis. Stacking faults are indicated by dashed lines. The position of the Lomer-Cottrell dislocation as an edge dislocation is indicated with a “ $\perp$ ” symbol. The crystallographic directions are indicated by an Al unit cell in a  $\langle 110 \rangle_{\text{Al}}$  direction.

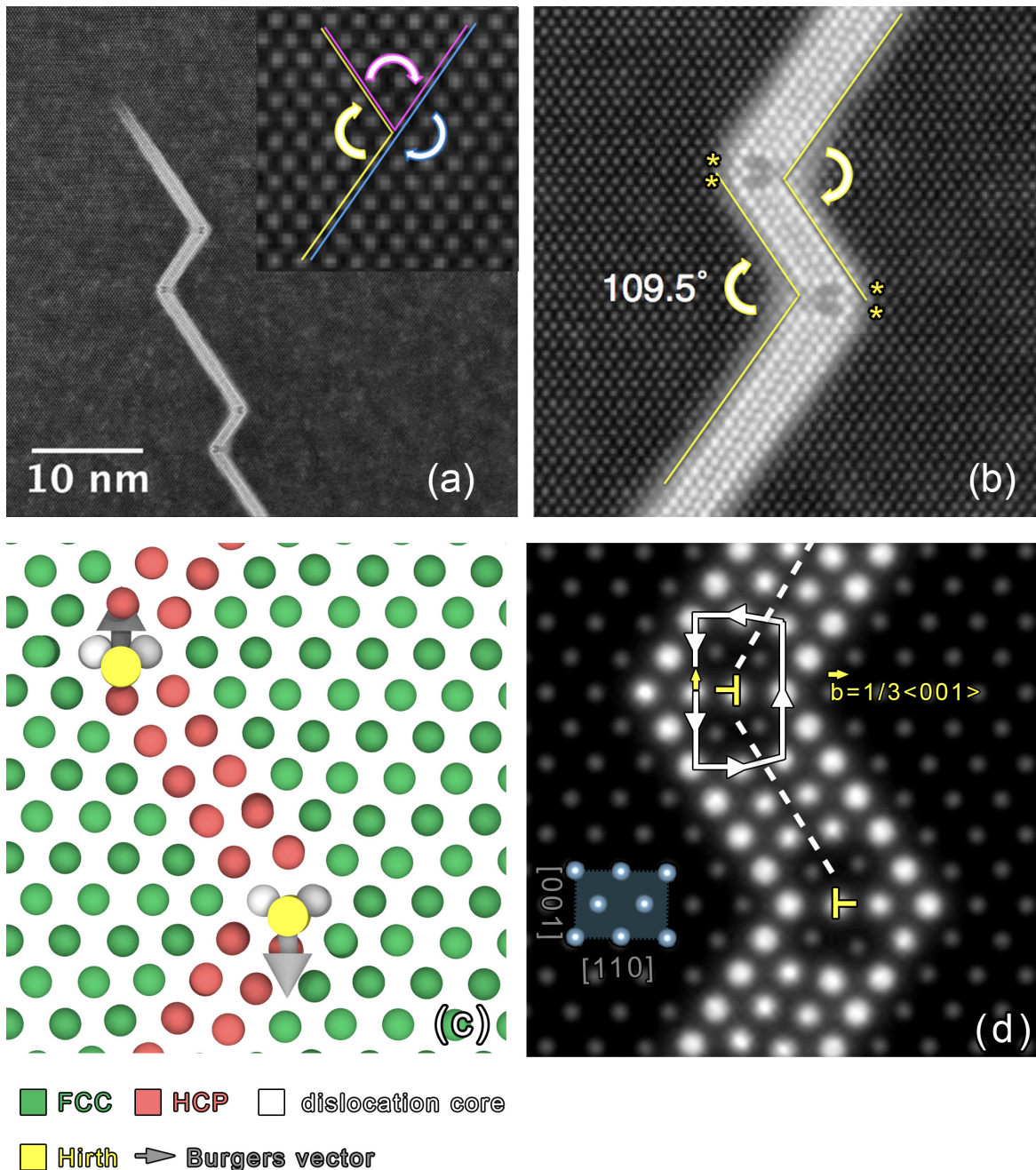


Fig. 6.13 The atomic structure and chemistry of Hirth dislocations at the precipitate-precipitate junctions of  $\gamma'$  precipitates viewed in a  $\langle 110 \rangle_{\text{Al}}$  direction. (a-b) HAADF-STEM images showing precipitates are on the close-packed planes tilted  $109.5^\circ$  relative to each other. The junctions have a pair of two-column Ag depletion at the dislocation cores. The sample is an Al-0.85at.%Ag-0.85at.%Cu alloy water quenched and aged at  $200^\circ\text{C}$  for 4 hr. Alloy courtesy: Julian M. Rosalie (fabrication details are recorded in Ref. [78]). (c) Dislocation extraction analysis based on the experimentally informed 3D model with the colour representation of the local crystal structures and dislocations as labelled. (d) Simulated HAADF-STEM image with Burgers vector analysis. Stacking faults are indicated by dashed lines. The position of the Hirth dislocation as an edge dislocation is indicated with a “ $\perp$ ” symbol. The crystallographic directions are indicated by an Al unit cell in a  $\langle 110 \rangle_{\text{Al}}$  direction.

Beside the Lomer-Cottrell dislocation described above, two Shockley partial dislocations on different close-packed planes can react into a Hirth dislocation. Fig. 6.13(a-b) shows a precipitate assembly in a ternary Al-Ag-Cu alloy, which consists of  $\gamma'$  precipitates on close-packed planes tilted  $109.5^\circ$  relative to each other. A symmetric pair of 2-column Ag depletion region were found at each junction as suggested by the contrast in the HAADF-STEM image. Similarly, the experimentally-informed 3D model was built and the dislocation extraction algorithm was used to reveal the presence of Hirth dislocation ( $\vec{b} = 1/3\langle 001 \rangle$ ), Fig. 6.13(c). The zig-zag morphology of the precipitate assemblies is accompanied with Hirth dislocation pairs with the opposite Burgers vectors. Fig. 6.13(d) shows the simulated HAADF-STEM image based on the experimentally informed 3D structure. Each  $\gamma'$  precipitate is four atomic layers in thickness with a stacking fault in the centre (relative to FCC Al) and Ag segregation at the precipitate-matrix interface. Burgers vector analysis was performed manually on the 2D image that confirms the dislocation extraction algorithm result. A Hirth dislocation is also an edge dislocation. Because the associated Burgers vector is twice the modulus of that of a Lomer-Cottrell dislocation, there is noticeable distortion around the dislocation core in both experimental and simulated images. It is interesting to note that the  $109.5^\circ$  angle associated with a Hirth dislocation junction plus the  $70.5^\circ$  angle associated with a Lomer-Cottrell dislocation junction makes  $180^\circ$ , which corresponds to the two choices of close-packed planes in a  $\langle 110 \rangle_{\text{Al}}$  direction (see the inserted image in Fig. 6.13(a)). Their Burgers vectors are normal to each other as illustrated in Fig. 6.11.

The junctions described above were found at precipitate assemblies nucleating on quenched-in dislocation loops. The growth and impingement of individual  $\gamma'$  precipitate plates also lead to an intersection. However, the interfacial structures and chemistries are very different. Fig. 6.14(a-b) shows that the central region of the precipitate-precipitate intersection was distorted to form a twin relative to lattices of those two precipitate plates. The red lines in Fig. 6.14(b) indicate the basal planes of the  $\gamma$  phase while the blue lines indicate the twin boundaries. Interestingly, Ag was depleted at every second column on the twin boundaries, resulting in a ring of hexagonal features decorating the twin boundaries. A close-up inspection of the twin structure showed that the twinning occurred in the  $\langle \bar{1}012 \rangle \{10\bar{1}1\}$  system (where  $\{10\bar{1}1\}$  is the twinning plane and  $\langle \bar{1}012 \rangle$  is the twinning direction in the twinning plane), Fig. 6.15. Al was clearly enriched in the compressed site (A site) while Ag was slightly enriched in the expansion site (B site) at the twin boundary. Not every intersection has a twin in the centre. In most cases without *in situ* annealing, one precipitate plate penetrated another, displaying defects with accompanied Ag depletions at the joining lines, Fig. 6.14(c-d). No periodicity of those defects was observed. It is possible that *in situ* annealing transforms the non-periodic defects at the intersection into a twin

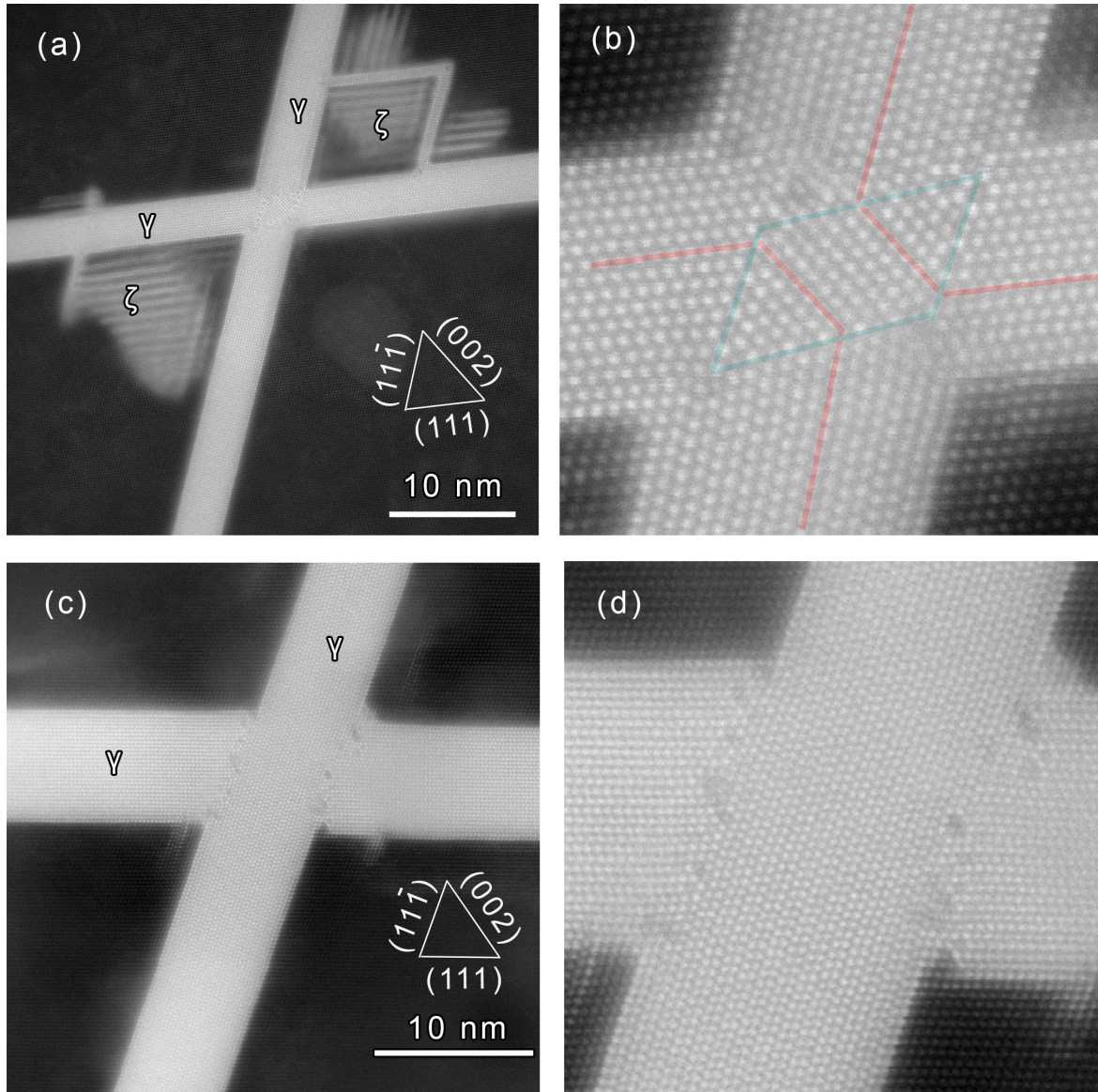


Fig. 6.14 Intersections of individual  $\gamma'$  precipitate plates in over-aged samples. (a-b) Twinning at the centre of the precipitate-precipitate junction. The twin boundaries are indicated by blue lines while the basal planes of the HCP  $\gamma'$  phase are indicated by red lines. The sample was aged at 200°C for 7 days and *in situ* annealed at 200°C for 3 min. (c-d) Penetration of one precipitate through another at the precipitate-precipitate junction. The sample was aged at 200°C for 7 days.

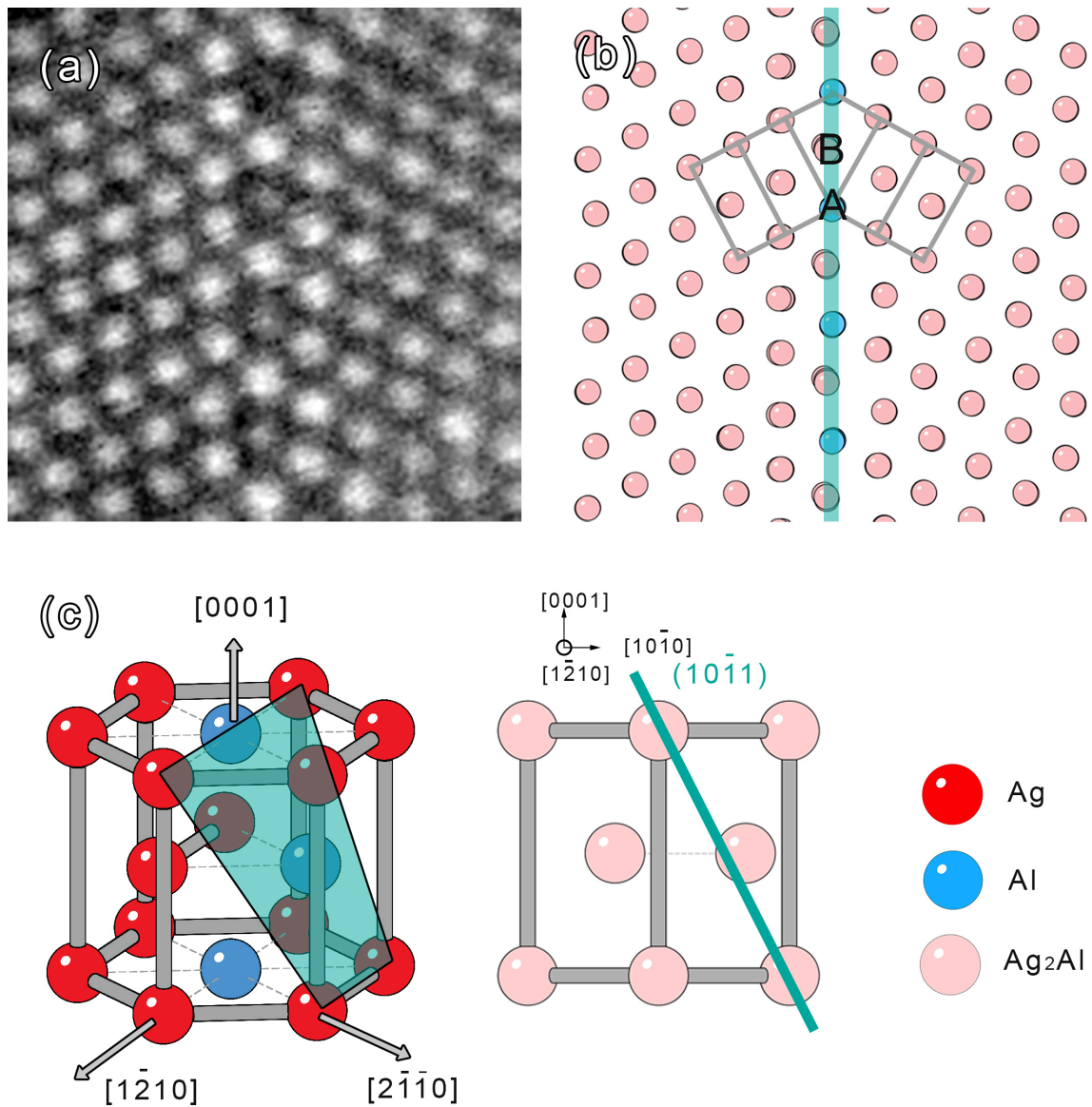


Fig. 6.15 Periodic segregation of Al in  $\{10\bar{1}1\}$   $\gamma$  twin boundary. (a) An enlarged view of HAADF-STEM image in Fig. 6.14(b). (b) Atomic model of the  $\{10\bar{1}1\}$  twin structure. (c) Schematic illustration and (d)  $[1\bar{2}10]$ -perspective view of HCP  $\gamma$  structure.

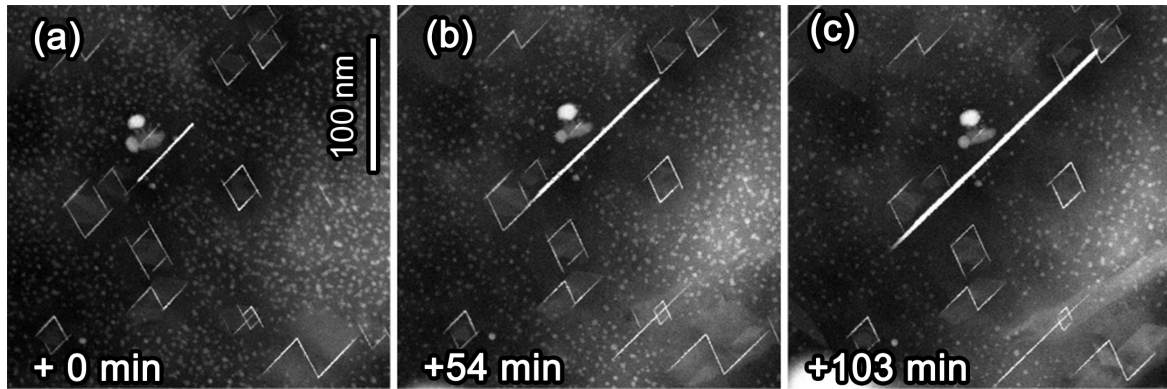


Fig. 6.16 *In situ* STEM showing the growth behaviours of  $\gamma'$  assemblies and individual  $\gamma'$  plates while annealing at 200°C. The original sample was water-quenched, aged at 200°C for 2 hr.

structure, which also forms  $\zeta$  phase beside  $\gamma$  precipitates, Fig. 6.15(a). This needs to be examined in a future study.

The different defect structures and chemistries at the precipitate interface may lead to completely different precipitation behaviours. Fig. 6.16 shows the microstructure evolution of a pre-aged alloy during *in situ* annealing at 200°C. The  $\gamma'$  precipitate assemblies were associated with Lomer-Cottrell dislocations at the precipitate junctions, as revealed in Fig. 6.12. The growth in both length and thickness of those precipitate assemblies was completely inhibited in the duration of the *in situ* annealing experiment. In contrast, a single  $\gamma'$  precipitate grew in both length and thickness directions with no restriction, which even consumed precipitate assemblies in its growth path, Fig. 6.16(c). The *in situ* observations are consistent with the findings from the bulk treatment in Fig. 4.5: namely,  $\gamma'$  precipitation assemblies resist coarsening during ageing at 200°C until replaced by individual  $\gamma$  precipitate plates.

## 6.5 Discussion

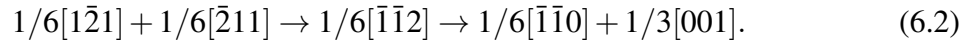
The structures and chemistry at the interfaces are different from the composing bulk phases. Similar to the Cu segregation at the coherent interface of  $\theta'$  ( $\text{Al}_2\text{Cu}$ ) precipitate, the coherent interface of  $\gamma'$  ( $\text{Ag}_2\text{Al}$ ) precipitate is clearly enriched in Ag for the early stages of growth. Viewing in both  $\langle 110 \rangle_{\text{Al}}$  and  $\langle 112 \rangle_{\text{Al}}$  directions, the strong contrast in HAADF-STEM images suggested that the Ag composition at the interface is higher than that within the precipitate ( $\text{Ag}_2\text{Al}$ ). But the Ag segregation was no longer visible for thick  $\gamma'$  precipitate. This observation motivated us to investigate the energetics associated with interfacial segregation

for different precipitate thicknesses. DFT calculations showed that the interfacial segregation energy varies during precipitate thickening. For the thinnest precipitate (1c-thick), Ag segregation at the coherent interface is associated with a significant energy reduction of 0.5 eV/Ag atom compared to the solid solution state. This value should be compared with the thermal energy at 200°C (0.04 eV), which implies that once an Ag atom hopped to the coherent interface, it has a low probability of diffusing back to the matrix. The interfacial energy is consequently lowered by Ag segregation, Fig. 6.4(b). As reviewed in Appendix A, the interfacial energy is the critical factor that dominates the nucleation energy barrier. Thus, the interfacial Ag segregation is likely to be strongly favoured for the  $\gamma'$  nucleation. This energy reduction caused by Ag segregation decreases with precipitate thickness and converges to 0.13 eV/Ag atom. Note that this value (-0.13 eV/Ag atom) is comparable with that of an Ag monolayer on  $\{111\}_{\text{Al}}$  planes (-0.15 eV/Ag atom) or GP zones (-0.16 eV/Ag atom). Thus, there is almost no enthalpy benefit for Ag atoms to diffuse from nearby GP zones to segregate at  $\gamma'$  coherent interface at the late stage of ageing. Of course, Ag atoms still diffuse towards  $\gamma$  phase as the equilibrium phase (-0.20 eV/Ag atom). The results presented here are aligned with earlier work of coherent interfaces in other aluminium alloys [11, 13, 33]. Those studies demonstrate that we can understand the interfacial segregation behaviours reasonably well with the combination of atomic structure characterisations and first-principles calculations.

A key feature of the semicoherent interface is the fact that the original high-index planes are reconstructed by nano-steps parallel to low-index planes. Such reconstruction is a common phenomenon for solid-solid interfaces in materials. Well-known examples are the reconstructed BCC-FCC interfaces in steels and Ti-Al alloys [205]. It is often postulated that the steps form on low-index planes due to the associated low interfacial energies [205]. In this study, we explained the nano-steps formation with the DFT deduced interfacial energies and an energetics-based reconstruction criterion, Fig. 6.7. Specifically, though reconstruction increases the interfacial area, the overall interfacial energy is compensated with the significantly decreased interfacial energies associated with low-index nano-steps. This approach is hopefully applicable to the interfacial reconstructions in other systems.

Dislocations are confined to the semicoherent FCC/HCP interfaces, but their exact types and locations have not been resolved until now. It is well accepted that Shockley partial dislocations are present at the FCC/HCP interface with three equivalent directions. However, we observed two types of semicoherent interfaces with distinct chemical distributions, Fig. 6.5. It naturally raises the question whether those two interfaces share the same dislocation structure. Type-I interface involves one column depleted in Ag surrounded by six column enriched in Ag as previously reported [70]. The Burgers vector analysis was performed

on the experimentally informed 3D interface model, which shows three Shockley partial dislocations are indeed periodically in place along the interface. Since there are two  $30^\circ$  Shockley partial dislocations and one  $90^\circ$  Shockley partial dislocation every 6 close-packed layers, one may well suspect that such hexagonal feature echoes the periodicity of  $90^\circ$  Shockley partial dislocation. However, our detailed analysis shows that it is not the case. A  $90^\circ$  Shockley partial dislocation is located in between the layers that exchange the stacking, Fig. 6.8. Meanwhile, the Ag depletion is in between two  $30^\circ$  Shockley partial dislocations, which has the same periodicity every six close-packed planes. This phenomenon should be based on an energetics reason. The first-principles calculations have not been performed yet due to the size of the interface model. But we have attempted structural optimisation of the interface model using EAM method. Surprisingly, the calculation suggests that three periodic Shockley partial dislocations will decompose further into another periodic structure that involves a  $90^\circ$  Shockley partial, a Lomer-Cottrell and a Hirth dislocation, Fig. 6.9. The transition state consists of a  $90^\circ$  Shockley partial dislocation and a  $90^\circ$  anti-Shockley partial dislocation, which are on the intersection line of  $\{111\}_{\text{Al}}$  and  $\{110\}_{\text{Al}}$  planes (see Fig. 6.10 and Fig. 6.11). Overall, the reaction proceeds by reconstructing dislocations on the close-packed  $\{111\}_{\text{Al}} \parallel \{0001\}_{\gamma}$  planes into their perpendicular planes  $\{110\}_{\text{Al}} \parallel \{1\bar{2}10\}_{\gamma}$ . The dislocation reaction can be written as:



The driving force for the dislocation reaction involves a reduction in strain energy. Assuming the strain energy associated with dislocations is proportional to the sum of the square of their Burgers vectors [21], this reaction reduces the strain energy by 50%. Of course, the exact energy may involve other electronic interactions, where calculations are out of the scope of this work. Though proven to be challenging, DFT calculations are still on-going to investigate the energetics associated with different stages of the dislocation reaction at the interface. A Lomer-Cottrell dislocation is associated with a 3-atomic-column region depleted in Ag as shown in Fig. 6.12. And Type-II interface consists of the periodic chemical distribution that involves a 3-atomic-column region depleted in Ag in adjacent to a 1-atomic-column region depleted in Ag. This is evidence that Lomer-Cottrell dislocations are involved in the Type-II interface, which could evolve from the Type-I interface with three periodic Shockley partial dislocations. Higher quality STEM images of the Type-II interface are needed to enable the dislocation analysis to support this hypothesis.

Different types of dislocations are associated with unique chemistries at their dislocation cores. In this study, a periodic one-column Al enrichment is present in between of two  $30^\circ$  Shockley partial dislocations at the Type-I FCC/HCP semicoherent interface. In addition,

a pair of two-column Al enrichment is present above and below a Hirth dislocation at the junction of two  $\gamma'$  precipitates tilted  $109.5^\circ$  relative to each other. In parallel, a 3-column Al enrichment is present at the Lomer-Cottrell dislocation at the junction of two  $\gamma'$  precipitates tilted  $70.5^\circ$  relative to each other, and at the Type-II FCC/HCP semicoherent interface. Those two contacting angles are results of the heterogeneous nucleation of  $\gamma'$  precipitates on different quenched-in dislocation loops. The addition of Cu to Al-Ag alloys changes the quenched-in dislocation loops from  $\{111\}_{\text{Al}}$  planes to  $\{110\}_{\text{Al}}$  planes as studied previously in Ref. [78], which consequently changes the type of dislocation present at the precipitate junctions. This interesting phenomenon shows the controllability of the interfacial dislocations that may also occur with other elements but yet to be studied. The chemical segregation at dislocations is a common phenomenon in materials science. The concept of Cottrell atmosphere was proposed in 1949 [206], before the first observation of dislocations in TEM in 1956 [207]. It suggested the dislocation motion is impeded by the capturing of small interstitial atoms, like carbon and nitrogen, which consequently improves the yield strength of alloys. This theory has been verified by TEM and ATP experiments [208]. A recent example showed that Mn atoms segregate at the dislocations in a Fe-Mn alloy that retains the austenite state (FCC) at the dislocation core in martensite (BCC/BCT) [209]. A cubic meter of martensite contains such an enormous number of dislocations that their total length can be up to a light year. The confined chemical and structural states at the dislocation cores are expected to change the mechanical properties of alloys. Apart from the role of dislocations in determining the plasticity of metals, dislocation cores can also change the local electronic and optical states, which is particularly important for semiconductors. In a II-VI semiconductor CdTe, Lomer-Cottrell dislocations are either enriched in Cd or Te, while Hirth dislocations consist Cd-Te atomic dumbbells [210]. Similarly, in a III-V semiconductor GaAs, Lomer-Cottrell dislocations are either enriched in Ga or As [211]. In both cases, first-principles calculations showed reduced band gaps at the dislocation cores compared to the bulk materials, which add intermediate energy states for electron excitation [211, 212]. In addition, the alternative elements enriched at the Lomer-Cottrell dislocation core are associated with different charge transfer [211, 212]. The development of charge creates linear channels along the dislocations and strong electric field between the channels [211]. We have to note that those observations are very recent thanks to the development of aberration-corrected TEM. The fundamental mechanisms behind the unique chemistry at the dislocation cores are largely unknown.

One of such mechanisms for solute segregation at defects could be the strain. For example, Bi is known to be hazardous for alloys because their segregation embrittles the grain boundaries. First-principles calculations showed that the segregation of Bi at Cu grain boundaries is purely a size effect [213]. Another example is periodic segregation of Gd

and/or Zn at coherent twin boundaries in Mg alloys, which pins the movement of twin boundaries during annealing [115]. Gd atoms (which is larger than Mg) prefer to segregate at the expansion sites, while Zn atoms (which is smaller than Mg) prefer to segregate at the compression sites at the twin boundaries. First-principles calculations together with invariant plane strain calculations showed that those segregation choices reduce the strain energy. It is interesting to note that the segregation at  $\{10\bar{1}1\}_{\text{Mg}}$  twin boundary is similar to our observation of  $\{10\bar{1}1\}_{\gamma}$  twin boundary, where Al enriches at the compression site. In fact, Al also tends to segregate at the compression site for Lomer-Cottrell dislocation. Because a dislocation imposes an anisotropic strain field in the crystal (particularly around the core), a solute atom with a different atomic size may preferentially segregate at one side of dislocation core to mitigate the strain energy. Different dislocations are expected to display different symmetries of the strain field that may result in unique chemistries at the dislocation cores. However, the atomic size difference between Al and Ag is negligibly small ( $\approx 0.5\%$ ). Further detailed computation and analysis are needed to elucidate the contribution of strain for solute segregation at those interfacial dislocations.

Interfacial dislocations directly determine the interface mobility and hence the growth behaviours of precipitates. Hirth and Lomer-Cottrell dislocations are both called stair-rod dislocations, as they are located at the interaction of two close-packed planes, similarly to the rods that hold the carpet down a stair. Because the Lomer-Cottrell dislocations and Hirth dislocations are not on the close-packed planes, they cannot move unless a significant energy penalty is paid. Therefore, they are also called sessile dislocations. Fig. 6.12 and Fig. 6.13 have shown that two sessile dislocations form at the precipitate-precipitate junctions and are associated with unique Al segregations. With the coupling between atomic structures and chemistries at the sessile dislocation cores, the growth of precipitate assemblies are stopped, Fig. 6.16. It is intuitive that the lengthening is inhibited with the impingement of two precipitates. Moreover, the thickening is immobilised as well. This is possibly caused by the difficulty in initiating a new ledge at the precipitate-precipitate junction, which requires the formation of new Shockley partial dislocations and possibly de-locking of pre-existing sessile dislocations. In contrast, an individual  $\gamma'$  precipitate plate has no restriction in lengthening and thickening with the movement of glissile Shockley partial dislocations. This is still a hypothesis waiting for future examination. Nevertheless, our atomic-resolution dislocation characterisations are in good agreements with the precipitation behaviours observed in bulk heat treatments (Fig. 4.5) and *in situ* experiments (Fig. 6.16). It demonstrates different thermal stabilities for the same precipitate phase with different types of dislocations at the interfaces. This study points out a direction for controlling precipitation via engineering their interfacial defects.

## 6.6 Conclusion

In this chapter, the atomic structures of various  $\gamma'/\gamma$  interfaces were characterised by scanning transmission electron microscopy. First-principles (DFT) and semi-empirical (EAM) calculations were performed to explore the energetics associated with different interfaces. The main conclusions are as follows:

1. Ag segregates at the coherent interface of the  $\gamma'$  precipitate phase during nucleation and the early stages of growth. The interfacial segregation can be understood from the associated energy reduction for a thin precipitate.
2. The semicoherent interfaces of  $\gamma'$  precipitate plate are reconstructed by nano-steps parallel to  $\{111\}_{\text{Al}}$  and  $\{002\}_{\text{Al}}$  planes. The nano-steps formation can be explained from an energetic perspective with our interfacial energies calculations. There are two types of reconstructed semicoherent interfaces with different chemical distributions. For the Type-I interface, the precise positions of Shockley partial dislocations were determined in an experimentally-informed 3D model. EAM optimisation of the 3D model suggested dislocation reaction of three Shockley partial dislocations into a Shockley partial dislocation, a Lomer-Cottrell and a Hirth dislocation periodically spaced along the interface. The periodic chemical distribution associated with the Type-II interface supported the hypothesis that Lomer-Cottrell dislocations are present at the interface.
3. Stair-rod dislocations were identified at precipitate-precipitate junctions with unique chemistries. Depending on the contacting angle of the precipitates on different close-packed planes, the dislocation can be either Lomer-Cottrell ( $\vec{b} = 1/6\langle 110 \rangle$ ) or Hirth ( $\vec{b} = 1/6\langle 110 \rangle$ ). Both dislocations are sessile so that they impede  $\gamma'$  precipitate growth during ageing at 200°C. In contrast, a precipitate with Shockley partial dislocations at its interface can grow freely.

# Chapter 7

## Conclusions and Future Work

Starting from the Wright Brothers' flight and Wilm's discovery, precipitation-hardened aluminium alloys have been used for every generation of aircraft and spacecraft. Alloy innovation requires a deep understanding of the art and science of precipitation. However, the atomic mechanisms associated with precipitation are not fully understood, thus preventing a rational alloy design based on first principles. The main purpose of this project was to understand the role of interfaces and defects associated with precipitate nucleation and growth in Al-Ag alloys. With such an understanding, new ways to tailor microstructures and hence the mechanical properties of alloys may be developed. The present study developed new processing schemes to manipulate phase transformation pathways through the interaction between defects and pre-existing phases. Using this strategy, we discovered new precipitation behaviours and a new precipitate phase  $\zeta$  in the textbook Al-Ag system. The  $\zeta$  phase has a bi-layered structure analogous to the Ag interfacial segregation in various high-strength aluminium alloys. Interfaces of the known HCP  $\gamma'/\gamma$  phases were also investigated in detail, including coherent and semicoherent precipitate-matrix interfaces and precipitate-precipitate junctions. The coupling between dislocations and chemistry confined at the interfaces enables new atomistic insight into the precipitation growth behaviours.

In summary, this study demonstrates controlling precipitation by manipulating precipitate interfaces and lattice defects in the textbook Al-Ag system. The phase transformations revealed in this binary system are richer than previously established, with a new precipitate phase  $\zeta$  and the associated transition pathways. In addition, the proposed processing strategy is expected to lead discoveries of new phases in other systems and provides a platform for engineering the metastable alloy microstructure against environmental degradation. This study also showcases manipulating precipitation growth behaviours through the nature of interfacial structures. In the following sections, we will conclude each result chapters and point out directions for future work.

## 7.1 Modifying Phase Transformation Pathways through the Interaction Between Defects and Pre-existing Phases

Lattice defects – such as dislocations, stacking faults, vacancies and solute clusters – adjust the kinetics of precipitation by providing heterogeneous nucleation sites for precipitate phases. The local environment of a defect differs from the bulk: the lattice is distorted in a way that may activate structural transformations; solute segregation may provide a local compositional enrichment favourable to precipitation. Thus, defects are often deliberately introduced to alloys to promote precipitation during processing. In the Al-Ag system,  $\gamma'$  precipitates are known to heterogeneously nucleate on stacking faults decomposed from dislocation loops. Our embedded atom method simulations agree very well with electron tomography reconstructions, revealing the associated atomic mechanisms of dislocation reactions. A core-shell Ag-rich structure was also observed, composed of a quenched-in void embedded in an Ag-enriched GP zone  $\epsilon$ . By changing the quenching media and hence the quenched-in defects, we manipulated the microstructure evolution of the alloy during ageing. Slow quenching reduced quenched-in defects and hence suppressed  $\gamma'$  precipitation.

This study highlighted the importance of the timing and manner in which defects are induced to an alloy. After the FCC-HCP phase transformation was suppressed, vacancies and dislocations were introduced into a pre-aged alloy. This was performed in two ways: in the TEM foils by *in situ* annealing or in the bulk alloy by deformation and secondary ageing. The introduced defects triggered phase transformations on pre-existing metastable GP zones, i.e. nucleation of the  $\gamma'$  phase and that of a new ordered  $\zeta$  phase. This phenomenon is possibly due to the vacancy flux generated from the surface of a thin TEM foil during *in situ* annealing or from the movement of introduced dislocations. Direct observations of dislocation motion in association with  $\gamma'$  phase nucleation supported our proposed mechanism.

This work demonstrated the feasibility of manipulating phase transformation pathways through the interaction between defects and pre-existing phases. There are two core requirements of the proposed processing strategy: (a) the alloy must have metastable pre-existing phases; (b) lattice defects must be introduced and secondary ageing should be performed. We suggested that these conditions are widely available during the servicing of engineering alloys. Thus, this mechanism could be important in determining the stabilities of alloys against environmental degradation, such as during fatigue and creep, which usually involve metastable microstructures.

## 7.2 Atomic Structure and Phase Transformations of The Bi-layered Precipitate $\zeta$ Phase

We characterised the atomic structure of the newly discovered metastable  $\zeta$  phase. The  $\zeta$  phase differs from the known FCC and HCP structures with Ag- and Al-enriched bi-layers on alternating close-packed planes. Our EDXS analysis suggests that the  $\zeta$  phase has a composition close to AgAl, which also suggests the  $\varepsilon$ - $\zeta$  transformation simply involves rearrangement of atoms. This composition hypothesis is supported by comparing the experimental HAADF-STEM intensities with multislice image simulations of the DFT-optimised AgAl model. The experimental and calculated atomic positions were found to be in excellent agreement. It is worth noting that the  $\zeta$  phase inherits the stacking of FCC and is fully coherent with the Al matrix. However, the alternating chemistry results in noticeable alternating displacements in the direction normal to the close-packed planes, which is associated with the electronic structures between close-packed planes. The displacements are inherent to the  $\zeta$  phase, revealed by comparing the results from geometric phase analysis (GPA) of HAADF-STEM images with the calculated displacements of the DFT-optimised structure. The space group is  $R\bar{3}m$  with experimentally-measured lattice parameters of  $a = 2.88 \pm 0.05 \text{ \AA}$  and  $c = 27.35 \pm 0.05 \text{ \AA}$  and atomic positions of Ag at (0 0 0.878) and Al at (0 0 0.375).

By imagining the  $\zeta$  phase transformations under heating and/or irradiation within a transmission electron microscope, we revealed the time-resolved phase transformations at nano and even atomic scale. A clear ordered contrast emerged from a GP zone  $\varepsilon$  due to the formation of the bi-layered  $\zeta$  phase during *in situ* annealing. The  $\gamma'$  precipitate assemblies nucleated beside the  $\zeta$  phase and formed a complex morphology. *In situ* STEM experiments clearly showed that the  $\zeta$  phase is an intermediate phase between the GP zone  $\varepsilon$  and the equilibrium  $\gamma'/\gamma$  phases. Stacking faults were found to be critical for the nucleation of the HCP  $\gamma'$  structure.

Various configurations of Ag atomic clusters in aluminium were analysed, showing that the  $\zeta$  phase is a local energy minimum state during Ag clustering in the aluminium matrix. Ag atoms are not stable in the solid solution and prefer to aggregate on the  $\{111\}_{\text{Al}}$  close-packed planes. The chemical ordering inside GP zones  $\varepsilon$  can be explained by the favourable spacing between the Ag layers in aluminium, which leads to the formation of the  $\zeta$  phase. Theoretically, precipitates with high-aspect ratios on  $\{111\}_{\text{Al}}$  planes are most effective in strengthening FCC alloys. The fast decomposition from solid solution, the strong preference on  $\{111\}_{\text{Al}}$  planes, and the intimate interactions with defects are intrinsic properties of Ag in Al. These properties are expected to provide heterogeneous nucleation sites on  $\{111\}_{\text{Al}}$

planes at the very early stage of ageing, which may explain the microalloying effects of Ag in high-strength aluminium alloys.

### 7.3 Interfacial Structures of the HCP Precipitate $\gamma'/\gamma$ Phases

Resolving the FCC/HCP interfaces of the  $\gamma'/\gamma$  phases is another classic topic re-examined in this project. It is well accepted that the broad interface of the  $\gamma'$  phase is coherent, matching the close-packed planes between FCC and HCP. The coherent interface was found to be enriched in Ag at the early stage of  $\gamma'$  thickening but not at the late stages. This segregation phenomenon was explained with the energy reduction per Ag segregated as a function of precipitate thickness.

The semicoherent interface of the  $\gamma'/\gamma$  phase is reconstructed by nano-steps parallel to low-index planes. In every six close-packed layers,  $\{112\}_{\text{Al}} \parallel \{1\bar{2}10\}_{\gamma}$  facets are decomposed into a four-layered step parallel to  $\{111\}_{\text{Al}} \parallel \{10\bar{1}1\}_{\gamma}$  and a two-layered step parallel to  $\{002\}_{\text{Al}} \parallel \{10\bar{1}1\}_{\gamma}$ . The observed interfacial reconstruction was explained with DFT-deduced interfacial energies and an energetics-based reconstruction criterion. By locating the atomic positions on HAADF-STEM images and applying the periodicity of FCC and HCP in the viewing direction, we built experimentally-informed 3D models of the precipitate-matrix interfaces. Burgers vector analysis was performed for each atom in the 3D model and Shockley partial dislocations in three equivalent directions were identified as expected. However, our atomistic calculations showed that the three Shockley partial dislocations can decompose into a  $90^\circ$  Shockley partial dislocation, a Lomer-Cottrell dislocation and a Hirth dislocation. The two different models of interfacial dislocations are possibly associated with two types of chemical distributions observed at the semicoherent interfaces.

It is the nature of interfacial dislocations which control the growth behaviour of the  $\gamma'/\gamma$  phases. The presence of sessile dislocations was identified at the precipitate-precipitate junctions of  $\gamma'$  assemblies. Depending on their contacting angles, two glissile Shockley partial dislocations on different close-packed planes can react into a Lomer-Cottrell dislocation or a Hirth dislocation. Moreover, twins found to exist at the precipitate-precipitate intersections for thick  $\gamma$  plates. Interestingly, each type of defect is associated with unique chemical segregation. As revealed by bulk heat treatment and *in situ* annealing, the thickening of precipitate assemblies was hindered by sessile dislocations at their junctions, while the growth of individual precipitate plates had no restriction with glissile dislocations at their semicoherent interfaces. This study demonstrates different thermal stabilities of the same precipitate phase with different interfacial structures.

## 7.4 Future Work

On the basis of the work presented here, we suspect that interactions between defects and pre-existing phases could be a general phenomenon across many alloy systems. To confirm our hypothesis, it is worthwhile to re-investigate the phase transformations of other well-known alloy systems using the proposed processing strategy. Future work should not be limited to textbook alloy system but also be extended to include alloy systems with engineering significance, for example, high-strength aluminium alloys and magnesium alloys. The defects-induced phase transformations could influence the durability of engineering applications where defects are generated in alloys under thermal, mechanical, or even irradiative conditions. In other words, phase transformations may never stop during the servicing of alloys. It is important to confirm the associated mechanisms in engineering applications and develop the theory of dynamic precipitation. Such knowledge is critical to developing new strategies to enhance the stabilities of alloys against environmental degradation.

The bulk processing scheme developed in this project involves deforming a pre-aged alloy and performing secondary ageing. It is interesting that small deformations yielded phase transformations within GP zones as the pre-existing phase. In contrast, large deformations sheared the GP zones and resulted in  $\gamma'$  precipitate nucleation in the matrix. A systematic study is needed to correlate the extent of deformation and the change in microstructure during secondary ageing. In particular, one should determine the dislocation density, the degree of shearing for pre-existing phases, the density and distribution of newly formed precipitate phases and the ageing response. Such study should be a useful reference for developing new thermomechanical processing that utilises defects to engineer microstructures and mechanical properties.

Complicated phase transformations are difficult to study at the atomic scale. With the development of aberration-corrected instruments and stable *in situ* holders, it is possible to reveal the dynamics of phase transformations at a high temporal and spatial resolution. In this study, electro-polished TEM samples were *in situ* annealed and the resolution was limited to the nanoscale due to thermal drifting. In the future, one could try to use a focused ion beam microscopy (FIB) to manufacture alloy lamellae for protochip *in situ* heating holders. The significantly improved *in situ* stability should yield detailed transformation mechanisms.

The growth behaviour of a precipitate can be manipulated by engineering the interfacial structures. For instance, the growth of  $\gamma'$  assemblies is stopped with sessile dislocations at the precipitate-precipitate junctions. Improved thermal stability of a precipitate phase is an interesting feature for thermal resistant applications. Thus, it is interesting to generalise this mechanism to the other systems. For example, the  $T_1$  phase in Al-Cu-Li alloys, the

$\Omega$  phase in Al-Cu-Mg-Ag alloys and the  $\eta$  phase in Al-Zn-Mg-Cu alloys are promising candidates for reproducing the phenomenon, as they all precipitate on the  $\{111\}_{\text{Al}}$  planes. In particular, the  $T_1$  phase and the  $\eta$  phase have HCP structures that should give Shockley partial dislocations at the FCC/HCP interfaces. Inevitably, those Shockley partial dislocations on different close-packed planes are expected to react into sessile dislocations. It shall be interesting to verify this dislocation reaction in those systems and even expand the mechanism beyond FCC/HCP transformations. The mechanisms governing unique chemical segregation at sessile dislocation cores are still unknown. Advanced atomistic calculations and strain quantification are needed at those precipitate-precipitate junctions to resolve the mystery. By understanding the role of interfacial dislocations and ways to generate them, we should be able to tailor the microstructures and hence the mechanical and thermal properties during artificial ageing.

Despite its textbook status, the Al-Ag system still has not revealed all its secrets. Atomic resolution HAADF-STEM is required to confirm the short-range ordering suggested by Neumann's model and the order-disorder transformation. One can examine the phase aged at low temperatures (i.e. 100°C) viewing along a  $\langle 112 \rangle_{\text{Al}}$  direction. For the FCC/HCP semicoherent interface, a high-resolution HAADF-STEM image with the better quality of the Type-II interface is needed for a dislocation analysis, which is critical to support our interfacial dislocation reaction model. The interfacial energies of the two types of semicoherent interfaces and two types of precipitate-precipitate junctions could be calculated by DFT. We may use the first-principles deduced interfacial energies to predict precipitate growth kinetics and compare with experiments.

Precipitation is more than what has been exposed; so is our journey in the universe.

# References

- [1] F. W. Gayle and M. Goodway, “Precipitation hardening in the first aerospace aluminum alloy: the wright flyer crankcase,” *Science*, pp. 1015–1015, 1994.
- [2] T. D. Crouch, *The bishop’s boys: A life of Wilbur and Orville Wright*. W. W. Norton & Company, 2003.
- [3] S. Venetski, ““Silver” from clay,” *Metallurgist*, vol. 13, no. 7, pp. 451–453, 1969.
- [4] I. J. Polmear, D. StJohn, J. F. Nie, and M. Qian, “2 - physical metallurgy of aluminium alloys,” in *Light Alloys*, pp. 31 – 107, Boston: Butterworth-Heinemann, fifth ed., 2017.
- [5] A. Guinier, “Structure of age-hardened aluminium-copper alloys,” *Nature*, vol. 142.3595, no. 569-570, 1938.
- [6] G. D. Preston, “Structure of age-hardened aluminium-copper alloys,” *Nature*, vol. 142.3595, no. 570, 1938.
- [7] J. M. Silcock, T. Heal, and H. K. Hardy, “Structural ageing characteristics of aluminum-copper alloys,” *Journal of the Institute of Metals*, vol. 82, pp. 239–248, 1953-1954.
- [8] U. Dahmen and K. H. Westmacott, “Ledge structure and the mechanism of  $\theta'$  precipitate growth in Al-Cu,” *Physica Status Solidi*, vol. 80, no. 1, pp. 249–262, 1983.
- [9] J. F. Nie, “20 - physical metallurgy of light alloys,” in *Physical Metallurgy* (D. E. Laughlin and K. Hono, eds.), pp. 2009 – 2156, Oxford: Elsevier, fifth ed., 2014.
- [10] H. Aaronson, M. Enomoto, and J. Lee, *Mechanisms of Diffusional Phase Transformations in Metals and Alloys*, pp. 433–491. CRC Press, 2010.
- [11] L. Bourgeois, C. Dwyer, M. Weyland, J.-F. Nie, and B. C. Muddle, “Structure and energetics of the coherent interface between the  $\theta'$  precipitate phase and aluminium in Al-Cu,” *Acta Materialia*, vol. 59, no. 18, pp. 7043–7050, 2011.
- [12] L. Bourgeois, N. V. Medhekar, A. E. Smith, M. Weyland, J.-F. Nie, and C. Dwyer, “Efficient atomic-scale kinetics through a complex heterophase interface,” *Physical Review Letters*, vol. 111, no. 4, p. 046102, 2013.
- [13] S. J. Kang, Y. W. Kim, and J. M. Zuo, “Determination of interfacial atomic structure, misfits and energetics of  $\Omega$  phase in Al-Cu-Mg-Ag alloy,” *Acta Materialia*, vol. 81, pp. 501–511, 2014.

- [14] C. R. Hutchinson, "15 - modeling the kinetics of precipitation in aluminium alloys," in *Fundamentals of Aluminium Metallurgy* (R. Lumley, ed.), Woodhead Publishing Series in Metals and Surface Engineering, pp. 422 – 467, Woodhead Publishing, 2011.
- [15] D. A. Porter, K. E. Easterling, and M. Sherif, *Phase Transformations in Metals and Alloys, (Revised Reprint)*, pp. 285–286. CRC press, 2011.
- [16] D. Williams and C. Carter, *Transmission Electron Microscopy: A Textbook for Materials Science*. Springer US, 2013.
- [17] I. J. Polmear, D. StJohn, J. F. Nie, and M. Qian, "4 - wrought aluminium alloys," in *Light Alloys*, pp. 157 – 263, Boston: Butterworth-Heinemann, fifth ed., 2017.
- [18] I. J. Polmear, "A trace element effect in alloys based on the aluminium-zinc-magnesium system," *Nature*, vol. 186, pp. 303–304, 04 1960.
- [19] J. H. Auld, J. T. Vietz, and I. J. Polmear, "T-phase precipitation induced by the addition of silver to an aluminium-copper-magnesium alloy," *Nature*, vol. 209, no. 5024, pp. 703–704, 1966.
- [20] C. Hutchinson, X. Fan, S. Pennycook, and G. Shiflet, "On the origin of the high coarsening resistance of  $\Omega$  plates in Al–Cu–Mg–Ag Alloys," *Acta Materialia*, vol. 49, pp. 2827–2841, Aug. 2001.
- [21] D. Hull and D. J. Bacon, *Introduction to dislocations*. Butterworth-Heinemann, 2001.
- [22] V. Vaithyanathan, C. Wolverton, and L. Chen, "Multiscale modeling of  $\theta'$  precipitation in Al–Cu binary alloys," *Acta Materialia*, vol. 52, no. 10, pp. 2973 – 2987, 2004.
- [23] R. Sankaran and C. Laird, "Kinetics of growth of platelike precipitates," *Acta Metallurgica*, vol. 22, no. 8, pp. 957 – 969, 1974.
- [24] C. Wolverton, "Solute–vacancy binding in aluminum," *Acta Materialia*, vol. 55, no. 17, pp. 5867–5872, 2007.
- [25] H. K. Hardy, "The ageing characteristics of ternary aluminium copper alloys with cadmium, indium, or tin," *Journal of the Institute of Metals*, vol. 80, no. 9, pp. 483–492, 1952.
- [26] J. Silcock and H. Flower, "Comments on a comparison of early and recent work on the effect of trace additions of Cd, In, or Sn on nucleation and growth of  $\theta'$  in Al–Cu alloys," *Scripta Materialia*, vol. 46, no. 5, pp. 389–394, 2002.
- [27] L. Bourgeois, J. F. Nie, and B. C. Muddle, "Assisted nucleation of  $\theta'$  phase in Al–Cu–Sn: the modified crystallography of tin precipitates," *Philosophical Magazine*, vol. 85, no. 29, pp. 3487–3509, 2005.
- [28] L. Bourgeois, C. Dwyer, M. Weyland, J. Nie, and B. C. Muddle, "The magic thicknesses of  $\theta'$  precipitates in Sn-microalloyed Al–Cu," *Acta Materialia*, vol. 60, no. 2, pp. 633–644, 2012.
- [29] J. M. Silcock, "Intermediate precipitates in aged binary alloys of aluminium with cadmium, indium or tin," *Journal of the Institute of Metals*, vol. 84, pp. 19–22, 1955.

- [30] Y. Zhang, Z. Zhang, N. V. Medhekar, and L. Bourgeois, "Vacancy-tuned precipitation pathways in Al-1.7 Cu-0.025 In-0.025 Sb (at.%) alloy," *Acta Materialia*, vol. 141, pp. 341–351, 2017.
- [31] Y. Chen, Z. Zhang, Z. Chen, A. Tsalanidis, M. Weyland, S. Findlay, L. J. Allen, J. Li, N. V. Medhekar, and L. Bourgeois, "The enhanced theta-prime ( $\theta'$ ) precipitation in an Al-Cu alloy with trace Au additions," *Acta Materialia*, vol. 125, pp. 340–350, 2017.
- [32] H. Bhadeshia, "21 - physical metallurgy of steels," in *Physical Metallurgy* (D. E. Laughlin and K. Hono, eds.), pp. 2157 – 2214, Oxford: Elsevier, fifth ed., 2014.
- [33] L. Bourgeois, Z. Zhang, J. Li, and N. V. Medhekar, "The bulk and interfacial structures of the  $\eta$  ( $Al_2Au$ ) precipitate phase," *Acta Materialia*, vol. 105, pp. 284–293, 2016.
- [34] K. D. Ralston, N. Birbilis, M. Weyland, and C. R. Hutchinson, "The effect of precipitate size on the yield strength-pitting corrosion correlation in Al-Cu-Mg alloys," *Acta Materialia*, vol. 58, no. 18, pp. 5941–5948, 2010.
- [35] L. Reich, M. Murayama, and K. Hono, "Evolution of  $\Omega$  phase in an Al-Cu-Mg-Ag alloy—a three-dimensional atom probe study," *Acta Materialia*, vol. 46, no. 17, pp. 6053–6062, 1998.
- [36] I. J. Polmear, "Role of trace elements in aged Aluminium-Alloys," *Materials Science Forum*, vol. 13, pp. 195–214, 1987.
- [37] M. Murayama and K. Hono, "Three dimensional atom probe analysis of pre-precipitate clustering in an Al-Cu-Mg-Ag alloy," *Scripta Materialia*, vol. 38, no. 8, pp. 1315–1319, 1998.
- [38] T. Uesugi, M. Kohyama, and K. Higashi, "Ab initio study on divacancy binding energies in aluminum and magnesium," *Physical Review B*, vol. 68, no. 18, p. 184103, 2003.
- [39] W. Cai and W. Nix, *Imperfections in Crystalline Solids*. MRS-Cambridge Materials Fundamentals, Cambridge University Press, 2016.
- [40] A. Guinier, "Le mécanisme de la précipitation dans un cristal de solution solide métallique.-cas des systèmes aluminium-cuivre et aluminium-argent," *Journal de Physique et Le Radium*, vol. 3, no. 7, pp. 124–136, 1942.
- [41] H. Jagodzinski and F. Laves, "Über die deutung der entmischungsvorgänge in mischkristallen unter besonderer berucksichtigung der systeme aluminium-kupfer und aluminium-silber," *Zeitschrift fur Metallkunde*, vol. 40, no. 8, pp. 296–305, 1949.
- [42] F. Seitz, "On the generation of vacancies by moving dislocations," *Advances in Physics*, vol. 1, no. 1, pp. 43–90, 1952.
- [43] L. A. Girifalco and H. Herman, "A model for the growth of guinier-preston zones-the vacancy pump," *Acta Metallurgica*, vol. 13, no. 6, pp. 583–590, 1965.
- [44] J. B. Clark, "Electron probe test of two theories of "denuded zone" formation in aged alloys," *Acta Metallurgica*, vol. 12, no. 10, pp. 1197–1201, 1964.

- [45] C. Dwyer, M. Weyland, and L. Y. Chang, "Combined electron beam imaging and ab initio modeling of  $T_1$  precipitates in Al–Li–Cu alloys," *Applied Physics Letters*, vol. 98, no. 20, p. 201909, 2011.
- [46] S. J. Kang, T. H. Kim, C. W. Yang, J. I. Lee, E. S. Park, T. W. Noh, and M. Kim, "Atomic structure and growth mechanism of  $T_1$  precipitate in Al–Cu–Li–Mg–Ag alloy," *Scripta Materialia*, vol. 109, pp. 68–71, 2015.
- [47] P. C. Varley, *The technology of aluminium and its alloys*. CRC Press, 1970.
- [48] B. Averill and P. Eldredge, *General Chemistry: Principles, Patterns, and Applications*. The Saylor Foundation, 2011.
- [49] C. Laird and H. Aaronson, "The growth of  $\gamma$  plates in an Al-15% Ag alloy," *Acta Metallurgica Materialia*, vol. 17, no. 4, pp. 505–519, 1969.
- [50] K. Inoke, K. Kaneko, M. Weyland, P. A. Midgley, K. Higashida, and Z. Horita, "Severe local strain and the plastic deformation of Guinier–Preston zones in the Al–Ag system revealed by three-dimensional electron tomography," *Acta Materialia*, vol. 54, no. 11, pp. 2957–2963, 2006.
- [51] S. V. Aert, K. J. Batenburg, M. D. Rossell, R. Erni, and G. V. Tendeloo, "Three-dimensional atomic imaging of crystalline nanoparticles," *Nature*, vol. 470, no. 7334, pp. 374–377, 2011.
- [52] A. McAlister, "The Ag–Al (Silver–Aluminum) system," *Bulletin of Alloy Phase Diagrams*, vol. 8, no. 6, pp. 526–533, 1987.
- [53] R. Baur and V. Gerold, "The existence of a metastable miscibility gap in aluminium–silver alloys," *Acta Metallurgica*, vol. 10, no. 6, pp. 637–645, 1962.
- [54] R. B. Nicholson and J. Nutting, "The metallography of precipitation in an Al-16% Ag alloy," *Acta metallurgica*, vol. 9, no. 4, pp. 332–343, 1961.
- [55] J. E. Gragg and J. B. Cohen, "The structure of Guinier–Preston zones in aluminum-5 at.% silver," *Acta Metallurgica*, vol. 19, no. 6, pp. 507–519, 1971.
- [56] T. Al-Kassab and P. Haasen, "Early stages of precipitation in dilute Al–Ag alloys," *Zeitschrift für Metallkunde*, vol. 84, no. 4, pp. 248–250, 1993.
- [57] F. K. LeGoues, R. N. Wright, Y. W. Lee, and H. I. Aaronson, "Influence of crystallography upon critical nucleus shapes and kinetics of homogeneous fcc–fcc nucleation—V. The origin of GP zones in Al–Ag and Al–Cu alloys," *Acta Metallurgica*, vol. 32, no. 10, pp. 1865–1870, 1984.
- [58] M. Asta and J. J. Hoyt, "Thermodynamic properties of coherent interfaces in fcc-based Ag–Al alloys: a first-principles study," *Acta materialia*, vol. 48, no. 5, pp. 1089–1096, 2000.
- [59] K. B. Alexander, F. K. LeGoues, H. I. Aaronson, and D. E. Laughlin, "Faceting of GP zones in an Al–Ag alloy," *Acta Metallurgica*, vol. 32, no. 12, pp. 2241–2249, 1984.

- [60] R. Erni, H. Heinrich, and G. Kostorz, "High-resolution Z-contrast STEM of Guinier–Preston zones in Al–3 at.% Ag," *Materials chemistry and physics*, vol. 81, no. 2, pp. 227–229, 2003.
- [61] E. A. Marquis, "A reassessment of the metastable miscibility gap in Al–Ag alloys by atom probe tomography," *Microscopy and Microanalysis*, vol. 13, no. 06, pp. 484–492, 2007.
- [62] P. A. Dubey, B. Schönfeld, and G. Kostorz, "Shape and internal structure of Guinier–Preston zones in Al–Ag," *Acta metallurgica et materialia*, vol. 39, no. 6, pp. 1161–1170, 1991.
- [63] A. Guinier, "On the birth of GP zones," in *Materials Science Forum*, vol. 217, pp. 3–6, Trans Tech Publications, 1996.
- [64] C.-C. Chen, C. Zhu, E. White, C. Chiu, M. Scott, B. Regan, L. Marks, Y. Huang, J. Miao, J. Miao, C. Chen, C. Zhu, E. White, M. Scott, B. Regan, C. Chiu, Y. Huang, and L. Marks, "Three-dimensional imaging of dislocations in a nanoparticle at atomic resolution," *Nature*, 2013.
- [65] R. Xu, C.-C. Chen, L. Wu, M. C. Scott, W. Theis, C. Ophus, M. Bartels, Y. Yang, H. Ramezani-Dakhel, M. R. Sawaya, H. Heinz, L. D. Marks, P. Ercius, and J. Miao, "Three-dimensional coordinates of individual atoms in materials revealed by electron tomography," *Nature Materials*, vol. 14, no. 11, pp. 1099–1103, 2015.
- [66] Y. Yang, C.-C. Chen, M. C. Scott, C. Ophus, R. Xu, A. Pryor, L. Wu, F. Sun, W. Theis, J. Zhou, M. Eisenbach, P. R. C. Kent, R. F. Sabirianov, H. Zeng, P. Ercius, and J. Miao, "Deciphering chemical order/disorder and material properties at the single-atom level," *Nature*, vol. 542, no. 7639, pp. 75–79, 2017.
- [67] C. S. Barrett, A. H. Geisler, and R. F. Mehl, "Mechanism of precipitation from the solid solution of silver in aluminum," *Trans. AIME*, vol. 143, no. 134, pp. 158–180, 1941.
- [68] J. P. Neumann, "Determination of the ordering in the intermetallic compound  $\text{Ag}_2\text{Al}$ ," *Acta Metallurgica*, vol. 14, no. 4, pp. 505–511, 1966.
- [69] J. M. Howe, U. Dahmen, and R. Gronsky, "Atomic mechanisms of precipitate plate growth," *Philosophical Magazine A*, vol. 56, no. 1, pp. 31–61, 1987.
- [70] J. M. Rosalie, C. Dwyer, and L. Bourgeois, "On chemical order and interfacial segregation in  $\gamma'$  ( $\text{AlAg}_2$ ) precipitates," *Acta Materialia*, vol. 69, pp. 224–235, 2014.
- [71] J. M. Howe, H. I. Aaronson, and R. Gronsky, "Atomic mechanisms of precipitate plate growth in the Al–Ag system—I. Conventional transmission electron microscopy," *Acta Metallurgica*, vol. 33, no. 4, pp. 639–648, 1985.
- [72] J. M. Howe, H. I. Aaronson, and R. Gronsky, "Atomic mechanisms of precipitate plate growth in the Al–Ag system—II. High-resolution transmission electron microscopy," *Acta Metallurgica*, vol. 33, no. 4, pp. 649–658, 1985.

- [73] S. Y. Yu, B. Schönfeld, and G. Kostorz, "Diffuse x-ray scattering of Ag–13.4 at. % Al," *Physical Review B*, vol. 56, no. 14, pp. 8535–8541, 1997.
- [74] N. A. Zarkevich and D. D. Johnson, "Predicted hcp Ag-Al metastable phase diagram, equilibrium ground states, and precipitate structure," *Physical Review B*, vol. 67, no. 6, p. 064104, 2003.
- [75] K. T. Moore and J. M. Howe, "Characterization of gamma plate-shaped precipitates in an Al–4.2 at.% Ag alloy—growth kinetics, solute field, composition and modeling," *Acta Materialia*, vol. 48, no. 16, pp. 4083–4098, 2000.
- [76] M. Ferrante and R. D. Doherty, "Influence of interfacial properties on the kinetics of precipitation and precipitate coarsening in aluminium-silver alloys," *Acta Metallurgica*, vol. 27, no. 10, pp. 1603–1614, 1979.
- [77] J. M. Rosalie, L. Bourgeois, and B. C. Muddle, "Precipitate assemblies formed on dislocation loops in aluminium-silver-copper alloys," *Philosophical Magazine*, vol. 89, no. 25, pp. 2195–2211, 2009.
- [78] J. M. Rosalie, *The Nucleation and Growth of the  $\gamma'$  Phase in Aluminium-Silver-(Copper) Alloys*. PhD thesis, Monash University, 2007.
- [79] S. Ogata, J. Li, and S. Yip, "Ideal pure shear strength of aluminum and copper," *Science*, vol. 298, no. 5594, pp. 807–811, 2002.
- [80] D. Finkenstadt and D. D. Johnson, "Solute/defect-mediated pathway for rapid nano-precipitation in solid solutions:  $\gamma$  surface analysis in fcc Al–Ag," *Physical Review B*, vol. 73, no. 2, p. 024101, 2006.
- [81] J. M. Rosalie, L. Bourgeois, and B. C. Muddle, "Nucleation and growth of the gamma prime (AlAg<sub>2</sub>) precipitate in Al-Ag (-Cu) alloys," *Acta Materialia*, vol. 59, no. 19, pp. 7168–7176, 2011.
- [82] H. I. Aaronson and C. Laird, "Structures and migration kinetics of alpha: theta prime boundaries in Al-4% Cu: Part I-Interfacial structures," *Trans. AIME*, vol. 242, no. 7, 1968.
- [83] D. Finkenstadt and D. D. Johnson, "Analysis of nonequilibrium hcp precipitate growth in fcc matrices: Application to Al–Ag," *Materials Science and Engineering: A*, vol. 525, no. 1, pp. 174–180, 2009.
- [84] J. M. Howe, *Atomic mechanisms of  $\gamma'$  precipitate plate growth in the Al-Ag system*. PhD thesis, University of California, Berkley, 1986.
- [85] J. M. Rosalie and L. Bourgeois, "Silver segregation to  $\theta'$  (Al<sub>2</sub>Cu)-Al interfaces in Al-Cu-Ag alloys," *Acta Materialia*, vol. 60, no. 17, pp. 6033–6041, 2012.
- [86] R. Ramanujan, J. Lee, and H. Aaronson, "A discrete lattice plane analysis of the interfacial energy of coherent F.C.C.: H.C.P. interfaces and its application to the nucleation of  $\gamma$  in Al-Ag alloys," *Acta Metallurgica et Materialia*, pp. 3421–3432, 1992.

- [87] D. Finkenstadt and D. D. Johnson, "Interphase energies of hcp precipitates in fcc metals: A density-functional theory study in Al-Ag," *Physical Review B*, vol. 81, no. 1, p. 014113, 2010.
- [88] C. Wolverton and V. Ozoliņš, "First-principles aluminum database: Energetics of binary Al alloys and compounds," *Physical Review B*, vol. 73, no. 14, p. 144104, 2006.
- [89] M. Kubota and B. C. Muddle, "Effect of trace additions of Ag on precipitation in Al-Mg alloys," *Materials Transactions*, vol. 46, no. 12, pp. 2968–2974, 2005.
- [90] M. Kubota, J. F. Nie, and B. C. Muddle, "Formation of quasicrystalline particles in an isothermally aged Al-10 Mg-0.5 Ag (mass%) alloy," *Materials Transactions*, vol. 46, no. 2, pp. 365–368, 2005.
- [91] M. Kubota, J. F. Nie, and B. C. Muddle, "Identification of metastable Rod-Like particles in an isothermally aged Al-10Mg-0.5Ag (mass%) alloy," *Materials Transactions*, vol. 46, no. 6, pp. 1288–1294, 2005.
- [92] C. D. Marioara, J. Nakamura, K. Matsuda, S. J. Andersen, R. Holmestad, T. Sato, T. Kawabata, and S. Ikeno, "HAADF-STEM study of  $\beta'$ -type precipitates in an over-aged Al-Mg-Si-Ag alloy," *Philosophical Magazine*, vol. 92, no. 9, pp. 1149–1158, 2012.
- [93] M. Fiawoo, X. Gao, L. Bourgeois, N. Parson, X. Q. Zhang, M. Couper, and J. F. Nie, "Formation of multiple orientation relationships of Q precipitates in Al-Mg-Si-Cu alloys," *Scripta Materialia*, vol. 88, pp. 53–56, 2014.
- [94] S. Wenner, L. Jones, C. D. Marioara, and R. Holmestad, "Atomic-resolution chemical mapping of ordered precipitates in Al alloys using energy-dispersive X-ray spectroscopy," *Micron*, vol. 96, pp. 103–111, 2017.
- [95] S. Wenner, C. D. Marioara, Q. M. Ramasse, D.-M. Kepaptsoglou, F. S. Hage, and R. Holmestad, "Atomic-resolution electron energy loss studies of precipitates in an Al-Mg-Si-Cu-Ag alloy," *Scripta Materialia*, vol. 74, pp. 92–95, 2014.
- [96] E. A. Mørtsell, S. J. Andersen, and J. Friis, "Atomistic details of precipitates in lean Al-Mg-Si alloys with trace additions of Ag and Ge studied by HAADF-STEM and DFT," *Philosophical Magazine*, vol. 97, pp. 851–866, 2017.
- [97] T. Ogura, S. Hirose, A. Cerezo, and T. Sato, "Atom probe tomography of nanoscale microstructures within precipitate free zones in Al-Zn-Mg (-Ag) alloys," *Acta Materialia*, 2010.
- [98] S. K. Caraher, I. J. Polmear, and S. P. P. Ringer, "Effects of Cu and Ag on precipitation in Al-4Zn-3Mg (wt.%)", in *Proceedings of the 6th International Conference on Aluminum Alloys (ICAA6)*, pp. 5–10, 1998.
- [99] S. K. Maloney, K. Hono, I. J. Polmear, and S. P. Ringer, "The effects of a trace addition of silver upon elevated temperature ageing of an Al-Zn-Mg alloy," *Micron*, vol. 32, no. 8, pp. 741–747, 2001.

- [100] C. E. Macchi, A. Somoza, A. Dupasquier, and I. J. Polmear, "Secondary precipitation in Al-Zn-Mg-(Ag) alloys," *Acta Materialia*, vol. 51, no. 17, pp. 5151–5158, 2003.
- [101] M. Mihara, C. D. Marioara, S. J. Andersen, R. Holmestad, E. Kobayashi, and T. Sato, "Precipitation in an Al-Mg-Cu alloy and the effect of a low amount of ag," *Materials Science and Engineering: A*, vol. 658, pp. 91–98, 2016.
- [102] B. C. Muddle and I. J. Polmear, "The precipitate  $\omega$  phase in Al-Cu-Mg-Ag alloys," *Acta Metallurgica*, vol. 37, no. 3, pp. 777–789, 1989.
- [103] J. M. Howe, "Analytical transmission electron microscopy analysis of Ag and Mg segregation to  $\{111\}$   $\theta$  precipitate plates in an Al-Cu-Mg-Ag alloy," *Philosophical Magazine Letters*, vol. 70, no. 3, pp. 111–120, 1994.
- [104] K. Hono, T. Sakurai, and I. J. Polmear, "Pre-precipitate clustering in an Al-Cu-Mg-Ag alloy," *Scripta Metallurgica et Materialia*, vol. 30, no. 6, pp. 695–700, 1994.
- [105] S. P. Ringer, W. Yeung, B. C. Muddle, and I. J. Polmear, "Precipitate stability in Al-Cu-Mg-Ag alloys aged at high temperatures," *Acta Metallurgica et Materialia*, vol. 42, no. 5, pp. 1715–1725, 1994.
- [106] A. Somoza, A. Dupasquier, I. J. Polmear, P. Folegati, and R. Ferragut, "Positron-annihilation study of the aging kinetics of AlCu-based alloys. II. Ag microalloying," *Physical Review B*, vol. 61, no. 21, p. 14464, 2000.
- [107] E. Gariboldi, P. Bassani, M. Albu, and F. Hofer, "Presence of silver in the strengthening particles of an Al-Cu-Mg-Si-Zr-Ti-Ag alloy during severe overaging and creep," *Acta Materialia*, vol. 125, pp. 50–57, 2017.
- [108] V. Araullo-Peters, B. Gault, D. F. Geuser, and A. Deschamps, "Microstructural evolution during ageing of Al-Cu-Li-x alloys," *Acta Materialia*, 2014.
- [109] R. P. Winarski, M. V. Holt, V. Rose, P. Fuesz, D. Carbaugh, C. Benson, D. Shu, D. Kline, G. B. Stephenson, I. McNulty, *et al.*, "A hard x-ray nanoprobe beamline for nanoscale microscopy," *Journal of synchrotron radiation*, vol. 19, no. 6, pp. 1056–1060, 2012.
- [110] K. Hono and S. Babu, "15 - atom-probe field ion microscopy," in *Physical Metallurgy (Fifth Edition)* (D. E. Laughlin and K. Hono, eds.), pp. 1453 – 1589, Oxford: Elsevier, fifth edition ed., 2014.
- [111] H. L. Fraser, D. W. McComb, and R. E. Williams, "Transmission electron microscopy for physical metallurgists," in *Physical Metallurgy (Fifth Edition)* (D. E. Laughlin and K. Hono, eds.), pp. 1143–1226, Elsevier, 2015.
- [112] R. Brydson, *Aberration-Corrected Analytical Transmission Electron Microscopy*. RMS - Royal Microscopical Society, Wiley, 2011.
- [113] M. Weyland, "Electron tomography," in *Transmission Electron Microscopy* (C. B. Carter and D. B. Williams, eds.), pp. 343–376, Springer, 2016.

- [114] S. Wenner and R. Holmestad, “Accurately measured precipitate–matrix misfit in an Al–Mg–Si alloy by electron microscopy,” *Scripta Materialia*, vol. 118, pp. 5 – 8, 2016.
- [115] J. F. Nie, Y. M. Zhu, J. Z. Liu, and X. Y. Fang, “Periodic segregation of solute atoms in fully coherent twin boundaries,” *Science*, vol. 340, no. 6135, pp. 957–960, 2013.
- [116] N. A. Zarkevich, *First-principles prediction of thermodynamics and ordering in metallic alloys*. PhD thesis, University of Illinois at Urbana-Champaign, 2003.
- [117] D. K. Finkenstadt, *Mechanism for gamma-precipitation in aluminum-silver alloys and self-assembly of polyelectrolytes: Modeling of complex layered materials*. PhD thesis, University of Illinois at Urbana-Champaign, 2005.
- [118] L. De Broglie, *Recherches sur la théorie des quanta*. PhD thesis, Migration-université en cours d’affectation, 1924.
- [119] C. Davisson and L. H. Germer, “Diffraction of electrons by a crystal of nickel,” *Physical Review*, vol. 30, no. 6, pp. 705–740, 1927.
- [120] M. Knoll and E. Ruska, “Beitrag zur geometrischen elektronenoptik. i,” *Annalen der Physik*, vol. 404, no. 5, pp. 607–640, 1932.
- [121] S. Pennycook and P. Nellist, *Scanning Transmission Electron Microscopy: Imaging and Analysis*. Springer New York, 2011.
- [122] A. Pogany and P. Turner, “Reciprocity in electron diffraction and microscopy,” *Acta Crystallographica Section A: Crystal Physics, Diffraction, Theoretical and General Crystallography*, vol. 24, no. 1, pp. 103–109, 1968.
- [123] J. Barthel, “Dr. Probe Light – STEM probe and ronchigram simulation software.” <http://www.er-c.org/barthel/drprobelight>, 2014.
- [124] J. Radon, “über die Bestimmung von Funktionen durch ihre Integralwerte längs gewisser Mannigfaltigkeiten,” *Berichte Über Die Verhandlungen der Königlich-Sächsischen Akademie der Wissenschaften zu Leipzig, Mathematisch-Physische Klasse [Reports on the Proceedings of the Royal Saxonian Academy of Sciences at Leipzig, Mathematical and Physical Section]*, vol. 69, pp. 262–277, 1917.
- [125] P. A. Midgley and R. E. Dunin-Borkowski, “Electron tomography and holography in materials science,” *Nature Materials*, vol. 8, no. 4, pp. 271–280, 2009.
- [126] P. A. Midgley and M. Weyland, “3D electron microscopy in the physical sciences: the development of Z-contrast and EFTEM tomography,” *Ultramicroscopy*, vol. 96, no. 3, pp. 413–431, 2003.
- [127] J. M. LeBeau, S. D. Findlay, L. J. Allen, and S. Stemmer, “Position averaged convergent beam electron diffraction: Theory and applications,” *Ultramicroscopy*, vol. 110, no. 2, pp. 118–125, 2010.
- [128] P. A. Stadelmann, “JEMS - EMS java version.” <http://www.jems-saas.ch/Home/jemsWebSite/jems.html>, 2004.

- [129] J. A. Pollock, M. Weyland, D. J. Taplin, L. J. Allen, and S. D. Findlay, “Accuracy and precision of thickness determination from position-averaged convergent beam electron diffraction patterns using a single-parameter metric,” *Ultramicroscopy*, vol. 181, pp. 86–96, 2017.
- [130] D. B. Williams and C. B. Carter, *Quantitative X-ray Analysis*, pp. 639–662. Boston, MA: Springer US, 2009.
- [131] B. L. Henke, E. M. Gullikson, and J. C. Davis, “X-ray interactions: photoabsorption, scattering, transmission, and reflection at  $e= 50\text{--}30,000$  eV,  $z= 1\text{--}92$ ,” *Atomic Data and Nuclear Data Tables*, vol. 54, no. 2, pp. 181–342, 1993.
- [132] H. Bethe, “Theorie der beugung von elektronen an kristallen,” *Annalen der Physik*, vol. 392, no. 17, pp. 55–129, 1928.
- [133] J. M. Cowley and A. F. Moodie, “The scattering of electrons by atoms and crystals. I. A new theoretical approach,” *Acta Crystallographica*, vol. 10, no. 10, pp. 609–619, 1957.
- [134] K. Fujiwara, “Relativistic dynamical theory of electron diffraction,” *Journal of the Physical Society of Japan*, vol. 16, no. 11, pp. 2226–2238, 1961.
- [135] J. M. Zuo and J. C. Spence, *Advanced transmission electron microscopy*. Springer, 2017.
- [136] E. J. Kirkland, *Advanced computing in electron microscopy*. Springer Science & Business Media, 2010.
- [137] L. Allen, A. D’Alfonso, and S. Findlay, “Modelling the inelastic scattering of fast electrons,” *Ultramicroscopy*, vol. 151, pp. 11–22, 2015.
- [138] L.-M. Peng, G. Ren, S. Dudarev, and M. Whelan, “Debye–waller factors and absorptive scattering factors of elemental crystals,” *Acta Crystallographica Section A: Foundations of Crystallography*, vol. 52, no. 3, pp. 456–470, 1996.
- [139] A. De Backer, K. van den Bos, W. Van den Broek, J. Sijbers, and S. Van Aert, “StatSTEM: an efficient approach for accurate and precise model-based quantification of atomic resolution electron microscopy images,” *Ultramicroscopy*, vol. 171, pp. 104–116, 2016.
- [140] C. T. Koch, *Determination of core structure periodicity and point defect density along dislocations*. PhD thesis, Arizona State University, 2002.
- [141] M. J. Hÿtch, E. Snoeck, and R. Kilaas, “Quantitative measurement of displacement and strain fields from HREM micrographs,” *Ultramicroscopy*, vol. 74, no. 3, pp. 131–146, 1998.
- [142] M. J. Hÿtch, J.-L. Putaux, and J.-M. Pénisson, “Measurement of the displacement field of dislocations to  $0.03 \text{ \AA}$  by electron microscopy,” *Nature*, vol. 423, no. 6937, pp. 270–273, 2003.

- [143] C. L. Johnson, M. J. Hytch, and P. R. Buseck, “Nanoscale waviness of low-angle grain boundaries,” *Proceedings of the National Academy of Sciences*, vol. 101, no. 52, pp. 17936–17939, 2004.
- [144] A. Stukowski and A. Arsenlis, “On the elastic–plastic decomposition of crystal deformation at the atomic scale,” *Modelling and Simulation in Materials Science and Engineering*, vol. 20, no. 3, p. 035012, 2012.
- [145] A. Stukowski, “Visualization and analysis of atomistic simulation data with OVITO—the open visualization tool,” *Modelling and Simulation in Materials Science and Engineering*, vol. 18, no. 1, p. 015012, 2010.
- [146] C. Ophus, J. Ciston, and C. T. Nelson, “Correcting nonlinear drift distortion of scanning probe and scanning transmission electron microscopies from image pairs with orthogonal scan directions,” *Ultramicroscopy*, vol. 162, pp. 1–9, 2016.
- [147] D. J. Griffiths, *Introduction to quantum mechanics*. Cambridge University Press, 2016.
- [148] W. Heisenberg, “Mehrkörperproblem und resonanz in der quantenmechanik,” *Zeitschrift für Physik A Hadrons and Nuclei*, vol. 38, no. 6, pp. 411–426, 1926.
- [149] P. A. M. Dirac, “On the theory of quantum mechanics,” in *Proceedings of the Royal Society of London A: Mathematical, Physical and Engineering Sciences*, vol. 112, pp. 661–677, The Royal Society, 1926.
- [150] P.-O. Löwdin, “Quantum theory of many-particle systems. III. Extension of the Hartree-Fock scheme to include degenerate systems and correlation effects,” *Physical Review*, vol. 97, no. 6, p. 1509, 1955.
- [151] E. Wigner, “On the interaction of electrons in metals,” *Physical Review*, vol. 46, no. 11, p. 1002, 1934.
- [152] P. Hohenberg and W. Kohn, “Inhomogeneous electron gas,” *Physical Review*, vol. 136, no. 3B, pp. B864–B871, 1964.
- [153] W. Kohn and L. J. Sham, “Self-consistent equations including exchange and correlation effects,” *Physical Review*, vol. 140, no. 4A, p. A1133, 1965.
- [154] D. S. Sholl and J. A. Steckel, *Density functional theory: a practical introduction*. John Wiley & Sons, 2011.
- [155] D. M. Ceperley and B. J. Alder, “Ground state of the electron gas by a stochastic method,” *Physical Review Letters*, vol. 45, no. 7, pp. 566–569, 1980.
- [156] J. P. Perdew and A. Zunger, “Self-interaction correction to density-functional approximations for many-electron systems,” *Physical Review B*, vol. 23, no. 10, pp. 5048–5079, 1981.
- [157] F. Giustino, *Materials Modelling Using Density Functional Theory: Properties and Predictions*. Oxford University Press, 2014.
- [158] J. P. Perdew, K. Burke, and M. Ernzerhof, “Generalized gradient approximation made simple,” *Physical Review Letters*, vol. 77, no. 18, pp. 3865–3868, 1996.

- [159] J. Tao, J. P. Perdew, V. N. Staroverov, and G. E. Scuseria, “Climbing the density functional ladder: Nonempirical meta-generalized gradient approximation designed for molecules and solids,” *Physical Review Letters*, vol. 91, no. 14, p. 146401, 2003.
- [160] A. D. Becke, “A new mixing of hartree-fock and local density-functional theories,” *The Journal of Chemical Physics*, vol. 98, no. 2, pp. 1372–1377, 1993.
- [161] C. Edmiston and K. Ruedenberg, “Localized atomic and molecular orbitals,” *Reviews of Modern Physics*, vol. 35, no. 3, p. 457, 1963.
- [162] D. R. Hamann, M. Schlüter, and C. Chiang, “Norm-conserving pseudopotentials,” *Physical Review Letters*, vol. 43, no. 20, p. 1494, 1979.
- [163] J. S. Lin, A. Qteish, M. C. Payne, and V. Heine, “Optimized and transferable nonlocal separable ab initio pseudopotentials,” *Physical Review B*, vol. 47, no. 8, pp. 4174–4180, 1993.
- [164] D. Vanderbilt, “Soft self-consistent pseudopotentials in a generalized eigenvalue formalism,” *Physical Review B*, vol. 41, no. 11, pp. 7892–7895, 1990.
- [165] N. Troullier and J. L. Martins, “Efficient pseudopotentials for plane-wave calculations,” *Physical review B*, vol. 43, no. 3, pp. 1993–2006, 1991.
- [166] P. E. Blöchl, “Projector augmented-wave method,” *Physical Review B*, vol. 50, pp. 17953–17979, 1994.
- [167] G. Kresse and D. Joubert, “From ultrasoft pseudopotentials to the projector augmented-wave method,” *Physical Review B*, vol. 59, no. 3, pp. 1758–1775, 1999.
- [168] K. Lejaeghere, G. Bihlmayer, T. Björkman, P. Blaha, S. Blügel, V. Blum, D. Caliste, I. E. Castelli, S. J. Clark, A. Corso, S. de Gironcoli, T. Deutsch, J. Dewhurst, I. Marco, C. Draxl, M. Duřak, O. Eriksson, F. J. A. K. F. Garrity, L. Genovese, P. Giannozzi, M. Giantomassi, S. Goedecker, X. Gonze, O. Grånäs, E. Gross, A. Gulans, F. Gygi, D. Hamann, P. J. Hasnip, N. Holzwarth, D. Iuřan, D. B. Jochym, F. Jollet, D. Jones, G. Kresse, K. Koepnik, E. Küçükbenli, Y. O. Kvashnin, I. L. Locht, S. Lubeck, M. Marsman, N. Marzari, U. Nitzsche, L. Nordström, T. Ozaki, L. Paulatto, C. J. Pickard, W. Poelmans, M. I. Probert, K. Refson, M. Richter, G. Rignanese, S. Saha, M. Scheffler, M. Schlipf, K. Schwarz, S. Sharma, F. Tavazza, P. Thunström, A. Tkatchenko, M. Torrent, D. Vanderbilt, M. J. van Setten, V. Speybroeck, J. M. Wills, J. R. Yates, G. Zhang, and S. Cottenier, “Reproducibility in density functional theory calculations of solids,” *Science*, vol. 351, no. 6280, p. aad3000, 2016.
- [169] H. J. Monkhorst and J. D. Pack, “Special points for brillouin-zone integrations,” *Physical review B*, vol. 13, no. 12, pp. 5188–5192, 1976.
- [170] M. P. A. T. Methfessel and A. T. Paxton, “High-precision sampling for brillouin-zone integration in metals,” *Physical Review B*, vol. 40, no. 6, pp. 3616–3621, 1989.
- [171] P. E. Blöchl, O. Jepsen, and O. K. Andersen, “Improved tetrahedron method for brillouin-zone integrations,” *Physical Review B*, vol. 49, no. 23, pp. 16223–16233, 1994.

- [172] G. Kresse and J. Furthmüller, “Efficient iterative schemes for ab initio total-energy calculations using a plane-wave basis set,” *Physical Review B*, vol. 54, no. 16, pp. 11169–11186, 1996.
- [173] W. P. Davey, “Precision measurements of the lattice constants of twelve common metals,” *Physical Review*, vol. 25, no. 6, p. 753, 1925.
- [174] Z. Zhang, L. Bourgeois, J. M. Rosalie, and N. V. Medhekar, “The bi-layered precipitate phase  $\zeta$  in the Al-Ag alloy system,” *Acta Materialia*, vol. 132, pp. 525–537, 2017.
- [175] A. Jain, S. P. Ong, G. Hautier, W. Chen, W. D. Richards, S. Dacek, S. Cholia, D. Gunter, D. Skinner, G. Ceder, and K. a. Persson, “The Materials Project: A materials genome approach to accelerating materials innovation,” *APL Materials*, vol. 1, no. 1, p. 011002, 2013.
- [176] N. A. Zarkevich, D. D. Johnson, and A. V. Smirnov, “Structure and stability of hcp bulk and nano-precipitated  $\text{Ag}_2\text{Al}$ ,” *Acta Materialia*, vol. 50, no. 9, pp. 2443–2459, 2002.
- [177] M. S. Daw and M. I. Baskes, “Embedded-atom method: Derivation and application to impurities, surfaces, and other defects in metals,” *Physical Review B*, vol. 29, no. 12, pp. 6443–6453, 1984.
- [178] M. I. Baskes, “Modified embedded-atom potentials for cubic materials and impurities,” *Physical Review B*, vol. 46, no. 5, pp. 2727–2742, 1992.
- [179] S. Plimpton, “Fast parallel algorithms for short-range molecular dynamics,” *Journal of computational physics*, vol. 117, no. 1, pp. 1–19, 1995.
- [180] H. W. Sheng, M. J. Kramer, A. Cadien, T. Fujita, and M. W. Chen, “Highly optimized embedded-atom-method potentials for fourteen fcc metals,” *Physical Review B*, vol. 83, no. 13, p. 134118, 2011.
- [181] Y. Matsukawa and S. J. Zinkle, “One-Dimensional fast migration of vacancy clusters in metals,” *Science*, vol. 318, no. 5852, pp. 959–962, 2007.
- [182] J. D. Honeycutt and H. C. Andersen, “Molecular dynamics study of melting and freezing of small lennard-jones clusters,” *Journal of Physical Chemistry*, vol. 91, no. 19, pp. 4950–4963, 1987.
- [183] A. Stukowski, “Visualization and analysis strategies for atomistic simulations,” in *Multiscale Materials Modeling for Nanomechanics*, pp. 317–336, Springer, 2016.
- [184] F. C. Frank, “Lxxxiii. crystal dislocations.—elementary concepts and definitions,” *The London, Edinburgh, and Dublin Philosophical Magazine and Journal of Science*, vol. 42, no. 331, pp. 809–819, 1951.
- [185] M. I. Zakharova and N. A. Khatanova, “Identification of crystals of phases precipitating in an Al-Cu-Ag alloy and the topology of their growth,” *Kristallografiya*, vol. 11, no. 4, pp. 692–694, 1966.

- [186] R. Erni, H. Heinrich, and G. Kostorz, “Quantitative characterisation of chemical inhomogeneities in Al–Ag using high-resolution Z-contrast STEM,” *Ultramicroscopy*, vol. 94, no. 2, pp. 125–133, 2003.
- [187] K. Osamura, T. Nakamura, A. Kobayashi, T. Hashizume, and T. Sakurai, “Chemical composition of GP zones in Al–Ag alloys,” *Scripta metallurgica*, vol. 21, no. 3, pp. 255–258, 1987.
- [188] W. Zhu and W. Yang, “Molecular dynamics study of configuration and stability of vacancy clusters in fcc ag,” *Philosophical Magazine*, vol. 91, no. 29, pp. 3793–3809, 2011.
- [189] Z. Zhang, T. Liu, A. Smith, N. Medhekar, P. Nakashima, and L. Bourgeois, “Mechanisms of void shrinkage in aluminium,” *Journal of Applied Crystallography*, vol. 49, pp. 1459–1470, 10 2016.
- [190] T. E. Volin and R. W. Balluffi, “Annealing kinetics of voids and the self-diffusion coefficient in aluminum,” *Physica Status Solidi*, vol. 25, no. 1, pp. 163–173, 1968.
- [191] H. Landolt, P. Ehrhart, and H. Ullmaier, “Atomic defects in metals,” 1991.
- [192] S. S. Gupta, M. A. van Huis, M. Dijkstra, and M. H. F. Sluiter, “Depth dependence of vacancy formation energy at (100), (110), and (111) al surfaces: A first-principles study,” *Physical Review B*, vol. 93, no. 8, p. 085432, 2016.
- [193] B. C. Muddle, J. F. Nie, and G. R. Hugo, “Application of the theory of martensite crystallography to displacive phase transformations in substitutional nonferrous alloys,” *Metallurgical and Materials Transactions A*, vol. 25, no. 9, pp. 1841–1856, 1994.
- [194] C. Dwyer and J. Etheridge, “Scattering of Å-scale electron probes in silicon,” *Ultramicroscopy*, vol. 96, no. 3-4, pp. 343–360, 2003.
- [195] P. N. H. Nakashima, A. E. Smith, J. Etheridge, and B. C. Muddle, “The bonding electron density in aluminum,” *Science*, vol. 331, no. 6024, pp. 1583–1586, 2011.
- [196] K. Jungjohann, “In situ and operando,” in *Transmission Electron Microscopy-Diffraction, Imaging, and Spectrometry* (C. Carter and D. Williams, eds.), pp. 17–76, Springer, 2016.
- [197] M. Hillert, *Phase Equilibria, Phase Diagrams and Phase Transformations: Their Thermodynamic Basis*, pp. 482–486. Cambridge University Press, 1998.
- [198] M. Murayama and K. Hono, “Role of Ag and Mg on precipitation of  $T_1$  phase in an Al–Cu–Li–Mg–Ag alloy,” *Scripta Materialia*, vol. 44, no. 4, pp. 701–706, 2001.
- [199] J. H. Auld, “Structure of metastable precipitate in some Al–Cu–Mg–Ag alloys,” *Materials Science and Technology*, vol. 2, no. 8, pp. 784–787, 1986.
- [200] K. M. Knowles and W. M. Stobbs, “The structure of {111} age-hardening precipitates in Al–Cu–Mg–Ag alloys,” *Acta Crystallographica Section B*, vol. 44, pp. 207–227, Jun 1988.

- [201] Z. Zhang, L. Bourgeois, and N. V. Medhekar, "Database of solute clustering in aluminium alloys: a DFT study (unpublished)," 2016.
- [202] Y. Zhang, T. Alam, B. Gwalani, W. Rong, R. Banerjee, L. M. Peng, J. F. Nie, and N. Birbilis, "On the role of Ag in enhanced age hardening kinetics of Mg–Gd–Ag–Zr alloys," *Philosophical Magazine Letters*, vol. 96, no. 6, pp. 212–219, 2016.
- [203] Y. M. Zhu, K. Oh-ishi, N. C. Wilson, K. Hono, A. J. Morton, and J. F. Nie, "Precipitation in a Ag-Containing Mg–Y–Zn Alloy," *Metallurgical and Materials Transactions A*, vol. 47, no. 2, pp. 927–940, 2016.
- [204] R. D. Doherty and K. E. Rajab, "Kinetics of growth and coarsening of faceted hexagonal precipitates in an fcc matrix—ii. analysis," *Acta Metallurgica*, vol. 37, no. 10, pp. 2723–2731, 1989.
- [205] J. M. Howe, *Interfaces in materials: atomic structure, thermodynamics and kinetics of solid-vapor, solid-liquid and solid-solid interfaces*. Wiley-Interscience, 1997.
- [206] A. H. Cottrell and B. A. Bilby, "Dislocation theory of yielding and strain ageing of iron," *Proceedings of the Physical Society*, vol. 62, no. 1, pp. 49–62, 1949.
- [207] P. Hirsch, D. Cockayne, J. Spence, and M. Whelan, "50 Years of TEM of dislocations: Past, present and future," *Philosophical Magazine*, vol. 86, no. 29-31, pp. 4519–4528, 2006.
- [208] D. Blavette, E. Cadel, A. Fraczkiewicz, and A. Menand, "Three-Dimensional Atomic-Scale imaging of impurity segregation to line defects," *Science*, vol. 286, no. 5448, pp. 2317–2319, 1999.
- [209] M. Kuzmina, M. Herbig, D. Ponge, S. Sandlöbes, and D. Raabe, "Linear complexes: Confined chemical and structural states at dislocations," *Science*, vol. 349, no. 6252, pp. 1080–1083, 2015.
- [210] T. Paulauskas, C. Buurma, E. Colegrove, B. Stafford, Z. Guo, M. K. Chan, C. Sun, M. J. Kim, S. Sivananthan, and R. F. Klie, "Atomic scale study of polar lomer–cottrell and hirth lock dislocation cores in cdte," *Acta Crystallographica Section A: Foundations and Advances*, vol. 70, no. 6, pp. 524–531, 2014.
- [211] N. Bologna, P. Agrawal, M. Campanini, M. Knödler, M. D. Rossell, R. Erni, and D. Passerone, "Stair-rod dislocation cores acting as one-dimensional charge channels in GaAs nanowires," *Physical Review Materials*, vol. 2, no. 1, p. 014603, 2018.
- [212] C. Sun, T. Paulauskas, F. G. Sen, G. Lian, J. Wang, C. Buurma, M. K. Chan, R. F. Klie, and M. J. Kim, "Atomic and electronic structure of Lomer dislocations at CdTe bicrystal interface," *Scientific Reports*, vol. 6, p. 27009, 2016.
- [213] R. Schweinfest, A. T. Paxton, and M. W. Finnis, "Bismuth embrittlement of copper is an atomic size effect," *Nature*, vol. 432, no. 7020, p. 1008, 2004.
- [214] J. W. Gibbs, "On the equilibrium of heterogeneous substances," *American Journal of Science*, no. 96, pp. 441–458, 1878.

- 
- [215] P. Curie, “Sur la formation des cristaux et sur les constantes capillaires de leurs différentes faces,” *Bulletin de la Société Française de Minéralogie et de Cristallographie*, vol. 8, pp. 145–150, 1885.
- [216] G. Wulff, “Xxv. zur frage der geschwindigkeit des wachstums und der auflösung der krystallflächen,” *Zeitschrift für Kristallographie-Crystalline Materials*, vol. 34, no. 1, pp. 449–530, 1901.
- [217] C. Herring, “Some theorems on the free energies of crystal surfaces,” *Physical Review*, vol. 82, no. 1, pp. 87–93, 1951.
- [218] M. Perez, “Gibbs–thomson effects in phase transformations,” *Scripta Materialia*, vol. 52, no. 8, pp. 709–712, 2005.
- [219] K. Kinsman, E. Eichen, and H. Aaronson, “Thickening kinetics of proeutectoid ferrite plates in Fe-C alloys,” *Metallurgical and Materials Transactions A*, vol. 6, no. 2, pp. 303–317, 1975.

# Appendix A

## Thermodynamics and Kinetics of Interfaces during Precipitation

### A.1 Interfaces in General

An interface is the critical boundary that distinguishes two different phases. Its existence is widely spread in the universe: a black hole has the event horizon within which light cannot escape; deep-focus earthquakes occur exclusively at the oceanic-continental boundaries; neurons exchange electrical and chemical signals at their cell surface. All these interfaces, from radically different fields, share the same questions:

1. What is the interface structure?
2. How does the interface form and evolve?

High-strength light alloys often involve nanometre-seized precipitate phases with high aspect ratios, which correspond to a large area of precipitate-matrix interfaces. The nature of interfaces directly determines the precipitation behaviour. More challenging but practical questions for the precipitate interface are:

3. Can we control the interface?
4. Can we do the above at the atomic scale?

In contrast to the wide existence and critical role that the interface has in determining precipitation, we have a limited understanding of the atomic mechanisms. In the following sections, we will review the thermodynamics and kinetics of precipitation in alloys. The role of the precipitate-matrix interface is examined through different stages of precipitation, including nucleation, growth and coarsening.

## A.2 Nucleation

Starting from the homogeneous nucleation theory for simplicity, the free energy change is associated with three contributors [15]:

1. The precipitate phase is more stable than the matrix in supersaturated solid solution. The transformation causes a **volumetric** free energy **decrease** of  $V\Delta G_v$ , where  $V$  is the volume of phase changed and  $\Delta G_v$  is the enthalpy difference per unit volume.
2. The precipitate-matrix interface is created, which gives an **interfacial** free energy **increase** of  $A\gamma$ , where  $A$  is the area of interface and  $\gamma$  is the interfacial energy per unit area.
3. In general, the transformed precipitate volume does not fit perfectly with the original matrix region, which gives a **volumetric** free energy **increase** due to strain  $V\Delta G_s$ . Note that the classical nucleation equation does not include the shear strain energy associated with transformations, which is also **volumetric** [193].

Assuming a spherical precipitate with radius of  $r$  and summing those three contributors, the total free energy change  $\Delta G$  can be calculated as:

$$\Delta G = -\frac{4}{3}\pi r^3(\Delta G_v - \Delta G_s) + 4\pi r^2\gamma. \quad (\text{A.1})$$

The **critical nucleus size**  $r^*$  is taken at the peak of free energy when  $\frac{\partial \Delta G}{\partial r} = 0$ , which yields:

$$r^* = \frac{2\gamma}{\Delta G_v - \Delta G_s}. \quad (\text{A.2})$$

And the **energy barrier**  $\Delta G^*$  against nucleation is derived as:

$$\Delta G^* = \frac{16\pi\gamma^3}{3(\Delta G_v - \Delta G_s)^2}. \quad (\text{A.3})$$

As shown in the Eq. A.3 and Fig. A.1, the nucleation stage is dictated by interfacial energy while the growth stage is dominated by volumetric energy (enthalpy and strain energy) [15].

However, this equation treats interfacial energy isotropically which gives a spherical geometry. For non-spherical precipitates with more engineering significance, the orientation dependence of interfacial energy has to be considered. When ignoring the strain energy and only considering interfacial energy, an equilibrium geometry and orientation is obtained when [10]:

$$\int \gamma dA = \text{minimum}. \quad (\text{A.4})$$

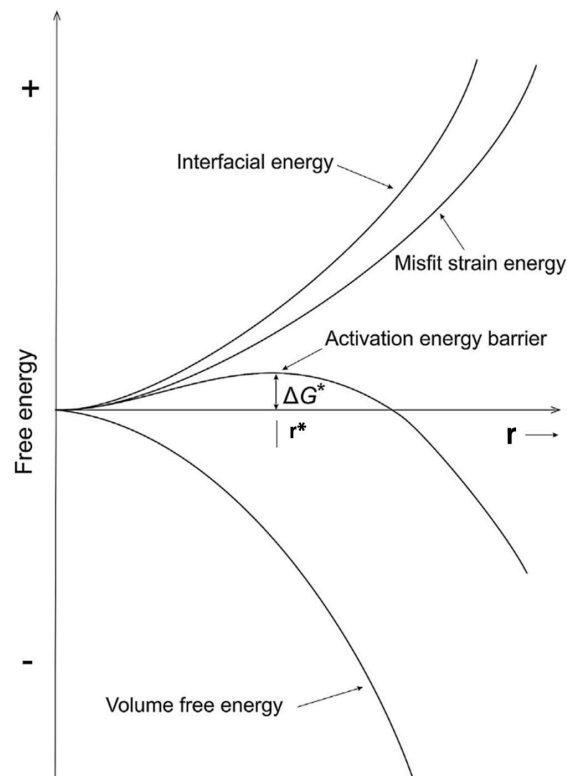


Fig. A.1 The free energy change associated with homogeneous nucleation. The nucleation energy barrier emerges as the competition between the interfacial energy term and volumetric energy term. Adapted from Ref. [15], p. 264 with permission from Taylor & Francis.

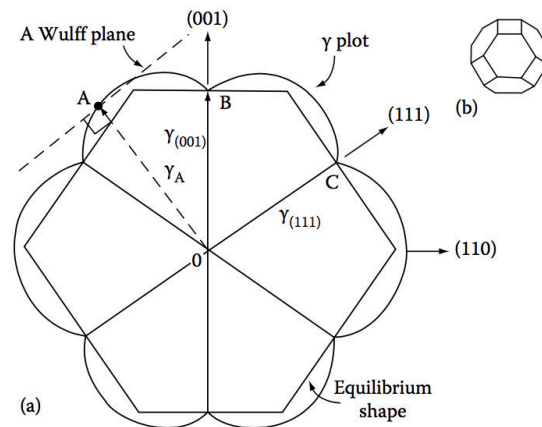


Fig. A.2 (a) A possible  $[110]$  section through the  $\gamma$ -plot of an FCC crystal. The length  $OA$  represents the free energy of a surface plane whose normal lies in the direction  $OA$ . Thus  $OB=\gamma_{(001)}$ ,  $OC=\gamma_{(111)}$  etc. Wulff planes are those such as that which lies normal to the vector  $OA$ . In this case, the Wulff planes at the cusps (B, C, etc.) give the inner envelope of all Wulff planes and thus the equilibrium shape. (b) The equilibrium shape in three dimensions showing  $\{100\}$  (square faces) and  $\{111\}$  (hexagonal faces). Reprinted from Ref. [15], p. 121 with permission from Taylor & Francis.

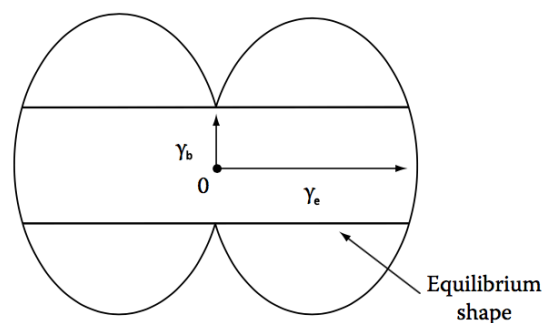


Fig. A.3 A section through a  $\gamma$ -plot for a precipitate showing one coherent or semicoherent interface, together with the equilibrium shape (a disc). The Wulff theorem would then predict the equilibrium shape to be a disc with a thickness/diameter ratio of  $\gamma_b/\gamma_e$  where  $\gamma_b$  and  $\gamma_e$  are the specific interfacial energies of the board and edge interfaces respectively. Reprinted from Ref. [15], p. 154 with permission from Taylor & Francis.

This criterion was first proposed by Gibbs in 1878 [214] and again by Curie in 1885 [215]. The solution to the equilibrium shape was found by Wulff in 1901 [216], thus it is known as Wulff construction, though with a wrong proof. The most general proof was given by Herring in 1951 [217]. Wulff construction is a crystal geometry enclosed in a way that:

$$\frac{\gamma_i}{r_i} = \text{constant}, \quad (\text{A.5})$$

where  $\gamma_i$  is the interfacial energy per unit area for an arbitrary facet, and  $r_i$  is the distance from the origin of geometry to that facet. The  $\gamma$ -plot represents the orientation dependence of surface energy so that the equilibrium shape is determined by drawing tangent lines at the cusps in such  $\gamma$ -plot. For an FCC crystal like aluminium, the Wulff construction is a truncated octahedron bounded by  $\{111\}$  facets and  $\{001\}$  facets, see Fig. A.2. The solution, though simple, gives a reason for our common intuition: the higher the interfacial energy in one orientation, the further those facets are separated and the smaller the corresponding area should be. The equilibrium shape of a precipitate requires strict conditions as following [10]:

1. The interfacial energy is dominating.
2. Other factors (like the strain) that can potentially modify the shape are not significant.
3. The diffusivity is sufficiently high or the diffusion distance is short.

The shape observed experimentally may be different from the Wulff construction as the precipitate nuclei are hard to be captured; we often see precipitates in their growth stage. And a growing precipitate often deviates from the equilibrium due to : (a) the strain cannot be ignored, (b) the mobility of interface is not isotropic [15]. If the equilibrium shape concerns just the equilibrium state, we may have fewer interests as the precipitation is a process away from equilibrium. But one should also realise that nucleation satisfies the equilibrium conditions exactly. Because of the large surface to volume ratio, the **shape and orientation relationship** of nuclei are determined primarily by the anisotropic interfacial energy. For a nucleus adopts the equilibrium shape of a circular plate with diameter  $d$  and thickness  $t$ , we can obtain the following equations [9]:

the **critical diameter**:

$$d^* = \frac{4\gamma_e}{\Delta G_v - \Delta G_s}, \quad (\text{A.6})$$

the **critical thickness**:

$$t^* = \frac{4\gamma_b}{\Delta G_v - \Delta G_s}, \quad (\text{A.7})$$

and the **nucleation energy barrier**:

$$\Delta G^* = \frac{8\pi\gamma_e^2\gamma_b}{(\Delta G_v - \Delta G_s)^2}, \quad (\text{A.8})$$

where  $\gamma_e$  and  $\gamma_b$  is the specific interfacial energy of the edge surface and broad surface of the plate, respectively. This equation can be further modified to adapted the detailed plate geometries, like the tetragonal plate on  $\{001\}$  planes [31] or the hexagonal plate on  $\{111\}$  planes [87]. The broad surface of the precipitate – also known as the habit plane of a precipitate – corresponds to the orientation with the lowest interfacial energy in the  $\gamma$ -plot, Fig. A.3. Precipitates share such broad surfaces with the matrix to minimise the total interfacial energy. Moreover, the nucleation energy barrier directly influences the **nucleation rate** as (assumed a spherical geometry):

$$\frac{dN}{dt} \cong N_0 Z \beta \exp\left(-\frac{\Delta G^*}{kT}\right) \quad (\text{A.9})$$

where  $N$  is the number of nuclei,  $t$  is the time,  $N_0$  is the number of atoms per unit volume ( $\sim N_A/V_m$ );  $Z$  is Zeldovich's factor ( $\sim 1/20$ );  $k$  is Boltzmann's constant and  $T$  is temperature; and  $\beta$  is the frequency factor:

$$\beta = \frac{4\pi r^* D_B^\alpha X_0}{a_0^4}. \quad (\text{A.10})$$

The term  $r^*$  is the critical radius of the nucleus,  $D_B^\alpha$  is the diffusivity of the solute  $B$  in the  $\alpha$  matrix,  $X_0$  is the solute content of the alloy,  $a_0$  is the lattice parameter. It implies the interface dominates the nucleation kinetics, with the critical energy barrier  $\Delta G^*$  in the exponential function.

Overall, interfacial energy takes a critical role in the nucleation process – controlling the critical size, orientation relationship and geometry, the nucleation energy barrier and the nucleation rate of precipitate phases. Recognising the significance that interfaces acquired during nucleation, we suspect it is possible to adjust the precipitation sequence by lowering the interfacial energy of the favourable phase and hence the corresponding nucleation barrier. No fundamental studies of such phase manipulation have been performed up to date. However, in practice, microalloying elements sometimes modify the interfacial structures and change the phase that forms, which was reviewed in Section. 2.1.2 and Ag in particular in Section. 2.2.2.

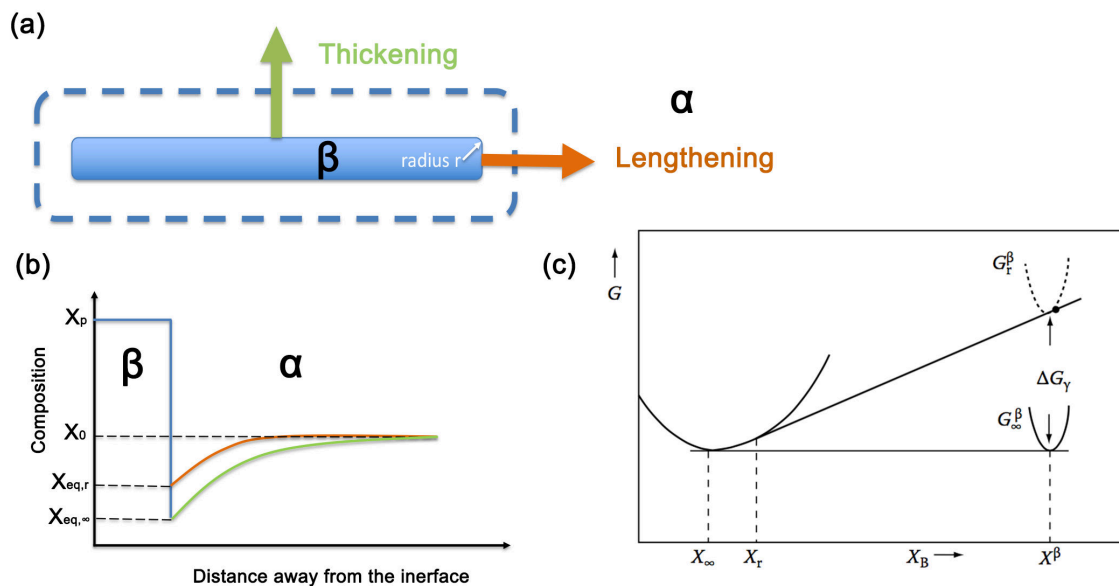


Fig. A.4 Schematic diagrams illustrating diffusional precipitate growth. (a) The lengthening and thickening directions of a precipitate plate. The edge curvature has a radius of  $r$ . The dashed line circles the solute depletion field around the precipitate. (b) Plot of the solute composition against the distance away from the precipitate-matrix interface, with the orange line represents the lengthening direction and the blue line represents the thickening direction, respectively. (c) Gibbs free energy against composition for the broad and edges interfaces, illustrating the Gibbs-Thompson effects, reprinted from Ref. [15], p.44 with permission from Taylor & Francis.

### A.3 Growth

After precipitates nucleated, they start to grow. The growth of a precipitate plate includes both thickening and lengthening, displaying a complicated, non-equilibrium, anisotropic kinetics. During the growth stage, the role of interface is manifested through two aspects: **Gibbs-Thomson effects** and **interfacial mobility** [10]. In the following analysis, we will consider the disordered interface first to discuss the Gibbs-Thomson effects and then the ordered interface to discuss the interfacial mobility. Among different kinetics models, the simplest equations are taken in this review. We are taking the convention of solute-rich precipitate in the following analysis. Let it be the precipitate  $\beta$  with the composition of  $A_xB_y$  formed within the  $\alpha$  matrix with the alloy composition of  $X_0$  (in term of B).  $X_p$  is noted as the molar concentration of B in the  $\beta$  phase:  $X_p = y/(x+y)$ .  $D_B^\alpha$  is the diffusivity of B in the  $\alpha$  matrix. For the disordered interface, the thickening of a plate is controlled by the bulk diffusion. As shown in Fig. A.4, the precipitate develops a solute depletion field at its broad interface.  $X_p$  is the precipitate composition and  $X_I$  is the solute concentration at the interface. Note that  $X_I$  varies with conditions. For instance, at the board interface which can be assumed to be infinitely large, the solute concentration reaches local equilibrium  $X_{eq,\infty}$ . The linearised gradient approximation gives the thickening rate as:

$$V_t = \frac{(X_0 - X_{eq,\infty})}{(X_p - X_{eq,\infty})^{1/2}(X_p - X_{eq,\infty})^{1/2}} \sqrt{\frac{D}{2t}}, \quad (\text{A.11})$$

which does not have any interfacial energy term. The lengthening of a precipitate plate, however, is strongly influenced by Gibbs-Thomson effects [10]. The finite size and high curvature at the plate edge are associated with high interfacial energy. As shown in Fig. A.4, this extra interfacial energy shifts up the Gibbs free energy of the precipitate phase and yields a solute concentration  $X_I$  at its interface higher than the infinite equilibrium solution  $X_{eq,\infty}$  [15]. For a spherical particle with 100% solute, the solubility at its interface is known as  $X_{eq,r} = X_{eq,\infty} \exp(\frac{2\gamma V}{rkT})$ , where  $V$  is the atomic volume of the particle. The edge of  $\beta$  plate can be approximated as a hemicylinder with of radius of  $r$  that gives  $X_{eq,r} = X_{eq,\infty} \exp(\frac{\gamma V_\beta}{rkT} \frac{1-X_{eq,\infty}}{X_p-X_{eq,\infty}})$ , where  $V_\beta$  is the atomic volume of  $\beta$  phase [10]. If the solid solution is diluted,  $X_{eq,\infty} \ll 1$ , the equation is simplified into  $X_{eq,r} = X_{eq,\infty} \exp(\frac{\gamma V_\beta}{X_p r k T})$  [218]. Using the Zener-Hillert equation, the lengthening rate is:

$$V_l = \frac{D_B^\alpha}{2r} \frac{X_0 - X_{eq,\infty}}{X_p - X_0} \left(1 - \frac{r_c}{r}\right), \quad (\text{A.12})$$

where  $r$  is the radius of curvature,  $r_c$  is the critical radius of curvature whereat  $X_{eq,r}$  is identical to  $X_{eq,\infty}$  and growth stops (a growth counterpart to  $r^*$  in nucleation). The stable lengthening

rate is taken when the curvature maximises the kinetics [10]:

$$r = 2r_c = \frac{2\gamma V_\beta}{X_p kT} \frac{1}{\ln\left(\frac{X_0}{X_{eq,\infty}}\right)}, \quad (\text{A.13})$$

The lengthening rate is controlled by the solute content gradient at the interface. As the Gibbs-Thomson effects increase the solute content at the edges of a precipitate, it slows down the lengthening kinetics. This effect is significant with large interfacial energy, particularly for edges with the semicoherent or non-coherent interface. Once the lengthening rate reaches the stable state, the radius of curvature is proportional to the interfacial energy. The higher the interfacial energy, the lower the lengthening rate, according to the diffusion-controlled growth model.

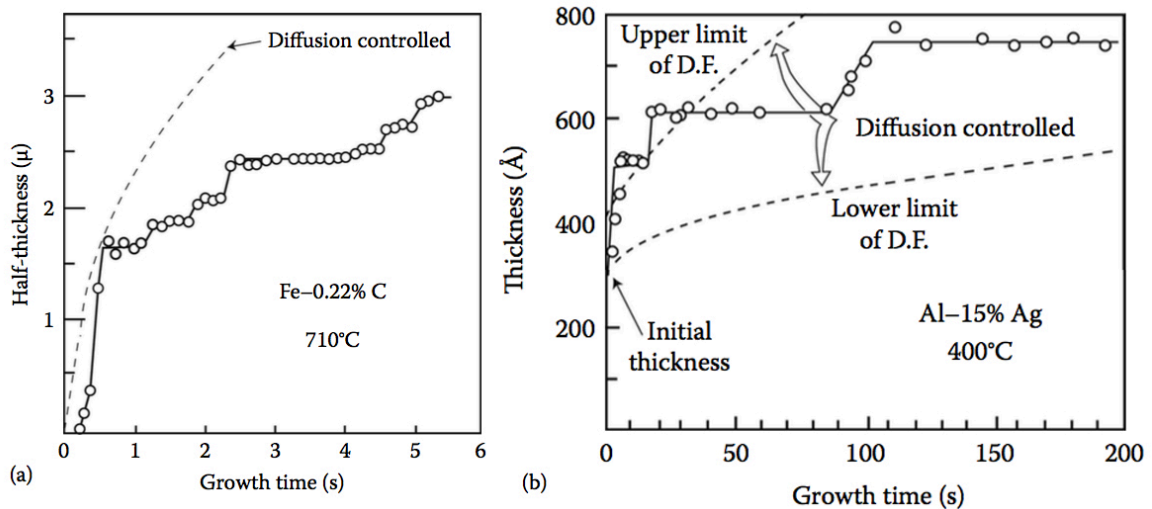


Fig. A.5 Typical plots of thickness (or half-thickness) vs. time for precipitate plates in (a) Fe-0.22% C [219], reprinted with permission from Springer and (b) Al-15% Ag [49] (in weight percent), reprinted with permission from Elsevier.

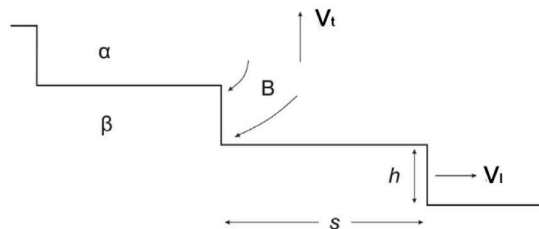


Fig. A.6 Schematic illustration of migration of an interphase boundary by lateral motion of ledges. Adapted from Ref. [15], p. 283 with permission from Taylor & Francis.

However, the precipitate interfaces are ordered in reality, often fully or partially coherent with the matrix. Their kinetics are beyond the descriptions of bulk diffusion because of the interfacial mobility. In various alloy systems, Fig. A.5, the thickening of precipitate plates is discrete, rather than continuous in the diffusion-controlled growth model [10]. This phenomenon is operated by ledge mechanism, Fig A.6, where the broad interface is assumed to be immobile while the thickness still can be increased with lateral movement of ledges as “raisers” [10]. Consider a set of parallel linear ledges with  $h$  as their height and  $s$  as their spacing, the thickening rate has a relationship with the lengthening rate as:

$$V_t = V_l \frac{h}{s}. \quad (\text{A.14})$$

The lengthening rate of ledge  $V_l$  is described by Zener-Hillert equation in Eq. A.12 with radius  $r$  equals to the ledge height  $h$ . It is obvious that the thickening of a plate is dependent on the availability of the ledge. Because the broad interface is usually coherent with scarce edges, thickening is prohibited by the interface. This slowed kinetics is described by the interfacial mobility as:

$$V = M \left( \frac{\Delta\mu}{V_\beta} \right), \quad (\text{A.15})$$

where  $V$  is the interfacial velocity for either lengthening or thickening,  $M$  is the corresponding interfacial mobility,  $\Delta\mu$  is the driving force. For a dilute solution, the driving force  $\Delta\mu$  is given by the potential energy difference of B solute in solid solution and in the precipitate phase  $\Delta\mu = kT \frac{X_l - X_{eq,\infty}}{X_{eq,\infty}}$ . If the kinetics is interface controlled, the local equilibrium cannot prevail at the interface. The overall kinetics is determined by the solute transportation across the interface, instead of the long-range bulk diffusion from the solid solution matrix to the interface. In other words, solutes are segregated at the interface waiting for its movement. The interfacial mobility is purely determined by interfacial structure, but the mechanisms are unknown. It is challenging to resolve the atomic structure of a precipitate-matrix interface. Even one resolved the interfacial structure, the above equations give no clue how to calculate the mobility from the first principles; rather, it serves as a fitting parameter for kinetics results. A qualitative experience tells that coherent interfaces (with low interfacial energies) have a low mobility, while semicoherent or incoherent interface (with high interfacial energies) have a high mobility, due to the supply of ledges [10]. This conclusion is opposite to that from the Gibbs-Thompson effects; often, the interfacial mobility dominates the growth in aluminium alloys.

## A.4 Coarsening

Once the solutes in the matrix are largely consumed by growing precipitates that their associated solute depletion fields overlap with each other, precipitates starts coarsening driven by **Gibbs-Thomson effects** [10]. Small precipitates have a higher solute concentration at their interfaces while large precipitates are associated with a lower value. The solute gradients between the particles with different sizes lead to the abnormal growth: the large grow larger and the small shrink smaller. For simplicity, consider spherical precipitates with negligible volume fraction and no elastic interaction, the process is fully bulk diffusion controlled. The analytical solution is given by the Lifshitz-Slyozov-Wagner (LSW) coarsening equation:

$$\bar{r}^3 - \bar{r}_0^3 = \frac{8 D_B^\alpha X_{eq,\infty} V_\beta^2 \gamma}{9 kT} t, \quad (\text{A.16})$$

where

$\bar{r}$  is the mean particle radius

$\bar{r}_0$  is the mean particle radius at the starting of coarsening

$\gamma$  is the interfacial energy

$D_B^\alpha$  is the diffusivity of solute  $B$  in matrix  $\alpha$

$X_{eq,\infty}$  is the composition at the infinite large interface

$V_\beta$  is the atomic volume of precipitate phase  $\beta$

$t$  is the coarsening time

The LSW equation suggests a kinetics relationship of  $\frac{dr}{dt} \sim t^{1/3}$ , with a coefficient that is proportional to the interfacial energy [10]. Doherty derived the coarsening equation for a precipitate plate, which gives a similar relationship [76]. The higher the interfacial energy, the faster coarsening proceed. The coarsening usually occurs during the overageing of alloys. However, sometimes, it may happen at the early stage, like the coarsening of GP zones in the Al-Cu and Al-Ag alloys. Coarsening of the alloy microstructure is not favoured in general – it threatens the thermal stability of alloy products, particularly at high temperature.



# Appendix B

## Publication List

The following papers were published during the PhD candidature. A copy of the  $\zeta$  phase paper and its supplementary materials are attached only for the examination purpose. As the author of this article, I retain the right to include it in a thesis or dissertation, provided it is not published commercially (confirmed with Elsevier Copyright Clearance Centre).

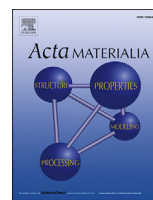
Zhang, Z., Bourgeois, L., Rosalie, J. M. and Medhekar, N. V. (2017). The bi-layered precipitate phase  $\zeta$  in the Al-Ag alloy system. *Acta Materialia*, 132, 525-537.

Zhang, Z., Liu, T., Smith, A. E., Medhekar, N. V., Nakashima, P. N. and Bourgeois, L. (2016). Mechanisms of void shrinkage in aluminium. *Journal of Applied Crystallography*, 49(5), 1459-1470.

Bourgeois, L., Zhang, Z., Li, J. and Medhekar, N. V. (2016). The bulk and interfacial structures of the  $\eta$  (Al<sub>2</sub>Au) precipitate phase. *Acta Materialia*, 105, 284-293.

Chen, Y., Zhang, Z., Chen, Z., Tsalanidis, A., Weyland, M., Findlay, S., Allen, L.J., Li, J., Medhekar, N.V. and Bourgeois, L. (2017). The enhanced theta-prime ( $\theta'$ ) precipitation in an Al-Cu alloy with trace Au additions. *Acta Materialia*, 125, 340-350.

Zhang, Y., Zhang, Z., Medhekar, N. V. and Bourgeois, L. (2017). Vacancy-tuned precipitation pathways in Al-1.7 Cu-0.025 In-0.025 Sb (at.%) alloy. *Acta Materialia*, 141, 341-351.



## Full length article

The bi-layered precipitate phase  $\zeta$  in the Al-Ag alloy systemZezhong Zhang<sup>a</sup>, Laure Bourgeois<sup>a,b,\*</sup>, Julian M. Rosalie<sup>c</sup>, Nikhil V. Medhekar<sup>a,\*\*</sup><sup>a</sup> Department of Materials Science and Engineering, Monash University, Victoria 3800, Australia<sup>b</sup> Monash Centre for Electron Microscopy, Monash University, Victoria 3800, Australia<sup>c</sup> Erich Schmid Institute of Materials Science, Austria

## ARTICLE INFO

## Article history:

Received 7 April 2017

Accepted 25 April 2017

Available online 28 April 2017

## Keywords:

Precipitation

Atomic structure

Scanning transmission electron microscopy

(STEM)

Density functional theory (DFT) calculation

Aluminium alloys

## ABSTRACT

The Al-Ag system is thought to be a well-understood model system used to study diffusional phase transformations in alloys. Here we report the existence of a new precipitate phase,  $\zeta$ , in this classical system using scanning transmission electron microscopy (STEM). The  $\zeta$  phase has a modulated structure composed of alternating bilayers enriched in Al or Ag. Our *in situ* annealing experiments reveal that the  $\zeta$  phase is an intermediate precipitate phase between GP zones and  $\gamma'$ . First-principles calculations show that  $\zeta$  is a local energy minimum state formed during Ag clustering in Al. The layered structure of  $\zeta$  is analogous to the well-known Ag segregation at the precipitate-matrix interfaces when Ag is microalloyed in various aluminium alloys.

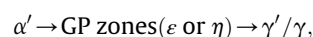
© 2017 Acta Materialia Inc. Published by Elsevier Ltd. All rights reserved.

## 1. Introduction

Al-Ag alloys have been studied extensively since last century and now serve as a textbook alloy system [1–4]. It is a model system to study solid-solid phase transformations for several reasons. First, one of the transformations associated with the decomposition of the supersaturated solid solution involves a structural change from face-centred cubic (FCC) to hexagonal close-packed (HCP) that is straightforward to understand [2,3]. Second, the atomic size difference between Al and Ag is negligible, which gives a minimal volumetric strain associated with the solute clustering and phase transformations [5]. In addition, the large difference between the atomic numbers ( $Z_{\text{Al}} = 13$  and  $Z_{\text{Ag}} = 47$ ) is particularly favourable for Z-contrast imaging in the transmission electron microscope [6–8]. Thus, Al-Ag alloys are often chosen to demonstrate advanced electron microscopy techniques, such as *in situ* annealing to observe the atomic mechanisms of precipitates growth in real time [9,10] and electron tomography to reconstruct embedded precipitates with high spatial resolution [11,12].

The precipitation sequence in the Al-Ag alloy system is

commonly recognised as [2,3]:



where  $\alpha'$  represents the supersaturated solid solution. Guinier-Preston (GP) zones are the early-stage solute enriched regions. Unlike most aluminium alloys, GP zones in the Al-Ag system form immediately after quenching [13]. Given an asymmetric miscibility gap [13], two types of GP zones are proposed, with their compositions depending on ageing temperature:  $\varepsilon$  forms at high temperature ( $>170$  °C) with relatively low Ag concentration (below 44 at.%) while  $\eta$  forms at low temperature ( $<170$  °C) with relatively high Ag concentration (44 at.-%–60 at.%) [13–15]. GP zone  $\eta$  is thought to be uniform in composition while GP zone  $\varepsilon$  is believed to have a core-shell structure and there has been much debate as to whether Ag enriches the core or the shell [5,16]. The  $\gamma'$  phase is a metastable precipitate phase formed before the equilibrium  $\gamma$  phase. Both phases display the same composition ( $\text{Ag}_2\text{Al}$ ) and the same atomic structure (HCP with space group  $P6_3/mmc$ ) but with slightly different lattice parameters [17,18]. The nucleation and growth of  $\gamma'$  require Shockley partial dislocations to accommodate the shear associated with the FCC to HCP transformation [19]. However, Al has a particularly high stacking fault energy [20], which means HCP precipitates are generally hard to nucleate. The difficult nucleation inevitably gives a low precipitate number density of  $\gamma'/\gamma$ . As a consequence, Al-Ag alloys have a poor mechanical performance [21].

\* Corresponding author. Monash Centre for Electron Microscopy and Department of Materials Science and Engineering, Monash University, Victoria 3800, Australia.

\*\* Corresponding author. Department of Materials Science and Engineering, Monash University, Victoria 3800, Australia.

E-mail addresses: [redacted] (L. Bourgeois), [redacted] (N.V. Medhekar).

Though binary Al–Ag alloys only have limited structural applications, Ag is a popular microalloying element in aluminium alloys. A small amount (from 0.1 at.% to 0.5 at.%) of Ag was found to exert dramatic improvements on the mechanical properties, thermal stability and stress-corrosion cracking resistance of aluminium alloys [22,23]. This effect is widely seen in aluminium systems, particularly in the high-strength alloys for advanced aerospace and defence applications, including Al–Cu–Mg based alloys and Al–Zn–Mg based alloys [24,25]. The underlying mechanisms, however, seem different from case to case. For instance, Ag incorporates within existing precipitate phases and accelerates their nucleation kinetics in Al–Zn–Mg based alloys [26] or Al–Mg–Si based alloys [27–29]. But in Al–Cu based alloys, Ag segregates at the precipitate–matrix interfaces, which changes precipitation behaviour and also modifies the type of precipitates that form [30]. Field ion microscopy [31,32] and atom probe tomography [33,34] have shown that Ag clusters with other solute elements (particularly Mg) at the start of ageing and segregates to  $\{111\}_{\text{Al}}$  planes, thus, initiating the  $\Omega$  phase but suppressing the S phase in Al–Cu–Mg–Ag alloys. Positron annihilation lifetime spectroscopy (PALS) has also suggested that Ag binds with Mg, Cu and vacancies during ageing [35]. Studies by scanning transmission electron microscopy (STEM) have confirmed that Ag segregation is via one or two layers at the precipitate–matrix interfaces for various precipitates with different alloying compositions, including  $\Omega$  in Al–Cu–Mg–Ag [36,37],  $\theta'$  in Al–Cu–Ag [38] and  $T_1$  in Al–Cu–Li–Mg–Ag [39]. Ag segregation at interfaces is believed to lower the interfacial energy [37,38]. Ag atoms are also suspected to cluster on  $\{111\}_{\text{Al}}$  planes whereas Cu GP zones form on  $\{001\}_{\text{Al}}$  planes [40]. However, what drives Ag to cluster before formation of a precipitate is still a mystery. Moreover, how the early-stage clustering modifies the nucleation of precipitates is largely unknown. Accurate descriptions of solute clustering are essential to address one of the most intriguing questions in Al alloys: why does the minor addition of Ag play a crucial role in precipitation in a wide variety of Al alloy systems [30]?

With the evidence that Ag facilitates phase transformations for a broad range of aluminium alloys, we hypothesise that this is due to some intrinsic properties of Ag in aluminium. Therefore, we revisited the Al–Ag system and characterised the atomic structures of the different precipitate phases using scanning transmission electron microscopy (STEM). In particular, we examined the ordering of GP zones and  $\gamma'$  precipitates. Surprisingly, we found a new metastable precipitate phase consisting of a bi-layered structure, which we named  $\zeta$ . Based on our experiments and first-principles calculations,  $\zeta$  is a metastable phase that forms before transforming into HCP phases. The layered structure of  $\zeta$  on  $\{111\}_{\text{Al}}$  planes is analogous to Ag segregation at the precipitates–matrix interfaces. We find that Ag naturally prefers to decompose from the supersaturated solid solution and aggregate on  $\{111\}_{\text{Al}}$  planes.

## 2. Experimental and computational methods

### 2.1. Sample preparation

The alloy composition used in this work was Al–1.68 at.% Ag, as cast from high-purity aluminium (Cerac alloys, 99.99% purity) and silver (AMAC alloys, 99.9+%). The pure metals were melted in air at 700 °C in a graphite crucible, stirred and poured into graphite-coated steel moulds. The compositions were measured by inductively coupled plasma atomic emission spectrometry, showing very low levels of impurities [41]. The cast ingots were homogenised at 525 °C for 7 days, then hot- and cold-rolled to 0.5 mm alloys sheets. The samples were in the form of disks 3 mm in diameter and 0.5 mm in thickness, punched from an alloy sheet after rolling. They

were solutionised at 525 °C for 30 min in a nitrate salt bath and quenched to room temperature. Different quenching media, including water and oil, were tested to manipulate the quenched-in vacancy concentration before ageing. Then the samples were aged at 200 °C in an oil bath for a range of times (from 30 min to 7 days). The TEM specimens were made by mechanically grinding the disks and electro-polishing them in a 67% methanol–33% nitric acid mixture at –25 °C and 13 V with a current average of 200 mA.

### 2.2. Electron microscopy

The alloy microstructure and precipitate atomic structures were characterised by scanning transmission electron microscopy (STEM). In particular, high-angle annular dark-field (HAADF) STEM was performed to exploit the large difference in the atomic numbers between Ag and Al. Preliminary investigations of the microstructures were carried out on a JEOL JEM 2100F field-emission gun transmission electron microscope (FEGTEM) and a FEI Tecnai G<sup>2</sup> F20 Super-Twin lens FEGTEM. The JEOL 2100F was operated at 200 kV and has a STEM probe size of 2 Å. The semi-convergence angle used was 10 mrad and the HAADF detector had an inner collection semi-angle of 65 mrad and an outer collection semi-angle of 185 mrad. The *in situ* annealing experiments were conducted in the JEOL 2100F using a Gatan 652 double-tilt heating holder at various temperatures (100 °C, 150 °C and 200 °C) for a short amount of time, ranging from 3 min to 70 min. In these experiments, samples were imaged either during *in situ* annealing or after cooling down to room temperature. The Tecnai F20 was operated at 200 kV and also has a STEM probe size of about 2 Å. The semi-convergence angle used was 9.3 mrad and the HAADF detector had an inner collection semi-angle of 41 mrad and an outer collection semi-angle of 220 mrad. A tilt series was performed in the Tecnai F20 using a Fischione model 2020 single-tilt axis high-tilt sample holder. Higher resolution HAADF–STEM imaging was conducted in a dual-aberration-corrected FEI Titan<sup>3</sup> 80–300 FEGTEM. The Titan<sup>3</sup> was operated at 300 kV and a convergence semi-angle of 15 mrad, which gave a probe size of about 1.2 Å. HAADF imaging used an inner collection semi-angle of 55 mrad and an outer collection semi-angle of 200 mrad. BF imaging used an inner collection semi-angle of 13 mrad. The spherical aberration coefficient  $C_s$  is about 1  $\mu\text{m}$  in this Titan<sup>3</sup>.

Compositional analysis was performed on the JEOL 2100F and the Tecnai F20 using energy-dispersive X-ray spectroscopy (EDS). The JEOL 2100F has a JEOL 50 mm<sup>2</sup> Si(Li) detector with ultra-thin window. The Tecnai F20 has a Bruker XFlash 6120T 30 mm<sup>2</sup> silicon drift windowless detector. The composition measured by EDS across the sample thickness is contributed by the Ag enriched precipitate and the Al matrix. The precipitates examined in this study have a roughly spherical geometry. Thus, the diameter of a precipitate in the electron transmission direction is approximated to be equal as its averaged diameter on the HAADF image. The thickness of the specimen in the vicinity of a precipitate was determined by comparing on-zone position-averaged convergent-beam electron diffraction (PACBED) of the surrounding matrix [42] obtained experimentally and calculated PACBED patterns with the Bloch wave method in JEMS software. The error in the thickness measurements was  $\pm 2$  nm. The sample was tilted away from its zone axis to the optimum angle for EDS detection, also ensuring strong dynamical diffraction conditions are avoided. A position-averaged spectrum was taken at the centre of each precipitate over a  $3 \times 3$  nm<sup>2</sup> area in order to remove the effect of local chemical inhomogeneity. A schematic diagram of the method is illustrated in Fig. S1 in the Supplementary Material. Starting from the Cliff–Lorimer equation,

$$\frac{C_{\text{Ag}}^{\text{dect}}}{C_{\text{Al}}^{\text{dect}}} = k_{\text{Ag-Al}} \cdot \frac{I_{\text{Ag}}^{\text{dect}}}{I_{\text{Al}}^{\text{dect}}} \quad (1)$$

$$= \frac{C_{\text{Ag}}^{\text{prec}} \cdot d}{C_{\text{Al}}^{\text{prec}} \cdot d + (t - d)},$$

we can deduce the composition of an embedded precipitate as follows:

$$C_{\text{Ag}}^{\text{prec}} = \frac{C_{\text{Ag}}^{\text{dect}} \cdot t}{d \cdot \cos\theta}, \quad (2)$$

where  $C^{\text{prec}}$  is the deduced composition of the precipitate,  $C^{\text{dect}}$  is the measured composition,  $k_{\text{Ag-Al}}$  is the Cliff-Lorimer k-factor between Ag and Al,  $I^{\text{dect}}$  is the detected characteristic intensities for quantification,  $t$  is the thickness of the matrix near the precipitate,  $d$  is the diameter of the precipitate and  $\theta$  is the tilting angle difference between that for the thickness determination and the EDS detection. We checked the k-factor by measuring the composition of the as-water-quenched sample, as the theoretical value stored in the quantification software may easily vary by > 10% [43]. The measured composition of 1.8 at.% to 2.0 at.% Ag across the sample is in good agreement with the alloy composition (Al-1.68 at.% Ag). Although errors of the deduced compositions arising from neglecting the geometrical X-ray absorption and fluorescence remain, these errors were found not to be significant for a thin foil: according to mass-energy X-ray absorption calculations [44], about 2% of the major characteristic X-ray for Ag ( $L_{\alpha}=3$  KeV) is absorbed by the Al matrix for a 100 nm-thick sample. Thus, the results should still be comparable between two different phases. Furthermore, the composition of one of the phases (GP zone  $\epsilon$ ) is already known from the phase diagram [45] and many previous experiments (see for example Ref. [46]).

### 2.3. STEM image simulations

HAADF-STEM simulations were performed using the  $\mu$ STEM software [47], implementing the multislice method with quantum excitation of phonons to incorporate elastic and inelastic phonon scattering. The simulations used the optimised crystal structures of Al and  $\zeta$ , obtained using first principles density functional theory methods (see below). Each slice had a thickness of 1.485 Å and the total sample thickness was modelled from 100 Å to 600 Å. Microscope parameters were matched with the experimental settings of Titan<sup>3</sup> as specified above.

The experimental and simulated images were analysed using ImageJ software. The brightness of the simulated images was scaled linearly to the same dynamic range as the experiment. The contrast was then adjusted to that of an experimental image by modifying the gamma correction value ( $\Gamma$ ). The intensity was given by  $I' = I^{\Gamma}$ , where  $I'$  is the output intensity, and  $I$  is the input intensity. Except the brightness and contrast adjustments, no other image manipulation were performed.

### 2.4. Lattice displacements relative to Al matrix: calculations and mapping

Geometric phase analysis (GPA) filters a lattice image according to the peaks in its fast Fourier transform (FFT) and compares that image to a reference lattice to resolve local strain in real space [48]. GPA has demonstrated an excellent spatial accuracy in agreement with classical strain theory [49,50]. In this study, as the  $\zeta$  precipitates have a super-lattice of FCC aluminium and are coherently

embedded within the matrix, the value calculated by GPA reflects the lattice displacements relative to FCC Al for both the precipitate phase and the matrix. An experimental STEM image with a pixel size of  $1024 \times 1024$  was used as input, where Al matrix away from the precipitate in the same image was used as the reference. The theoretical values of lattice displacements for bulk  $\zeta$  phase were calculated by comparing the DFT-optimised structure of  $\zeta$  (see details in DFT methods) in reference to the DFT-optimised Al lattice parameter using elastic strain calculation [51] in Ovito software [52]. The lattice parameter values of aluminium obtained from both experimental measurements ( $4.04 \pm 0.05$  Å) and DFT optimisation (4.05 Å), as the reference for both calculations, were in good agreement. Because STEM moves the probe in a raster, scanning artefacts arise due to the time delay between measurements and accumulated error in probe position [53]. The linear scanning distortion was corrected with a standard gold cross-grating sample before imaging for geometric phase analysis. The noise, usually non-linear in nature due to the external field, is more predominant in the slow scanning direction comparing to the fast scanning direction. The non-linear scanning distortion was corrected with image pairs in orthogonal scan directions using the algorithm described in Ref. [53]. The uncertainties in our GPA results were better than  $\pm 1\%$  after the distortion correction. Note that the atomic size difference between Al and Ag is negligible (about 0.5%). Therefore, our geometric phase analysis is not sensitive to the composition. However, it is sensitive to any structural change larger than 1%. All the calculated images were coloured with the same scale from  $-7\%$  (contraction) to  $7\%$  (extension) for visualisation.

### 2.5. Density functional theory calculations

First-principles density functional theory (DFT) calculations were performed using the Vienna *Ab initio* Simulation Package (VASP) [54] using the generalised gradient approximation of Perdew, Burke, and Ernzerhof (GGA-PBE) [55] with projector augmented wave potentials [56,57]. Geometrical relaxations were performed to optimise the supercells until Hellmann-Feynman forces were less than 0.01 eV/Å, where all lattice parameters and all internal coordinates were optimised if not stated otherwise. The convergence of the relevant energy differences with respect to energy cut-off, k-point sampling and supercell size was better than 1 meV/atom.

The formation energies of different phases are given relative to the energy of FCC Al and Ag in the ground state. The defect energy of Ag in solid solution was calculated by an isolated Ag substitutional point defect in an Al supercell containing 108 atoms, giving a substitutional defect energy of 0.09 eV, in reasonable agreement with previous calculations of 0.02 eV using the local density approximation (LDA) [58]. The formation energies of Ag clusters, including di-atom clusters and tri-atom clusters, were also calculated using a 108-atom Al supercell with Ag substitutions in different configurations. Planar Ag-Al structures were modelled using tetragonal or trigonal supercells in which the precipitates were surrounded above and below by Al (representing the infinitely wide two-dimensionally coherent Ag plane(s) surrounded by Al matrix), containing the equivalent of 20–24 atomic planes ( $\{001\}_{\text{Al}}$ ,  $\{110\}_{\text{Al}}$  or  $\{111\}_{\text{Al}}$ ). Sufficient numbers of Al atomic layers were used to simulate the effect of an infinitely large Al matrix. The  $\zeta$  phase was investigated by assuming each bilayer was pure Ag or Al, which resulted in a composition of AgAl. The embedded  $\zeta$  phase was calculated by the sandwiched structure of AgAl with the Al matrix using the supercell as described above. The  $\gamma'$  phase was calculated using the model by Neumann [18] with lattice parameters constrained to experimental measurements [41].

The bulk phases of Al, Ag,  $\zeta$  (AgAl) and  $\gamma$  (Ag<sub>2</sub>Al) were fully optimised; their calculated lattice parameters were in good agreement with experiments [18,19] and their formation energies were consistent with previous calculations [58,59].

### 3. Results

#### 3.1. Atomic structure: HAADF-STEM imaging, simulation and analysis

An Al-1.68%Ag alloy aged at 200 °C for times varying from as-quenched to 7 days exhibits the microstructure expected from previous studies [21,60]: finely distributed Ag-enriched coherent precipitates known as GP zones and sparsely distributed  $\gamma'$  precipitates. Fig. 1(a) shows a typical view of the alloy quenched in water and aged at 200 °C for 2 h. The  $\gamma'$  precipitates are in the shape of structured assemblies, in agreement with previous findings [21]. Fig. 1(b) confirms that  $\gamma'$  precipitates have an ABAB stacking embedded in the FCC aluminium matrix (ABCABC stacking). The  $\gamma'$  precipitates also display the expected orientation relationship of  $\{111\}_{\text{Al}} \parallel \{0001\}_{\gamma'}$  and  $\langle 110 \rangle_{\text{Al}} \parallel \langle 11\bar{2}0 \rangle_{\gamma'}$  with an exceptionally good lattice matching with aluminium [19,61]. Fig. 1(c) shows GP zones  $\epsilon$  formed above the  $\eta$ - $\epsilon$  transition temperature displaying chemical inhomogeneity within the precipitates, where the darker columns correspond to Ag depletion. This observation is consistent

with earlier X-ray [5] and STEM results [7] that show Ag depletes in the core and enriches in the shell. However, the detailed structure of  $\epsilon$  can be considered as a multiple core-shell complex, rather than the simple model with one core as proposed previously [5]. These GP zones  $\epsilon$  are likely the growth product of small Ag clusters. Fig. 1(d) shows that small Ag enriched clusters with few atoms readily exist in the as-quenched state due to decomposition, in agreement with work published over 50 years ago [13].

The chemical inhomogeneities within GP zones  $\epsilon$  develop gradually by diffusion of Ag in Al. Fig. 2(a–c) shows  $\epsilon$  GP zones are more homogeneous at the early stage in the oil quenched sample. Fig. 2(c–e) shows that Ag on  $\{111\}_{\text{Al}}$  planes becomes increasingly ordered, while the widths of the Ag depletion regions remains relatively constant at about two to four  $\{111\}_{\text{Al}}$  layers. This unique behaviour will be explained with first-principles calculations in a later section. The purpose of oil quenching was to reduce the quenched-in vacancy concentration to suppress the formation of  $\gamma'$  and preserve the growth of GP zones (see the different precipitation behaviours between water quenched and oil quenched samples in Fig. S2 in the Supplementary Material). This process enabled us to obtain large GP zones with diameters up to 25 nm (see Fig. 2(e)) that were subsequently used in the following *in situ* annealing in the TEM.

Fig. 3 shows the microstructural change of the alloy containing large GP zones after 7 days ageing at 200 °C before and after the

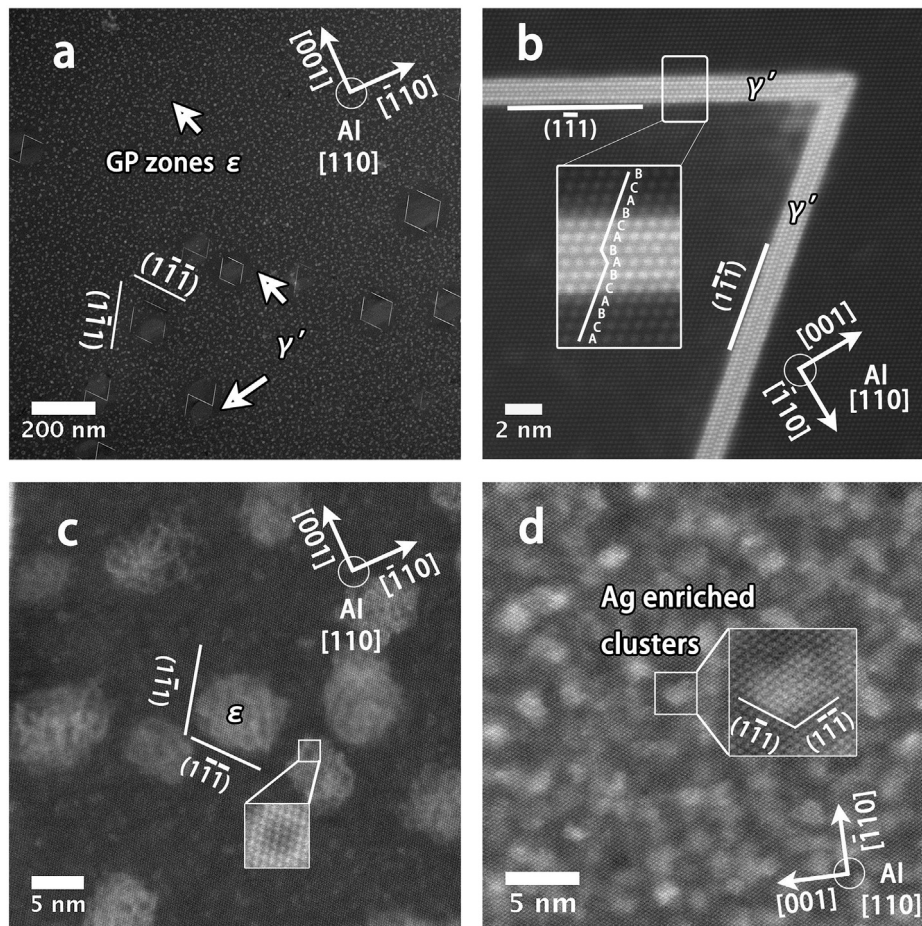


**Fig. 1.** HAADF-STEM images of the typical microstructure for Al-1.68 at.% Ag aged 2 h at 200 °C after water quenching. (a) Low magnification image of  $\gamma'$  precipitate assemblies and GP zones; (b) high magnification image showing a  $\gamma'$  precipitate with the enlarged image illustrating the characteristic stacking fault associated with a HCP precipitate (ABAB stacking) embedded within the FCC matrix (ABCABC stacking); (c) high magnification images showing the  $\epsilon$  GP zones. The enlarged images show the Ag depletion area inside a GP zone. (d) High magnification image of small Ag clusters formed in the as-water-quenched state. The electron beam is parallel to  $\langle 110 \rangle_{\text{Al}}$ .

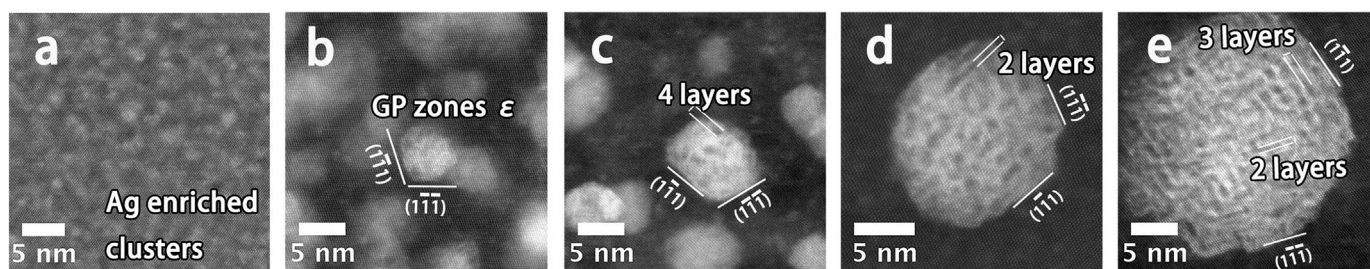


**Fig. 2.** HAADF-STEM images of GP zones aged at 200 °C after quenching in oil for various ageing times: (a) as-oil-quenched (b) 1 h; (c) 2 h; (d) 24 h; (e) 7 days. The ordering of Ag solute becomes increasingly defined on the  $\{111\}_{\text{Al}}$  planes while the width of the Ag depletion remains about two to four  $\{111\}_{\text{Al}}$  layers. The electron beam is parallel to  $\langle 110 \rangle_{\text{Al}}$ .

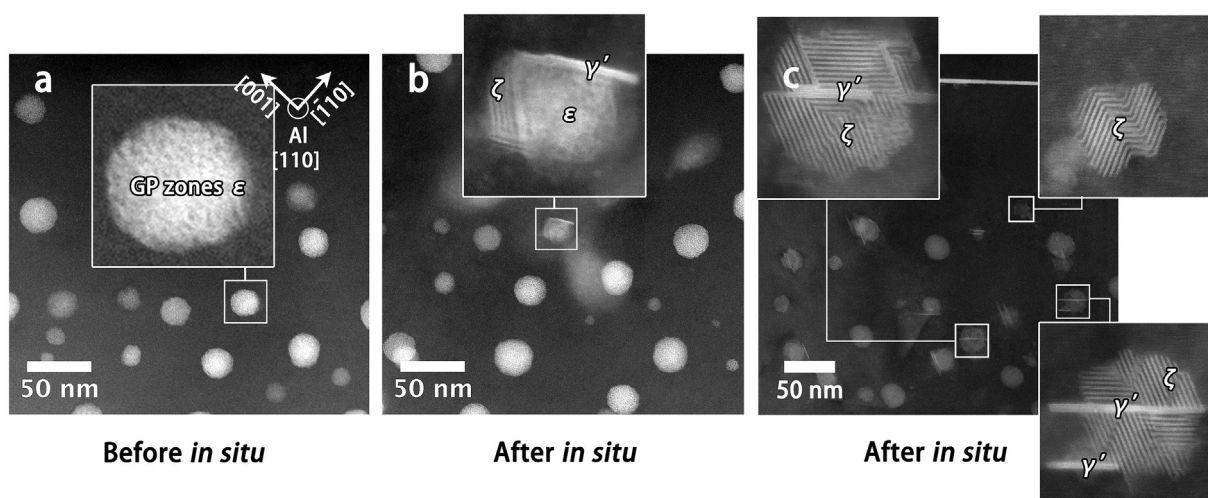


**Fig. 3.** HAADF-STEM images of the microstructure before and after *in situ* annealing at 200 °C for 3 min. The original sample is oil quenched and aged at 200 °C for 7 days. (a) Before *in situ* annealing, where the enlarged image shows the GP zone before transformation; (b) after *in situ* annealing, where the enlarged image shows the GP zone shown in (a) now containing  $\gamma'$  precipitates; (c) after *in situ* annealing in a different area from (a), where the enlarged images show more transformed GP zones with a layered structure. The electron beam is parallel to  $\langle 110 \rangle_{\text{Al}}$ .

secondary ageing within the electron microscope. A transformation occurred within a GP zone  $\epsilon$  after a short time (3 min) annealing at 200 °C inside the microscope, as shown in Fig. 3(a–b). This transformation did not occur for every GP zone, and the density was not uniform across the sample. Fig. 3(c) shows a different area of the same sample with a higher density of the transformed GP zones and a clear layered structure inside (see insets). In addition, Fig. S3 in the Supplementary Material shows the microstructure evolution during *in situ* annealing at 150 °C. The layered structure originated from the local ordering of  $\epsilon$ . Later,  $\gamma'$  assemblies nucleated and grew beside the layered structure. A time-resolved phase transformation movie was recorded with an interval of 28 s between each frame (SM\_movie\_1). We tested different *in situ* annealing temperatures (100 °C, 150 °C and 200 °C) and samples with different GP zones sizes. The results indicate that the transformation needs large GP zones and a relatively high annealing temperature ( $\geq 150$  °C). Interestingly, Fig. S4 in the Supplementary Material shows that small GP zones actually shrunk during *in situ* annealing, as a result of Ag diffusion to the sample surface. In order to examine the potential effect of electron irradiation on phase transformations, we performed *in situ* annealing experiments without the electron beam. Results show that, without the interaction with the electron beam, newly formed layered structure and  $\gamma'$  precipitates were still found (see Fig. S5 in the Supplementary Material).

Supplementary video related to this article can be found at <http://dx.doi.org/10.1016/j.actamat.2017.04.061>.

Fig. 4(a) shows that the ordered phase is clearly distinct from GP

zones  $\epsilon$  or  $\gamma'$  plates. We named this new phase as  $\zeta$ . Specifically,  $\gamma'$  has an ABAB stacking while  $\zeta$  follows the ABCABC stacking of FCC Al. The phase exhibits different domains corresponding to different  $\{111\}_{\text{Al}}$  variants, as viewed along a  $\langle 110 \rangle_{\text{Al}}$  direction (see Fig. 4(a)). Fig. 4(b) shows that Ag can be depleted in some atomic columns within the Ag-enriched bilayers, as viewed along  $\langle 112 \rangle_{\text{Al}}$ . But the depletion has no periodicity, and the overall intensity is quite uniform. After imaging in the  $\langle 110 \rangle_{\text{Al}}$  and  $\langle 112 \rangle_{\text{Al}}$  directions, we conclude that the new phase has a super-lattice structure of FCC Al and consists of alternative Ag enriched bilayers and Al enriched bilayers on  $\{111\}_{\text{Al}}$  planes.

In many cases,  $\gamma'$  precipitates formed inside GP zones  $\epsilon$  and introduced Ag depletion at their coherent interfaces ( $\{111\}_{\text{Al}/\epsilon} \parallel \{0001\}_{\gamma'}$ ). As shown in Fig. 4(c), the widths of the Ag depletion gaps are about two to three atomic layers. Away from the coherent interfaces of  $\gamma'$  precipitates, Ag enriches and then depletes again in a specific frequency that is similar to the modulation of  $\zeta$ , suggesting these regions are poorly ordered version of  $\zeta$  phase. The precipitates,  $\zeta$  and  $\gamma'$ , transformed from GP zones, can be easily found on a large scale after *in situ* annealing (see Fig. 3(c)). However, these structures are rarely found in samples obtained using conventional heat treatment with one example shown in Fig. 4(d). This sample was water quenched and aged at 200 °C for 2 h without *in situ* annealing. The original GP zone developed Ag depletion inside and formed  $\gamma'$  and  $\zeta$  at its edges. Interestingly,  $\gamma'$  precipitates also induced the ordering of Ag at their coherent interfaces similar

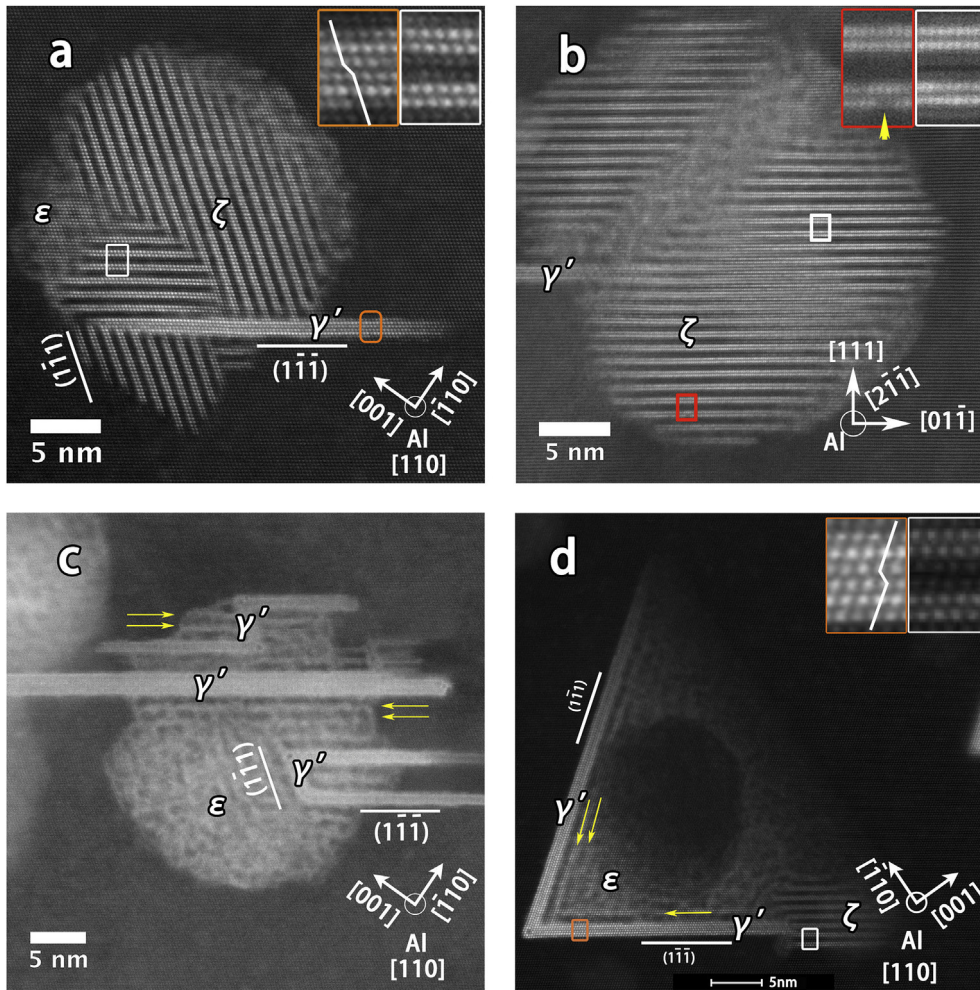


**Fig. 4.** HAADF-STEM images of the transformed GP zones. (a) A bi-layered phase formed on  $\{111\}_{Al}$  planes and viewed along  $\langle 110 \rangle_{Al}$ , where the white framed region shows that the bi-layered phase has an ABCABC stacking and the orange framed region shows the characteristic stacking fault of  $\gamma'$ ; (b) a bi-layered phase viewed along a  $\langle 112 \rangle_{Al}$  direction, where the white framed region shows the uniformly enriched Ag layers while the red framed region shows non-uniformly enriched Ag layers as indicated by a yellow arrow; (c)  $\gamma'$  plates formed inside a GP zone introducing ordering as indicated by yellow arrows; (d) a bi-layered phase formed at the tail of a  $\gamma'$  assembly, as viewed along  $\langle 110 \rangle_{Al}$ . Images (a–c) were from the sample that underwent *in situ* annealing as shown in Fig. 3. Image (d) was from a sample that underwent a conventional heat treatment: water quenched and aged at 200 °C for 2 h without *in situ* annealing. (For interpretation of the references to colour in this figure legend, the reader is referred to the web version of this article.)

to Fig. 4(c) (as indicated by arrows).

The metastable  $\zeta$  phase will eventually transform into HCP  $\gamma'$ . This is evident by Fig. 5 where the transformation during *in situ* annealing was recorded. Fig. 5(a) shows a GP zone in which both  $\zeta$  and  $\gamma'$  formed inside. Fig. 5(b–d) shows  $\zeta$  and the remaining GP

zone shrinking gradually with increasing ageing time until their full dissolution, to the benefit of the growing  $\gamma'$  precipitates. This suggests that Ag atoms diffuse from the metastable phases to the more stable HCP phase.

Precipitation of  $\zeta$  accompanies  $\gamma'$  in most cases, but some

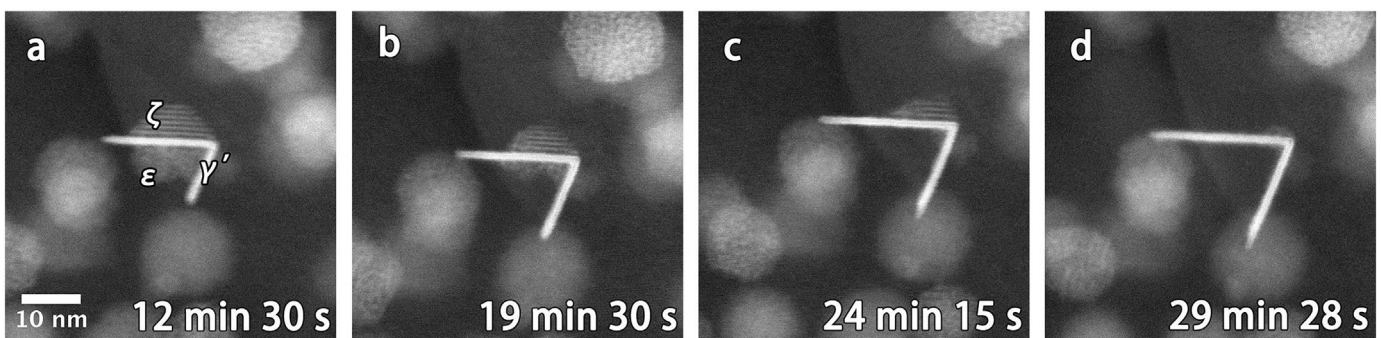


**Fig. 5.** HAADF-STEM images of evolution of  $\zeta$  to  $\gamma'$  during *in situ* annealing at 200 °C for times as labelled. The original sample was oil quenched and aged at 200 °C for 24 h. The electron beam is parallel to  $\langle 110 \rangle_{Al}$ .

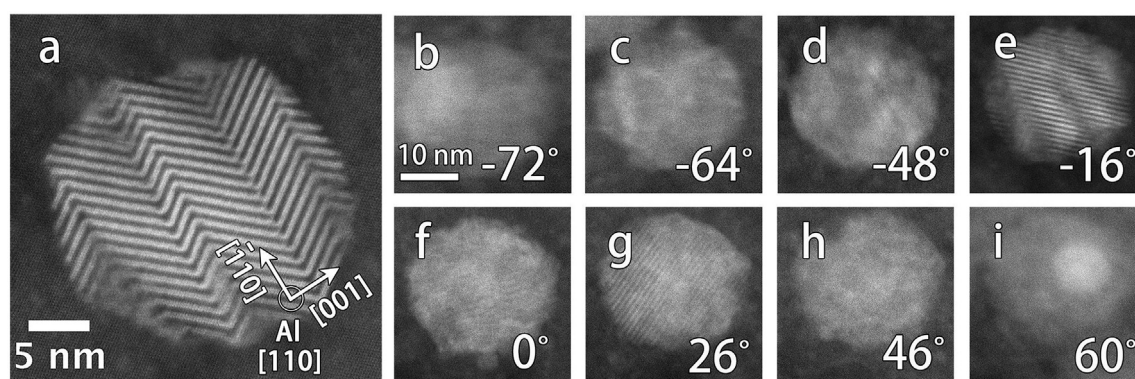


**Fig. 6.** (a) HAADF-STEM images of a bi-layered phase viewed along the  $\langle 110 \rangle_{\text{Al}}$  zone axis, showing domains formed by two variants of  $\{111\}_{\text{Al}}$  bi-layers. (b–i) HAADF-STEM tilt series of the same bi-layered precipitate phase for a tilt range from  $-73^\circ$  to  $64^\circ$ . The tilt angles are as labelled in each image.

isolated examples of  $\zeta$  without  $\gamma'$  were also found. A tilt series was performed for a given  $\zeta$  precipitate as shown in Fig. 6. Fig. 6(a) shows a  $\zeta$  precipitate viewed along the  $\langle 110 \rangle_{\text{Al}}$  zone axis with different domains of  $\{111\}_{\text{Al}}$  bilayers and their domain boundaries on  $\{001\}$  planes. Fig. 6(b–i) shows the tilt series of the same precipitate in an angular range of  $-73^\circ$  to  $64^\circ$ , where we performed  $2^\circ$  per tilt under  $\pm 60^\circ$  and  $1^\circ$  per tilt above  $\pm 60^\circ$ . The layered contrast can be seen in Fig. 6(e) and (g), corresponding to the  $\{111\}_{\text{Al}}$  bilayered variants. Throughout the tilt series, no  $\gamma'$  precipitate is visible. The drift-corrected tilt series can be found in the Supplementary Material (SM\_movie\_2), showing the structural difference between the  $\zeta$  phase and surrounding GP zones  $\varepsilon$  during tilting.

Supplementary video related to this article can be found at <http://dx.doi.org/10.1016/j.actamat.2017.04.061>.

It is important to address the chemical composition and crystal structure of  $\zeta$ . However, determining the composition of each layer is challenging for an embedded precipitate, particularly having matrix above and below the precipitate in the electron beam direction. Thus, we propose the simplest model in which each layer is pure Al or Ag and examine the validity of the model in terms of EDS analysis, HAADF-STEM image simulations, atomic positions and energetics. We examined 8 different GP zones  $\varepsilon$  and 10 different  $\zeta$  precipitates from 3 different grains with sizes ranging from 10 nm to 25 nm and the thickness of each surrounding matrix ranging from 20 nm to 100 nm with two different EDS systems. The deduced compositions are essentially the same for GP zone  $\varepsilon$  (38 at.% Ag at 200 °C) and  $\zeta$  (40 at.% Ag at 200 °C) with a small standard deviation between different datasets (3 at.% Ag for each phase). The uncertainties are 6 at.% Ag for each phase when quantified spectrums using the Cliff-Lorimer ratio method. Notably, the measured  $\varepsilon$  composition is in excellent agreement with previous X-ray results (38 at.% Ag at 200 °C) [5] and atom probe tomography (40 at.% Ag at 200 °C) [46]. The compositional analysis strongly suggests that the  $\varepsilon$ - $\zeta$  transformation involves a minimal chemical change, if any, and only rearrangement of the solute atoms within GP zones.

Fig. 7 shows the embedded  $\zeta$  phase and nearby Al matrix from the HAADF-STEM image, where both regions had approximately the same thickness. Therefore, the structures were considered as  $\zeta$  and Al with the same thickness sandwiched by Al matrix above and below the phases along the beam direction. The experimental images were compared with the simulated images for  $\zeta$  (AgAl) and Al without matrix. The peak positions of Al or  $\zeta$  (AgAl) determined in the experiments and simulations match reasonably well. The shoulders in the experimental intensity profile of  $\zeta$  phase correspond to Al columns in the AgAl model. In the experimental images, the Al-enriched columns in  $\zeta$  are brighter than the Al matrix.

However, it does not necessarily mean there is Ag within those columns, as the simulated images also show the same phenomenon. This means that the recorded intensities corresponding to Al columns actually contains a contribution from the scattering by neighbouring Ag columns. It is hard to preclude the presence of Ag in the Al-enriched columns, but there is a distinct possibility that beam spreading [62] causes the increase in intensity. The matrix above and below the precipitate would lower the contrast between the Ag-enriched and Al-enriched layers compared to the model. Besides, the atomic positions of bulk Al differs from that of  $\zeta$  in both experiments and simulations, which means that matrix above and below the precipitate might blur the HAADF-STEM image of atomic columns for an embedded  $\zeta$ . The  $\mu$ STEM algorithm takes no account of source size that also significantly blurs any experimental STEM image. But the HAADF-STEM intensity is dominated by Ag, and hence those effects should not change the validity of our results.

The modulation in the chemical composition by 4 (2 Ag and 2 Al) and the stacking ordering by 3 (ABCABC) require at least 12  $\{111\}_{\text{Al}}$  planes to achieve the periodicity of  $\zeta$ , as shown in the atomic structure in Fig. 7(b). The bi-layered AgAl model of  $\zeta$  is a trigonal crystal with a space group of  $R\bar{3}m$  (hexagonal axes). The lattice parameters for the bulk  $\zeta$  phase are  $a_{\text{DFT}} = 2.97 \text{ \AA}$  and  $c_{\text{DFT}} = 26.88 \text{ \AA}$  after DFT optimisation, which agree reasonably well with the experimental measurements for embedded  $\zeta$  precipitates of  $a_{\text{exp}} = 2.88 \pm 0.05 \text{ \AA}$  and  $c_{\text{exp}} = 27.35 \pm 0.05 \text{ \AA}$ . The embedded  $\zeta$  precipitate calculation gives a much better match with  $a_{\text{DFT}}^{\text{emb}} = 2.92 \text{ \AA}$  and  $c_{\text{DFT}}^{\text{emb}} = 27.26 \text{ \AA}$ , which means  $\zeta$  precipitates are deformed to accommodate the change in lattice parameters compared with Al. When embedded within the Al matrix,  $\zeta$  is coherent with the matrix with an orientation relationship of  $\{111\}_{\text{Al}} \parallel \{001\}_{\zeta}$  and  $\langle 110 \rangle_{\text{Al}} \parallel \langle 100 \rangle_{\zeta}$ . Table 1 lists the coordinates of Ag- and Al-containing sites in  $\zeta$ , showing an exceptionally good agreement between experiments and calculations. Close inspection of the lattice sites reveals that the spacings of the basal planes (including Ag–Ag, Ag–Al and Al–Al) vary along  $\langle 001 \rangle_{\zeta} \parallel \langle 111 \rangle_{\text{Al}}$ . This is further demonstrated in Fig. 8 using geometric phase analysis (GPA) of a distortion-corrected HAADF-STEM image in order to map these lattice displacements. Theoretical displacements of  $\zeta$  relative to Al were calculated based on the DFT-optimised structure of the AgAl model and compared with GPA results in each direction. The effect of scanning noise is demonstrated in Fig. S6 in the Supplementary Material. Fig. 8(c) shows the displacements in the direction normal to  $\zeta$  basal planes have a clear modulation in both the GPA result and the DFT-optimised structure. Within the  $\zeta$  phase, the local contraction of the lattice is significant at the Al sites as deduced from both GPA and DFT (GPA:  $-6.5\%$  and DFT:  $-6.6\%$ ), but

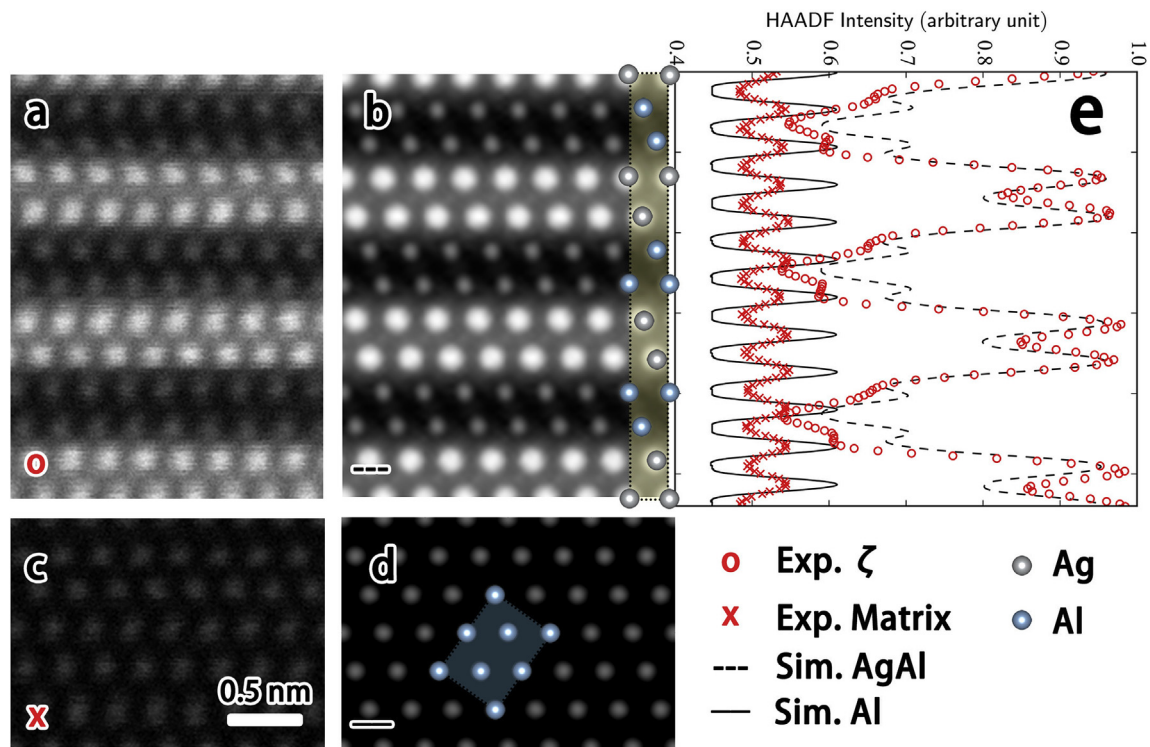


**Fig. 7.** Atomic-resolution HAADF-STEM images obtained from experiments and simulations for a  $\zeta$  precipitate: (a) raw image section of embedded  $\zeta$  precipitate; (b) simulated image of bi-layered AgAl [thickness: 30 nm] with the atomic structure overlaid [grey: Ag, blue: Al]; (c) raw image section of the matrix near the embedded  $\zeta$  shown in (a); simulated image of Al [thickness: 30 nm] with the atomic structure overlaid. (e) intensity profile of the experimental and simulated images in  $\zeta$  compared to that of the Al matrix. The orientation of the intensity profile is aligned with images (a) and (c). The electron beam is parallel to  $\langle 110 \rangle_{Al}$ . (For interpretation of the references to colour in this figure legend, the reader is referred to the web version of this article.)

less at the Ag sites (GPA: 0% and DFT:  $-1.9\%$ ). This remarkable lattice variation between the bilayers of a  $\zeta$  precipitate is not due to the atomic size difference between Al and Ag; instead, it is a result of different spacings of the basal planes in  $\zeta$  phase. Specifically, the interplanar distance between Al–Ag in  $\zeta$  phase is greatly decreased to 2.26 Å compared to the spacing of 2.34 Å between  $\{111\}_{Al}$  planes, as shown in Fig. 7. The chemical composition has to be significantly different between the sequential bilayers to cause a change of the bond length, which also demonstrate the validity of our model regarding the atomic positions. The displacements are

small in the direction along the basal planes of  $\zeta$  (GPA: 0.8% and DFT: 1.8%) in Fig. 8(d) and negligible in the shear direction in Fig. 8(e), which also represents good agreement between GPA and DFT. Finally, the  $\zeta$  precipitate is coherent within the matrix without any misfit dislocation as evident from the BF-STEM image (see Fig. 8(a)). The remaining GP zone  $\varepsilon$  (as labelled in Fig. 8(b)) is almost strain-free in all directions, as shown in Fig. 8(c–e).

### 3.2. Energetics: first-principles calculations, strain energy and entropy

The clustering process during the decomposition of the solid solution is governed by the energy of different solute configurations and the barriers between them. To understand the clustering of Ag in Al, we calculated the formation energy of various Ag clusters by DFT as shown in Table 2. The solid solution is not energetically stable with a defect energy of 89 meV/Ag atom, which drives the solid solution to decompose. For bi-atom Ag clusters, the nearest neighbours along  $\langle 110 \rangle_{Al}$  are preferred compared with the second nearest neighbours along  $\langle 001 \rangle_{Al}$ . A tri-atom cluster on either  $\{110\}_{Al}$  or  $\{111\}_{Al}$  planes is almost as stable as segregated Al and Ag in bulk. The calculated formation energy of Ag monolayer aggregation on  $\{111\}_{Al}$  is  $-65$  meV/Ag atom, which is significantly more stable than Ag on the other low-index crystallography planes. This energy is substantial, given the thermal energy at 200 °C is 40 meV. Not surprisingly,  $\{111\}_{Al}$  planes become the basal planes for  $\zeta$  and the HCP phases  $\gamma'/\gamma$ .

With Ag placed on  $\{111\}_{Al}$  planes, we investigated the preferential distance between two Ag layers in aluminium. A series of calculations were performed with varying Al layers between two Ag layers as shown in Fig. 9. Interestingly, a distance range of two to four  $\{111\}_{Al}$  Al layers between the two Ag layers is favourable, as a

**Table 1**

Atomic coordinates of the precipitate  $\zeta$  phase. The listed coordinates are fractional in respect to the simplest trigonal cell with space group of  $P3$ . It is equivalent to a trigonal cell with a space group of  $R\bar{3}m$  (hexagonal axis) and Wyckoff positions of Ag at (0 0 0.878) and Al at (0 0 0.375). The experimental parameters are  $a_{exp} = 2.88 \pm 0.05$  Å and  $c_{exp} = 27.35 \pm 0.05$  Å. The DFT-optimised parameters are  $a_{DFT} = 2.97$  Å and  $c_{DFT} = 26.88$  Å for the bulk  $\zeta$  phase and  $a_{DFT}^{emb} = 2.92$  Å and  $c_{DFT}^{emb} = 27.26$  Å for the embedded  $\zeta$  precipitate phase. The uncertainty in the experimentally determined  $z$  coordinates is 0.005.

Site	Experiment			DFT		
	x	y	z	x	y	z
Al(1)	1/3	2/3	0.086	1/3	2/3	0.081
Al(2)	2/3	1/3	0.165	2/3	1/3	0.163
Al(3)	2/3	1/3	0.417	2/3	1/3	0.414
Al(4)	0	0	0.500	0	0	0.496
Al(5)	0	0	0.741	0	0	0.747
Al(6)	1/3	2/3	0.836	1/3	2/3	0.830
Ag(1)	0	0	0	0	0	0
Ag(2)	0	0	0.248	0	0	0.244
Ag(3)	1/3	2/3	0.336	1/3	2/3	0.333
Ag(4)	1/3	2/3	0.580	1/3	2/3	0.577
Ag(5)	2/3	1/3	0.668	2/3	1/3	0.667
Ag(6)	2/3	1/3	0.917	2/3	1/3	0.910

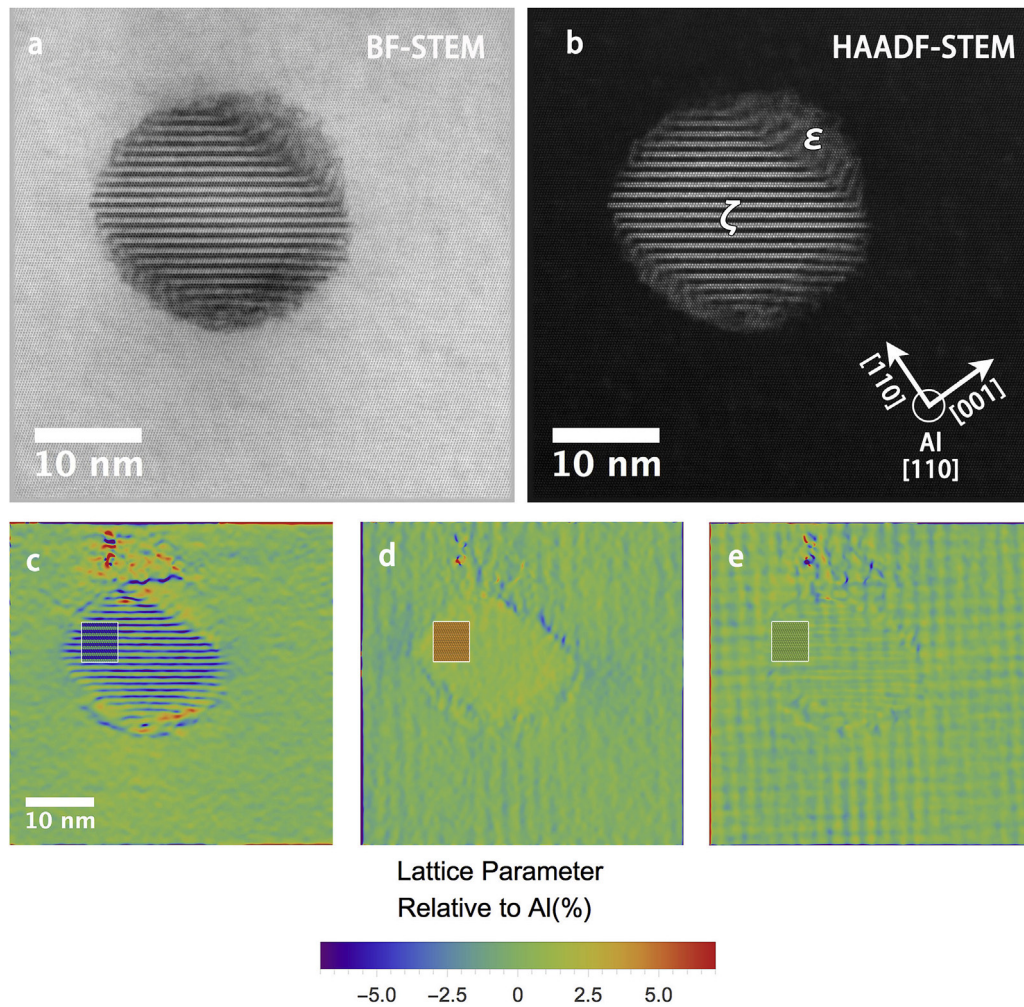


**Fig. 8.** Lattice displacements mapping of a  $\zeta$  precipitate in aluminium. Original (a) bright field (BF)-STEM and (b) HAADF-STEM images for geometric phase analysis (GPA). The GPA results were compared with simulations based on the DFT-optimised structure of the bi-layered AgAl model (in the white box) in the following directions (c) normal, (d) parallel and (e) sheared with respect to the  $\zeta$  basal planes.

closer spacing yields a considerably higher energy state. The lowest energy structure corresponds to two Al layers between two Ag layers. The energy is further lowered when Ag layers are assembled according to a periodic layered array as shown in Fig. 9(b). For a fixed composition of AgAl and ABCABC stacking, the bi-layered array is the most stable, which demonstrates the validity of our model for the  $\zeta$  phase from an energetics perspective. As summarised in Fig. 10, each phase transformation is accompanied by a decrease in energy. From clusters containing only a few atoms to

the equilibrium phase  $\gamma$ , the Al-Ag system lowers its energy by ordering Ag solute on  $\{111\}_{\text{Al}}$  planes in the Al matrix. The formation energy of the complex GP zone  $\epsilon$  is about 72–81 meV/Ag atom, as approximated by the energy range calculated for layered Ag aggregation with favourable spacings in aluminium. The formation energy of the new phase  $\zeta$  (AgAl) is 89 meV/Ag atom, the lowest in terms of ordered Ag planes on  $\{111\}_{\text{Al}}$  prior to the FCC-HCP transformation, which agrees with our *in situ* observations (see Fig. 5).

The enthalpy difference between the GP zone  $\epsilon$  and the  $\zeta$  phase is as little as 8–17 meV/Ag atom. The free energy difference between those two phases should be even smaller: the strain energy and configurational entropy do not favour the  $\epsilon$ - $\zeta$  transformation. Specifically, GP zones  $\epsilon$  are coherent with almost no strain in the Al matrix, as evident in Fig. 8. But  $\zeta$  precipitates are coherent with strain according to our experiments and simulations, which gives  $\zeta$  precipitates a higher strain energy comparing to GP zones  $\epsilon$ . Based on elastic theory for a spherical precipitate with anisotropic strain, the strain energy contribution  $E_e$  of an embedded  $\zeta$  precipitate is estimated using the following equation as

$$E_e = \mu \delta^2 V, \quad (3)$$

where  $\mu$  is the shear modulus, which is assumed to be the same

**Table 2**

DFT calculations for the preference of Ag clustering in Al matrix.  $E_F^{\text{Ag}}$  is the formation energy per Ag atom. 1<sup>st</sup> nearest neighbour stands for two Ag atoms in the nearest neighbour configuration in a  $\langle 110 \rangle_{\text{Al}}$  direction in FCC Al lattice. Similarly, the 2<sup>nd</sup> nearest neighbour is two Ag atoms next to each other in a  $\langle 001 \rangle_{\text{Al}}$  direction.

Number of Ag Atoms	Configurations	$E_F^{\text{Ag}}$ (meV)
1 Ag (Solid Solution)	N/A	89
2 Ag	1 <sup>st</sup> nearest neighbour	44
	2 <sup>nd</sup> nearest neighbour	99
3 Ag	$\{001\}_{\text{Al}}$	27
	$\{110\}_{\text{Al}}$	-1
	$\{111\}_{\text{Al}}$	-1
Ag plane	$\{001\}_{\text{Al}}$	431
	$\{110\}_{\text{Al}}$	66
	$\{111\}_{\text{Al}}$	-65

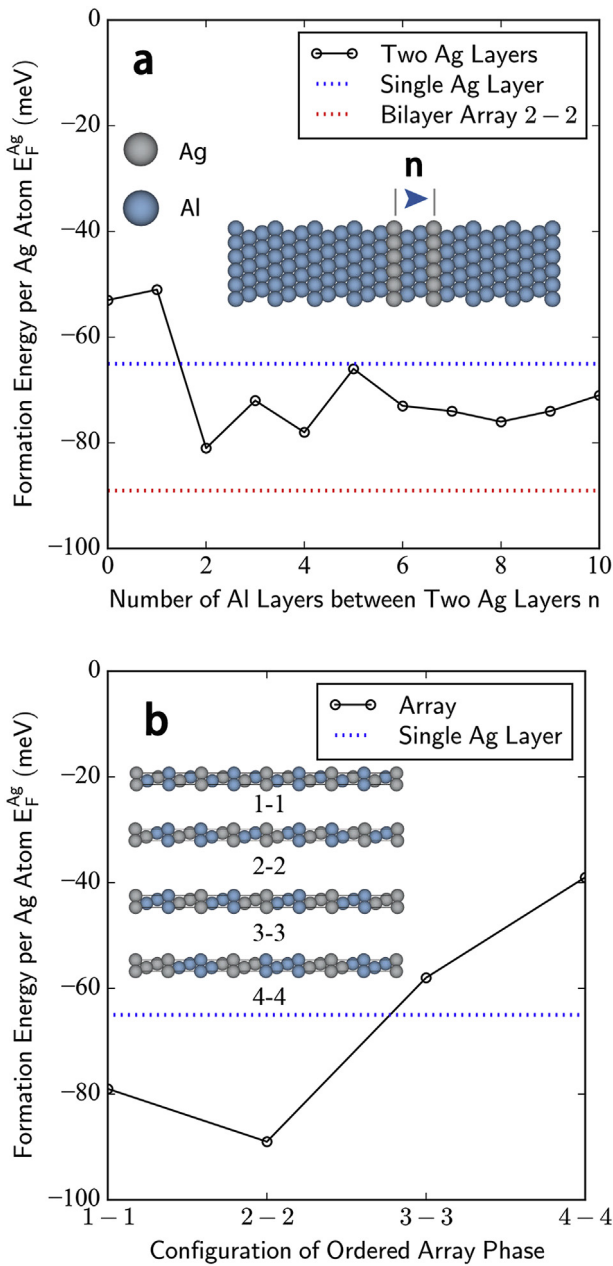


**Fig. 9.** DFT calculations illustrating the preference of  $\{111\}_{Al}$  planes for Ag aggregation in aluminium. (a) The energetics of two Ag  $\{111\}_{Al}$  planes separated by a varying number “ $n$ ” of Al planes. For instance, “2” means there are two Al atomic layers between two Ag layers as shown in the schematic diagram. (b) Energetics of different periodic arrays with a composition of AgAl. For instance, “1-1” means the modulation of one Ag layer and one Al layer as shown in the schematic diagram.

for both the  $\zeta$  precipitate and aluminium matrix;  $\delta$  is the averaged strain along  $\langle 001 \rangle_{\zeta} \parallel \langle 111 \rangle_{Al}$ , given the strains in other directions are negligible. Here we assume that Poisson's ratio is 1/3 for both the matrix and the precipitate.  $V$  is the atomic volume of  $\zeta$ , i.e. the ratio of the unit cell volume and the number of atoms within the cell. The strain energy is estimated to be 3 meV/atom, or 6 meV/Ag atom with the composition of AgAl. Also, GP zones  $\epsilon$  have a higher configurational entropy due to the chemical inhomogeneities, in contrast to a well-ordered phase like  $\zeta$  phase. The entropy of GP zones  $\epsilon$  is hard to estimated with the complex structure, but the value should be in between of that for a well-ordered phase and an ideal mixing alloy using the equation

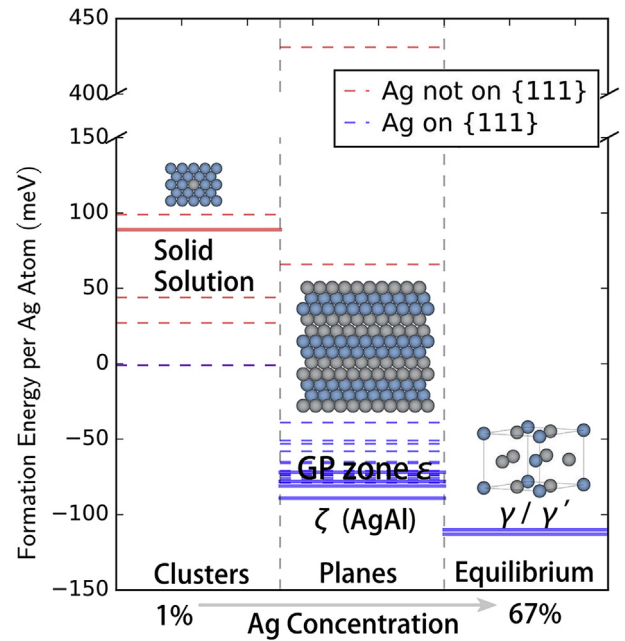


**Fig. 10.** Energetics of Ag clustering from the solid solution to the equilibrium  $\gamma$  phase. Different configurations of Ag on  $\{111\}_{Al}$  planes are shown in blue while Ag clustering on other crystallographic planes are shown in red. The phases in the transformation sequence are highlighted with a bold unbroken line with their corresponding names and atomic structures, while other configurations calculated are shown as dashed lines. (For interpretation of the references to colour in this figure legend, the reader is referred to the web version of this article.)

$$\Delta S_{\text{mix}} = -k_B(X \ln X + (1 - X) \ln(1 - X)), \quad (4)$$

where  $\Delta S_{\text{mix}}$  is the mixing entropy of the binary alloy,  $k_B$  is the Boltzmann constant,  $X$  is the composition of the binary alloy. For GP zones  $\epsilon$  with the composition of Al-40 at.%Ag, the configurational entropy is  $0.67 k_B/\text{atom}$ . In practice, the Bragg-Williams approximation of Eq. (4) overestimates the configurational entropy as it neglects any ordering. The short range and long range ordering can be incorporated into the equation by considering the probabilities of bonds between Al-Al, Ag-Ag and Al-Ag [63]. According to thermodynamics, such probabilities can be calculated based on the bond energies, usually between nearest neighbours. The bond energies are assumed to be constant while the bond fractions are varying for different configurations, no matter whether solute atoms are isolated or clustered. This simplification violates our DFT calculations that Al-Ag bond is unstable in solid solution but it is stable when Ag atoms are placed on  $\{111\}_{Al}$  planes. An accurate 3D reconstruction of the chemical distribution from the tilt series should be useful for the direct measurement of ordering (see SM\_movie\_2). New numerical computation techniques need to be developed for the purpose of entropy estimation. Nevertheless, the contribution from configurational entropy is small during phase transformations in the Al-Ag system, that otherwise prevents any kind of ordering and phase separation. We have not considered vibrational entropy in this paper.

#### 4. Discussion

The bilayer phase first reported herein is a new phase in the Al-Ag system. We propose to name it  $\zeta$  phase, by analogy with the patterned skin of the zebra. HAADF-STEM images show a clear picture of Ag ordering on  $\{111\}_{Al}$  planes starting from a small cluster to a large GP zone (see Fig. 2). The positive defect energy of

Ag in aluminium is consistent with previous calculations [64] that explain the driving force for the decomposition [13]. For comparison, Au has almost an identical size to Ag, yet Au displays a very negative defect energy in Al [65]. It is the electronic difference between Ag and Au in aluminium that leads to completely different clustering and precipitation behaviours, either in the binary alloys [65][this work] or when they are added to Al-Cu alloys [38,66]. Our DFT calculations also illustrate the preference of Ag aggregation on  $\{111\}_{\text{Al}}$  planes in Al-Ag binary alloys, which also occurs at the early stage of ageing in Al-Cu-Mg-Ag alloys [31,33] and Al-Cu-Li-Mg-Ag alloys [67]. During ageing,  $\{111\}_{\text{Al}}$  planes enriched in Ag within GP zones  $\epsilon$  begin to move away from each other and form Ag depletion regions as shown in Fig. 2. The ordering of Ag clearly increases with ageing time, while the depletion width remains about two to four  $\{111\}_{\text{Al}}$  layers. The unique clustering behaviour can be understood from our DFT calculation that Ag prefers to be on  $\{111\}_{\text{Al}}$  planes but not with the  $\{111\}_{\text{Al}}$  planes close to each other. The favourable spacing is around two to four Al  $\{111\}_{\text{Al}}$  planes, which is in excellent agreement with our experiments. The local ordering within GP zones  $\epsilon$  develops faster in the water-quenched sample than the oil-quenched sample, because more quenched-in vacancies are present to mediate diffusion. Ag needs diffusion to achieve the long range ordering exhibited by the bi-layered  $\zeta$  phase to further lower the energy of the system. Based on DFT alone, one cannot rationalise the difference in  $\zeta$  phase formation between conventional heat treatments and *in situ* annealing experiments. The free energy landscape locates the transformation pathways between different phases. After considering the strain energy and the entropy contribution, there is almost no energy difference between GP zone  $\epsilon$  and the  $\zeta$  phase. But the rearrangement of Ag atoms associated with the  $\epsilon$ - $\zeta$  transformation is expected to have a high energy barrier. Therefore, the local energy minimum state of  $\zeta$  is hardly visited during the precipitation in Al-Ag alloys. However, the experimental fact that GP zones  $\epsilon$  transform to the  $\zeta$  phase and eventually  $\gamma'$  phase demonstrates that the free energy of  $\zeta$  phase is indeed lower than that of  $\epsilon$  phase. It means that their thermal histories must be taken into account to understand different phase transformation pathways. We may appreciate this phenomenon by considering that the  $\zeta$  phase evolves through the local ordering of GP zone  $\epsilon$  on  $\{111\}_{\text{Al}}$ . Vacancies can lower the energy barrier of substitutional diffusion during the ordering of Ag atoms. For conventional heat treatments with water quenching and sequential ageing, a substantial number of quenched-in vacancies are present, thus helping early stage clustering or providing defects for heterogeneous nucleation (see Fig. S2 in the Supplementary Material). Indeed,  $\gamma'/\gamma$  assemblies nucleate at dislocation loops [21], which bypasses intermediate phases like  $\epsilon$  phase and  $\zeta$  phase. The quenched-in vacancies usually run out quickly at the early stage of ageing before GP zones  $\epsilon$  grow large enough to exhibit the local ordering of Ag on  $\{111\}_{\text{Al}}$ . This may explain why the  $\epsilon$ - $\zeta$  transformation is rarely observed using conventional heat treatments, given the extensive studies on this system in the last century. Often the reaction within the thin TEM specimen differs from that in the bulk, both due to the surface effect and the electron irradiation. Electron irradiation indeed can substantially lower the energy barrier for diffusion of vacancies, as we quantitatively measured in our recent study of *in situ* annealing of voids in aluminium [68]. However, according to our *in situ* annealing experiment without electron beam,  $\zeta$  and  $\gamma'$  were still found to form within GP zones (see Fig. S5 in the Supplementary Material). This demonstrates that electron beam irradiation is not responsible for those transformations. When considering surface effects, there is a depth dependency of the vacancy formation energy at the Al surface [69]. In general, a vacancy has a lower formation energy at the surface than

in the bulk, which leads to a vacancy flux from the surface to the bulk. Diffusion calculations using Fick's equations similar to what was used in our previous work [68] suggest that such a vacancy flux can be significant for an ultra-thin sample at a temperature higher than 100 °C, as was the case for *in situ* annealing experiments. The fact that small GP zones shrink during *in situ* annealing is an indication of such vacancy flux (see Fig. S4 in the Supplementary Material). The induced vacancies are also likely to be the source for Shockley partial dislocations, which is required for  $\gamma'$  formation within GP zones  $\epsilon$ . The oil quenched samples with large GP zones after long ageing times are depleted of vacancies. When vacancies are induced to mediate solute diffusion, those large GP zones with the local ordering of Ag on  $\{111\}_{\text{Al}}$  act as a template for  $\zeta$  formation. We will report a quantitative study on the *in situ* experiments to elucidate the vacancy-induced transformation in the future.

The existence of the  $\zeta$  phase suggests a new phase transformation approach that gives a more gradual change in terms of the chemical compositions and atomic structures. A  $\zeta$  precipitate (50 at.% of Ag in the AgAl model) develops from the increased local ordering of a GP zone  $\epsilon$  (40 at.% of Ag at 200 °C) [45,46] before transforming into HCP  $\gamma'/\gamma$  (67 at.% Ag) [18,19]. Figs. 3 and 5 clearly show that  $\zeta$  is an intermediate phase between GP zone  $\epsilon$  and  $\gamma'$ . The absence of shear in  $\zeta$  minimises the energy barrier for its formation, which is considered to restrict  $\gamma'$  nucleation [60]. Previous calculations also have shown that pure Ag layers lower the stacking fault energy in Al [70], which offers a pathway for a  $\zeta$  to  $\gamma'$  transformation. However, some questions are still open regarding the relationship between  $\zeta$  and  $\gamma'$ . Although the tilt series indicates that  $\zeta$  can form independently from  $\gamma'$  (See Fig. 6), the two metastable phases are generally seen in association with one another (Fig. 3(b–c), 4, 5). The *in situ* movie also suggests that the formation of one phase may assist in the nucleation and/or growth of the other. However, the transformation from  $\zeta$  to  $\gamma'$  is not understood yet at the atomistic level. We have seen  $\zeta$  absorbed by an existing  $\gamma'$  assembly in Fig. 5, instead of initiating new  $\zeta$  precipitates. In the previous phase diagram [45], there is no intermediate phase in the composition range between  $\text{Ag}_2\text{Al}$  and Al except the metastable GP zones. However, several possible structures with the composition of AgAl were predicted using cluster expansions of DFT results [58,71]. For the HCP-based structures, the bi-layered AgAl phase was predicted to be an equilibrium ground state, which has a stacking along any direction normal to the prismatic planes [71]. For the FCC-based structures, a super-lattice of bi-layered AgAl stacking along  $(110)_{\text{Al}}$  was found to be a low energy state [58]. The large periodic size of  $\zeta$  along  $(001)_{\zeta} \parallel (111)_{\text{Al}}$  means such structures are difficult to predict via the cluster expansion method. This points out the importance of atomic resolution electron microscopy for providing critical structural information for atomistic calculations.

The  $\zeta$  phase in the Al-Ag system has structural similarities with layered Ag segregations to precipitate interfaces in various aluminium alloys. It is very interesting that Al-Ag alloys have a poor mechanical performance but numerous aluminium alloys with a minor addition of Ag constitute the strongest and most thermally stable series [24]. Taking the famous example of Al-Cu-Mg-Ag alloys, the  $\Omega$  phase is responsible for their outstanding mechanical performance and thermal stability [24]. The  $\Omega$  phase is considered as a distorted  $\theta$  ( $\text{Al}_2\text{Cu}$ ) on  $\{111\}_{\text{Al}}$ , which is originally body-centred tetragonal, forming on  $\{100\}_{\text{Al}}$  planes [72,73]. To reorient Cu atoms from  $\{100\}_{\text{Al}}$  planes to  $\{111\}_{\text{Al}}$  planes, Mg is essential to minimise the misfit of the  $\Omega$  phase along its c-axis, which can be as large as  $-9.3\%$  matching half unit cell of the  $\Omega$  phase with multiples of  $\{111\}_{\text{Al}}$  d-spacing [37]. Indeed, the  $\Omega$  phase is not found in Al-Cu or Al-Cu-Ag alloys [38], and only very few  $\Omega$  precipitates appear in Al-

Cu-Mg alloys where the dominant precipitate phase is the S phase [24,25]. However, this fact as well as our unpublished DFT calculations [74] suggest Mg itself does not have much tendency to drive the aggregation of Cu atoms on  $\{111\}_{\text{Al}}$ . As we have shown above that Ag prefers to aggregate on  $\{111\}_{\text{Al}}$  planes in aluminium (see Table 2). Furthermore, Ag and Mg are known to interact strongly [30]. The addition of Ag attracts Mg to the  $\{111\}_{\text{Al}}$  planes, which greatly promotes the  $\Omega$  phase and suppresses the S phase. This is evident by the existence of a mono-layer of Ag associated with a mono-layer of Mg at the coherent interface of  $\Omega$ -Al; such interfacial phase can independently exist at the early stages of precipitation [37]. Precipitates nucleate from solute clusters, and hence the determination of the location of the clusters is important. As Ag decomposes quickly from the solid solution and interacts strongly with other solute elements and quenched-in vacancies, the preference of Ag aggregation provides a special kind of heterogeneous nucleation site. The nucleation sites are strongly biased on  $\{111\}_{\text{Al}}$  planes, thus giving Ag the ability to modify subsequent precipitation. Interestingly, Ag also aggregates on  $\{0001\}$  planes in Mg ( $\{0001\}/\{111\}$  planes are the close-packed planes in HCP/FCC), stimulating precipitation in magnesium alloys [75,76]. It is not the purpose of this paper to unify the microalloying mechanisms of Ag in aluminium, but we hope the present study on the Al-Ag binary system will provide a useful reference to the phase transformations of complicated aluminium alloys containing Ag. Particularly, the preference of specific crystallographic planes for Ag aggregation may shed light on its microalloying effects in aluminium.

## 5. Conclusion

We performed scanning transmission electron microscopy to examine the phases and phase transformations in an Al-1.68 at.% Ag alloy. The energetics of Ag clustering within aluminium were studied by density functional theory. The main conclusions are as follows:

1. We discovered a new precipitate phase which we named  $\zeta$  in the Al-Ag system. The  $\zeta$  phase is an intermediate precipitate phase between GP zone  $\epsilon$  and  $\gamma'/\gamma$  in the Al-Ag precipitation sequence. The structure of  $\zeta$  is characterised by the long range ordering of bilayers enriched in Al and Ag on alternative  $\{111\}_{\text{Al}}$  planes. The  $\zeta$  phase is coherent and displays alternating lattice displacements relative to the aluminium matrix in  $\langle 111 \rangle_{\text{Al}}$ . The composition of  $\zeta$  is close to AgAl.
2. Small Ag enriched clusters are formed during quenching and these grow into GP zones  $\epsilon$  with inhomogeneous Ag distribution during ageing at 200 °C. This chemical inhomogeneity is caused by the Ag aggregation on  $\{111\}_{\text{Al}}$  planes with favourable spacing. GP zone  $\epsilon$  with a local ordering of Ag solute may transform into  $\zeta$ , particularly via *in situ* annealing of a TEM sample with induced vacancies.
3. The fast decomposition from the solid solution and the preferred  $\{111\}_{\text{Al}}$  planes for aggregation are intrinsic properties of Ag in aluminium. It provides heterogeneous nucleation sites on  $\{111\}_{\text{Al}}$  planes when Ag is microalloyed in aluminium alloys and fundamentally influences precipitation.

## Acknowledgements

The authors acknowledge funding from the Australian Research Council (LE0454166, LE110100223), the Victorian State Government and Monash University for instrumentation, and use of the facilities within the Monash Centre for Electron Microscopy. LB and NM acknowledge the financial support of the Australian Research

Council (DP150100558). Authors also gratefully acknowledge the computational support from Monash Sun Grid cluster, the National Computing Infrastructure and Pawsey Supercomputing Centre. ZZ is thankful to Monash University for a Monash Graduate Scholarship, a Monash International Postgraduate Research Scholarship and a Monash Centre for Electron Microscopy Postgraduate Scholarship. ZZ is indebted to Matthew Weyland for his training on tilt series, Scott Findlay for his help on image simulations, Tianyu Liu for a Gatan Digital Micrograph script, Peter Miller for X-ray absorption analysis, Jonathan Peter for discussing geometric phase analysis, Xiang Gao for alloy casting, Ian Polmear for advice, and Yiqiang Chen and Xuan Chen for reading the manuscript.

## Appendix A. Supplementary data

Supplementary data related to this article can be found at <http://dx.doi.org/10.1016/j.actamat.2017.04.061>.

## References

- [1] A. Guinier, Le mécanisme de la précipitation dans un cristal de solution solide métallique—cas des systèmes aluminium-cuivre et aluminium-argent, *J. Phys. Radium* 3 (7) (1942) 124–136.
- [2] D.A. Porter, K.E. Easterling, M. Sherif, *Phase Transformations in Metals and Alloys*, CRC press, 2011, pp. 285–286 (Revised Reprint).
- [3] H. Aaronson, M. Enomoto, J. Lee, *Mechanisms of Diffusional Phase Transformations in Metals and Alloys*, CRC Press, 2010, pp. 433–491.
- [4] D. Askeland, P. Fulay, W. Wright, *The Science and Engineering of Materials*, Cengage Learning, 2010, p. 462.
- [5] P.A. Dube, B. Schönfeld, G. Kostorz, Shape and internal structure of Guinier-Preston zones in Al-Ag, *Acta Metal. Mater.* 39 (6) (1991) 1161–1170.
- [6] K.T. Moore, J.M. Howe, Characterization of gamma plate-shaped precipitates in an Al-4.2 at.% Ag alloy—growth kinetics, solute field, composition and modeling, *Acta Mater.* 48 (16) (2000) 4083–4098.
- [7] R. Erni, H. Heinrich, G. Kostorz, Quantitative characterisation of chemical inhomogeneities in Al-Ag using high-resolution Z-contrast STEM, *Ultra-microscopy* 94 (2) (2003) 125–133.
- [8] R. Erni, H. Heinrich, G. Kostorz, High-resolution z-contrast STEM of Guinier-Preston zones in Al-3 at.% Ag, *Mater. Chem. Phys.* 81 (2) (2003) 227–229.
- [9] J.M. Howe, N. Prabhu, The structure of kinks at dislocation interphase boundaries and their role in boundary migration I. Experimental observation of kink motion, *Acta Metal. Mater.* 38 (6) (1990) 881–887.
- [10] J.M. Howe, W.E. Benson, Determination of the atomic structure, mechanisms and kinetics of precipitate growth in solids by *in situ* hot-stage high-resolution transmission electron microscopy, *Interface Sci.* 2 (4) (1995) 347–363.
- [11] K. Inoke, K. Kaneko, M. Weyland, P.A. Midgley, K. Higashida, Z. Horita, Severe local strain and the plastic deformation of Guinier-Preston zones in the Al-Ag system revealed by three-dimensional electron tomography, *Acta Mater.* 54 (11) (2006) 2957–2963.
- [12] S.V. Aert, K.J. Batenburg, M.D. Rossell, R. Erni, G.V. Tendeloo, Three-dimensional atomic imaging of crystalline nanoparticles, *Nature* 470 (7334) (2011) 374–377.
- [13] R. Baur, V. Gerold, The existence of a metastable miscibility gap in aluminium-silver alloys, *Acta Metal.* 10 (6) (1962) 637–645.
- [14] J.E. Gragg, J.B. Cohen, The structure of Guinier-Preston zones in aluminum-5 at.% silver, *Acta Metall.* 19 (6) (1971) 507–519.
- [15] T. Al-Kassab, P. Haasen, Early stages of precipitation in dilute Al-Ag alloys, *Z. für Met.* 84 (4) (1993) 248–250.
- [16] A. Guinier, On the birth of GP zones, in: *Materials Science Forum*, vol. 217, Trans Tech Publications, 1996, pp. 3–6.
- [17] R.B. Nicholson, J. Nutting, The metallography of precipitation in an Al-16% Ag alloy, *Acta Metall.* 9 (4) (1961) 332–343.
- [18] J.P. Neumann, Determination of the ordering in the intermetallic compound  $\text{Ag}_2\text{Al}$ , *Acta Metall.* 14 (4) (1966) 505–511.
- [19] J.M. Howe, U. Dahmen, R. Gronsky, Atomic mechanisms of precipitate plate growth, *Philos. Mag. A* 56 (1) (1987) 31–61.
- [20] S. Ogata, J. Li, S. Yip, Ideal pure shear strength of aluminum and copper, *Science* 298 (5594) (2002) 807–811.
- [21] J.M. Rosalie, L. Bourgeois, B.C. Muddle, Precipitate assemblies formed on dislocation loops in aluminium-silver-copper alloys, *Philos. Mag.* 89 (25) (2009) 2195–2211.
- [22] I.J. Polmear, A trace element effect in alloys based on the aluminium-zinc-magnesium system, *Nature* 186 (4721) (1960) 303–304.
- [23] J.H. Auld, J.T. Vietz, I.J. Polmear, T-phase precipitation induced by the addition of silver to an aluminium-copper-magnesium alloy, *Nature* 209 (5024) (1966) 703–704.
- [24] I.J. Polmear, *Wrought Aluminium Alloys*, fourth ed., Butterworth-Heinemann, Oxford, 2005, pp. 97–204.

- [25] G. Sha, R. Marceau, S. Ringer, *Fundamentals of Aluminium Metallurgy: Production, Processing and Applications*, Woodhead Publishing Series in Metals and Surface Engineering, Elsevier Science, 2010, pp. 345–366. Ch. Precipitation and solute clustering in aluminium: advanced characterisation techniques.
- [26] S.P. Ringer, K. Hono, Microstructural evolution and age hardening in aluminium alloys: atom probe field-ion microscopy and transmission electron microscopy studies, *Mater. Charact.* 44 (1) (2000) 101–131.
- [27] J. Nakamura, K. Matsuda, T. Kawabata, T. Sato, Y. Nakamura, S. Ikeno, Effect of silver addition on the  $\beta'$  phase in Al-Mg-Si-Ag alloy, *Mater. Trans.* 51 (2) (2010) 310–316.
- [28] C. Marioara, J. Nakamura, K. Matsuda, S. Andersen, R. Holmestad, T. Sato, T. Kawabata, S. Ikeno, HAADF-STEM study of  $\beta'$ -type precipitates in an over-aged Al-Mg-Si-Ag alloy, *Philos. Mag.* 92 (9) (2012) 1149–1158.
- [29] S. Wenner, C.D. Marioara, Q.M. Ramasse, D.-M. Kepaptsoglou, F.S. Hage, R. Holmestad, Atomic-resolution electron energy loss studies of precipitates in an Al-Mg-Si-Cu-Ag alloy, *Scr. Mater.* 74 (2014) 92–95.
- [30] I.J. Polmear, Role of trace elements in aged Aluminium-Alloys 13 (1987) 195–214.
- [31] K. Hono, T. Sakurai, I.J. Polmear, Pre-precipitate clustering in an Al-Cu-Mg-Ag alloy, *Scr. Metal. Mater.* 30 (6) (1994) 695–700.
- [32] S.P. Ringer, W. Yeung, B.C. Muddle, I.J. Polmear, Precipitate stability in Al-Cu-Mg-Ag alloys aged at high temperatures, *Acta Metal. Mater.* 42 (5) (1994) 1715–1725.
- [33] M. Murayama, K. Hono, Three dimensional atom probe analysis of pre-precipitate clustering in an Al-Cu-Mg-Ag alloy, *Scr. Mater.* 38 (8) (1998) 1315–1319.
- [34] L. Reich, M. Murayama, K. Hono, Evolution of  $\Omega$  phase in an Al-Cu-Mg-Ag alloy—a three-dimensional atom probe study, *Acta Mater.* 46 (17) (1998) 6053–6062.
- [35] A. Somoza, A. Dupasquier, I.J. Polmear, P. Folegati, R. Ferragut, Positron-annihilation study of the aging kinetics of AlCu-based alloys. II. Ag micro-alloying, *Phys. Rev. B* 61 (21) (2000) 14464.
- [36] C. Hutchinson, X. Fan, S. Pennycook, G. Shiflet, On the origin of the high coarsening resistance of  $\Omega$  plates in Al-Cu-Mg-Ag Alloys, *Acta Mater.* 49 (14) (2001) 2827–2841.
- [37] S.J. Kang, Y.W. Kim, J.M. Zuo, Determination of interfacial atomic structure, misfits and energetics of  $\Omega$  phase in Al-Cu-Mg-Ag alloy, *Acta Mater.* 81 (2014) 501–511.
- [38] J.M. Rosalie, L. Bourgeois, Silver segregation to  $\theta'$  (Al<sub>2</sub>Cu)-Al interfaces in Al-Cu-Ag alloys, *Acta Mater.* 60 (17) (2012) 6033–6041.
- [39] S.J. Kang, T.H. Kim, C.W. Yang, J.I. Lee, E.S. Park, T.W. Noh, M. Kim, Atomic structure and growth mechanism of  $T_1$  precipitate in Al-Cu-Li-Mg-Ag alloy, *Scr. Mater.* 109 (2015) 68–71.
- [40] Y. Baba, Influence of some additional elements on the aging kinetics in Al-Cu and Al-Cu-Mg alloys, *Trans. Jpn. Inst. Metals* 10 (3) (1969) 188–195.
- [41] J.M. Rosalie, C. Dwyer, L. Bourgeois, On chemical order and interfacial segregation in  $\gamma'$ (AlAg<sub>2</sub>) precipitates, *Acta Mater.* 69 (2014) 224–235.
- [42] J.M. LeBeau, S.D. Findlay, L.J. Allen, S. Stemmer, Position averaged convergent beam electron diffraction: theory and applications, *Ultramicroscopy* 110 (2) (2010) 118–125.
- [43] D.B. Williams, C.B. Carter, *Quantitative X-ray Analysis*, Springer US, Boston, MA, 2009, pp. 639–662.
- [44] B.L. Henke, E.M. Gullikson, J.C. Davis, X-ray interactions: photoabsorption, scattering, transmission, and reflection at  $e= 50\text{--}30,000$  eV,  $z= 1\text{--}92$ , Atomic data and nuclear data tables 54(2), 1993, pp. 181–342.
- [45] A. McAlister, The Ag-Al (Silver-Aluminum) system, *Bull. Alloy Phase Diag.* 8 (6) (1987) 526–533.
- [46] E.A. Marquis, A reassessment of the metastable miscibility gap in Al-Ag alloys by atom probe tomography, *Microsc. Microanal.* 13 (06) (2007) 484–492.
- [47] L.J. Allen, A.J. D'Alfonso, S.D. Findlay, Modelling the inelastic scattering of fast electrons, *Ultramicroscopy* 151 (2015) 11–22.
- [48] M.J. Hÿtch, E. Snoeck, R. Kilaas, Quantitative measurement of displacement and strain fields from HREM micrographs, *Ultramicroscopy* 74 (3) (1998) 131–146.
- [49] M.J. Hÿtch, J.-L. Putaux, J.-M. Pénisson, Measurement of the displacement field of dislocations to 0.03 Å by electron microscopy, *Nature* 423 (6937) (2003) 270–273.
- [50] C.L. Johnson, M.J. Hÿtch, P.R. Buseck, Nanoscale waviness of low-angle grain boundaries, *Proc. Natl. Acad. Sci.* 101 (52) (2004) 17936–17939.
- [51] A. Stukowski, A. Arsenlis, On the elastic-plastic decomposition of crystal deformation at the atomic scale, *Model. Simul. Mater. Sci. Eng.* 20 (3) (2012) 035012.
- [52] A. Stukowski, Visualization and analysis of atomistic simulation data with OVITO—the open visualization tool, *Model. Simul. Mater. Sci. Eng.* 18 (1) (2010) 015012.
- [53] C. Ophus, J. Ciston, C.T. Nelson, Correcting nonlinear drift distortion of scanning probe and scanning transmission electron microscopies from image pairs with orthogonal scan directions, *Ultramicroscopy* 162 (2016) 1–9.
- [54] G. Kresse, J. Furthmüller, Efficient iterative schemes for ab initio total-energy calculations using a plane-wave basis set, *Phys. Rev. B* 54 (16) (1996) 11169.
- [55] J.P. Perdew, K. Burke, M. Ernzerhof, Generalized gradient approximation made simple, *Phys. Rev. Lett.* 77 (18) (1996) 3865.
- [56] P.E. Blöchl, Projector augmented-wave method, *Phys. Rev. B* 50 (1994) 17953–17979.
- [57] G. Kresse, D. Joubert, From ultrasoft pseudopotentials to the projector augmented-wave method, *Phys. Rev. B* 59 (3) (1999) 1758.
- [58] C. Wolverton, V. Ozoliņš, First-principles aluminum database: energetics of binary Al alloys and compounds, *Phys. Rev. B* 73 (14) (2006) 144104.
- [59] N.A. Zarkevich, D.D. Johnson, A.V. Smirnov, Structure and stability of hcp bulk and nano-precipitated Ag<sub>2</sub>Al, *Acta Mater.* 50 (9) (2002) 2443–2459.
- [60] J.M. Rosalie, L. Bourgeois, B.C. Muddle, Nucleation and growth of the gamma prime (AlAg<sub>2</sub>) precipitate in Al-Ag (-Cu) alloys, *Acta Mater.* 59 (19) (2011) 7168–7176.
- [61] M.I. Zakharova, N.A. Khatanova, Identification of crystals of phases precipitating in an Al-Cu-Ag alloy and the topology of their growth, *Kristallografiya* 11 (4) (1966) 692–694.
- [62] C. Dwyer, J. Etheridge, Scattering of Å-scale electron probes in silicon, *Ultramicroscopy* 96 (3–4) (2003) 343–360.
- [63] M. Hillert, *Phase Equilibria, Phase Diagrams and Phase Transformations: their Thermodynamic Basis*, Cambridge University Press, 1998, pp. 482–486.
- [64] C. Wolverton, Solute-vacancy binding in aluminum, *Acta Mater.* 55 (17) (2007) 5867–5872.
- [65] L. Bourgeois, Z. Zhang, J. Li, N.V. Medhekar, The bulk and interfacial structures of the  $\eta$  (Al<sub>2</sub>Au) precipitate phase, *Acta Mater.* 105 (2016) 284–293.
- [66] Y. Chen, Z. Zhang, Z. Chen, A. Tsalanidis, M. Weyland, S. Findlay, L.J. Allen, J. Li, N.V. Medhekar, L. Bourgeois, The enhanced theta-prime ( $\theta'$ ) precipitation in an Al-Cu alloy with trace Au additions, *Acta Mater.* 125 (2017) 340–350.
- [67] M. Murayama, K. Hono, Role of Ag and Mg on precipitation of  $T_1$  phase in an Al-Cu-Li-Mg-Ag alloy, *Scr. Mater.* 44 (4) (2001) 701–706.
- [68] Z. Zhang, T. Liu, A. Smith, N. Medhekar, P. Nakashima, L. Bourgeois, Mechanisms of void shrinkage in aluminium, *J. Appl. Crystallogr.* 49 (5) (2016) 1459–1470.
- [69] S. Gupta, M. van Huis, M. Dijkstra, M. Sluiter, Depth dependence of vacancy formation energy at (100), (110), and (111) Al surfaces: a first-principles study, *Phys. Rev. B* 93 (8) (2016) 085432.
- [70] D. Finkenstadt, D.D. Johnson, Solute/defect-mediated pathway for rapid nanoprecipitation in solid solutions:  $\gamma$  surface analysis in fcc Al-Ag, *Phys. Rev. B* 73 (2) (2006) 024101.
- [71] N.A. Zarkevich, D.D. Johnson, Predicted hcp Ag-Al metastable phase diagram, equilibrium ground states, and precipitate structure, *Phys. Rev. B* 67 (6) (2003) 064104.
- [72] J.H. Auld, Structure of metastable precipitate in some Al-Cu-Mg-Ag alloys, *Mater. Sci. Technol.* 2 (8) (1986) 784–787.
- [73] K.M. Knowles, W.M. Stobbs, The structure of {111} age-hardening precipitates in Al-Cu-Mg-Ag alloys, *Acta Crystallogr. Sect. B* 44 (3) (1988) 207–227.
- [74] Z. Zhang, L. Bourgeois, N. V. Medhekar, Database of solute clustering in aluminium alloys: a DFT study (unpublished).
- [75] Y. Zhang, T. Alam, B. Gwalani, W. Rong, R. Banerjee, L.M. Peng, J.F. Nie, N. Birbilis, On the role of Ag in enhanced age hardening kinetics of Mg-Gd-Ag-Zr alloys, *Philos. Mag. Lett.* 96 (6) (2016) 212–219.
- [76] Y.M. Zhu, K. Oh-ishi, N.C. Wilson, K. Hono, A.J. Morton, J.F. Nie, Precipitation in a Ag-containing Mg-Y-Zn alloy, *Metal. Mater. Trans. A* 47 (2) (2016) 927–940.

# The bi-layered precipitate phase $\zeta$ in the Al-Ag system

## Supplementary Material

Ze Zhong Zhang<sup>a</sup>, Laure Bourgeois<sup>a,b,\*</sup>, Julian M. Rosalie<sup>c</sup>, Nikhil V. Medhekar<sup>a,\*\*</sup>

<sup>a</sup>*Department of Materials Science and Engineering, Monash University, Victoria 3800, Australia*

<sup>b</sup>*Monash Centre for Electron Microscopy, Monash University, Victoria 3800, Australia*

<sup>c</sup>*Erich Schmid Institute of Materials Science, Austria*

---

---

---

\*Corresponding author

\*\*Corresponding author

*Email addresses:* [REDACTED] (Laure Bourgeois), [REDACTED]  
(Nikhil V. Medhekar)

*Preprint submitted to Acta Materialia*

*April 7, 2017*

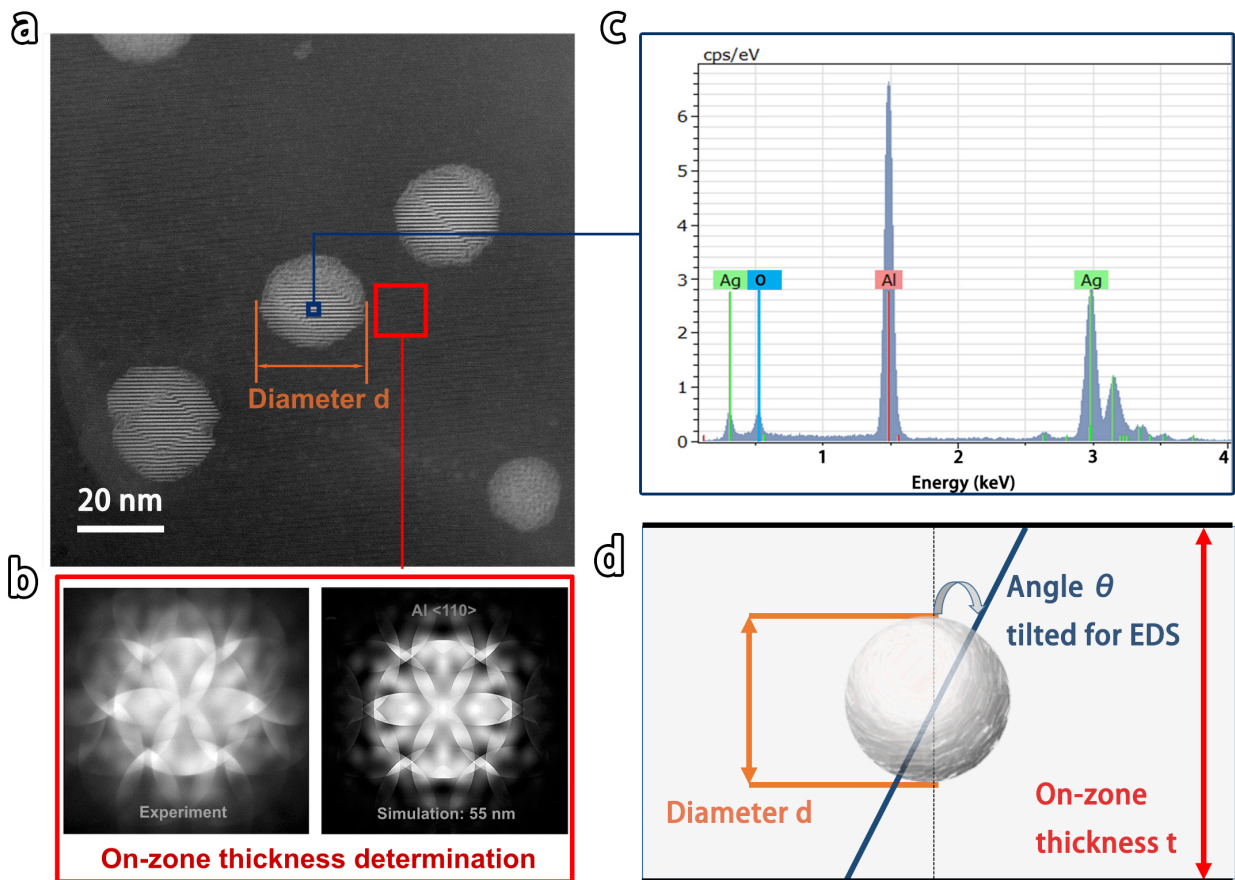


Figure S1: Compositional analysis for an embedded, spherical precipitate by energy-dispersive X-ray spectroscopy (EDS). (a) HAADF-STEM image showing the measurements of a precipitate. The diameter of a precipitate,  $d$ , in the electron transmission direction was estimated by its averaged size on the HAADF-STEM image. The electron beam was parallel to  $\langle 110 \rangle_{Al}$ . (b) The thickness,  $t$ , in the vicinity of a precipitate was determined by comparing an on-zone position-averaged convergent beam electron diffraction (PACBED) pattern of its surrounding matrix with simulations. (c) A position-averaged spectrum was taken at the centre of the precipitate and the composition was quantified by the software supplied with TEM, using the Cliff-Lorimer ratio method. The sample was tilted away from its zone axis to the optimal angle for EDS detector and avoiding strong dynamical diffraction conditions (the electron channelling would be problematic otherwise). We ignored the thin oxide film at the surface of samples. (d) A schematic diagram illustrating the parameters needed for determining the composition as written in the equation in the main text.

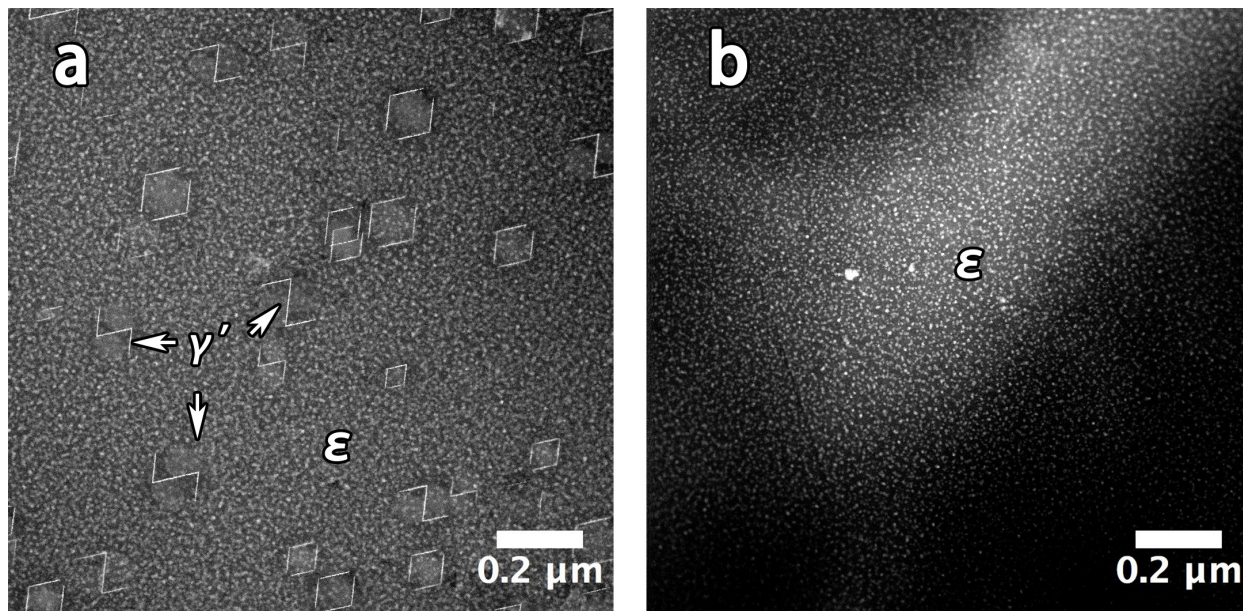


Figure S2: Low magnification HAADF-STEM images showing the microstructure for Al-1.68 at.% Ag aged 2 h at 200°C after (a) quenched in water and (b) quenched in oil from the solid solution temperature at 525°C. The differences in the microstructures between those two conditions are caused by quenched-in vacancies and defects that provide the heterogeneous nucleation sites for  $\gamma'$  precipitates. The electron beam is parallel to  $\langle 110 \rangle_{\text{Al}}$ .

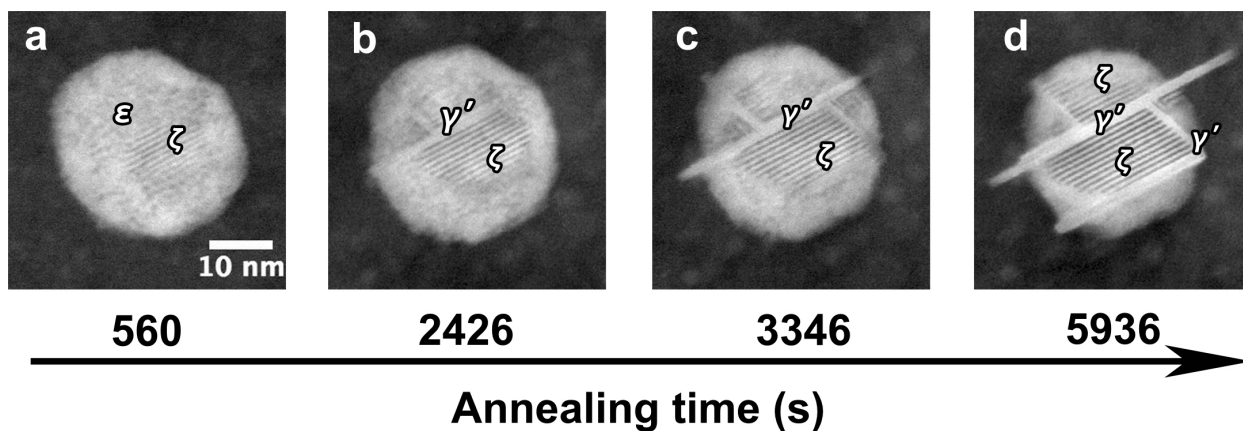


Figure S3: Time-resolved HAADF-STEM images showing  $\epsilon$ - $\zeta$ - $\gamma'$  transformation while *in situ* annealed at 150°C. The original sample was oil quenched and aged at 200°C for 7 days. The recording was started 560 s after *in situ* annealing began, giving the time to correct the drift and reorientation of the crystal due to heating. We used a Gatan Digital Micrograph script to automatically acquire STEM images with an acquisition time of 7.86 s for each frame (a pixel dwell-time of 30  $\mu\text{s}$  for 512 $\times$ 512 pixel) and an interval of 20 s between each frame.  $\zeta$  clearly formed by local ordering of  $\epsilon$  on  $\{111\}_{\text{Al}}$ . The  $\gamma'$  assemblies also formed beside the  $\zeta$ . The full process can be found in the Supplementary Movie. We should note that the distortions in the images and movie were due to the thermal drift during acquisition. The electron beam is parallel to  $\langle 110 \rangle_{\text{Al}}$ .

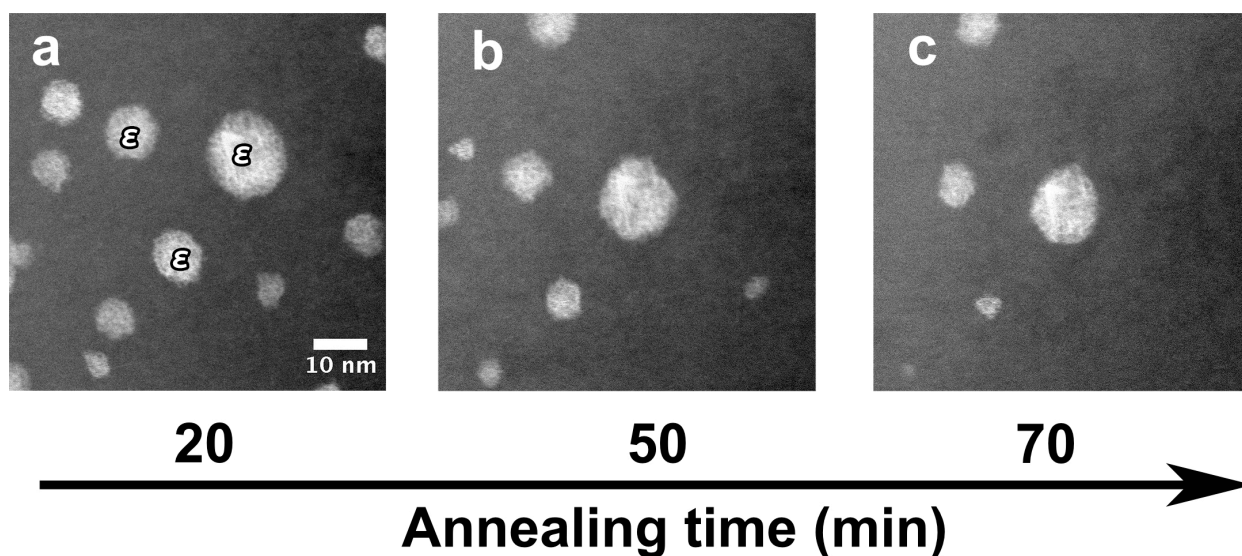


Figure S4: HAADF-STEM images showing the shrinkage of small GP zones during *in situ* annealing at 200°C. The original sample was water quenched and aged at 200°C for 2 h. The electron beam is parallel to  $\langle 110 \rangle_{Al}$ .

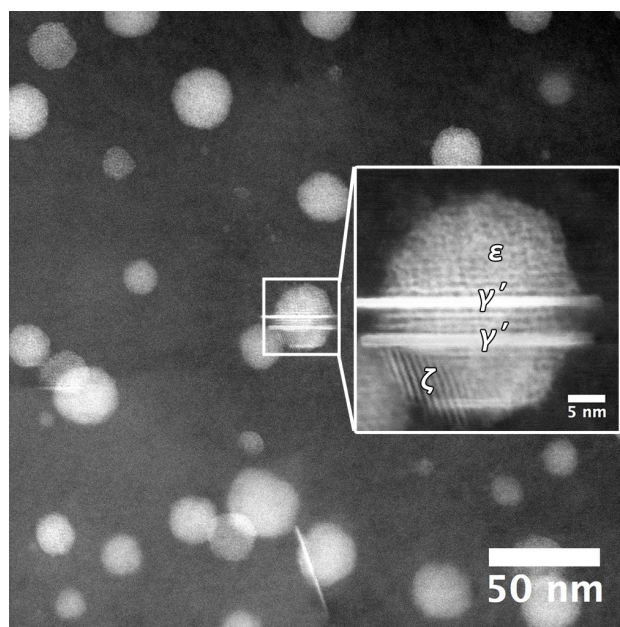


Figure S5: HAADF-STEM images showing the  $\zeta$  phase and  $\gamma'$  phase were found in a sample *in situ* annealed at 200°C for 3 min without beam irradiation during *in situ* annealing. The original sample was oil quenched and aged at 200°C for 7 days. The electron beam is parallel to  $\langle 110 \rangle_{Al}$ .

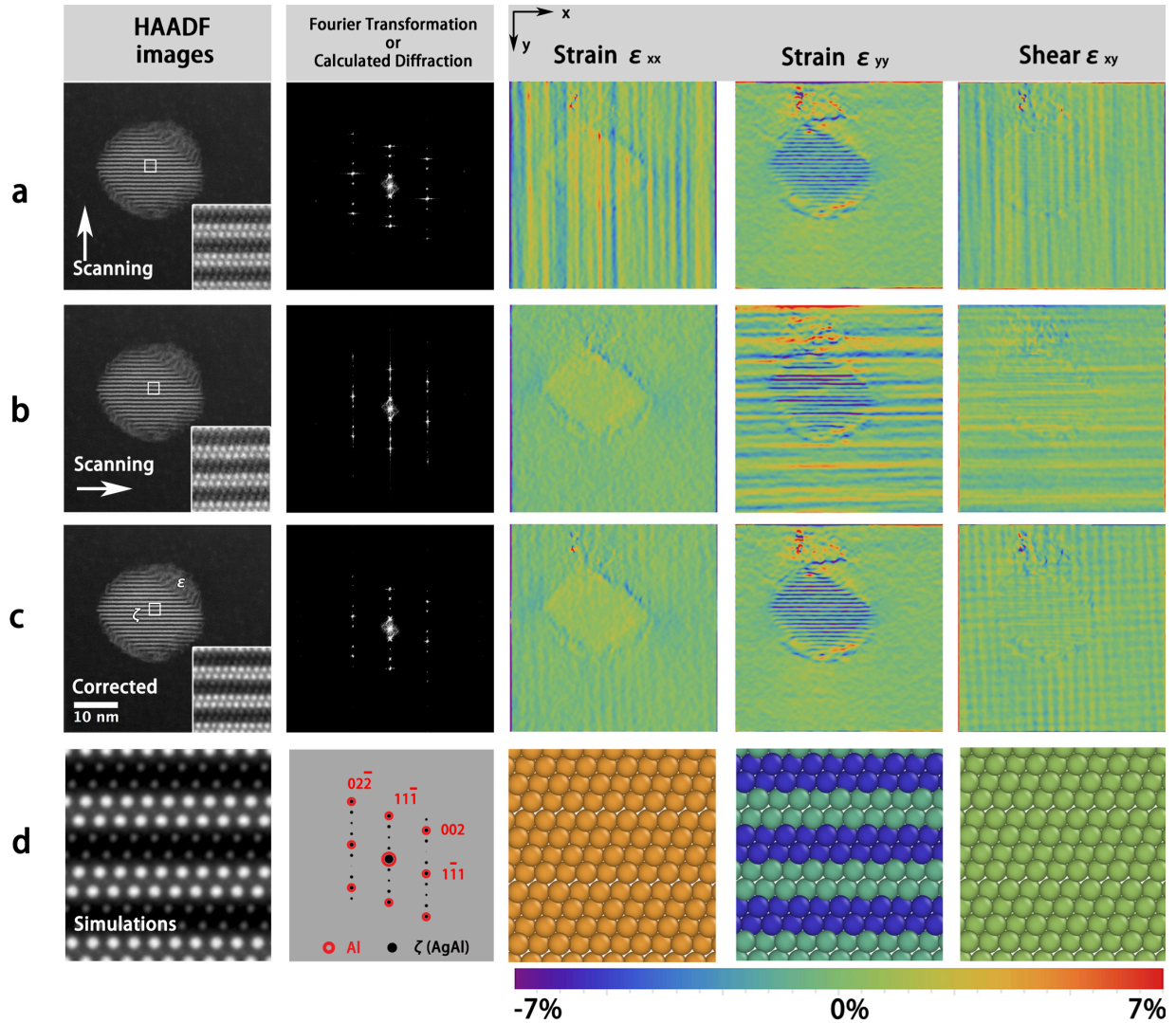


Figure S6: Nonlinear drift correction for geometric phase analysis, in comparison to simulations of bulk AgAl structure. HAADF images (with enlarged inserts), Fourier transform amplitudes and strain field measurements for (a) vertical scan direction, (b) horizontal scan direction, (c) drift-corrected images from (a) and (b), (d) simulations ( $\mu$ STEM and elastic lattice strain calculations) of bulk AgAl structure respectively. The arrows in (a) and (b) indicate the fast scanning directions for each case. The electron beam is parallel to  $\langle 110 \rangle_{\text{Al}}$ . There are noticeable noise in the direction normal to the fast scanning direction as shown in the GPA results, which corresponds to the strikes in Fourier transformations. The kinematic diffraction pattern was calculated by CrystalMaker SingleCrystal software, based on bulk AgAl structure after optimisation by DFT calculations. Red circles highlight the reflections of AgAl that are overlapped with Al (the reflections are indexed).

